UNICAMP

Universidade Estadual de Campinas

Faculdade de Engenharia Elétrica e de Computação

ANDRES DE JESUS ARGUELLO GUILLEN

METHODOLOGIES FOR ANALYSIS, MANAGEMENT AND MITIGATION OF RESONANCE IN WIND PARKS

METODOLOGIAS PARA ANÁLISE, GERENCIAMENTO E MITIGAÇÃO DE RESSONÂNCIA EM PARQUES EÓLICOS

CAMPINAS

2022

Universidade Estadual de Campinas

Faculdade de Engenharia Elétrica e de Computação

ANDRES DE JESUS ARGUELLO GUILLEN

METHODOLOGIES FOR ANALYSIS, MANAGEMENT AND MITIGATION OF RESONANCE IN WIND PARKS

METODOLOGIAS PARA ANÁLISE, GERENCIAMENTO E MITIGAÇÃO DE RESSONÂNCIA EM PARQUES EÓLICOS

Thesis presented to the School of Electrical and Computer Engineering of the University of Campinas in partial fulfillment of the requirements for the degree of Doctor in Electrical Engineering, in the area of Electrical Energy.

Tese apresentada à Faculdade de Engenharia Elétrica e de Computação da Universidade Estadual de Campinas como parte dos requisitos exigidos para a obtenção do título de Doutor em Engenharia Elétrica, na Área de Energia Elétrica

Supervisor/*Orientador*: Prof. Dr. Walmir de Freitas Filho

Co-Supervisor/*Co-Orientador*: Dr. Ricardo Torquato Borges

Este exemplar corresponde à versão final da tese defendida pelo aluno Andres de Jesus Arguello Guillen, orientada pelo Prof. Dr. Walmir de Freitas Filho e co-orientada pelo Dr. Ricardo Torquato Borges.

____

CAMPINAS

2022

Ficha catalográfica
Universidade Estadual de Campinas
Biblioteca da Área de Engenharia e Arquitetura
Rose Meire da Silva - CRB 8/5974

Ar38m

Arguello Guillen, Andres de Jesus, 1991-
Methodologies for analysis, management and mitigation of resonance in wind parks / Andres de Jesus Arguello Guillen. – Campinas, SP : [s.n.], 2022.

Orientador: Walmir de Freitas Filho.
Coorientador: Ricardo Torquato Borges.
Tese (doutorado) – Universidade Estadual de Campinas, Faculdade de Engenharia Elétrica e de Computação.

1. Harmônicos (Ondas elétricas). 2. Ressonância. 3. Sistemas de energia elétrica - Estabilidade. 4. Energia eólica. I. Freitas Filho, Walmir de, 1971-. II. Borges, Ricardo Torquato, 1989-. III. Universidade Estadual de Campinas. Faculdade de Engenharia Elétrica e de Computação. IV. Título.

Informações para Biblioteca Digital

Título em outro idioma: Metodologias para análise, gerenciamento e mitigação de ressonância em parques eólicos
Palavras-chave em inglês:
Harmonics (Electric waves)
Resonance
Electric power systems - Stability
Wind energy
Área de concentração: Energia Elétrica
Titulação: Doutor em Engenharia Elétrica
Banca examinadora:
Walmir de Freitas Filho [Orientador]
José Antenor Pomilio
Daniel Dotta
Pedro André Carvalho Rosas
Renato Machado Monaro
Data de defesa: 07-07-2022
Programa de Pós-Graduação: Engenharia Elétrica

Identificação e informações acadêmicas do(a) aluno(a)
- ORCID do autor: https://orcid.org/0000-0003-2084-4342
- Currículo Lattes do autor: http://lattes.cnpq.br/7633249164190917

COMISSÃO EXAMINADORA - TESE DE DOUTORADO

Candidato: Andres de Jesus Arguello Guillen RA: 190723

Data da Defesa: 7 de julho de 2022

Título da Tese (em inglês): Methodologies for Analysis, Management and Mitigation of Resonance in Wind Parks

Título da Tese (em português): Metodologias para Análise, Gerenciamento e Mitigação de Ressonância em Parques Eólicos

Prof. Dr. Walmir de Freitas Filho (Presidente, FEEC/UNICAMP)

Prof. Dr. José Antenor Pomilio (Membro Titular Interno, FEEC/UNICAMP)

Prof. Dr. Daniel Dotta (Membro Titular Interno, FEEC/UNICAMP)

Prof. Dr. Pedro André Carvalho Rosas (Membro Titular Externo, GEPAE/UFPE)

Prof. Dr. Renato Machado Monaro (Membro Titular Externo, EP/USP)

A ata de Defesa, com as respectivas assinaturas dos membros da Comissão Examinadora, encontra-se no SIGA/Sistema de Fluxo de Dissertação/Tese e na Secretaria de Pós-Graduação da Faculdade de Engenharia Elétrica e de Computação.

ACKNOWLEDGEMENTS

I want to express my acknowledgements to:

- My supervisor Prof. Walmir de Freitas Filho for his guidance and the opportunity to conduct my M.Sc. and Ph.D. research in the LE-41 laboratory. Prof. Walmir has help me grow as a professional with his vast knowledge and insights on the application of electrical engineering. He inspired me to be more pragmatic and always keep updated.
- Dr. Ricardo Torquato Borges for his friendship, patience and detailed guidance during the development of our work together and teaching me how to properly structure, execute and report technical research projects. Ricardo is an excellent person and professional with a bright future, as well as an example of hard work.
- My colleagues from the LE-41 laboratory for their valuable insight and recommendations for improvement. They welcomed me since day 1 with open arms being a foreigner.
- To my family for their love, support and patience. My mother Salomé Guillén Espinoza who taught me to always aim for my best, my father Léxter Argüello Zamora for introducing me into the world of electricity, my brother Emilio Argüello Guillén for making me want to constantly improve so I can be a good role model for him.
- To my dear wife Bruna Ribeiro Braga who stands by my side in all of our adventures, and for showing me that life should be lived in balance.
- To the Office of International Affairs and External Cooperation of the University of Costa Rica for its financial support through grant OAICE-CAB-165-2016. Special thanks to Yamileth Damazzio, Haydeé Ramos and Mauricio Saborío.
- To the School of Electrical Engineering of the University of Costa Rica for the opportunity of specializing in power quality topics. Special thanks to Dr. Gustavo Valverde and Dr. Orlando Arrieta who saw potential in me to be part of the team back in the day, and to Dr. Jairo Quirós for his advices and showing me the importance of network development.
- To Dr. Alecio Barreto Fernandes from Carpe Vie consulting, for providing the real wind park topology and parameters to conduct the studies of this thesis.

ABSTRACT

The connection of wind parks to the power system continues to grow and replace traditional generation sources. However, despite its many advantages, wind parks can also create adverse technical impacts to the electrical power quality, such as introduce new resonances to the circuit. This type of phenomenon can cause malfunctions and damages on both wind park and grid components, which translates to financial losses for the park operator and the utility. There are two main types of problematic resonances that can be caused by the interaction of wind park components with the grid: weakly damped resonances and unstable resonances. In most cases, these resonances are investigated with multiple highly detailed simulations that require abundant information from the system and the generators and must be conducted by specialized engineers. Even though such analysis provides detailed, precise results, it is time consuming and costly.

In response to this scenario, the main goal of this PhD thesis is to develop a series of methodologies based on charts and simple equations to improve the anticipation, detection, and mitigation of such resonances in wind parks with Type-III (doubly fed induction generators) or Type-IV (full-converter) generators. Initially, one chart is proposed to assess the risk of a weakly damped resonance at the point of common coupling (PCC) between the grid and the wind park by using only information from the park that is readily available in practice to engineers. Another chart-based method is developed to help monitor the risk of a resonance causing component overload inside the park. A third method is proposed to detect the risk of unstable subsynchronous resonances during wind park planning and to monitor the stability margin of the park in real time during its operation. These approaches based on charts and simple equations are useful on first-screening studies, to quickly filter out cases with no risk of resonances without running any computer simulation. More detailed studies should be conducted only for the few cases where the screening indicates a potential risk of resonance. Finally, a method is developed to design a passive harmonic filter to mitigate harmonic distortions in the park. This design method is proved to reach more cost-effective solutions than other design methods that exist in literature and that are typically used in practice.

Keywords: Doubly fed induction generator; Harmonics; Permanent magnet synchronous generator; Power quality; Resonance; Stability; Wind generation.

RESUMO

A conexão de parques eólicos no sistema de potência continua a crescer e substituir fontes de geração tradicionais. Apesar das suas múltiplas vantagens, os parques eólicos também podem criar impactos técnicos adversos na qualidade de energia elétrica, tais como introduzir novas ressonâncias ao circuito. Este fenômeno pode ocasionar funcionamento inadequado e danificar componentes do parque eólico e da rede, o que se traduz em perdas financeiras para os operadores do parque e da rede. Há dois tipos de ressonâncias problemáticas que são ocasionadas pela interação dos componentes do parque com os componentes da rede: ressonâncias fracamente amortecidas, e ressonâncias instáveis. Na maioria dos casos, estas ressonâncias são investigadas com múltiplas simulações altamente detalhadas que requerem informação abundante do sistema e dos geradores, e devem ser feitas por engenheiros especializados. Mesmo que este tipo de análise entregue resultados detalhados e precisos, requer muito tempo e alto custo econômico.

Em resposta a este cenário, o objetivo principal desta tese de doutorado é desenvolver uma série de metodologias baseadas em gráficos e equações simples para melhorar a antecipação, detecção, e mitigação de tais ressonâncias em parques eólicos com geradores Tipo-III (gerador de indução duplamente alimentado) ou Tipo-IV (conectado via inversor). Primeiramente, é proposto um gráfico para analisar o risco de ressonâncias fracamente amortecidas no ponto de conexão entre o parque e a rede, com informações do parque que estão facilmente disponíveis na prática. Outra metodologia gráfica é desenvolvida para monitorar a sobrecarga de componentes dentro do parque eólico por ressonâncias harmônicas. Um terceiro método é proposto para detectar o risco de ressonâncias subsíncronas em parques eólicos durante a fase de planejamento, e para monitorar a margem de estabilidade do parque em tempo real durante sua operação. Estes métodos propostos são úteis em estudos iniciais, para descartar rapidamente casos sem risco de ressonância, sem efetuar simulações computacionais. Assim, estudos mais detalhados são feitos apenas nos poucos casos em que os estudos de triagem indicam potencial risco de ressonância. Finalmente, é proposta uma metodologia para sintonizar filtros passivos para mitigação de distorções harmônicas no parque. Este método apresentou melhor custo-benefício que outras técnicas de sintonização existentes na literatura e utilizadas tipicamente na prática.

Palavras-chave: Gerador de indução duplamente alimentado; Harmônicos; Gerador síncrono de imã permanente; Qualidade de Energia; Ressonância; Estabilidade; Geração eólica.

LIST OF FIGURES

LIST OF TABLES

SUMMARY

1 INTRODUCTION

Wind is currently one of the main renewable energy resources. Worldwide, wind park installed capacity has grown considerably in the last decade reaching nearly 744 GW by 2020 [1]. This tendency is also present in Brazil, where wind power became the electrical energy resource with the second largest installed capacity in 2019, with about 16 GW, representing 9% of the Brazilian electricity matrix [2].

This increase in wind park connections can also lead to adverse technical impacts on the power quality of the grid, such as resonances in both sub-synchronous frequencies (below 60 Hz) and super-synchronous frequencies (above 60 Hz), which lead to lifetime reduction and even permanent damage of the components of the wind parks and the grid [3]. Overall, the resonance events can be broadly categorized into weakly damped resonance and unstable resonance.

1.1 Resonance in wind parks

1.1.1 Weakly damped resonances

Also known as “stable resonances” or “harmonic resonances”. From the system’s analysis perspective, these oscillations can be regarded as “forced oscillations” [4]. Resonances with positive but low damping can be problematic if they take place at low order harmonic frequencies (typically at the 5^{th}, 7^{th}, 11^{th} or 13^{th} harmonics) [5] because they can amplify the existing harmonic distortions of the background grid, potentially reducing the lifetime of grid and wind park components [6], [7]. Additionally, these resonances in the harmonic range of frequencies can also lead to violations of regulatory distortion limits on the grid [8], [9]. These resonances appear mainly due to the interaction between the wind park inductances (main park transformer, wind park feeders and generators), and nearby capacitances (shunt capacitors connected in the park (or close to it) for reactive power compensation, or the shunt capacitances of underground feeders of the park). Unlike unstable resonances, the weakly damped resonances do not cause major catastrophic events. They tend to be a “silent” phenomenon that can remain on the circuit for several months and gradually deteriorate equipment lifetime. These resonances are more common in the field but due to their quiet nature, they are many times unnoticed and there are fewer reports available in the literature specifically addressing field cases. Some examples are listed as follows:

- From 2013 to 2015, super-synchronous events were reported in the Borwin1 offshore project, Northern Sea of Germany in 2013 [10]. Oscillations in the 5th and 7th harmonics were amplified sufficiently to overload the filters, leading to their outage and subsequently, the outage of the HVDC line connecting the wind park to the shore.
- Important voltage distortions at harmonic frequencies were measured in several wind parks in India [11] during a project to recommend guidelines to improve the power quality indices of the grid and assess the harmonic impact of wind park connections.
- Harmonic resonance issues were also reported in [12] when specific stages of a shunt capacitor bank for power factor correction in a wind park were connected to the circuit.
- Different topologies of passive harmonic filters were designed and tested to mitigate the harmonic resonance problems of a wind park in Brazil [13].
- An active harmonic filtering strategy was implemented for an offshore wind park in Denmark to mitigate excessive harmonic distortions [14].

1.1.2 Unstable resonances

These are fast, large-scale events which arise due to a resonance caused by the interaction of grid inductances with series or shunt capacitors, combined with negative damping introduced by the controllers of the wind generators and by the negative slip of the induction machine of Type-III generators (induction machine effect, which takes place specifically at subsynchronous frequencies). These events also take place due to interaction between the phase-locked loop (PLL) of the generators and the terminal voltage when connected to a weak grid [3], [15]. From the system's analysis perspective, these oscillations can be regarded as "free oscillations" [4].

The current and voltage values reached during unstable resonance events may lead to instantaneous damage of components and loss of large blocks of generation. The following is a list of unstable resonance events reported in the literature:

- The first report of an unstable sub-synchronous resonance event involving a wind park and no mechanical oscillations from other generators occurred in Minnesota, United States [16]. As a part of planned grid reinforcements, a 60% series capacitive compensation was installed in a 54-mile transmission line. A system reconfiguration left this line radially connected to a wind park and a thermal generator. Unstable subsynchronous oscillations initiated and damaged some wind generators and busbars near the thermal generators.

Further analysis determined that the resonance modes of the thermal generator did not match the sub-synchronous oscillation frequencies. At the time, the phenomenon was not fully understood as subsynchronous resonance were typically associated with synchronous machines, but the control systems of the wind park were later found to be the culprit.

- The second event was reported in Texas, United States, in 2009 after a short circuit which produced a line outage, leaving two Type-III wind parks, i.e., Doubly-fed induction generator (DFIGs) based wind parks, radially connected to a 108 km line with 50% series compensation [17]. Such event reached a voltage of nearly 2 pu in less than 1 second, which damaged several crowbar circuits of the generators and stages of the series capacitor [18].
- From 2012 to 2013, over 58 unstable sub-synchronous resonance events were reported in Heibei, China. These occurred in a cluster of wind parks fed radially by two transmission lines with 40% and 45% capacitive compensation, respectively. The generators were a mix with 82.8% of Type-III, 15.4% of Type-IV and 1.8% of other technologies. Configurations of high series compensation and low wind created unstable sub-synchronous oscillations, which led to multiple generator trips. Mitigation was achieved by bypassing the series capacitor causing the problem [19].
- From 2014 to 2015, sub-synchronous resonance events were captured in the Xianjiang Uygur, China, involving Type-IV wind parks, i.e., permanent magnet synchronous generators (PMSG), connected to a weak network without capacitive compensation [20], [21]. In one occasion, the oscillation of the PMSGs matched a torsional mode of a nearby thermal generator site which led to the outage of all of its units of this site due operation of the vibrational relays.
- Three events after line trips were reported in Texas, United States, involving Type-III generators fed radially by transmission lines with series capacitive compensation. As in the previous event in 2009, sub-synchronous oscillations occurred. The wind generators had built-in mechanisms for sub-synchronous resonance mitigation, but this mechanism was not able to eliminate the event and multiple generators were disconnected.

1.2 Techniques to assess resonance in wind parks

There are three main techniques typically used to investigate these phenomena, and they are briefly discussed in this section [3], [15]. This thesis was developed using the frequency-domain approach based on impedance equivalents.

1.1.3 Time domain modeling and simulation

It consists of running numerous electromagnetic transient (EMT) simulations of different scenarios to map problematic parameter combinations. These simulations consider highly detailed non-linear models which require abundant information from both the circuit and the generators. This is the most accurate approach, yet it demands significant computational capabilities and specialization for modeling and results processing [10], [22].

1.1.4 Eigenvalue analysis

This approach calculates the oscillation modes from the linear state space model of the system, including the grid and the generators. This approach allows to determine the resonance frequencies and respective damping coefficients directly from the state transition matrix, as well as quantifying all states participations in each resonance [6], [23]. Although very powerful, this approach can become impractical due to the large matrices required for higher order systems. For example, changes in the system topology can lead to extensive algebraic manipulations, especially when modeling wind parks with multiple generators and feeders, or large grids.

1.1.5 Frequency domain modeling

This technique consists of using frequency-dependent equivalent impedance profiles of the generators [24], [25]. The profiles can be obtained numerically from the transfer functions of terminal voltages to terminal currents using the state space model, or from analytic expressions derived based on the generator and control characteristics. Complexity of the analytic expression depends on the level of modeling detail from the state space model. Bode diagrams are commonly used to identify the resonance frequencies, whereas Nyquist plots are used to study the stability.

The authors in [26] evaluated different techniques to study the stability at resonance of power electronic-based devices and concluded the impedance-based approach with average voltage source converter modeling is valid for frequencies lower than the switching frequency (*e.g.*, 2 kHz). As all control-to-grid interactions concerning this thesis occur below the converter switching frequencies, the impedance model can be used to design methodologies for resonance management in wind parks. The impedance-based approach provides information of both stable and unstable resonances without the necessity of complex calculations or simulations. However, the accuracy of the impedance equivalent depends on its level of modeling detail and on the type of phenomenon investigated. As will be discussed throughout this thesis, more detailed models are typically needed for stability studies as the damping of the converters is sensitive to controller simplifications, whereas more simplified models are possible when studying weakly damped (stable) resonances.

1.3 Thesis justification

As shown in the literature review and the summary of recent events, resonance problems in wind parks are an ongoing practical problem faced by system operators and wind park operators. In response, regulatory agencies have created standards and guidelines to address the problem of harmonic resonances, both from the agent and the utility perspectives [9], [27], [8]. For example, more specifically for the case of wind parks, in 2016, the National System Operator (ONS) in Brazil created a technical norm NT 009/2016 [28] with instructions for new wind park connection studies in order to prevent the problems observed in other countries. In addition, the IEEE PES Power System Dynamic Performance Committee recently released a technical report formalizing this new stability phenomena associated with power electronic interfaced technologies, and providing guidelines on how these phenomena should be investigated [15].

However, as these are relatively new phenomena, there is room for improvement in the methodologies used for resonance assessment. Time domain techniques should be used only in the most critical scenarios because they are costly, as they are time and computationally demanding and require detailed modeling and results processing. Frequency domain techniques, such as the impedance-based approach, are promising for general initial screening studies due to their lower computational and modeling cost but suffer from the tradeoff between modeling complexity vs. accuracy. In this sense, systematic and improved methodologies for resonance assessment in wind parks are needed to facilitate the decision-making process, on whether to take preventive / corrective actions to avoid component damages and fines. The present Ph.D. research aims to address the issue by providing a series of techniques to eliminate the necessity of repetitive computer simulations. These techniques can be applied to different grid and wind park configurations.

1.4 Thesis objectives

The main objective of this project is to promote advancements in the management of resonances in wind parks with Type-III (doubly fed induction generators) or Type-IV (full-converter) generators, which are the most common nowadays. The new methodologies developed in this work are aimed to facilitate the anticipation, detection and mitigation of the different types of resonance that may occur in wind parks. Such methodologies are mostly simplified procedures based on consulting charts or simple analytic expressions, without the necessity of complex computer simulations. This will reduce not only potential damages to wind park and grid equipment, but will also save many work hours of specialized engineers required to evaluate and mitigate the risk of resonance in wind parks. More specifically, the objectives of this thesis are:

- Develop a flexible procedure for accurate impedance modeling of Type-III and Type-IV wind generators to study resonance in wind parks.
- Develop a simple methodology to identify the risk of regulatory limit violations at the PCC of a wind park due to stable harmonic resonance.
- Develop a simple methodology to identify the risk of lifetime reduction or damage of wind park components due to stable harmonic resonance.
- Propose mitigation techniques to prevent and correct harmonic resonances in wind parks.
- Explore the practical likelihood of the necessary conditions for the different types of unstable resonance due to control interactions of the wind park with the grid.
- Develop a simple methodology to identify the risk of unstable sub-synchronous resonance due to control interactions of the wind park with the grid.

1.5 Thesis organization

Chapter 2 of this document is devoted to the impedance modeling of the Type-III and Type-IV wind generators. Chapter 3 presents the methodologies developed for stable harmonic resonance analysis, while Chapter 4 presents the studies related to unstable resonance analysis. Finally, Chapter 6 presents the conclusions of this work. The chapters content is:

- Chapter 2 presents a numerical procedure based on descriptor state space modeling to simplify the process of calculating accurate impedance models of Type-III and Type-IV wind generators. The resulting impedance models are validated with EMT simulations.
- Chapter 3 presents the studies of weakly damped resonance. First, it introduces a chart to assess the risk of regulatory limits violation due to grid distortions and harmonic resonance at the point of common coupling (PCC) between the wind park and the grid. Then, it presents a second chart to determine risk of wind park component damage due to the increased loading produced by grid distortions and harmonic resonance. Finally, it presents an impedance-based iterative methodology to tune passive filters which minimize the risk of harmonic resonance at the wind park PCC.
- Chapter 4 presents the studies of unstable resonance. First, it shows the results of a likelihood assessment for the necessary practical conditions to initiate each type of unstable control interaction between the wind park and the grid. Later on, it presents a chart to assess the risk of sub-synchronous resonance in Type-III wind parks connected to transmission systems with series capacitive compensation, which is the most common type of unstable control interaction between wind parks and the grid.
- Chapter 5 summarizes the conclusions of the thesis and presents possibilities for future work in this research topic.

The content and contributions of each chapter are summarized in Figure 1.1.

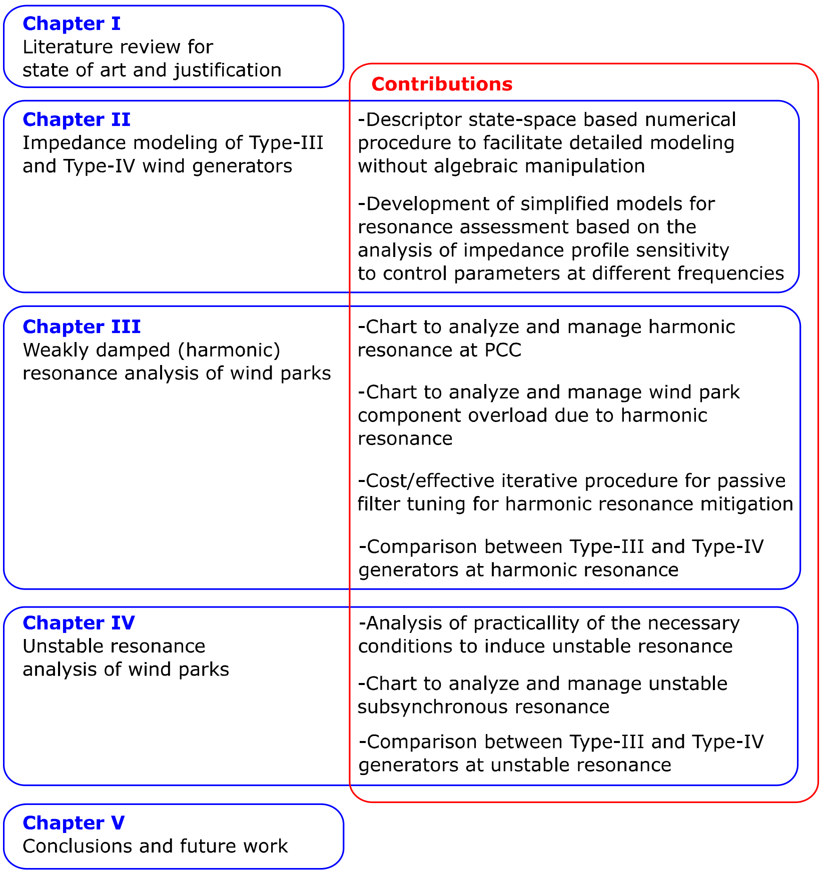

Figure 1.1: Content and contributions per chapter of the thesis

2 MODEL OF TYPE-III AND TYPE-IV WIND GENERATORS FOR RESONANCE ASSESSMENT IN WIND PARKS

To obtain the impedance profiles of the generators, their models are transformed according to the sequence in Figure 2.1. The EMT model of the generators is first converted to its linear state space (LSS) form. Later on, algebraic operations are applied to the LSS model to obtain the impedance model, where the literature typically aims for closed-form analytic expressions, [23] [24], [25]. Finally, the impedance model is validated with EMT simulation.

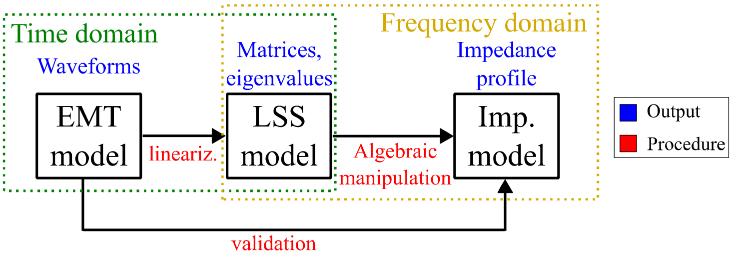

Figure 2.1: Transition between models for wind generator

As an alternative to facilitate accurate impedance modeling while avoiding repetitive algebraic manipulations, this chapter proposes a numerical procedure to calculate accurate frequency dependent impedance profiles from highly detailed models based on descriptor state-space approach, which uses the linear model equations already available for the frequency-domain methods in the literature. The main advantage of the proposed numerical procedure over closed-form analytical expressions is that the analytical expressions are exclusive to each generator topology, whereas the numerical procedure is generic for any generator topology, and does not require algebraic manipulation of the equations, which minimizes the risk of human error, saves time, and facilitates modifications.

Wind generator vendors do not reveal much detail of the internal control circuit [3], [21], [10], [15], [29]. However, they supply black-box EMT models of the generators and, with these black-box models, it is possible to conduct frequency scans and EMT simulations to measure the equivalent impedance profiles of the generators. This chapter describes a procedure to obtain such impedance profile from the generator black-box model and uses this procedure to validate the impedance profiles derived numerically.

2.1 Description of the wind generator models

A schematic of the Type-III and Type-IV wind generators is presented in Figure 2.2 and Figure 2.3, respectively.

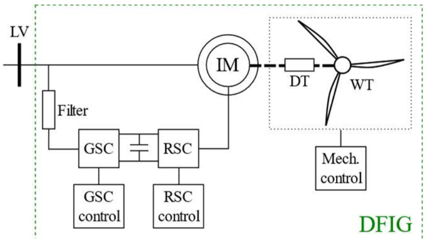

Figure 2.2: Schematic of Type-III wind generator

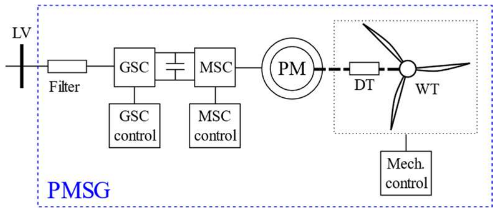

Figure 2.3: Schematic of Type-IV wind generator

Type-III generators use doubly-fed induction machines (IM), *i.e.*, DFIGs, with the stator directly coupled to the grid, and the rotor voltage is set by its power electronics converter bridge. As for the Type-IV generators, the rotating machine is physically decoupled from the grid by the action of its power electronics converter bridge, which is most commonly a permanent magnet synchronous generator (PMSG). The wind turbine (WT) is connected to the rotor of the machines through the drive train (DT). The pitch angle of the blades is used to regulate the rotor speed depending on the desired operational mode (generally active power tracking) depending on the available wind.

Both generators have a voltage source converter (VSC) bridge, connected through a DC link with a capacitor. The Type-III generator has a grid side converter (GSC) and a rotor side converter (RSC), sized to 30% of the generator rated capacity as most of the power is injected through the stator of the machine, whereas the Type-IV generator has a GSC and a machine side converter (MSC), and the power capacity of both converters is 100% of the generator rated capacity to transfer the power from the turbine to the grid. Each converter offers two degrees of freedom for control, being able to regulate active and reactive power, electromagnetic torque, DC bus voltage, and AC terminal voltage, as needed.

Finally, the GSC of both generators is connected to the grid through a passive front-end filter to damp the high frequency switching distortions. This filter typically has an RL or LCL topology. The induction machine of the Type-III generator partially acts as the filter for the RSC.

The EMT models of the Type-III and Type-IV generators used in this thesis are based on references [30] and [31] respectively. This chapter is focused on the impedance model calculation procedure, so the **<u>equations of the models and its parameters are provided in Appendix A</u>**. The following subsections summarize the most relevant aspects of the models for this thesis, relative to the control reference frame and the model of the converters, which are used in the process of calculating the impedance vs. frequency profiles.

2.1.1 Reference frame and synchronization

The positive and negative (pn) sequence impedance model of the generators is obtained by analyzing the equations in direct-quadrature (dq) domain using the reference frame in Figure 2.4. The corresponding transformations between abc frame and dq frame are given by expressions (2.1) and (2.2). The 0 axis is discarded as resonance in wind parks due to control interactions with the grid can be studied as a balanced phenomenon [21].

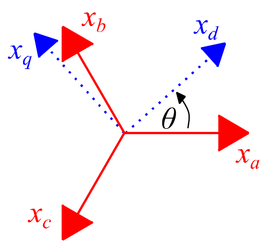

Figure 2.4: “abc” and “dq” reference frames

$$\begin{pmatrix} x_d \\ x_q \end{pmatrix} = \frac{2}{3} \begin{pmatrix} sin(\theta) & sin\left(\theta - \frac{2\pi}{3}\right) & sin\left(\theta + \frac{2\pi}{3}\right) \\ cos(\theta) & cos\left(\theta - \frac{2\pi}{3}\right) & cos\left(\theta + \frac{2\pi}{3}\right) \end{pmatrix} \begin{pmatrix} x_a \\ x_b \\ x_c \end{pmatrix} \quad \textbf{(2.1)}$$

$$\begin{pmatrix} x_a \\ x_b \\ x_c \end{pmatrix} = \begin{pmatrix} sin(\theta) & cos(\theta) \\ sin\left(\theta - \frac{2\pi}{3}\right) & cos\left(\theta - \frac{2\pi}{3}\right) \\ sin\left(\theta + \frac{2\pi}{3}\right) & cos\left(\theta + \frac{2\pi}{3}\right) \end{pmatrix} \begin{pmatrix} x_d \\ x_q \end{pmatrix} \quad \textbf{(2.2)}$$

The controllers of both the Type-III and Type-IV generators are synchronized to the grid by a phase-locked loop (PLL). A basic PLL topology is shown in Figure 2.5, where PI_{PLL} is a PI controller that tracks the q axis terminal voltage, F_V is a low pass filter to eliminate the noise from voltage measurement, and ω_0 is a constant denoting the fundamental frequency in rad/s. The terminal voltage v_t is first filtered and then input to the “abc to dq” transformation block, so the PLL tracks the q axis voltage v_{qt} to calculate the grid frequency in pu ω_{PLL}, which is integrated to calculate the grid phase angle $_{PLL}$. The rotor speed is also integrated to calculate the rotor angle θ_r. The typical bandwidth of a PLL ranges from 2 Hz to 10 Hz [32], so it is important mostly to study resonances near the fundamental frequency (60 Hz in this paper) and can be assumed ideal when studying subsynchronous (below 40 Hz) and high-frequency (above 120 Hz) resonances.

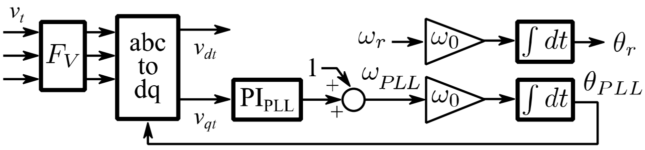

Figure 2.5: Phase-locked loop topology

The transformation of reference frames in the Type-III generator is shown in Figure 2.6, where F_I is a filter to eliminate the noise from the current measurements. The current of the stator $i_{abc,s}$, the current of the GSC $i_{abc,g}$, and the current of the rotor $i_{abc,r}$, are filtered and then transformed to dq frame by the "abc to dq" blocks with the Park transform. The abc frame voltage reference of the GSC $v_{abc,g}^{ref}$, and the abc frame voltage reference of the RSC $v_{abc,r}^{ref}$, are calculated using the "dq to abc" blocks with the inverse Park transform. Notice the frame of the rotor variables is shifted due to the asynchronous characteristic of the induction machine.

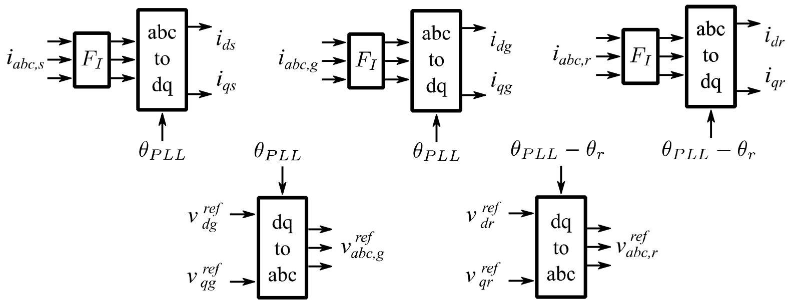

Figure 2.6: Reference frame conversion for Type-III wind generator

The transformations for the Type-IV generator are shown in Figure 2.7, where $i_{abc,g}$ is current of the GSC in abc frame, $i_{abc,m}$ is the current of the MSC, $v_{abc,g}^{ref}$ is the reference voltage for GSC switching in abc frame, and $v_{abc,m}^{ref}$ is the reference voltage for MSC switching.

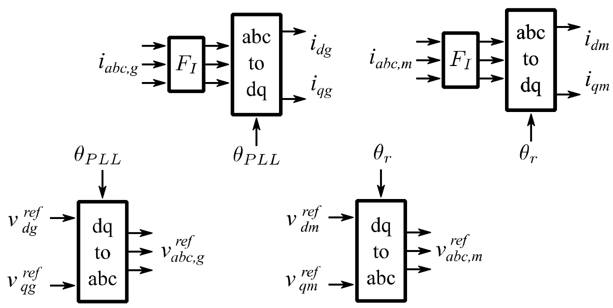

Figure 2.7: Reference frame conversion for Type-IV wind generator

2.1.2 Average converter model

The topology for the voltage source converters (VSC) of the wind generators in this thesis is shown in Figure 2.8. The sinusoidal three-phase reference voltage v_{abc}^{ref} output by the controllers is used to create the switching signal *S* after a pulse width modulation (PWM) algorithm and trigger the transistors. The resulting AC voltage v_{ac} at converter terminals is described in terms of the switching signal *S* and the DC bus voltage v_{dc} using expression (2.3).

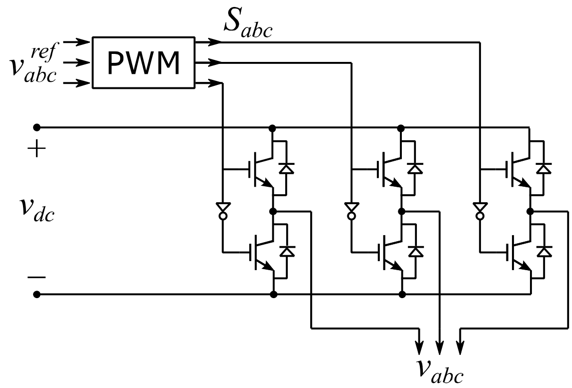

Figure 2.8: Voltage source converter topology for wind generators

$$v_{ac}(t) = v_{dc}(t) \cdot S(t) \tag{2.3}$$

S is built from a modulation signal from the control circuit (abc frame reference voltages) and a carrier signal (commonly a triangular wave) [33]. It can be described by expression (2.4), where $\omega_c = 2\pi f_c$ is the angular frequency of the carrier signal; θ_c is the phase angle of the carrier signal; $\omega_0 = 2\pi f_0$ is the angular frequency of the modulation signal (which corresponds to the fundamental frequency); θ_0 is the phase angle of the modulation signal; *M* is the modulation index (ratio between the amplitudes of the modulation signal and the carrier signal, and commonly normalized by the DC bus voltage to compensate for its dynamics at the output); *m* is the harmonic order of the carrier signal frequency; *n* is the harmonic order of the modulation signal frequency; θ_n is the phase angle of the harmonic order *n* of the modulation signal; $J_n(m\pi M)$ is the first kind Bessel function with order *n* and argument $m\pi M$, as in (2.5).

$$S = \sum_{n=1}^{+\infty} M\, sin(n\omega_1 t + \theta_n) + \sum_{m=1}^{+\infty} \sum_{n=-\infty}^{+\infty} \begin{bmatrix} \frac{2}{m\pi} \cdot J_n(m\pi M) \cdot sin\left(\frac{n\pi}{2}\right) \cdot \\ sin\big(m(\omega_c t + \theta_c) + n(\omega_1 t + \theta_1)\big) \end{bmatrix} \tag{2.4}$$

$$J_n(m\pi M) = \sum_{k=0}^{+\infty} \frac{(-1)^k (m\pi M/2)^{n+2k}}{k!\,(n+k)!} \tag{2.5}$$

This thesis assumes the front-end filter of the VSC eliminates the high frequency distortions due to the converter switching [34], [35] (no special control loops were included in the converter for compensation of harmonics). As a result, (2.4) becomes:

$$S \approx \sum_{n=1}^{+\infty} M\, sin(n\omega_1 t + \theta_n) \tag{2.6}$$

No losses are considered so the converters act as ideal active power couplings, and their modulation indices are compensated for the DC bus voltage v_{dc} value. With these considerations, the converter bridge + DC bus link can be represented by control delay blocks (one for each converter) and a capacitor as shown in Figure 2.9. The average converter model of each wind generator is enclosed by the dotted lines in Figure 2.9. This model has an important meaning, that is, these converters do not produce distortions in the studied range of frequency [36], so they can be modeled as linear elements (impedances) for all frequencies other than the fundamental and below their switching frequency.

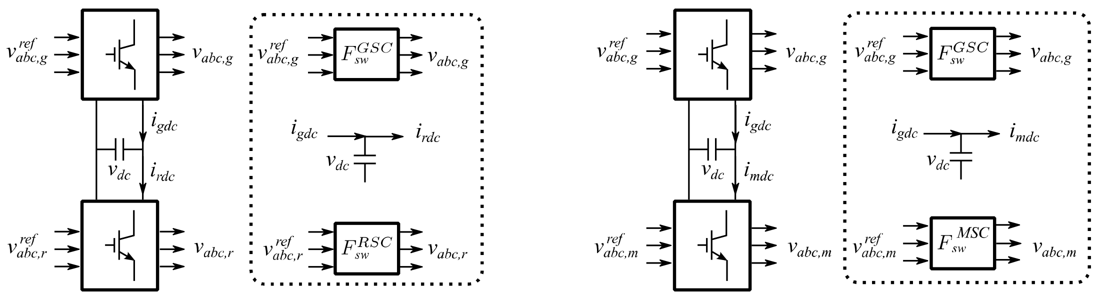

a) Type-III generator **b) Type-IV generator**

Figure 2.9: Switched converter bridge model to average converter bridge model

2.2 From EMT model to impedance vs. frequency profile

This section details the steps shown in Figure 2.1 to obtain the impedance vs. frequency profiles of the generator from their EMT models, using a series of algebraic expressions.

2.2.1 Linearization of the EMT model

The first step is to approximate all algebraic and differential equations of the EMT model with their first-order derivative. For example, consider the function *f* with three variables *x*, *y* and *z*. Changes in this function can be approximated by small disturbances Δ of each of its variables around the operating point [x_0, y_0, z_0] as shown in expression (2.7). Neglecting saturations and using the average converter model are also part of the linearization process.

$$f(x,y,z) \approx f(x_0,y_0,z_0) + \frac{df(x_0,y_0,z_0)}{dx}\Delta x + \frac{df(x_0,y_0,z_0)}{dy}\Delta y + \frac{df(x_0,y_0,z_0)}{dz}\Delta z \quad \textbf{(2.7)}$$

2.2.2 From descriptor state space model to state space model

After the linearization, the system can be described in state space form. Traditional state space models are composed of four matrixes $\boldsymbol{A}$, $\boldsymbol{B}$, $\boldsymbol{C}$ and $\boldsymbol{D}$, a state vector of differential variables x, an input vector u, and an output vector y as in expression (2.8).

$$\frac{dx}{dt} = \boldsymbol{A}x + \boldsymbol{B}u \qquad\qquad y = \boldsymbol{C}x + \boldsymbol{D}u \quad \textbf{(2.8)}$$

However, it is easier to describe systems with many states using an auxiliary set of algebraic variables instead of incorporating them into the differential equations. This can be done with a matrix $\boldsymbol{E}$ which leads to a "descriptor state space" model as in expression (2.9) [37], [38]. This $\boldsymbol{E}$ matrix greatly facilitates the modeling process because it considers algebraic equations without incorporating them directly into the differential equations by algebraic manipulation. All algebraic variables have a 0 in the diagonal of $\boldsymbol{E}$, and add a -1 to the diagonal of $\boldsymbol{A}$. All differential variables have a 1 in the diagonal of $\boldsymbol{E}$, and all off-diagonals of $\boldsymbol{E}$ are 0.

$$\boldsymbol{E}\frac{dx}{dt} = \boldsymbol{A}x + \boldsymbol{B}u \qquad\qquad y = \boldsymbol{C}x + \boldsymbol{D}u \quad \textbf{(2.9)}$$

The matrices and vectors can be split into algebraic-algebraic (*alal*), algebraic-differential (*aldi*), differential-algebraic (*dial*), and differential-differential (*didi*) subsets, as in expression (2.10), where $\boldsymbol{I}$ is the identity matrix.

$$\begin{gathered}
\begin{pmatrix} \boldsymbol{0}_{alal} & \boldsymbol{0}_{aldi} \\ \boldsymbol{0}_{dial} & \boldsymbol{I}_{didi} \end{pmatrix} \frac{d}{dt}\begin{pmatrix} x_{al} \\ x_{di} \end{pmatrix} = \begin{pmatrix} \boldsymbol{A}_{alal} & \boldsymbol{A}_{aldi} \\ \boldsymbol{A}_{dial} & \boldsymbol{A}_{didi} \end{pmatrix}\begin{pmatrix} x_{al} \\ x_{di} \end{pmatrix} + \begin{pmatrix} \boldsymbol{B}_{al} \\ \boldsymbol{B}_{di} \end{pmatrix} u \\
\begin{pmatrix} y_{al} \\ y_{di} \end{pmatrix} = \begin{pmatrix} \boldsymbol{C}_{alal} & \boldsymbol{C}_{aldi} \\ \boldsymbol{C}_{dial} & \boldsymbol{C}_{didi} \end{pmatrix}\begin{pmatrix} x_{al} \\ x_{di} \end{pmatrix} + \begin{pmatrix} \boldsymbol{D}_{al} \\ \boldsymbol{D}_{di} \end{pmatrix} u
\end{gathered} \quad \textbf{(2.10)}$$

The next step is to reduce the descriptor state space to a state space by including the effect of all algebraic variables into the differential variables. This allows to calculate an impedance profile numerically for any system while preserving modeling detail, instead of calculating closed form analytic expressions, which can be difficult or even impossible depending on the model complexity.

From the *alal* and *aldi* subsets in the upper row of (2.10), it is possible to describe the algebraic variables x_{al} in terms of the differential variables x_{di}:

$$x_{al} = -\boldsymbol{A}_{alal}^{-1}\boldsymbol{A}_{aldi}x_{di} - \boldsymbol{A}_{alal}^{-1}\boldsymbol{B}_{al}u \quad \textbf{(2.11)}$$

Using the previous result and the *dial* and *didi* subsets in the lower row of (2.10), the algebraic variables can be removed from the model:

$$\frac{dx_{di}}{dt} = \boldsymbol{A}_{dial}\boldsymbol{A}_{alal}^{-1}(-\boldsymbol{A}_{aldi}x_{di} - \boldsymbol{B}_{al}u) + \boldsymbol{A}_{didi}x_{di} + \boldsymbol{B}_{di}u \quad \textbf{(2.12)}$$

Finally, the reduced state space is defined by expression (2.13):

$$\frac{dx_{di}}{dt} = \boldsymbol{A}'x_{di} + \boldsymbol{B}'u \qquad y_{al} = \boldsymbol{C}_{al}{}'x_{di} + \boldsymbol{D}_{al}{}'u \qquad y_{di} = \boldsymbol{C}_{di}{}'x_{di} + \boldsymbol{D}_{di}{}'u \quad \textbf{(2.13)}$$

where the *prime* matrices are calculated as follows:

$$\begin{aligned} \boldsymbol{A}' &= \boldsymbol{A}_{didi} - \boldsymbol{A}_{dial}\boldsymbol{A}_{alal}^{-1}\boldsymbol{A}_{aldi} & \boldsymbol{B}' &= \boldsymbol{B}_{di} - \boldsymbol{A}_{dial}\boldsymbol{A}_{alal}^{-1}\boldsymbol{B}_{al} \\ \boldsymbol{C}_{al}{}' &= \boldsymbol{C}_{aldi} - \boldsymbol{C}_{alal}\boldsymbol{A}_{alal}^{-1}\boldsymbol{A}_{aldi} & \boldsymbol{C}_{di}{}' &= \boldsymbol{C}_{didi} - \boldsymbol{C}_{dial}\boldsymbol{A}_{alal}^{-1}\boldsymbol{A}_{aldi} \\ \boldsymbol{D}_{al}{}' &= \boldsymbol{D}_{al} - \boldsymbol{C}_{alal}\boldsymbol{A}_{alal}^{-1}\boldsymbol{B}_{al} & \boldsymbol{D}_{di}{}' &= \boldsymbol{D}_{di} - \boldsymbol{C}_{dial}\boldsymbol{A}_{alal}^{-1}\boldsymbol{B}_{al} \end{aligned} \quad \textbf{(2.14)}$$

Two examples on how the descriptor state-space modeling approach can facilitate the inclusion and removal of circuit components from the model are given in Appendix B.

2.2.3 From state space model to matrix of transfer functions

The admittance of the generators can be obtained from the transfer function of the dq components of the terminal current i_t in terms of the dq components of the terminal voltages v_t, which are highlighted in red font in Figure 2.10.

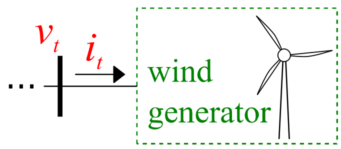

Figure 2.10: Terminal voltage and current for generator impedance calculation

To calculate the transfer functions, expression (2.13) is moved to the frequency domain of s by applying the Laplace transform:

$$x_{di} = (s\boldsymbol{I} - \boldsymbol{A}')^{-1}\boldsymbol{B}'u \qquad y_{al} = \boldsymbol{C}_{al}{}'x_{di} + \boldsymbol{D}_{al}{}'u = (\boldsymbol{C}_{al}{}'(s\boldsymbol{I} - \boldsymbol{A}')^{-1}\boldsymbol{B}' + \boldsymbol{D}_{al}{}')u \quad \textbf{(2.15)}$$

Isolating the current outputs y in terms of the voltage inputs u leads to expression (2.16):

$$\boldsymbol{H}(s) = \begin{pmatrix} H_{1,1}(s) & H_{1,2}(s) & \cdots & H_{1,n}(s) \\ H_{2,1}(s) & H_{2,2}(s) & \cdots & H_{2,n}(s) \\ \vdots & \vdots & \ddots & \vdots \\ H_{n,1}(s) & H_{n,2}(s) & \cdots & H_{n,n}(s) \end{pmatrix} = \frac{y_{al}}{u} = \boldsymbol{C}_{al}{}'(s\boldsymbol{I} - \boldsymbol{A}')^{-1}\boldsymbol{B}' + \boldsymbol{D}_{al}{}' \qquad \textbf{(2.16)}$$

In this work, Δi_{dt} and Δi_{qt} were set at the first two outputs in y_{al}, and Δv_{dt} and Δv_{qt} were set as the first two inputs in u, so the following transfer functions define the admittance matrix Y_{dq}:

$$\begin{aligned} H_{1,1}(s) &= y_{dd}(s) = \frac{\Delta i_{dt}}{\Delta v_{dt}} & H_{1,2}(s) &= y_{dq}(s) = \frac{\Delta i_{dt}}{\Delta v_{qt}} \\ H_{2,1}(s) &= y_{qd}(s) = \frac{\Delta i_{qt}}{\Delta v_{dt}} & H_{2,2}(s) &= y_{qq}(s) = \frac{\Delta i_{qt}}{\Delta v_{qt}} \end{aligned} \qquad \textbf{(2.17)}$$

Finally, the dq impedance matrix $\boldsymbol{Z}_{dq}$ of the generator can be calculated from the inverse of its admittance matrix $\boldsymbol{Y}_{dq}$ using expression (2.18):

$$\boldsymbol{Z}_{dq}(s) = \begin{pmatrix} z_{dd}(s) & z_{dq}(s) \\ z_{qd}(s) & z_{qq}(s) \end{pmatrix} = \boldsymbol{Y}_{dq}^{-1}(s) = \begin{pmatrix} y_{dd}(s) & y_{dq}(s) \\ y_{qd}(s) & y_{qq}(s) \end{pmatrix}^{-1} \qquad \textbf{(2.18)}$$

2.2.4 From dq domain into positive-negative sequence domain

The next step of the process is to transform the impedance matrices from dq frame into positive-negative (pn) sequence domain. Consider a set of three-phase voltages with positive and negative sequence disturbances [39]:

$$\begin{aligned} v_a(t) &= V_1 \sin(\omega_1 t + \varphi_{v1}) + V_p \sin(\omega_p t + \varphi_{vp}) + V_n \sin(\omega_n t + \phi_{vn}) \\ v_b(t) &= V_1 \sin\left(\omega_1 t + \varphi_{v1} - \frac{2\pi}{3}\right) + V_p \sin\left(\omega_p t + \varphi_{vp} - \frac{2\pi}{3}\right) + V_n \sin\left(\omega_n t + \varphi_{vn} + \frac{2\pi}{3}\right) \\ v_c(t) &= V_1 \sin\left(\omega_1 t + \varphi_{v1} + \frac{2\pi}{3}\right) + V_p \sin\left(\omega_p t + \varphi_{vp} + \frac{2\pi}{3}\right) + V_n \sin\left(\omega_n t + \varphi_{vn} - \frac{2\pi}{3}\right) \end{aligned} \qquad \textbf{(2.19)}$$

Using the transformation from abc to dq frame in expression (2.1) with $\theta = \omega t$:

$$\begin{pmatrix} v_d \\ v_q \\ v_0 \end{pmatrix} = \frac{2}{3} \begin{pmatrix} \sin(\omega t) & \sin\left(\omega t - \frac{2\pi}{3}\right) & \sin\left(\omega t + \frac{2\pi}{3}\right) \\ \cos(\omega t) & \cos\left(\omega t - \frac{2\pi}{3}\right) & \cos\left(\omega t + \frac{2\pi}{3}\right) \end{pmatrix} \begin{pmatrix} v_a \\ v_b \\ v_c \end{pmatrix} = \begin{pmatrix} v_{d1} \\ v_{q1} \end{pmatrix} + \begin{pmatrix} v_{dp} \\ v_{qp} \end{pmatrix} + \begin{pmatrix} v_{dn} \\ v_{qn} \end{pmatrix} \qquad \textbf{(2.20)}$$

Considering only the positive sequence and negative sequence disturbances:

$$\begin{aligned} v_d &= V_p \cos\left((\omega - \omega_p)t - \varphi_{vp}\right) - V_n \cos\left((\omega + \omega_n)t + \varphi_{vn}\right) \\ v_q &= V_p \cos\left((\omega - \omega_p)t - \varphi_{vp} - \pi/2\right) + V_n \cos\left((\omega + \omega_n)t + \varphi_{vn} - \pi/2\right) \end{aligned} \qquad \textbf{(2.21)}$$

Moving to phasor domain (denoted by $\bar{V}$) and expressing in matrix form:

$$v_d = V_p\, cos(\omega t)\, e^{-j(\omega_p t+\varphi_{vp})} - V_n\, cos(\omega t)\, e^{j(\omega_n t+\varphi_{vn})}$$
$$v_q = -jV_p\, cos(\omega t)\, e^{-j(\omega_p t+\varphi_{vp})} - jV_n\, cos(\omega t)\, e^{j(\omega_n t+\varphi_{vn})}$$
$$\begin{pmatrix} v_d \\ v_q \end{pmatrix} = cos(\omega t)\begin{pmatrix} 1 & -1 \\ -j & -j \end{pmatrix}\begin{pmatrix} \overline{V_p} \\ \overline{V_n} \end{pmatrix} \approx cos(\Delta\theta)\begin{pmatrix} 1 & -1 \\ -j & -j \end{pmatrix}\begin{pmatrix} \overline{V_p} \\ \overline{V_n} \end{pmatrix} \tag{2.22}$$

Given a small angle deviation $\Delta\theta = \omega t - \theta_0 \rightarrow \cos(\Delta\theta) \approx 1$ (Laplace operator s dependency was omitted from the right hand side of the expressions):

$$\begin{pmatrix} v_d \\ v_q \end{pmatrix} \approx \begin{pmatrix} 1 & -1 \\ -j & -j \end{pmatrix}\begin{pmatrix} \overline{V_p} \\ \overline{V_n} \end{pmatrix} \qquad \begin{pmatrix} i_d \\ i_q \end{pmatrix} \approx \begin{pmatrix} 1 & -1 \\ -j & -j \end{pmatrix}\begin{pmatrix} \overline{I_p} \\ \overline{I_n} \end{pmatrix}$$
$$\begin{pmatrix} v_d \\ v_q \end{pmatrix} \approx \boldsymbol{Z}_{dq}\begin{pmatrix} i_d \\ i_q \end{pmatrix} = \begin{pmatrix} z_{dd} & z_{dq} \\ z_{qd} & z_{qq} \end{pmatrix}\begin{pmatrix} i_d \\ i_q \end{pmatrix} \qquad \begin{pmatrix} v_p \\ v_n \end{pmatrix} \approx \boldsymbol{Z}_{pn}\begin{pmatrix} i_p \\ i_n \end{pmatrix} = \begin{pmatrix} z_{pp} & z_{pn} \\ z_{np} & z_{nn} \end{pmatrix}\begin{pmatrix} i_p \\ i_n \end{pmatrix} \tag{2.23}$$
$$\begin{pmatrix} \overline{V_p} \\ \overline{V_n} \end{pmatrix} \approx \begin{pmatrix} 1 & -1 \\ -j & -j \end{pmatrix}^{-1}\boldsymbol{Z}_{dq}\begin{pmatrix} 1 & -1 \\ -j & -j \end{pmatrix}\begin{pmatrix} \overline{I_p} \\ \overline{I_n} \end{pmatrix}$$

Which means the dq impedance matrix can be transformed into positive-negative sequence domain with expression (2.24). This demonstrates that a grid disturbance with a given sequence applied at generator terminals will also make the generator react in the opposite sequence due to its internal coupling. With this multi-input multi-output model, it is possible to use generalized Nyquist criterion to analyze the stability of inverter-based systems [40], explained in Chapter 4.

$$\boldsymbol{Z}_{pn} = \begin{pmatrix} 1 & -1 \\ -j & -j \end{pmatrix}^{-1}\boldsymbol{Z}_{dq}\begin{pmatrix} 1 & -1 \\ -j & -j \end{pmatrix} \tag{2.24}$$

The positive-negative impedance profile of the fully detailed EMT model of the Type-III and the Type-IV wind generators (available in Appendix A), is shown in Figure 2.11. For presentation purposes, the internal control loop parameters of the Type-III and Type-IV generators, their PLL, their DC bus voltage control, and the GSC switching frequency were set to the same values. The capacitor from the LCL filter was removed to evidence the negative resistance region provided by the converter controls in the range of harmonic frequencies. The impedance profile with the complete filter is shown in Figure 2.12.

For most of the frequency spectrum (except near the fundamental frequency and the resonance frequency of the front-end filter), the terms z_{pn} and z_{np} tend to zero, and have smaller magnitude than the diagonal terms z_{pp} and z_{nn}. This result can be used to decouple the positive from the negative sequence so the impedances can be described as scalars instead of a matrix.

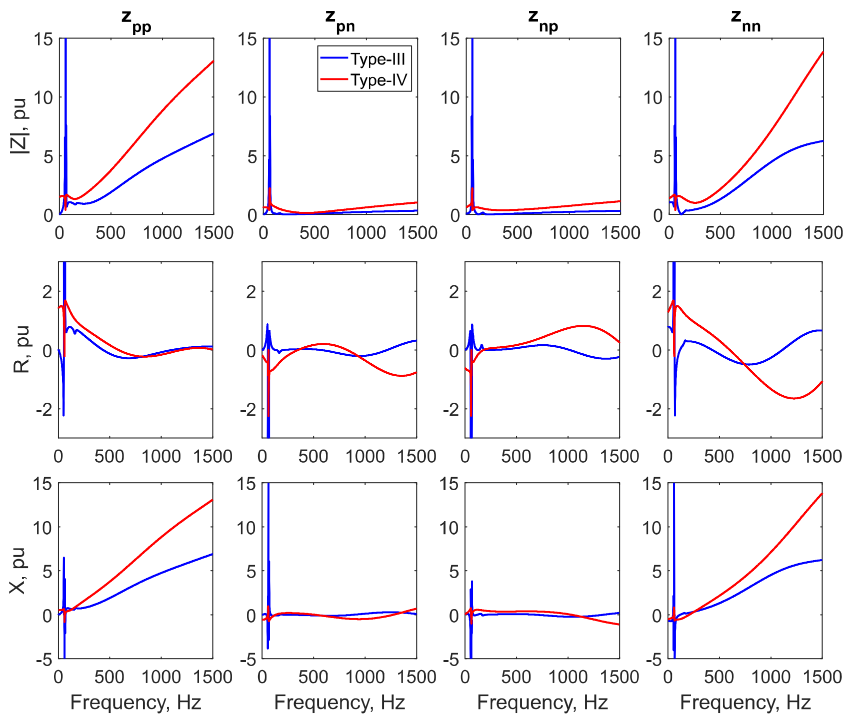

Figure 2.11: Positive-negative sequence impedance matrix vs. frequency profiles of wind generators, without LCL filter capacitor (690 V, 2 MVA)

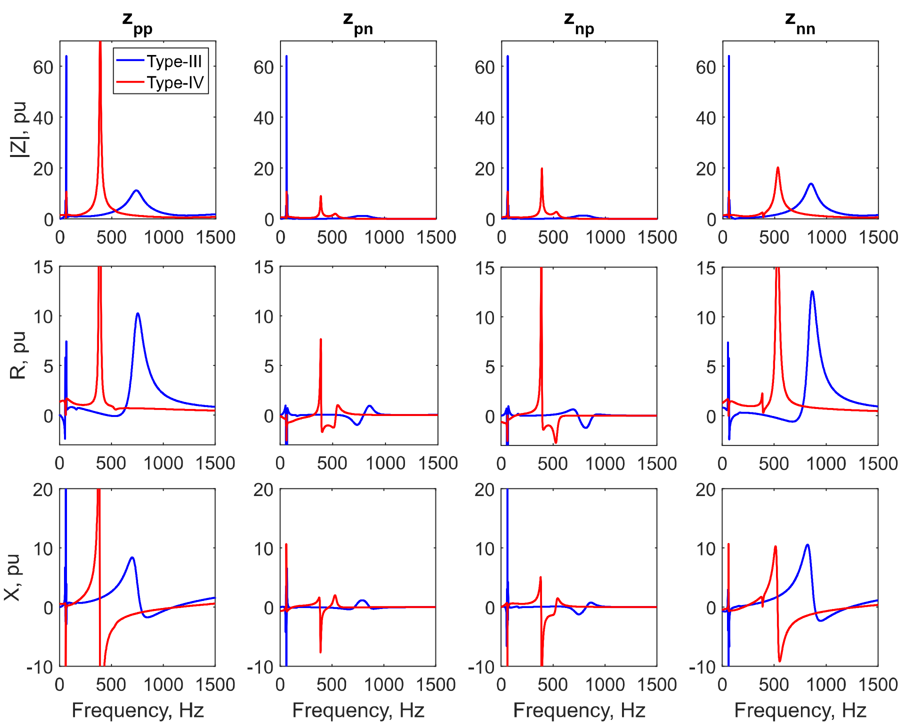

Figure 2.12: Positive-negative sequence impedance matrix vs. frequency profiles of wind generators, with LCL filter capacitor (690 V, 2 MVA)

2.2.5 Decoupling of positive and negative sequence components

Under some circumstances, the impedance profiles can be reduced from matrix to scalar values. One scenario is when off diagonal components of the matrix (z_{pn} and z_{np}) are negligible with respect to the diagonal components (z_{pp} and z_{nn}). This typically happens for stability studies at frequencies far from the synchronous frequency, more specifically for resonances in the high frequency range (up to 1.5 kHz) or subsynchronous resonances originating in the grid due to transmission lines with series compensation. For these two phenomena, there is always a capacitance in the grid which defines the resonance frequency [41]. In this case, the positive sequence impedance of the generator is $z_p(s) = z_{pp}(s)$ and the negative sequence is $z_n(s) = z_{nn}(s)$. Another scenario is when the background grid is passive (contains no sequence coupling) and its equivalent impedance is much smaller than the equivalent impedance of the generator, which is typically valid for strong grids. Under these conditions, there will be one dominant sequence in the phenomenon. For dominant positive sequence, i.e., $V_n(s) \approx 0$, expression (2.23) becomes:

$$z_p(s) = v_p(\mathrm{s})/i_p(\mathrm{s}) = z_{pp}(\mathrm{s}) - z_{pn}(\mathrm{s})z_{np}(\mathrm{s})z_{nn}^{-1}(\mathrm{s}) \qquad \textbf{(2.25)}$$

And for negative sequence, *i.e.*, $V_p(s) \approx 0$, expression (2.23) becomes:

$$z_n(s) = v_n(\mathrm{s})/i_n(\mathrm{s}) = z_{nn}(\mathrm{s}) - z_{np}(\mathrm{s})z_{pn}(\mathrm{s})z_{pp}^{-1}(\mathrm{s}) \qquad \textbf{(2.26)}$$

with $s = j2\pi(f - f_0)$ for the decoupled positive sequence impedance $z_p(s)$, and $s = j2\pi(f + f_0)$ for the negative.

This matrix (multi-input multi-output) to scalar (single-input single-output) reduction is not valid for phenomena with important frequency couplings, such as near-synchronous resonance. Alternatively, [42] shows that it is still possible to convert a multi-input multi-output (MIMO) model into a single-input single-output (SISO) model for near-synchronous stability analysis, but the resulting impedance model incorporates the impedance of the grid.

2.3 Impedance validation with EMT simulation

The impedance of a generator at any frequency f can be calculated with two sets of voltage and current phasors taken at different distortion conditions, namely, $[\overline{V}_1(f), \overline{I}_1(f)]$ and $[\overline{V}_2(f), \overline{I}_2(f)]$ [43]. These phasors can be obtained from EMT simulation or field measurements after applying Fast Fourier Transform (FFT) to the waveforms and selecting the desired frequency. To validate the sequence impedances, such measurements are split into their positive and negative sequence components to later use expression (2.27) (in case of noisy measurements, minimum squares fit can be used to calculate the impedances [44]).

$$z_p(f) = \frac{\overline{V_{1p}}(f) - \overline{V_{2p}}(f)}{\overline{I_{1p}}(f) - \overline{I_{2p}}(f)} \qquad z_n(f) = \frac{\overline{V_{1n}}(f) - \overline{V_{2n}}(f)}{\overline{I_{1n}}(f) - \overline{I_{2n}}(f)} \qquad \textbf{(2.27)}$$

If the generator does not inject distortions at the measured frequency, then it is possible to simplify expression (2.27) by using only one measurement set as in expression (2.28).

$$z_p(f) = \frac{\overline{V_{1p}}(f)}{\overline{I_{1p}}(f)} \qquad z_n(f) = \frac{\overline{V_{1n}}(f)}{\overline{I_{1n}}(f)} \qquad \textbf{(2.28)}$$

This procedure is the "measurement-based impedance" calculation method. It can also be used to calculate the impedance at any point of the wind park, (e.g., beginning of a feeder with multiple generators, at the PCC). The analytic decoupled sequence impedance from expressions (2.25) and (2.26) was validated with EMT simulations where all converters are modeled with their detailed switched model. Grid voltage distortion components of 1% of the fundamental were applied at machine terminals and the resulting currents were measured to calculate the impedances with expression (2.28). The results are in Figure 2.13 for the generators with front-end filter without the capacitor (again, to highlight the negative resistance characteristic), and in Figure 2.14 for the generators with the complete filter. The decoupled positive sequence impedance is presented in blue, and the negative sequence impedance is presented in red.

As a first result, notice the proposed numerical approach is accurate for the entire spectrum as it is able to incorporate the detail of the original EMT model into the impedance vs. frequency profiles. Both the positive and negative sequence impedances are accurate.

Notice how the Type-III impedance model captures the negative resistance characteristic, both at sub-synchronous (due to induction machine effect) and super-synchronous frequencies (due to converter control and filter delays). The Type-IV impedance model does not have a negative resistance region at sub-synchronous frequencies, and it behaves similarly to the Type-III at high frequencies.

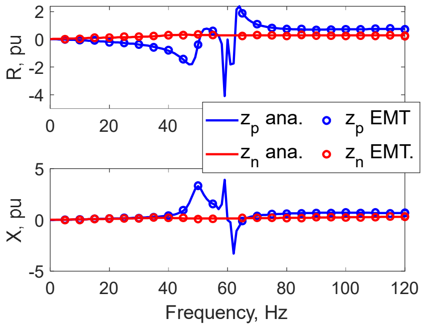

a) Type-III, low frequencies

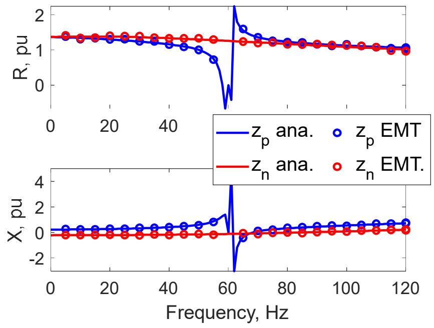

b) Type-IV, low frequencies

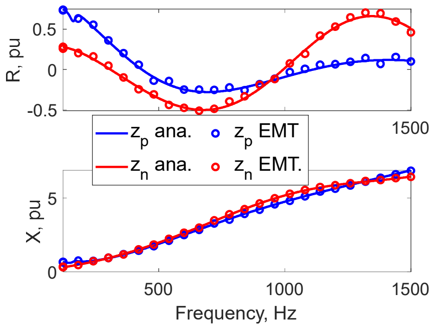

c) Type-III, high frequencies

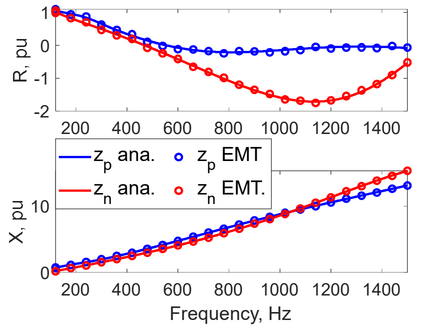

d) Type-IV, high frequencies

Figure 2.13: Generator impedance validation, no LCL filter capacitor (690 V, 2 MVA)

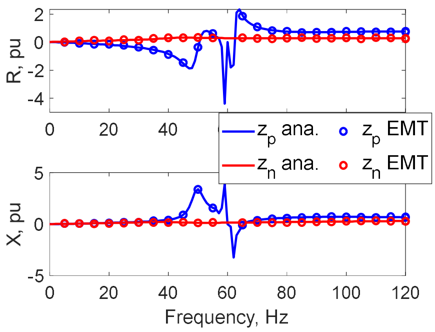

a) Type-III, low frequencies

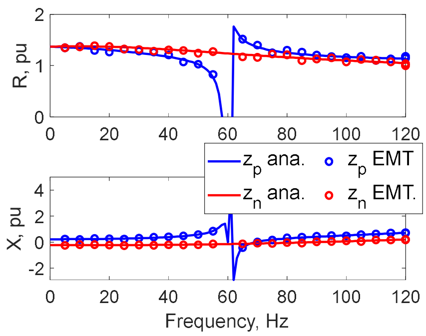

b) Type-IV, low frequencies

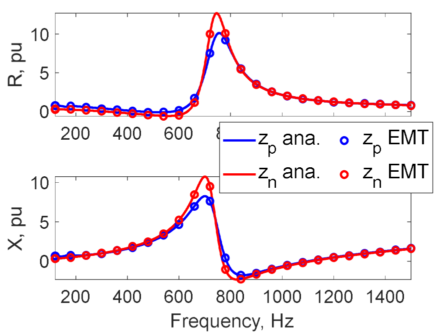

c) Type-III, high frequencies

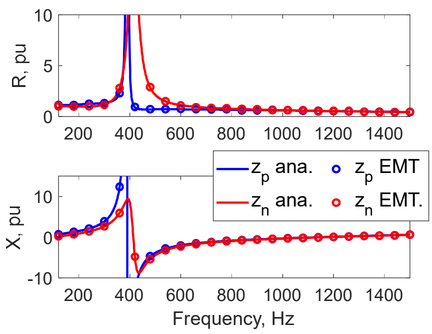

d) Type-IV, high frequencies

Figure 2.14: Generator impedance validation, with LCL filter capacitor (690 V, 2 MVA)

Notice that the Type-IV generator impedance magnitude is higher than the Type-III. This occurs as the Type-III has two converter branches in parallel (GSC + filter, and RSC + induction machine), whereas the Type-IV only has one branch (GSC + filter) connected to the grid.

The resonance frequency of the LCL filer of the Type-IV generator occurs at lower frequencies because the capacitance is larger.

2.4 Summary of the procedure to calculate the impedance profiles

This chapter presented a numerical procedure to calculate the sequence impedance profiles of Type-III and Type-IV wind generators with high modeling detail, without the need of algebraic manipulation. The only required inputs for the calculation are the descriptor state space matrixes (derived from the EMT model) and the desired frequencies of study. Such procedure is summarized as follows:

1) Linearize the EMT model with the first order derivatives, neglect all saturations and use the average converter model;
2) Build the descriptor state space as in expression (2.10);
3) Transform the descriptor state space to state space model using expression (2.13);
4) Calculate the admittance transfer functions in dq frame using expressions (2.16);
5) Build the dq impedance matrix with expression (2.18);
6) Transform the dq impedance matrix to positive-negative sequence domain with (2.24);
7) (Optional) Isolate the positive sequence impedance term with expression (2.25) evaluated at $s = j2\pi(f - f_0)$, and the negative sequence impedance term with expression (2.26) evaluated at $s = j2\pi(f + f_0)$ respectively.

The impedance models obtained with the procedure summarized above were validated with the equivalent impedance measured from detailed EMT simulations, which demonstrated the accuracy of the proposed method in both the resistance and reactance values. The model is able to describe the frequency bands of inverter-based generators with negative resistance, *i.e.*, negative damping. The negative damping regions are relevant to study stability of resonances. They occur due to the induction machine effect produced by the rotor slip in sub-synchronous frequencies, and due to delays in the controller introduced by the PWM algorithm and the filtering in super-synchronous frequencies.

2.5 Sensitivity of the impedance profiles to generator parameters

The resulting frequency-dependent impedance profile was analyzed through sensitivity studies to identify the most relevant generator parameters at different frequency ranges (the frequency ranges were set by the author to improve result visualization but can be changed):

- Subsynchronous range (SSR) from 0-40 Hz, observed at wind parks connected to long lines with series capacitive compensation.
- Near synchronous range (NSR) from 40-80 Hz, observed at wind parks connected to weak grids and poor synchronization control tunings.
- Harmonic frequency range (HFR) from 80-1500 Hz, observed during harmonic resonance events in wind parks with shunt capacitors for reactive power compensation and filtering.

The analysis is based on comparing the impedance profile of the generator for different values of each parameter. For example, in Figure 2.15 a), the measurement filter parameters only affect the HFR, whereas the proportional gains of the GSC affect all ranges in Figure 2.15 b). The capacitor from the LCL filter was removed to observe the HFR without its resonance.

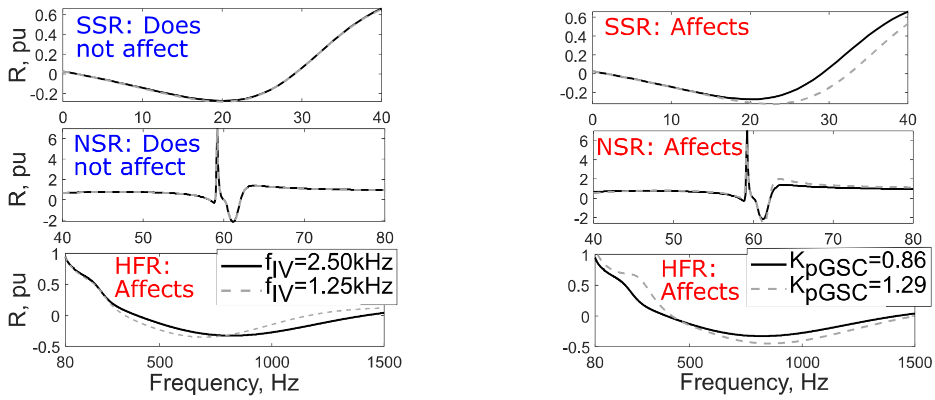

a) Measurement filter frequency **b) Proportional gain of GSC control**

Figure 2.15: Type-III generator sensitivity of the real part of the equivalent impedance to parameter variations for each frequency range

However, as many parameters must be analyzed, it is difficult to pinpoint which are the most important ones for each range based only on visual inspection of the profiles. In response, the Mean Absolute Sensitivity (MAS) index in expression (2.29) was designed to quantify the frequency-domain impedance profile sensitivity to each parameter and objectively identify the most influential at each frequency range. The higher the MAS value, the more relevant the parameter for impedance profile calculation.

$$MAS = \frac{1}{N}\sum_{n=1}^{N}\left|\frac{\int_{f_1}^{f_2}[Z_{orig}(f) - Z_{new}(f, k_n)]\,df}{(k_n - 1)(f_2 - f_1)}\right| \quad \textbf{(2.29)}$$

In (2.29), N is the number of values tested for each parameter; k_n is the multiplication constant in each test (*e.g.*, for the control delay, $T_d^{new} = T_d^{orig} \times k_n$ and $k_n \in [0.5, 1.0, 2.0]$). Z_{orig} is the original impedance profile without changes; and Z_{new} is the new profile after the modification; which are integrated numerically in frequency f from f_1 to f_2 to calculate the area between the curves. The MAS index is calculated separately for resistance R and reactance X of the generator. A more detailed description of each control parameter is available in Appendix A. The MAS index results for the Type-III and Type-IV generators are shown in Figure 2.16 and Figure 2.17.

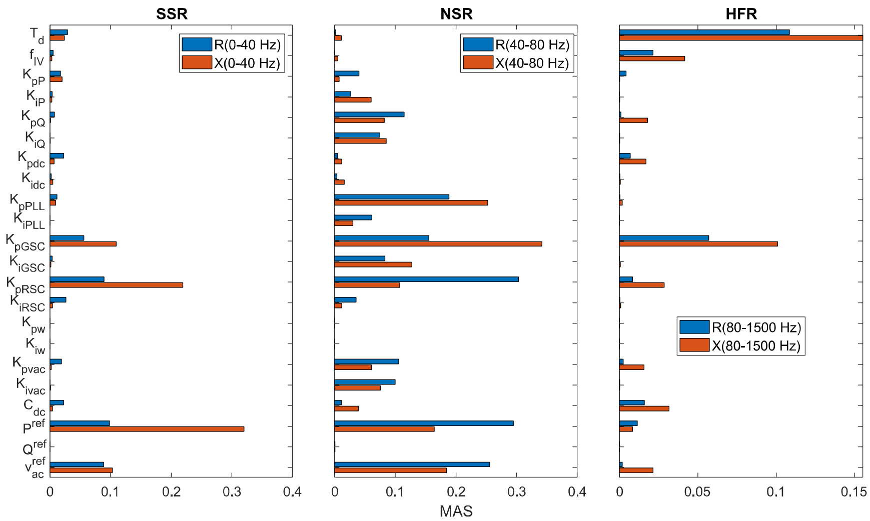

Figure 2.16: MAS results for Type-III generator

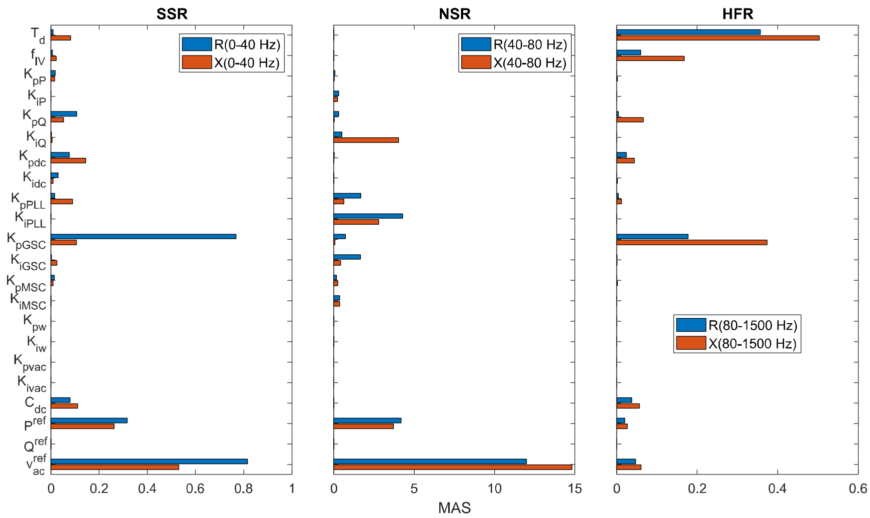

Figure 2.17: MAS results for Type-IV generator

The most important takeaways from the MAS index results are listed as follows:

2.5.1 Measurement filter and control delays

The control delay and the measurement filter are mostly relevant to the HFR. The delay has higher influence as the measurement filter cutoff frequency is typically higher than half the switching frequency. The Type-IV impedance is more sensitive to the control delay as it is defined only by the converter parameters, whereas the Type-III has an additional branch with the effect of an induction machine.

2.5.2 Control gains and DC bus coupling

The NSR is the most sensitive frequency range to control parameters due to the synchronization of the dq controllers and the fundamental frequency. The Type-III generator is more affected due to the direct coupling of the rotating machine with the grid.

The impedance profile is very sensitive to the GSC control gains for all frequency ranges. This also applies for the RSC in the Type-III generator, but not for the MSC in the Type-IV generator due to the decoupling effect of the DC bus.

All frequency ranges are slightly sensitive to the DC bus control, therefore, neglecting it can lead to inaccurate models [45]. This is further confirmed by the high sensitivity to the DC bus capacitor, particularly for the Type-IV generator.

The turbine speed controllers had no effect on the impedance profile for either generator at any range of frequency. This indicates all mechanical subsystems (turbine + generator masses, the turbine blades and its controllers) can be neglected for the studies of this thesis.

The outer control loops associated with power control are more relevant in the NSR. The reactive power control loop in the Type-IV generator is an exception as it affects all ranges.

The impedance profile of both generators is sensitive to the PLL subsystem in the NSR. And depending on the PLL gains, large PLL bandwidths can also affect the SSR [46]. This is shown in the studies of the Appendix D.

2.5.3 Power setpoints and terminal voltage

The setpoint of the active and reactive power changes the operational point of currents and voltages of the converters, which are necessary to calculate the impedance when including the outer control loops and the DC bus coupling [47]. The impedance model is more sensitive to the active power setpoint than the reactive power setpoint due to the larger magnitude of the related currents. These variables are more relevant in the NSR and the SSR.

Terminal voltage is important for the NSR in both generators. This importance is also visible in the SSR of the Type-IV generator as its grid-side converter dominates the overall impedance. And as expected, the power setpoints have a higher influence on the terminal voltage at weak grids [48].

The results of this study are a valuable input to narrow down the causes of problematic resonances in wind parks. Appendix C presents a series of recommendations to simplify the generator models at each frequency range, based on the MAS index results.

2.6 Chapter summary

This chapter presented the model of the Type-III and Type-IV wind generators, which is used in the following chapters of the thesis.

A descriptor-state space modeling procedure was proposed to derive the frequency-dependent equivalent impedance model of the generators from their detailed nonlinear electromagnetic transient model. Such procedure greatly simplifies the algebraic requirements to derive the models, while it also preserves high modeling detail. The impedance profiles resulting from this procedure were validated with detailed time-domain simulations.

With the proposed procedure, an investigation was conducted to verify the impedance-profile sensitivity to the different control parameters of the generators. The results of this study determined which control loops are more relevant to study each of three frequency ranges: 1) Sub-synchronous (0 Hz to 40 Hz); Near synchronous (40 Hz to 80 Hz); and Harmonic (80 Hz to 1.5 kHz). Such result was useful to narrow down the studies in the remaining chapters.

3 WEAKLY DAMPED RESONANCE

Weakly damped resonance (*i.e.*, harmonic resonance) in power systems can manifest as over-voltages and over-currents due to the amplification of harmonic distortions present in the circuit at points of the grid with either very high or very low impedance values. These lead to excessive heating, vibrations, insulation damage, accelerated aging, malfunction, and outages of grid components [49], [50].

A problematic harmonic resonance occurs when a natural oscillation mode of the grid is excited by a harmonic source at a frequency nearby the frequency of the oscillation mode. Such harmonic components that excite a resonance may originate from within the wind park as current emissions, or from other equipment in the grid, observed as a voltage distortion at the wind park point of common connection (PCC) [51].

Wind parks are susceptible to harmonic resonance-related problems due the presence of: large shunt capacitor banks for power factor correction installed inside the park; capacitors for filtering of converter switching harmonics installed at the generators; as well as important capacitive effect of long underground and submarine cables [52], [53]. These capacitances can create resonances in the range from 120 Hz to 1.5 kHz (2^{nd} to 25^{th} harmonics), where transmission system harmonics (especially 5^{th}, 7^{th}, 11^{th} and 13^{th} harmonics) are expected [54], [55].

Most of the studies in the literature of harmonic resonance are focused on the analysis of emissions from the wind generators [6]. However, modern wind generators (Type-III and Type-IV) are expected to have low emission levels at frequencies below the converter switching frequency as observed in the measurements from [56] and [57]. For instance, authors in [57] highlight that the effect of harmonics from the grid on the PCC voltage is predominant over the effect of the distortions emitted by the generators.

Due to the aforementioned reasons, this chapter proposes two charts to monitor, and one filter design method to mitigate the risk of problematic harmonic resonances in wind parks, which can be excited by background distortions from the grid. The first chart is aimed to assess the harmonic distortion levels at the PCC between the wind park and the grid in order to verify compliance with power quality compatibility standard levels. The second chart is aimed to determine the risk of wind park component overload due to harmonic resonance. Finally, a passive filter was designed to minimize the total harmonic distortion at PCC of the wind park and, as a result, solve both the previous compatibility and the overloading issues in a cost-effective fashion.

3.1 Resonance assessment at PCC between the wind park and the grid

In this section, a graphical method is developed to help monitor the risk of harmonic resonances in the wind park based only on information from the park that is readily available in practice to engineers, without the need to run any computer simulation.

3.1.1 Real wind park topology and power quality compatibility assessment

Consider the wind park in Figure 3.1, connected to a transmission grid with harmonic distortions. This circuit corresponds to a real 64 MVA wind park from the Northeastern region of Brazil. A complete description of the system parameters is given in the Appendix E. The point of common coupling (PCC) between the wind park and the grid is at the high voltage (HV) side of the main wind park main transformer. The step-up transformers of each generator link the generator at low voltage (LV) with the wind park feeders at medium voltage (MV). The shunt capacitor bank on the MV side of the main transformer is used for power factor correction.

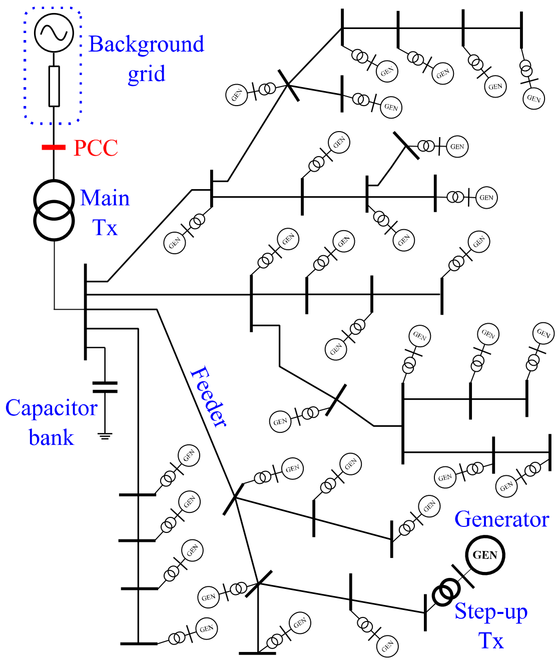

Figure 3.1: One-line diagram of real wind park in Brazil

The interaction between the circuit capacitances (the wind park capacitor bank being the most relevant) and the rest of the circuit can amplify harmonic distortions from the grid. Particularly, the PCC between the wind park and the grid is a key point for power quality compatibility assessment. The system operator requires harmonic assessment studies to estimate the PCC distortion level before wind park commissioning. After wind park commissioning, the system operator requests the wind park to comply with power quality regulations such as [8], so that harmonic distortions at PCC do not exceed a regulatory limit. However, among the many possible system operating scenarios, some may lead to a problematic harmonic resonance in the circuit, which increases the risk of excessive harmonic distortions at the PCC.

Existing approaches to pinpoint harmonic resonance conditions consist mainly in conducting numerous computer simulations with all possible operating points of the park and of the surrounding power system. This can be done either in time domain, through hundreds of electromagnetic transient (EMT) simulations with a detailed model of the wind park; or in frequency domain, where an equivalent model of the wind park is used. The former approach is the most accurate, but it is time consuming and requires a highly detailed model of the wind park circuit, which implies the need for engineers with high specialization to prepare and run these simulations. The latter approach requires less modeling detail, but still relies on exhaustive simulations. In addition, neither approach includes a systematic guideline to interpret the numerous simulation results and translate them into actionable information to be directly used by engineers. In fact, many times, the industry is interested in simple procedures that can provide a quick screening of potentially problematic conditions even before running any simulation. It is a desirable characteristic that such simplified procedure be able to identify, with limited information, the critical resonance scenarios which must be investigated in more detail.

3.1.2 Simplified graphical methodology to identify circuit configurations leading to problematic harmonic resonance at PCC

It is possible to describe key parameters of the circuit in physical quantities that are readily available to engineers in practice such as: S_{SC} as the short-circuit capacity of the grid at the PCC; S_{WP} as the rated wind park capacity; and Q_C as the rated reactive power of the capacitor bank. By using these factors, this section proposes the “Harmonic Resonance Chart” in Figure 3.2, defined in the S_{SC}/S_{WP} vs. Q_C/S_{WP} plane, which maps which circuit configurations lead to problematic resonances, that is, which circuit configurations that cause amplification of harmonics at the PCC above a fixed value A_{lim}. The harmonic amplification at PCC of the harmonic distortions from the grid is defined as $A(f)$ at every frequency f in expression (3.1), in terms of the harmonic voltage at PCC $V_{PCC}(f)$ after wind park connection, and the grid harmonic voltage prior to the wind park connection $V_{SC}(f)$ (the open circuit voltage).

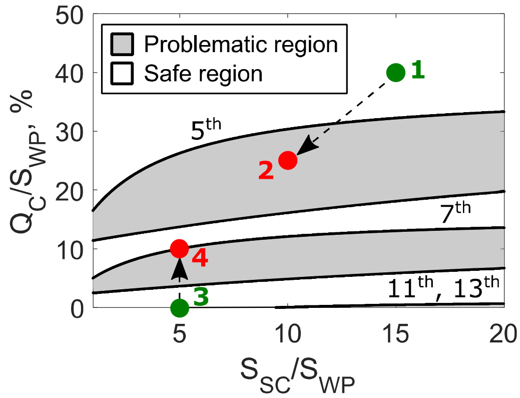

a) Type-III wind park

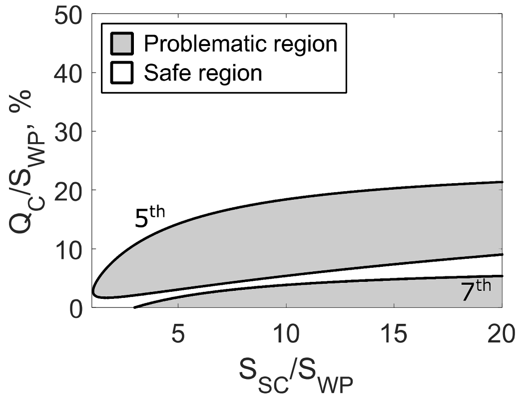

b) Type-IV wind park

Figure 3.2: Harmonic Resonance Chart

$$A(f) = \left|\frac{V_{PCC}(f)}{V_{SC}(f)}\right| \tag{3.1}$$

Only the 5th, 7th, 11th and 13th harmonics are considered to draw Figure 3.2 as these are the main grid distortions in high voltage levels [5]. However, if necessary, other harmonics can be included. The charts in Figure 3.2 were built for $A_{lim} = 1.2$, and the boundary of each problematic region represents the circuit configurations where $A(f) = A_{lim}$.

The Harmonic Resonance Chart is a practical, easy-to-use method for a first-cut assessment of the risk of harmonic resonance at wind parks as it shows that not all wind parks need such a detailed analysis (through time-domain simulation or harmonic power flows). If any point (S_{SC}/S_{WP}, Q_C/S_{WP}) representing a circuit configuration is in the safe region, it does not face problems due to harmonic resonance and no further investigation is required. However, if it is located inside any of the problematic regions, problems may arise due to excessive harmonic amplification and more detailed harmonic studies must be performed in the latter case.

The markers and arrows in Figure 3.2 a) are two examples to illustrate the use of the chart. For the first example, marker 1 represents a wind park without resonance problems. However, if the rated capacity S_{WP} is increased by a wind park expansion, while the reactive compensation Q_C remains constant, both Q_C/S_{WP} and S_{SC}/S_{WP} are reduced, so the wind park is now located at marker 2. The chart shows that this transition creates a risk of problematic resonance at the 5th harmonic. And for the second example, consider a wind park operating at marker 3 without a capacitor bank. The connection of one stage of the capacitor bank of about 10% of the wind park rated capacity corresponds to the transition to marker 4, where the wind park is at the very boundary of the problematic region of resonance at the 7th harmonic.

Amongst the potential applications of the Harmonic Resonance Chart, it is possible to use it to avoid combinations of S_{WP}, S_{SC} and Q_C resulting in problematic harmonic resonances when designing a new wind park, while it is also useful when studying grid reconfigurations, wind park expansions, switching of capacitor bank stages during operation etc. The chart significantly reduces the need for simulation studies, by quickly discarding circuit configurations which do not represent risk of harmonic resonance.

3.1.3 Analytic procedure to build the chart

Instead of using simulation to calculate the ratio of voltages in expression (3.1) for each circuit configuration, the problematic regions of the Harmonic Resonance Chart can be obtained in terms of the equivalent harmonic impedances of the simplified wind park circuit in Figure 3.3 and expression (3.2), where the grid is represented by a Thévenin equivalent with impedance $Z_{SC}(h) = R_{SC}(h) + jX_{SC}(h)$, and the wind park is represented by an impedance equivalent $Z_{WP}(h) = R_{WP}(h) + jX_{WP}(h)$ (at every harmonic frequency h).

$$A_{PCC}(h) = \left|\frac{V_{PCC}(h)}{V_{SC}(h)}\right| = \left|\frac{Z_{WP}(h)}{Z_{WP}(h) + Z_{SC}(h)}\right| \tag{3.2}$$

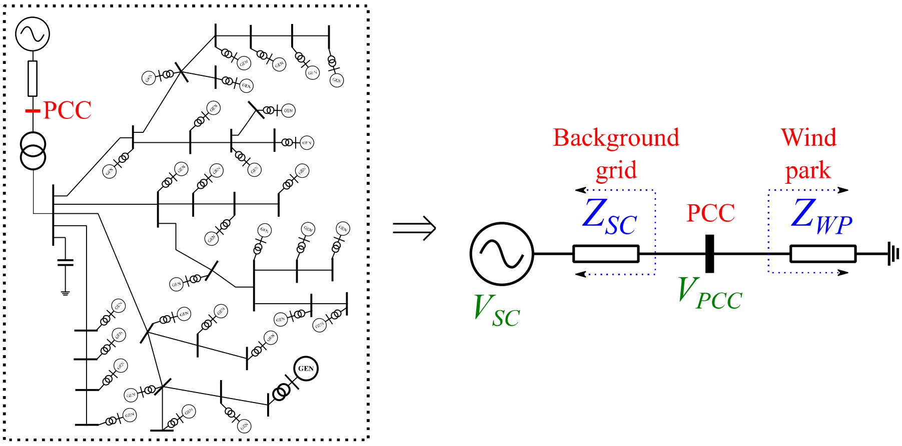

Figure 3.3: Equivalent wind park circuit for resonance analysis at PCC

The grid equivalent impedance can be modeled as a series RL branch, so that $Z_{SC}(h) = R_{SC} + jhL_{SC}$, where its components are calculated with expression (3.3) in terms of the short-circuit ratio at PCC S_{SC}/S_{WP} and the $X/R=L_{SC}/R_{SC}$ ratio, both at fundamental frequency. However, if available, an impedance profile of the grid at PCC can be used instead.

$$R_{SC} = \frac{[1+(X/R)^2]^{-0.5}}{S_{SC}/S_{WP}} \qquad L_{SC} = \frac{[1+(X/R)^{-2}]^{-0.5}}{S_{SC}/S_{WP}} \tag{3.3}$$

As for the equivalent wind park impedance $Z_{WP}(h)$, the main transformer and the step-up transformers are modeled with RL branches, the capacitor bank is modeled in terms of the reactive power compensation ratio $Z_C(h) = -j\,(h\,Q_C/S_{WP})^{-1}$, and all feeder segments are modeled with a pi equivalent circuit. All parameters are available in the Appendix E.

The wind generator is modeled as an equivalent impedance $Z_{gen}(h)$, which can be calculated numerically with the procedure from Section 2.2, analytically as in [25] and [54], or with waveform measurements as in Section 2.3, from either field records or simulation of "black-box" EMT models provided by vendors [29].

Now, for every Q_C/S_{WP} ratio of the wind park, it is possible to calculate $Z_{WP}(h)$ to use expression (3.2) and evidence the S_{SC}/S_{WP} ratio at the amplification boundary $A(h)=A_{lim}$ at harmonic order h. After algebraic manipulation, this results in a quadratic expression (3.5).

$$A_{PCC}(h) = \left|\frac{Z_{WP}(h)}{Z_{WP}(h)+Z_{SC}(h)}\right| = \frac{\sqrt{(R_{WP})^2+(X_{WP})^2}}{\sqrt{(R_{WP}+R_{SC})^2+(X_{WP}+X_{SC})^2}} = A_{lim} \tag{3.4}$$

$$0 = a(S_{SC}/S_{WP})^2 + b(S_{SC}/S_{WP}) + c \Rightarrow S_{SC}/S_{WP} = \frac{-b \pm \sqrt{b^2 - 4ac}}{2a} \tag{3.5}$$

where the coefficients in per unit (pu) basis of wind park rated capacity S_{WP} are:

$$\begin{gathered} a = (A_{lim}^2 - 1)\left(R_{WP}^2(h) + X_{WP}^2(h)\right) \\ b = 2A_{lim}^2\left(R_{WP}(h)R_{SC}(h) + X_{WP}(h)X_{SC}(h)\right) \\ c = A_{lim}^2\left(R_{SC}^2(h) + X_{SC}^2(h)\right) \end{gathered} \tag{3.6}$$

Coefficients a and c in expression (3.6) are always positive, but coefficient b can assume negative values when $R_{WP} < 0$ and/or $X_{WP} < 0$. Therefore, when $b < 0$ and $b^2 > 4ac$, the roots in (3.5) will be purely real and positive. These purely real, positive roots establish the boundary of the problematic region in the resonance chart, for harmonic order h and reactive power compensation Q_C/S_{WP}. The first root (positive sign) provides the upper boundary of the problematic region, and the second root (negative sign) provides the lower boundary. When the solutions are either negative or complex, it means there is no S_{SC}/S_{WP} value that leads to $A \geq A_{lim}$ at harmonic h.

The set of positive-real Q_C/S_{WP} vs. S_{SC}/S_{WP} solutions leading to amplification A_{lim} creates the boundary of the problematic regions. This procedure is carried out for each monitored harmonic order h, so the Harmonic Resonance Chart is calculated analytically without running any computer simulation. The value of A_{lim} can be set based on standards [8], or by utility requirements for voltage distortion at PCC. More details on this selection can be found in [58].

Summarizing, the Harmonic Resonance Chart is built analytically with the following steps:

1) For every Q_C/S_{WP} ratio, calculate the equivalent wind park impedance at PCC $Z_{WP}(h)$.
2) For every harmonic h, calculate the a, b and c coefficients using expression (3.6).
3) Calculate the boundary of harmonic amplification region using expression (3.5). Each purely real, positive solution of this equation is saved as one point of the problematic region boundary.
4) All combinations within the boundaries derived in Step 3 are considered part of the risk region.

3.1.4 Validation

The 64 MVA wind park topology from the Appendix E, and the 2 MVA wind generator models described in the Appendix A, were used to build the Harmonic Resonance Chart in Figure

3.4 after running multiple electromagnetic transient (EMT) simulations in the MATLAB / Simscape Power Systems software. The simulations sampling rate was set to 15.36 kHz (256 samples per cycle).

An initial simulation is conducted with an undistorted background grid, where it is confirmed that the wind parks do not produce significant harmonic distortions (that is, they can indeed be modeled as an impedance). Then, a 1.0% harmonic voltage distortion is added to the background grid as $V_{SC}(h)$ for the 5th (negative sequence), the 7th (positive sequence), 11th (negative sequence) and 13th (positive sequence) harmonics. This 1% distortion is within the allowable distortion levels established for high voltages in IEEE Std. 519-2014 [8]. Discrete Fourier Transform (DFT) is applied to a 12-cycle window (as recommended in IEC 61000-4-30 [59]) of the measured voltages at PCC, and the respective voltage component at the h^{th} harmonic frequency $V_{PCC}(h)$ is calculated. With these voltages, the amplification $A_{PCC}(h)$ from the simulation can be calculated using expression (3.2). All simulations that result in harmonic amplification at the PCC above the limit A_{lim} = 1.2 are marked with an "x" in the chart. Finally, the boundaries of the problematic regions (i.e., the solid black lines) are calculated analytically with the aforementioned procedure and also plotted in the chart in Figure 3.4.

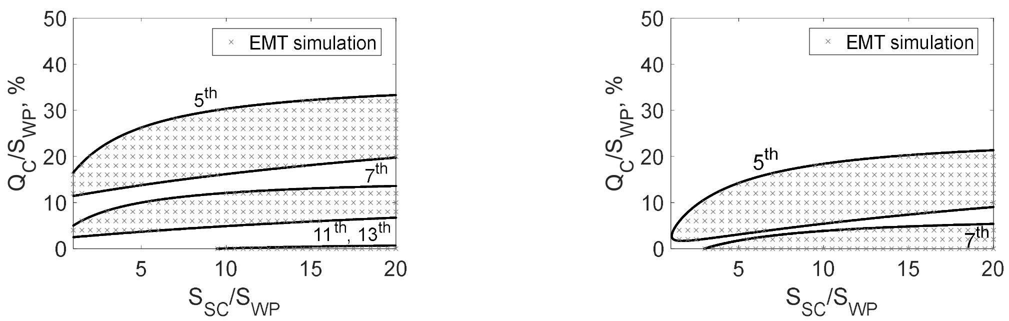

a) Type-III wind park **b) Type-IV wind park**

Figure 3.4: Validation of the Harmonic Resonance Chart with EMT simulation

From Figure 3.4, one can notice that fully detailed simulation and analytical results match well. This means that the analytic method proposed to derive the boundaries of the problematic regions is indeed accurate and these regions can be obtained without running any simulation. This feature greatly facilitates the practical implementation of the proposed method.

3.1.5 Sensitivity studies of the Harmonic Resonance Chart

This section provides sensitivity studies to characterize how different parameters affect the problematic regions of the proposed Harmonic Resonance Chart.

3.1.5.1 Amplification limit

Figure 3.5 presents a sensitivity study of the Harmonic Resonance Chart (HRC) to the maximum amplification A_{lim} that is used to delimit the problematic regions in the chart. For each chart, an overall "risk" index is also indicated on top of the chart. This index is the ratio between the area of the problematic region and the total area of the chart.

As A_{lim} increases, less circuit configurations are problematic, so the overall problematic region is smaller, leading to a risk reduction. As noted previously, the risk of harmonic resonance at the PCC of the Type-IV wind park is lower than the risk of the Type-III wind park. This can be explained using expression (3.2). Type-IV generators have a larger equivalent impedance $Z_{gen}(h)$ than Type-III generators, which leads to a larger $Z_{WP}(h)$ and, consequently, lower $A(h)$. This results in a lower risk of problematic harmonic resonance.

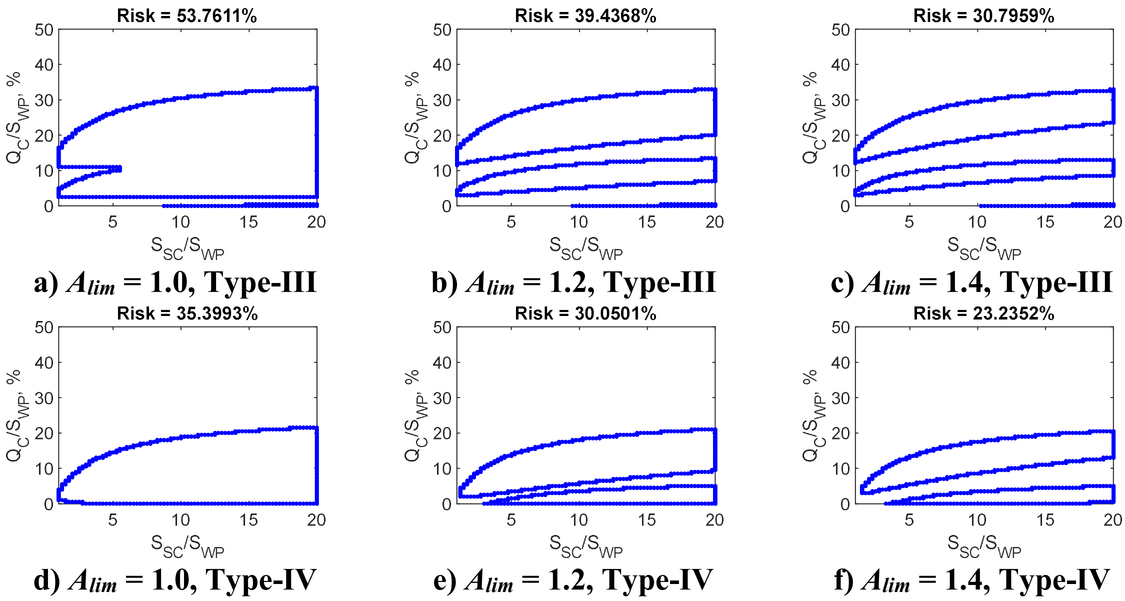

a) A_{lim} = 1.0, Type-III **b) A_{lim} = 1.2, Type-III** **c) A_{lim} = 1.4, Type-III**

d) A_{lim} = 1.0, Type-IV **e) A_{lim} = 1.2, Type-IV** **f) A_{lim} = 1.4, Type-IV**

Figure 3.5: Sensitivity of HRC to amplification limit

3.1.5.2 Control gains

The next sensitivity study evaluates how the parameters of the generator controllers affect the chart. According to Section 2.5, the parameters with the highest influence on the impedance profile at the range of harmonic frequencies are the proportional gain of the current controllers and the delays introduced by the control and by voltage and current measurement filters.

The effect of the proportional gains of the current controllers is presented in Figure 3.6. The results for the gain of the machine-side converter of the Type-IV generator are not presented as such gain does not impact the impedance profile of the Type-IV generator due to the decoupling action provided by the DC bus. Notice that increasing the gains tends to reduce the risk because it increases the damping provided by the generator converters. The GSC gain did not produce relevant changes for the Type-III generator, but it did for the Type-IV generator as the impedance of the Type-IV generator is more dependent on the GSC controller than the impedance of the Type-III generator (the latter generator also has the influence of the induction machine branch and the RSC). As for the RSC gain of the Type-III generator, the risk does not change significantly, but the regions are shifted towards higher reactive power compensation values (larger capacitors) due to the generator equivalent reactance becoming smaller, and shifting resonances to the 5^{th} and 7^{th} harmonics. The regions associated to the 11^{th} and 13^{th} harmonics did not result in any significant changes.

The sensitivity of the chart to the control delay of the converters is shown in Figure 3.7. Notice there is no simple linear pattern as both increasing and decreasing the delay can reduce the risk in the Type-III generator, whereas both increasing and decreasing the delay increases the risk in the Type-IV generator (no directly proportional correlation). This behavior is linked to the oscillation pattern introduced by the control delay in the frequency profile of the generator, which is visible in Figure 2.13, where the negative damping region shifts according to the control delay size. This non-linear impact of the control delays on the frequency profile of the generators justifies the importance of modeling the delays with accuracy on harmonic studies.

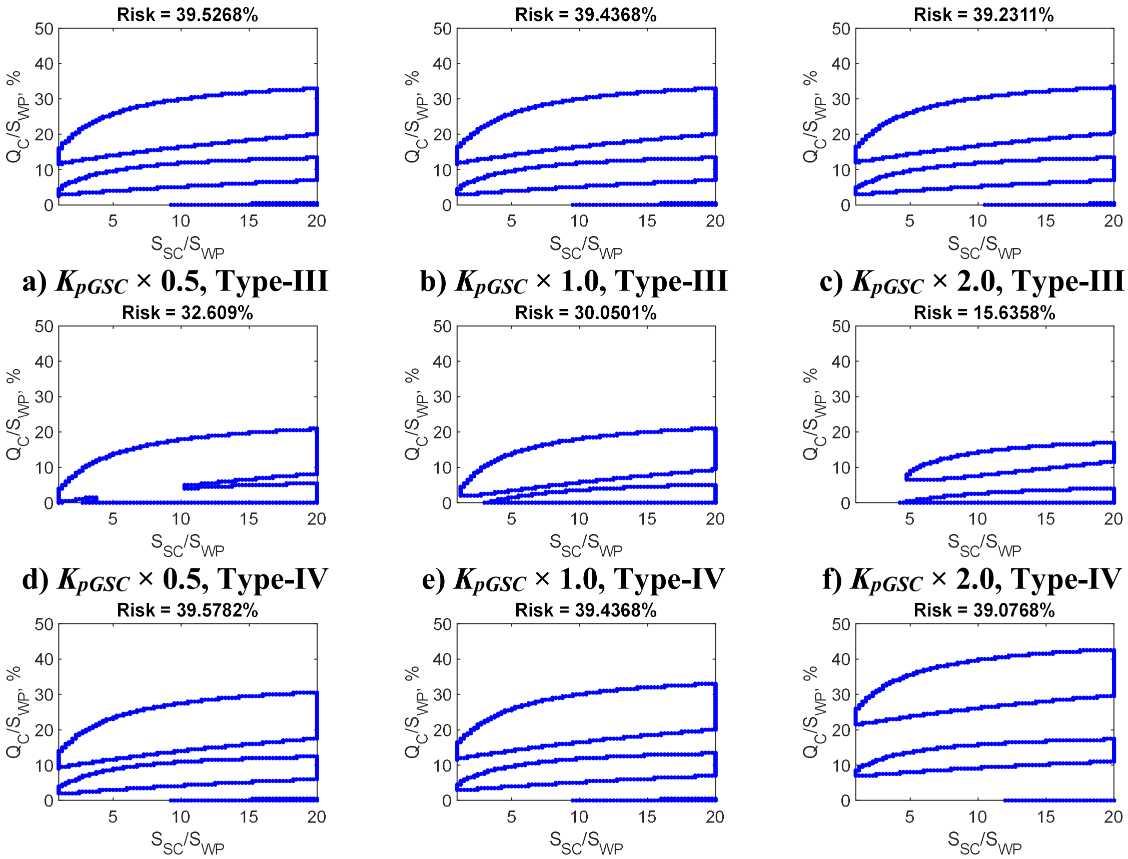

a) K_{pGSC} × 0.5, Type-III b) K_{pGSC} × 1.0, Type-III c) K_{pGSC} × 2.0, Type-III

d) K_{pGSC} × 0.5, Type-IV e) K_{pGSC} × 1.0, Type-IV f) K_{pGSC} × 2.0, Type-IV

g) K_{pRSC} × 0.5, Type-III h) K_{pRSC} × 1.0, Type-III i) K_{pRSC} × 2.0, Type-III

Figure 3.6: Sensitivity of HRC to proportional gains of current control

3.1.5.3 Capacitive elements in the wind park

The effect on the resonance chart of eliminating capacitive elements from the circuit is shown in Figure 3.8. Notice that both the feeders and the front-end filters of the generators have non-negligible shunt capacitive impedances in the harmonic range of frequencies that reduce the risk of resonance.

Eliminating the capacitance from the front-end filter of the generators leads to an increase in the size of the problematic resonance region associated to the higher order harmonics (11^{th} and 13^{th}) since such LCL filter of the GSC is designed to damp the switching distortions of the grid-side converter, which take place at higher frequencies close to the 11^{th} and 13^{th} harmonics.

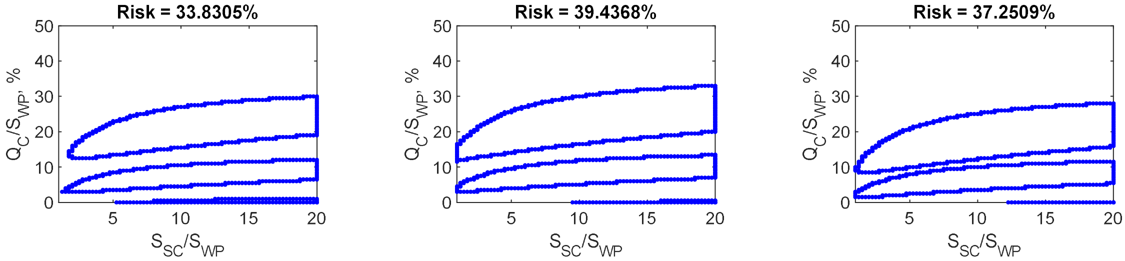

a) T_d × 0.5, Type-III b) T_d × 1.0, Type-III c) T_d × 2.0, Type-III

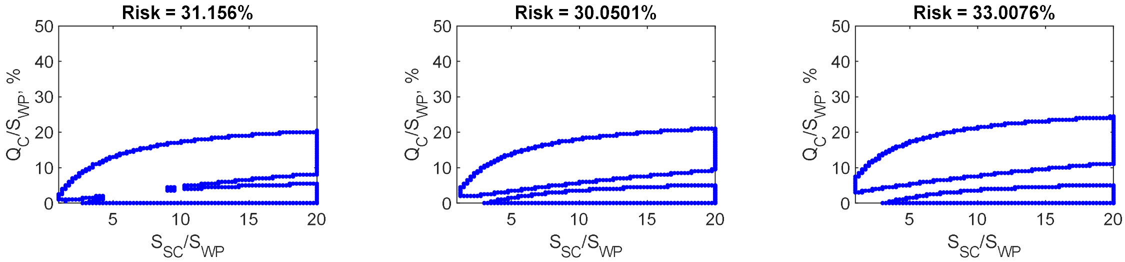

d) T_d × 0.5, Type-IV e) T_d × 1.0, Type-IV f) T_d × 2.0, Type-IV

Figure 3.7: Sensitivity of HRC to control delay

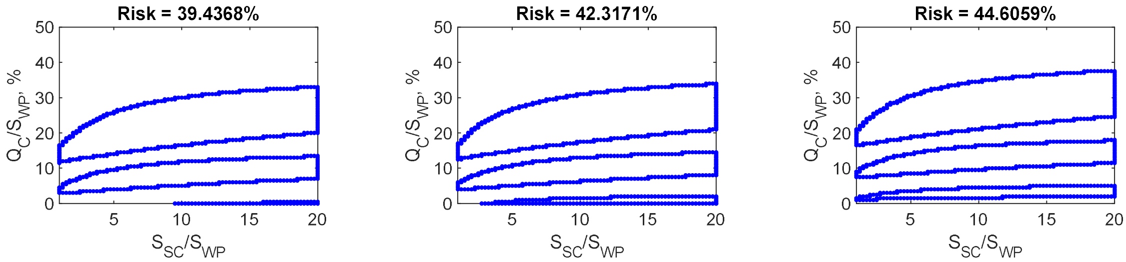

a) Type-III, LCL filter, underground feeders b) Type-III, L filter, underground feeders c) Type-III, LCL filter, overhead feeders

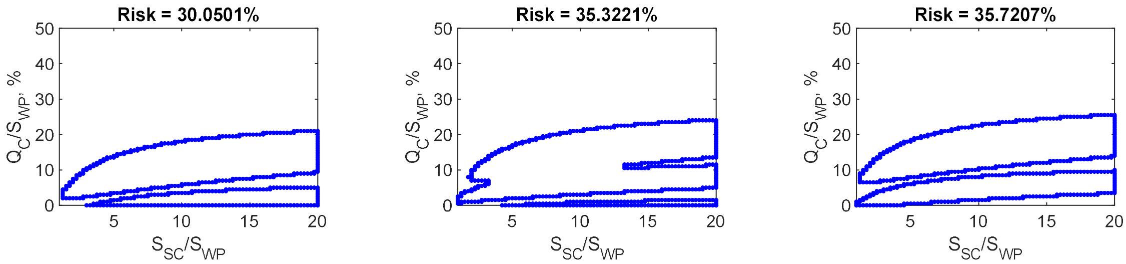

d) Type-IV, LCL filter, underground feeders e) Type-IV, L filter, underground feeders f) Type-IV, LCL filter, overhead feeders

Figure 3.8: Sensitivity of HRC to removing capacitive elements from the wind park

3.1.5.4 Grid equivalent impedance profile

The previous studies used an RL series branch (calculated from the short-circuit ratio at PCC) to model the equivalent impedance of the grid. A study was conducted to obtain the shape of the resonance chart considering a more complex grid equivalent, measured at bus 5 of the IEEE 14 buses test system [60]. This grid incorporates long transmission lines, loads, synchronous generators, and shunt capacitors. The resulting impedance profile is shown in Figure 3.9 a). The grid equivalent at bus 5 has a short-circuit ratio of S_{SC}/S_{WP} = 17.8 (S_{WP} = 64 MVA). In this case for example, the Type-III wind park has no risk region at the 7th harmonic due to the large positive damping provided by the grid. This grid equivalent has a much higher damping than the RL equivalent, so it plays an important role in reducing the risk of resonance in both Type-III and Type-IV wind parks.

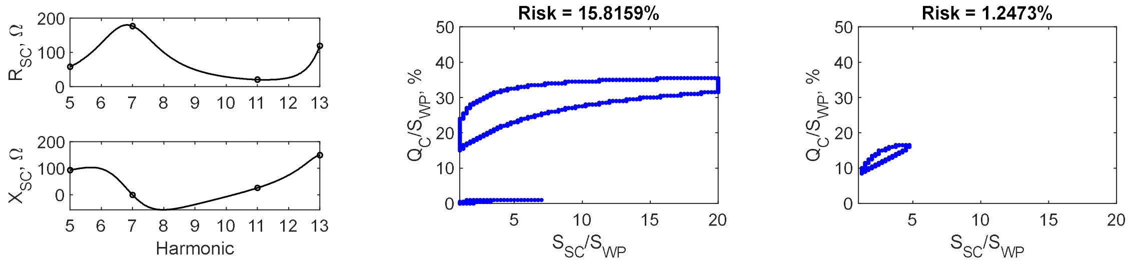

a) Grid impedance profile **b) HRC, Type-III** **c) HRC, Type-IV**

Figure 3.9: HRC with generic grid impedance profile

After extensive testing with many other grid equivalent impedance profiles, it was found the grid effect on the shape of the charts is case dependent, so it is advised to build the charts with grid information if available. Using the simplified RL branch yields in most cases, a conservative estimate, especially for profiles with important shunt capacitances leading to negative reactance and additional resonance frequencies.

3.1.5.5 Summary of the sensitivity studies

The following points summarize the most important findings of these sensitivity studies:

- Lower amplification limits (more restrictive) lead to larger risk regions. On the other hand, greater limits (less restrictive) produce smaller risk regions.

- Smaller control delays tend to reduce the size of the risk regions. However, even if these delays are completely removed, there still exists a risk region due to harmonic resonance.
- Increasing the proportional gains of the current controllers slightly reduces the risk of harmonic resonance because these gains can help increase the contribution of the generator to the system damping. However, tuning these gains as a mitigation measure can deteriorate their operation at fundamental frequency, thus, proving to be ineffective.
- The shunt capacitive elements play an important role in the harmonic resonance risk assessment and should be considered when modeling the wind park feeders and filters in detail for higher accuracy. These capacitive elements tend to eliminate the risk of resonance at the 11^{th} and 13^{th} harmonics.
- If available, the detailed frequency-dependent impedance profile of the background grid should be included in the resonance risk assessment as the problematic harmonic resonance conditions depend on this profile. The damping profile, as well as the additional resonances associated with capacitive elements from the grid can change the shape of the risk regions. In the studied cases, simplified grid models (such as a series RL circuit) were found to normally lead to more conservative results.

3.2 Resonance assessment of components inside the wind park

Another adverse effect of harmonic resonances in wind parks is the risk to overload wind park components. Methods such as the one proposed in Section 3.2 can identify harmonic resonances in the park, however, the existence of a resonance by itself is not enough to indicate if and which components are overloaded. This also depends on the amount of background distortions in the system and on the loading limits of each component.

There are three main types of approaches that can be used for investigating in-park distortions. First, there are measurement-based analyses such as those in [7], [61] where specific points of a wind park are monitored to analyze the behavior of harmonic distortions in the park and their impact on the grid. Unfortunately, measurements at internal points of the wind park (other than the PCC) are not always available in practice. Another approach is to use detailed electromagnetic transient simulations for the harmonic resonance-related analyses [62].

Although this approach can provide precise results, it is time consuming, requires highly detailed models and information of wind park components and users with high specialization. The third approach consists in using frequency-domain models of the park components to identify resonances and investigate the park behavior under such conditions [63], [6]. This is a simple and adequate model for first-screening studies, but existing works still rely on numerous simulations to investigate the resonance conditions, which is also time consuming. All these approaches do not provide a systematic, easy-to-use method that can be adopted in practice by engineers to quickly analyze the risk of component overload due to excessive in-park distortions (such as in harmonic resonance conditions). In fact, these works are mostly focused on the impact of the wind park on the grid [64], [65]. Therefore, it is important to investigate in more detail the loading conditions of internal wind park components during harmonic resonances.

In this context, this section proposes a chart for a quick initial assessment of potential component overloads in a wind park based only on information that is readily available in practice for engineers responsible for its operation and without the need to run any simulation. To achieve this, the first part of this section investigates the harmonic resonance effects on loading characteristics of the wind park components. The idea is to identify the most critical components and operating conditions that must be considered in a simplified, first-screening assessment. Results outline that capacitor bank is the most vulnerable component in resonance conditions. Such result is used to derive the chart for engineers to quickly identify if any wind park component is operating overloaded. The chart can be obtained analytically, without running any computer simulation and can be consulted by using only voltage distortion levels measured at the PCC and basic information from the park available in practice (the wind park capacity and reactive power compensation level used in the park). This is useful, for instance, to offer quick insights into what is the maximum allowable voltage distortion at the PCC of wind park so that no component becomes overloaded.

3.2.1 Loading of wind park components

To illustrate the loading concept, consider the scenarios in Figure 3.10 for one wind park component operating with voltage harmonic distortion at its terminals. Here, wind park components have two types of loading: at fundamental frequency; and at harmonic frequencies.

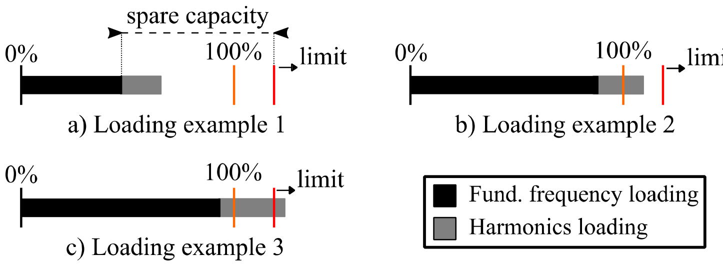

Figure 3.10: Representation of the loading of wind park components

If the combination of these two loadings surpasses a certain limit value, the component is considered overloaded. The amount of additional loading due to harmonics tolerated by the component depends on the spare capacity after the fundamental frequency loading, as shown in Figure 3.10 a). The component operates under acceptable conditions in Figure 3.10 a), with plenty spare capacity for harmonic loading. In Figure 3.10 b), it operates above rated capacity, *i.e.*, over 100%. However, most components are designed to withstand loading levels above their rated value, while still not violating the limit defined by standards or vendor recommendation. In Figure 3.10 c), the component is overloaded due to excessive harmonic distortion and insufficient spare capacity, even with the fundamental frequency loading below the rated loading (100%). Therefore, the scenario in Figure 3.10 c) is considered problematic.

3.2.1.1 Loading indices

This loading of wind park components due to grid distortions can be quantified by running harmonic power flows, and then, calculating the following indices [8]: rms voltage V_{rms}, rms current I_{rms}; apparent power S; and peak voltage V_{peak} for each component.

The rms voltage V_{rms} and the rms current I_{rms} are calculated with (3.7) and (3.8), respectively. V_{nom} is the rated single-phase voltage and S_{nom} is the rated three-phase power capacity of the component, so that the rated phase current is $I_{nom} = S_{nom} / (3V_{nom})$. V_h is the single-phase voltage and I_h is the phase current, both at harmonic order h. Although (3.7) and (3.8) are limited here to the 5th, 7th, 11th and 13th harmonics, they can be expanded for any other harmonics.

$$V_{rms} = \frac{1}{V_{nom}} \sqrt{\sum_{h=1,5,7,11,13} {V_h}^2} \quad \textbf{(3.7)} \qquad I_{rms} = \frac{1}{I_{nom}} \sqrt{\sum_{h=1,5,7,11,13} {I_h}^2} \quad \textbf{(3.8)}$$

Expression (3.7) is used for all wind park components. When a component has more than one live terminal (such as cable segments and transformers), the bus with the largest V_{rms} value is considered. Expression (3.8) is used for all wind park components except for the transformers as they require an adjustment to account for the thermal effects of the winding hot-spot [66]. The adjusted rms current for the transformers I_{rms_Tx} is calculated with (3.9), where P_{ECR} is the pu value of eddy current losses and P_{OSLR} is the rated pu value of other stray losses, both at rated transformer loading. For oil-filled transformers, $P_{ECR} = 0.3$ pu and $P_{OSLR} = 0.6$ pu [66]. The adjustment can be seen as current that produces an equivalent heating effect in the windings to that from the losses.

$$I_{rms\_Tx} = \sqrt{\frac{{I_{rms}}^2 + P_{ECR} \sum_{h=1,5,7,11,13}\left(h^2 {I_h}^2\right) + P_{OSLR} \sum_{h=1,5,7,11,13}\left(h^{0.8} {I_h}^2\right)}{1 + P_{ECR} + P_{OSLR}}} \quad \textbf{(3.9)}$$

Notice (3.9) becomes (3.8) if the eddy current losses and other stray losses are neglected. One can also note that the additional loading due to thermal effects also depends on the harmonic order. Higher harmonic orders have greater impact on the index.

For components with one live terminal and one grounded terminal (capacitor and generators), the apparent power is calculated with expression (3.10). For components with two live terminals (feeders), the apparent power is calculated with expression (3.11), and for the transformers with expression (3.12) after adjusting their rms current.

$$S = V_{rms} I_{rms} \quad \textbf{(3.10)} \qquad S = (V_{rms1} - V_{rms2}) I_{rms} \quad \textbf{(3.11)}$$

$$S = (V_{rms1} - V_{rms2}) I_{rms\_Tx} \quad \textbf{(3.12)}$$

The peak voltage index is obtained with expression (3.13), where V_{nom_peak} is the rated peak value of the single-phase voltage. The index is the algebraic sum of peak voltages at all frequencies. This indicates that the peak values of all voltages are assumed to occur simultaneously (with zero phase angle displacement) due to the lack of phase angle information. This worst-case condition is chosen so that a conservative estimate of the index can be obtained with less information (*i.e.*, without phase angle information). The peak voltage loading index is only used for the capacitor bank.

$$V_{peak} = \frac{\sqrt{2}}{V_{nom\_peak}} \sum_{h=1,5,7,11,13} V_h \qquad \textbf{(3.13)}$$

3.2.1.2 Loading limits

The limit values of the loading indices for the different wind park components are summarized in Table 3.1, which are given in per unit of the component ratings. These were extracted from grid standards and vendor datasheets for operation under harmonic distortions: IEEE Std C57.110 [67] and IEEE Std C57.12.00 [68] define rms voltage and current limits of the transformers; IEEE Std 1036-2010 [69] is used for the shunt capacitor of the park, as it defines limits for the peak and rms voltages across the capacitor bank, rms current flow, and apparent power; Datasheets and standards such as Enel GSC-001 [70] are used for the underground cables as it defines limits for the rms current, apparent power flow and rms voltage; and datasheets and converter saturation limits are used for generators [71] as they define maximum values for the rms voltage, rms current, and apparent power.

Table 3.1: Limit values for loading indices

Component / Index	V_{rms}, pu	I_{rms}, pu	V_{peak}, pu	S, pu
Transformers	1.10	1.05	-	-
Capacitor	1.10	1.35	1.2	1.35
Feeder	1.20	1.00	-	1.00
Generator	1.10	1.10	-	1.10

3.2.2 Assessment of Component Loading Level

This section presents an investigation of the behavior of individual component loading in wind parks with background harmonic distortions. The main goal is to extract tendencies about what are the most critical conditions to be studied in a first-screening assessment.

3.2.2.1 Configuration of the harmonic power flows

The following parameters and circuit configurations were tested: short circuit ratio at the PCC (S_{SC}/S_{WP}) was varied from 2 to 20; Reactive power compensation ratio (Q_C/S_{WP}) was varied from 0 to 50%; Active power setpoint at PCC (P_{sp}) was varied from 0.1 to 1.0 pu; PCC voltage distortion magnitude at harmonic h (v_h) was varied from 0 to 5% of the fundamental frequency voltage at the PCC; and the harmonic orders tested (h) were the 5^{th}, 7^{th}, 11^{th} and 13^{th} orders.

To map the circuit configurations leading to wind park component overloads, thousands of power flows were run in the wind park circuit with the aforementioned parameters and configurations, first at fundamental frequency and then at the harmonic frequencies. After that, the loading indices were calculated from the nodal voltages and the currents through the components using expressions (3.7) to (3.13). If any of the indices violate their limit, such scenario is flagged as problematic.

The nodal voltages at fundamental and harmonic frequencies were calculated with expression (3.14), where $\mathbf{Y}(h)$ is the admittance matrix of the system, $\mathbf{V}(h)$ is the vector with nodal voltages and $\mathbf{I}(h)$ is the vector with current injections, at the harmonic order h.

$$\mathbf{Y}(h) \times \mathbf{V}(h) = \mathbf{I}(h) \tag{3.14}$$

All wind park components are modeled as equivalent impedances and included in the admittance matrix $\mathbf{Y}(h)$ both at fundamental and harmonic frequencies (see Appendix E for the parameters and models). The grid is modeled as a Thévenin equivalent at fundamental frequency and harmonic frequency. The wind generators are modeled as constant current sources at fundamental frequency with current value matching their power injection, and as impedance equivalents at harmonic frequencies which includes their controller effects.

3.2.2.2 Results and discussion

Figure 3.11 was elaborated with the simulations and shows the percentage of problematic scenarios where each loading index was violated. The main findings in this figure are that: 1) the capacitor has the highest problem rates, with apparent power, current and peak voltage being more problematic than the rms voltage; 2) rms voltage is a common problem for all wind park components, although with lower rates (around 10% of all problematic scenarios); 3) apparent powers and currents at the generator and feeder are not as problematic as voltage; and 4) transformer currents are more problematic than their voltages. These results initially highlight that a first-screening analysis can be focused only on the capacitor bank apparent power, so that a component overload will be identified first in practically all problematic scenarios.

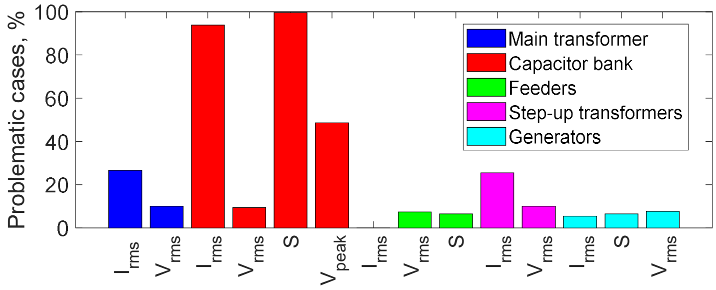

Figure 3.11: Problematic loading indices from harmonic power flow results

Figure 3.12 presents the correlation between loading indices for all studied scenarios. The more scenarios two indices are flagged equally, the higher their correlation. Notice all indices are highly correlated (lowest correlation is 94%). This means that, most of the time, problems will not arise in a component or index individually, but in several indices and components simultaneously. This is a key finding as along with the results in Figure 3.11, it suggests that a first-screening analysis of wind park component loading can be focused on the capacitor. This result makes sense technically as the risk of component overload is greater near harmonic resonances, where the capacitor is the main culprit (largest participation factor in harmonic modal analysis of matrix $\mathbf{Y}(h)$ [41]).

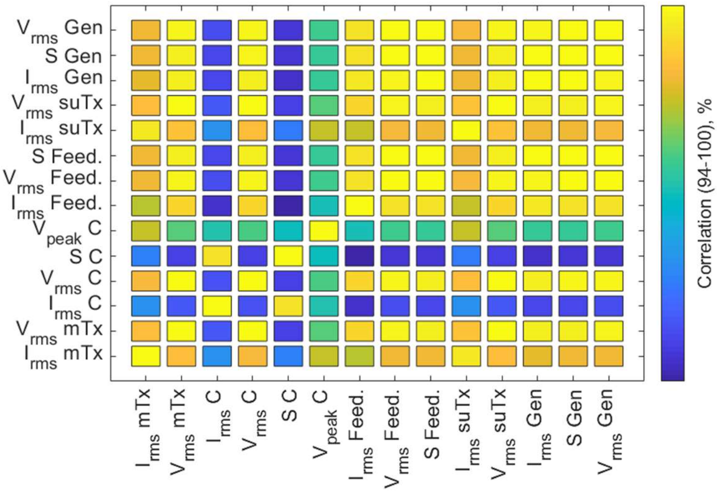

Figure 3.12: Correlation between loading indices

3.2.3 Component Loading Chart

Based on the previous findings, a graphical method is proposed to help engineers quickly diagnose if there is risk of component overload in the wind park due to harmonic resonance by simply monitoring the state of the capacitor bank.

For a wind park with the generic layout shown in Figure 3.1, the idea is to derive a curve in the space relating information from the capacitor bank of the wind park (Q_C/S_{WP} ratio on the x-axis) with its operating characteristics ($V_{PCC}(h)$ maximum individual harmonic voltage distortion at PCC on the y-axis), so that this curve divides the Q_C/S_{WP} vs. $V_{PCC}(h)$ plane in two regions as illustrated in Figure 3.13. The region below the boundary is the safe region. If the wind park is operating in this region, no component of the park is overloaded, and no further analysis is needed. On the other hand, if the wind park is operating above the boundary, in the problematic region, one should conduct detailed investigations on the loading level of wind park components as one or more components (especially the shunt capacitor) are potentially overloaded.

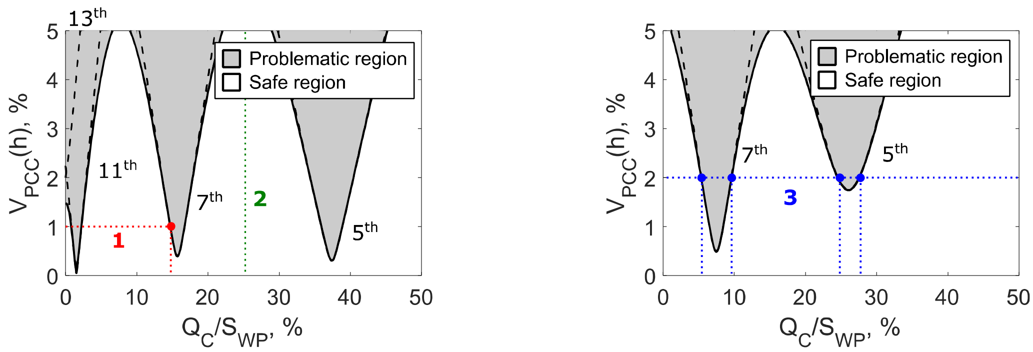

a) Type-III wind park **b) Type-IV wind park**

Figure 3.13: Component Loading Chart

Each lump (dashed line) in the chart is dominated by one particular harmonic order. The junction of the regions corresponds to the problematic region boundary (solid line). Only the 5th, 7th, 11th and 13th harmonics were considered, but it can be extended to other frequencies.

The chart is useful to determine the maximum voltage distortion value, measured at PCC, that the wind park components are able to tolerate before incurring in overload of wind park components. Three cases are presented to demonstrate its use: case 1 (red) shows that if the capacitor bank operates at a stage of 15% of reactive power compensation, it can result in overloads for harmonic distortions of 1% or higher at the 7th harmonic; case 2 (green) shows that operating the capacitor bank at a stage of 25% of reactive power compensation will not overload wind park components for distortion values up to 5% of the fundamental at any harmonic; and finally, case 3 (blue) shows that if there is a 2% harmonic voltage distortion at PCC of the studied wind park with Type-IV generators in the 5th or 7th harmonic, there are forbidden bands of operation of the capacitor bank, from 5.4% to 9.5% for the 7th harmonic, and from 24.6% to 27.5% for the 5th harmonic.

3.2.4 Analytic procedure to build the chart

Consider the schematic in Figure 3.14, representing the wind park in Figure 3.1, where Z_{Tx} is the main transformer impedance, Z_{gf} is the equivalent impedance of the generators, feeders and step-up transformers, and Z_C is the impedance of the capacitor bank.

The voltage at the PCC is represented by V_{PCC}, and at the bus of the capacitor by V_C. According to the results in Figure 3.11, the overload due to harmonic resonances in wind park components can be first screened by calculating the apparent power at the capacitor as it is the most restrictive index. To this end, consider the rms voltage at the capacitor bus:

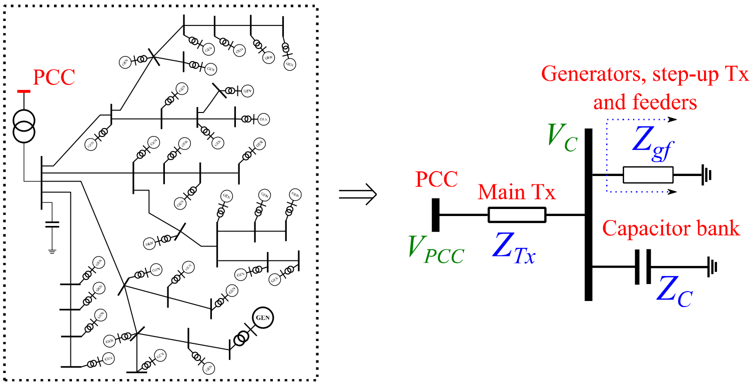

Figure 3.14: Equivalent wind park circuit for component loading analysis

$$V_{C,rms} = \sqrt{V_C^2(1) + \sum_{h=5,7,11,13} \left(V_C(h)\right)^2} = \sqrt{V_C^2(1) + \sum_{h=5,7,11,13} \left(A_C(h) \cdot V_{PCC}(h)\right)^2} \qquad \textbf{(3.15)}$$

It is reasonable to assume that $V_C(1)$ is known as the generators control the voltage at their terminals. $A_C(h)$ is the amplification of PCC voltages at capacitor terminals and it is also known as it can be represented in terms of the wind park impedance equivalents.

$$A_C(h) = \left| \frac{Z_{gf}(h) || Z_C(h)}{Z_{Tx}(h) + Z_{gf}(h) || Z_C(h)} \right| \qquad \textbf{(3.16)} \qquad |Z_C(h)| = \frac{1}{h \cdot (Q_C / S_{WP})} \qquad \textbf{(3.17)}$$

Now, the rms current through the capacitor (in pu basis of its rated capacity Q_C) is given by:

$$I_{C,rms} = \frac{1}{(Q_C/S_{WP})}\sqrt{I_C^2(1) + \sum_{h=5,7,11,13}\left(I_C(h)\right)^2} = \frac{1}{(Q_C/S_{WP})}\sqrt{\frac{V_C^2(1)}{|Z_C(1)|^2} + \sum_{h=5,7,11,13}\left(\frac{A_C(h)\cdot V_{PCC}(h)}{|Z_C(h)|}\right)^2} \quad \textbf{(3.18)}$$

By combining (3.15) to (3.18) and (3.10), it is possible to obtain the apparent power of the capacitor in terms of the voltage distortion at PCC, the fundamental frequency voltage at capacitor terminals, and the circuit impedances. The boundary between the problematic region and safe region of the chart corresponds to the point where $S=S_{lim}$, so that:

$$S_{lim} = \sqrt{V_C^2(1) + \sum_{h=5,7,11,13}\left(A_C^2(h)\cdot V_{PCC}^2(h)\right)}\sqrt{V_C^2(1) + \sum_{h=5,7,11,13}\left(h^2\cdot A_C^2(h)\cdot V_{PCC}^2(h)\right)} \quad \textbf{(3.19)}$$

Finally, by rearranging expression (3.19) and considering all harmonics at PCC have equal magnitude V_{PCC}, the polynomial expression (3.20) is reached, with the coefficients in expression (3.21). However, expression (3.20) can be seen as a quadratic equation by making the change of variables $x = V_{PCC}^2$, so the resulting quadratic has only one real root, described by expression (3.22) that defines the boundary of the problematic region in the Component Loading Chart.

$$0 = aV_{PCC}^4 + bV_{PCC}^2 + c \quad \textbf{(3.20)}$$

$$a = \sum_{h=5,7,11,13}\left(A_C^2(h)\right)\cdot\sum_{h=5,7,11,13}\left(h^2\cdot A_C^2(h)\right)$$
$$b = V_{PCC}^2(1)\cdot\left(\sum_{h=5,7,11,13}\left(A_C^2(h)\right) + \sum_{h=5,7,11,13}\left(h^2\cdot A_C^2(h)\right)\right) \quad \textbf{(3.21)}$$
$$c = V_{PCC}^4(1) - S_{lim}^2$$

$$V_{PCC} = \sqrt{\frac{\left(-b+\sqrt{b^2-4ac}\right)}{2a}} \quad \textbf{(3.22)}$$

Summarizing, the steps to obtain the boundary of the problematic region in the Component Loading Chart are:

1) Calculate the $Z_{gf}(h)$ for every harmonic. This calculation is only done once, at the beginning of the analysis.
2) For all Q_C/S_{WP} ratios to be considered, calculate the harmonic amplification at capacitor terminal $A_C(h)$ with expression (3.16).
3) Calculate the a, b and c coefficients in expression (3.21).
4) Calculate the distortion value at the boundary of the problematic region with expression (3.22) after fixing the fundamental frequency voltage to, for example, $V_{PCC}(1) = 1$ pu, and the apparent power limit to S_{lim}=1.35 pu.

3.2.5 Validation

The method for obtaining the Component Loading Chart is verified through detailed electromagnetic transient (EMT) simulations. In this study, the wind park shown in Figure 3.1 with all its 32 wind generators, line segments and other components were modeled in detail in MATLAB Simscape Power Systems software. The reactive power compensation ratio Q_C/S_{WP} was varied from zero to 50% (in steps of 1%), and V_{PCC} was varied from zero to 5% (in steps of 0.2%). Simulation scenarios that resulted in violations of the capacitor loading limit are marked with an "x" in Figure 3.15. As these points are indeed above the boundary obtained analytically, the results confirm the accuracy of proposed analytical curve derived in Section 3.2.4.

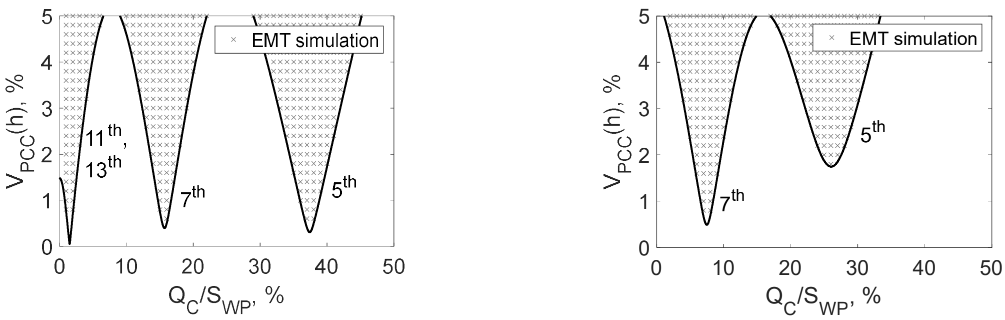

a) Type-III wind park **b) Type-IV wind park**

Figure 3.15: Validation of the Component Loading Chart with EMT simulation

In Figure 3.15, the chart boundary is traced with $V_{PCC}(1) = 1.00$ pu. Although this proved to be in good agreement with the detailed EMT simulation, one may draw a more conservative risk region by considering $V_{PCC}(1) = 1.05$ pu , the maximum allowable voltage level at the PCC.

For further validation, Table 3.2 outlines the values of the four capacitor loading indices for two operating conditions, $Q_C/S_{WP} = 15\%$ and $Q_C/S_{WP} = 10\%$. In both cases, the maximum harmonic voltage distortion at the PCC is $V_{PCC}(h) = 1\%$. According to the proposed chart in Figure 3.15 a), the first case is in the problematic region, while the second case is in the safe region. This is confirmed in Table 3.2, where the rms current and apparent power limits are violated when $Q_C/S_{WP} = 15\%$, whereas no index is violated when $Q_C/S_{WP} = 10\%$.

Table 3.2: Capacitor loading indices for two operating conditions, Type-III wind park

Indices at $V_{PCC}(h)$ =1% distortion	Q_C/S_{WP}	
	15%	10%
V_{rms}	1.03	1.03
V_{peak}	1.11	1.05
I_{rms}	**1.40**	1.04
S	**1.43**	1.07

3.2.6 Sensitivity studies of the Component Loading Chart

This section discusses how different parameters affect the problematic regions in the proposed chart.

3.2.6.1 Background harmonic spectrum

This study shows how the boundary of the problematic region in the Component Loading Chart (CLC) can be approximated by superposition of the regions corresponding to individual harmonics. To this end, recall the a, b and c coefficients in expression (3.21). If only one harmonic is evaluated, these coefficients can be simplified to those in expression (3.23).

$$a = h^2 \cdot A_C^4(h) \qquad b = V_{PCC}^2(1) \cdot (1 + h^2) \cdot A_C^2(h) \qquad c = V_{PCC}^4(1) - S_{lim}^2 \tag{3.23}$$

Now, it is possible to draw the "individual" risk regions using expression (3.22) with the coefficients in expression (3.23). This was compared to the "collective" boundary of the region calculated with the original methodology that considers all harmonics present in the circuit simultaneously. The results are shown in Figure 3.16.

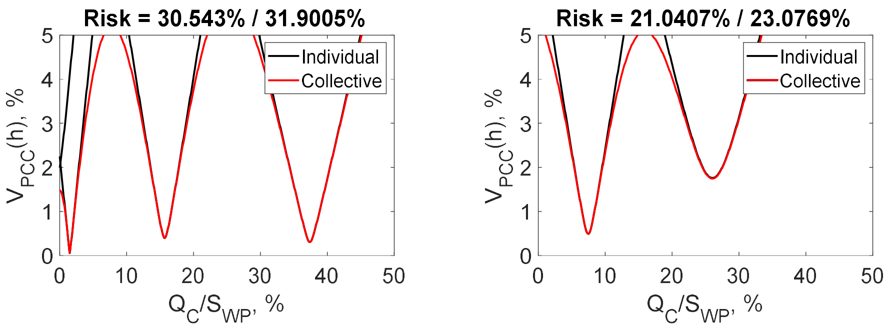

a) Type-III wind park **b) Type-IV wind park**

Figure 3.16: Sensitivity of CLC to number of simultaneous harmonics

Notice the shape of the boundary calculated with individual harmonics (black line), and consequently its risk, are very similar to those of the boundary calculated with all harmonics (red line). In the collective approach, each lump is also associated with one particular harmonic order which is dominant at resonance, which explains the similarity between both curves.

The differences between the boundaries appear near the points where the boundaries of the individual regions cross, as neither one is clearly dominant. However, this difference is only relevant at very high distortion levels ($V_{PCC}(h) \geq 4\%$). This result indicates it is possible to simplify the calculation of the boundary to the superposition of boundaries calculated with individual harmonics without significant loss of accuracy.

3.2.6.2 Fundamental frequency voltage

It is also important to evaluate the effect of the fundamental frequency voltage at the capacitor terminals $V_C(1)$ as it defines the fundamental frequency loading, which is the largest portion of the total loading. This parameter is typically affected by the active power injection from the park (P_{sp}) and by the amount of reactive power compensation connected to the circuit (*i.e.*, the Q_C/S_{WP} ratio). Their effect on $V_C(1)$ can be seen in Figure 3.17. Both, higher active power injection and higher Q_C/S_{WP} ratio lead to higher $V_C(1)$ values and, consequently, higher loading level of the capacitor bank. This reduces the headroom for harmonic distortions in the system without causing component overload. Therefore, in theory, higher P_{sp} or Q_C/S_{WP} values may increase the problematic region of the component loading chart.

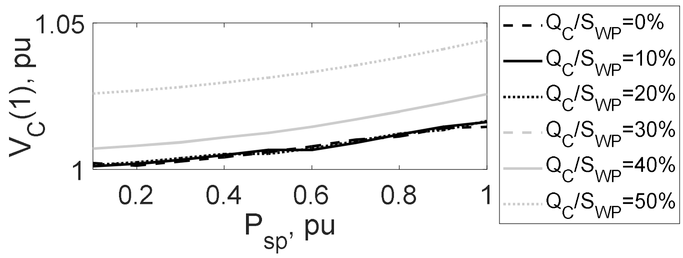

Figure 3.17: Operational point vs. fundamental frequency voltage at capacitor terminals

However, the fundamental frequency voltage varies within a narrow margin regardless of the P_{sp} and Q_C/S_{WP} values due to the generator terminal voltage control, which tracks a given setpoint. The Component Loading Charts in Figure 3.18 where calculated after changing the setpoint of the generators, in order to change $V_C(1)$.

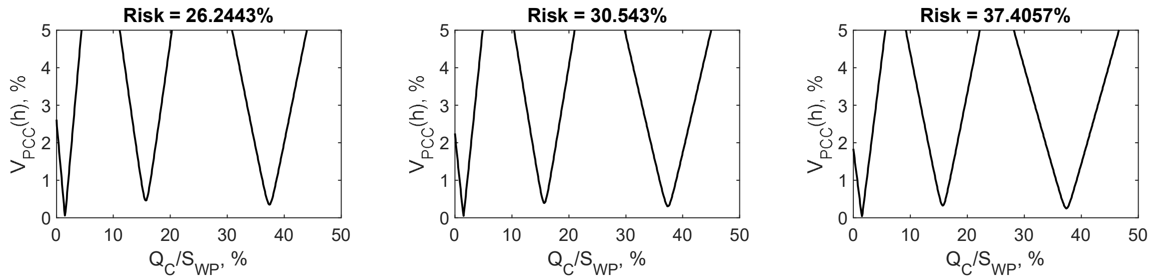

a) Type-III, $V_C(1)$=0.95pu **b) Type-III, $V_C(1)$=1.0pu** **c) Type-III, $V_C(1)$=1.05pu**

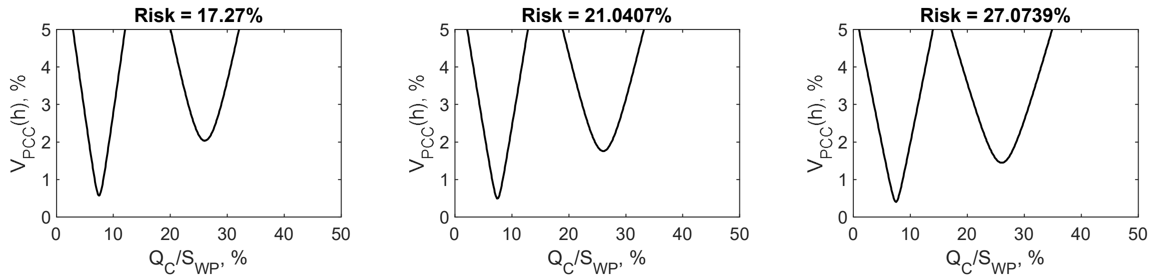

d) Type-IV, $V_C(1)$=0.95pu **e) Type-IV, $V_C(1)$=1.0pu** **f) Type-IV, $V_C(1)$=1.05pu**

Figure 3.18: Sensitivity of CLC to fundamental frequency voltage

The effect of the fundamental frequency voltage is more visible for the lower order harmonics, especially the 5th harmonic (rightmost lump), as this harmonic has the largest amplification values due to lower damping. Overall, it can be seen that the regions grow larger with larger voltages (risk increases) as there is less spare capacity left by the fundamental loading for the harmonic loading. At the same time, lower voltages lead to less risk due to the increase in spare capacity.

The shape of the boundary does not change significantly with variations of ±5% of the fundamental frequency voltage for the Type-III wind park, but its effect is more visible on a Type-IV wind park. This can be explained by the Type-IV generator impedance profile as it is dominated by the equivalent impedance of the GSC, which depends on the operational setpoint.

3.2.6.3 Capacitive elements

The results in Figure 3.19 demonstrate the importance of modeling the capacitive elements of the circuit to obtain an accurate shape of the boundary. As overhead feeders have lower capacitance, the circuit requires a larger capacitor bank for the same values of harmonic resonance, thus, the lumps for each harmonic are shifted to higher Q_C/S_{WP} ratios.

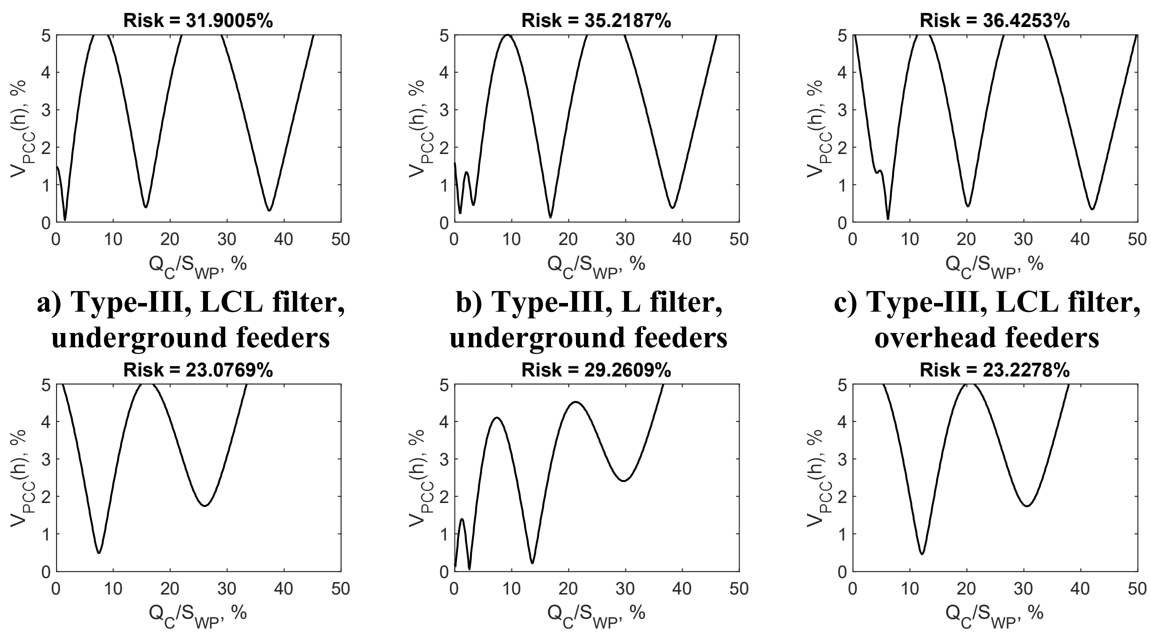

a) Type-III, LCL filter, underground feeders

b) Type-III, L filter, underground feeders

c) Type-III, LCL filter, overhead feeders

d) Type-IV, LCL filter, underground feeders

e) Type-IV, L filter, underground feeders

f) Type-IV, LCL filter, overhead feeders

Figure 3.19: Sensitivity of CLC to removing capacitive elements from the wind park

As for the capacitor in the front-end filter, its effect is greater for the Type-IV wind park than for the Type-III, given that the capacitance of the Type-IV generator filter is larger. Moreover, the effect is more pronounced for the 11th and 13th harmonics, which is expected as the filter is designed to damp the noise produced by the converter switching at higher frequencies.

3.2.6.4 Number of generator units in operation

During wind park operation, it is possible that one or more generator units are temporarily disconnected from the circuit, for instance, for planned maintenance. This study investigates the effect of these disconnections on the chart boundaries.

Recall the wind park has 32 generators. Figure 3.20 outlines the boundary of the Component Loading Chart for 0 generator outages (100% in operation), 6 generator outages (19% disconnected and 81% in operation) and 10 generator outages (37% disconnected and 63% in operation). Notice the chart boundaries are not affected significantly up to 20% of outages. This occurs because the per unit equivalent impedance of the generators and the feeders $Z_{gen+feeder}$ remains relatively constant (as the S_{WP} of the wind park is updated accordingly) and, as such, the harmonic voltage amplification profile A_C also remains relatively constant.

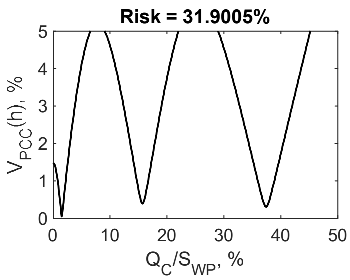

a) Type-III, 0 outages

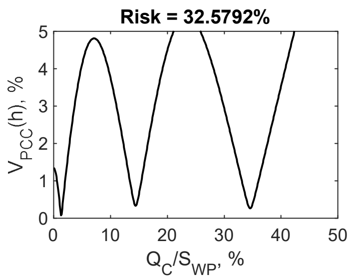

b) Type-III, 6 outages

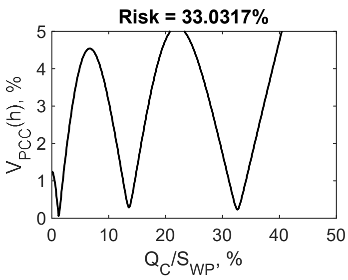

c) Type-III, 10 outages

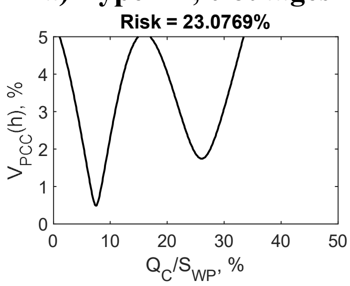

d) Type-IV, 0 outages

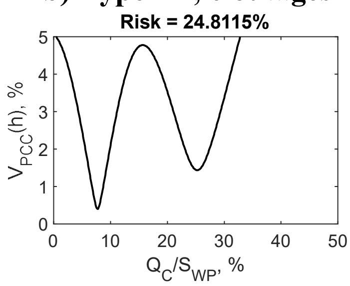

e) Type-IV, 6 outages

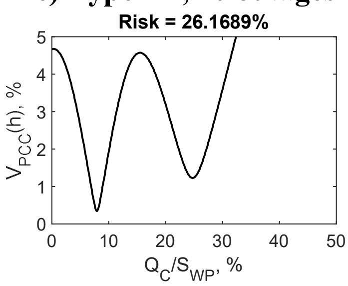

f) Type-IV, 10 outages

Figure 3.20: Sensitivity of CLC to generator outages

If several units are disconnected (such as in a major event in the park like a feeder branch outage), it is advised to update the chart boundaries with the new wind park topology. Based on the results of this study, the problematic regions of the chart can remain unchanged if up to 20% of generators are disconnected. This indicates the chart rarely needs to be updated as disconnection of multiple units is not frequent in practice.

3.2.6.5 Summary of the sensitivity studies

The following remarks are the most relevant results from the studies:

- Overall, the risk of component overload due to harmonic resonance is higher for Type-III wind parks than for Type-IV wind parks. This behavior is compatible with the results from Section 3.1 for the harmonic resonance analysis at the PCC.
- Higher voltages at fundamental frequency reduce the spare capacity margin of harmonic loading, which increases the risk of component overloads.
- Considering all harmonics simultaneously with the same magnitude to draw the problematic region boundary outputs similar results to using one harmonic at the time and then using superposition of the boundaries. This can be used as a simplification for distortion levels below 4% of the fundamental frequency.
- It is relevant to model the capacitance of the feeders as they shift the resonance frequencies to different values of reactive power compensation ratio. The capacitor of the LCL front-end filter for the GSC mitigates the problematic circuit configurations at 11^{th} and 13^{th} harmonics.
- The boundary of the problematic region does not change significantly for scenarios that consider the disconnection of 20% or less of the generators. This means, updating the equivalent wind park impedance, and consequently the chart, is not necessary unless more than 20% of the generators are disconnected.

3.3 Harmonic resonance mitigation with passive filters

As shown in Sections 3.1 and 3.2, the connection of wind parks to transmission grids can result in problematic harmonic resonances that amplify pre-existing background distortions both at the PCC, and inside the wind park, leading to fines and component damages. One simple solution is to remove the capacitor bank and implement a static compensator, or use the generators spare capacity for reactive power compensation. However, if this is not possible, harmonic resonances can be mitigated by passive filters, active filters, or incorporating damping functions in the generators [72], [73], [74]. The most common and cheapest approach for harmonic mitigation is the use of passive filters. The authors in [75] determined passive filters are effective and cost-effective for applications over 1 MVA, which is the case of wind parks. And the same type of filters used in industrial facilities [76], [77], [78] and distribution systems [75], [79], [80] can be used for harmonic distortion mitigation in wind parks [73], [81], [82].

The literature shows passive filters come in a wide variety of topologies and methodologies to tune their parameters. The authors in [79] and [83] conducted a thorough comparison of the characteristics of several passive filter topologies in terms of both performance and cost. A comprehensive characterization on the selection of high-pass harmonic filter topologies is presented in [84]. The authors in [75] evaluated the advantages and disadvantages of several passive filter topologies and presented an iterative tuning methodology. More complex approaches to tune passive filters use meta-heuristics [85] and optimization [86]. Other methodologies propose tunings through simplified analytic expressions [58].

A common characteristic shared by most methodologies in the literature is that the filters are tuned according to the harmonic characteristics at their terminals. However, for the case of the wind park, the problematic element is the shunt capacitor bank, which is located at the medium voltage (MV) bus, *i.e.*, at the secondary side of the main park transformer, while the mitigation is desired at point of common connection (PCC) of the wind park, *i.e.*, the primary side of the main transformer. The presence of the main transformer impedance, as well as the equivalent impedance of the rest of the wind park, need to be considered when calculating the filter parameters for the solution to be effective while still preserving a low cost.

This section proposes an impedance-based, iterative methodology to tune passive filters at the secondary of the main transformer, with the goal of minimizing the total harmonic voltage distortion (THD_V) at the PCC of the wind park. The methodology is illustrated using a C-type filter topology but can be applied to others. The cost, robustness and performance of the tuning are evaluated and compared to existing methods. The resulting filters minimize the THD_V at PCC as designed, have low losses at fundamental frequency, provide the desired reactive power compensation of the original capacitor bank, are robust to detuning, and have a reasonable cost.

3.3.1 Strategy to mitigate harmonic resonances at the PCC

The harmonic resonance problem at the PCC of a wind park can be quantified through the total harmonic voltage distortion $\mathrm{THD_V}$. The $\mathrm{THD_V}$ considering the 5th, 7th, 11th and 13th harmonics is calculated with (3.24), but other harmonics can be included if needed. Expression (3.2) is used to calculate the amplification of grid harmonic distortions at PCC $A_{PCC}(h)$ in terms of the grid and wind park impedances from Figure 3.21.

$$\mathrm{THD_V} = \sqrt{\sum_{h=5,7,11,13} V_{PCC}^2(h)} = \sqrt{\sum_{h=5,7,11,13} [V_{SC}(h) \cdot A_{PCC}(h)]^2} \quad \mathbf{(3.24)}$$

Now consider that the capacitor bank for power factor correction of the wind park in Figure 3.21 is replaced by a passive filter with impedance $Z_F(h) = R_F(h) + jX_F(h)$. The filter is designed to emulate the original capacitor bank at fundamental frequency and to minimize the $\mathrm{THD_V}$ by avoiding the resonance in the circuit. But first, a filter topology has to be selected, such as the C-type filter topology in Figure 3.22.

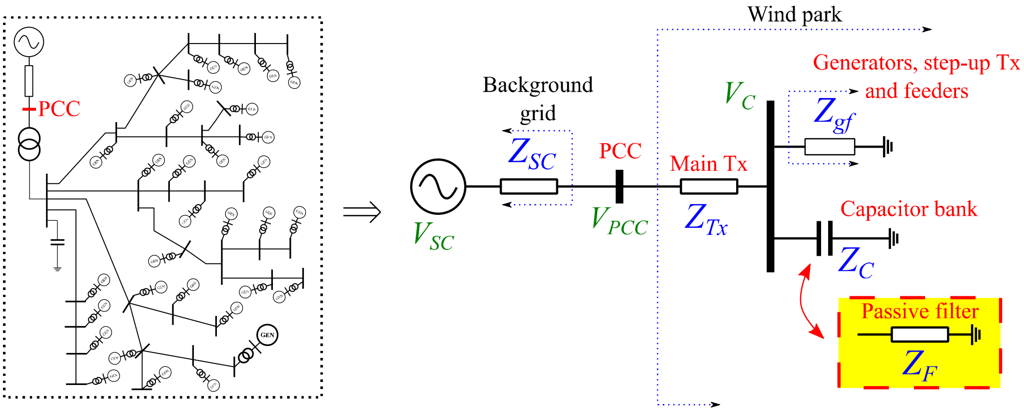

Figure 3.21: Equivalent wind park circuit for passive filter design

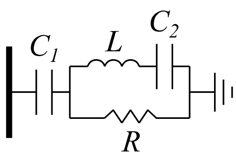

Figure 3.22: C-type filter topology

The C-type filter impedance in pu is calculated with expression (3.25).

$$Z_F(h) = R_F(h) + jX_F(h) = \frac{1}{jhC_1} + \left(R^{-1} + \left(jhL + \frac{1}{jhC_2}\right)^{-1}\right)^{-1} \quad \mathbf{(3.25)}$$

This topology offers four degrees of freedom for tuning, where two degrees are used to ensure proper performance at fundamental frequency with the following constraints:

- C_1 provides the reactive power compensation at fundamental frequency of the smallest stage of the original capacitor bank, *e.g.*, if the bank operates in stages of Q_C/S_{WP} = [0 %, 15 %, 30%], C_1 is designed for the Q_C/S_{WP} =15% stage;
- C_2 minimizes the active power losses of the filter at fundamental frequency, and the interference of the additional elements with the reactive power compensation provided by C_1 at fundamental frequency.

The calculation of C_1 (in pu of wind park rated capacity S_{WP}) is rather straightforward using expression (3.26). And for the calculation of C_2, L and C_2 must resonate at the fundamental frequency h_{res} = 1 so that their reactive contribution cancels out, while simultaneously bypassing R to avoid losses at fundamental frequency. This is achieved with expression (3.27).

$$C_1 = Q_C/S_{WP} \qquad \textbf{(3.26)}$$

$$h_{res} = \frac{1}{\sqrt{LC_2}} \Rightarrow C_2 = L^{-1} \qquad \textbf{(3.27)}$$

Now, the problem of tuning the filters is reduced to choosing a value for R and L. Consider a 64 MVA Type-III wind park with a 34.5 kV capacitor bank with two discrete stages, each of Q_C/S_{WP}=15%. The wind park is connected to a 230 kV grid with short-circuit ratio S_{SC}/S_{WP}=5, reactance to resistance ratio of X/R=10, and a voltage distortion at the 5th, 7th, 11th and 13th harmonics of $V_{SC}(5) = \cdots = V_{SC}(13) = 1\%$. A sweep of R and L values is presented in Figure 3.23 to map the response of the circuit to the filter, where four characteristics are shown: THD_V at PCC; the cost of the filter (see section 3.3.7); the active power losses at fundamental frequency; and the effective reactive power compensation ration Q_C/S_{WP} after filter implementation. For reference purposes, the cost of the original capacitor bank is 0.88 M$.

The red marker denotes the tuning for R and L with the lowest THD_V at PCC. Notice how this tuning matches the lowest filter cost of 0.9 M$. This is not surprising because the resulting harmonic voltages at PCC are greatly damped (minimum THDV level), and consequently, the harmonic voltages at filter terminals are also damped, which reduces the harmonic loading of the components (dissipated power and RMS voltage) and lowers their cost. The filter has no losses at fundamental frequency and it provides the original reactive power compensation. Similarly, poor tuning choices can lead to high THD_V values and high cost.

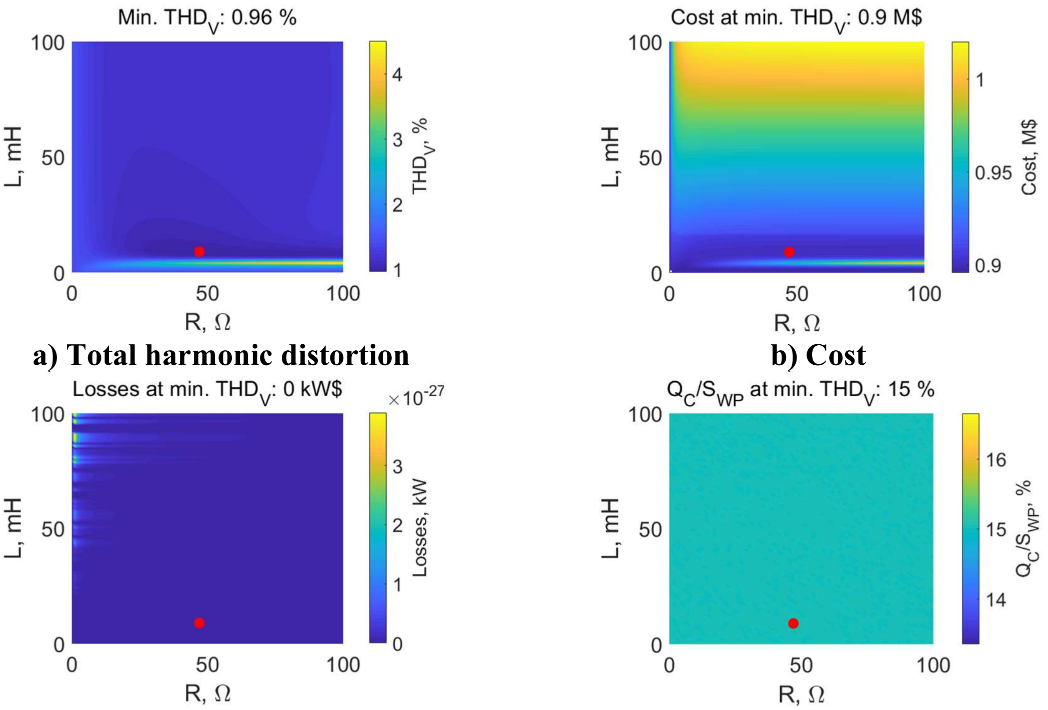

a) Total harmonic distortion **b) Cost**

c) Losses **d) Compensation ratio**

Figure 3.23: Sweep of *R* and *L* parameters for C-type filter

3.3.2 Filter tuning

The red marker in Figure 3.23 denoting the filter tuning which minimizes the THD_V at PCC can be described analytically with the impedance equivalents in Figure 3.21, and then, an iterative algorithm can be used to solve them instead of using complex optimization software and formulations. First, expression (3.24) is rewritten as (3.28) as it facilitates the calculations. The squared value of the amplifications at PCC can be developed with the real and imaginary parts of the impedances in Figure 3.21 as (3.29) and the a_1, …, a_{12} coefficients of Table 3.3.

$$\text{THD}_\text{V}^2 = \sum_{h=5,7,11,13} \left[V_{SC}^2(h) \cdot A_{PCC}^2(h) \right] \tag{3.28}$$

$$A_{PCC}^2(h) = \frac{A_{2n}(h)}{A_{2d}(h)} = \frac{\begin{pmatrix} (a_1^2 + a_2^2)R_F^2 + 2(a_1 a_5 + a_2 a_6)R_F \\ +(a_3^2 + a_4^2)X_F^2 + 2(a_3 a_5 + a_4 a_6)X_F \\ +2(a_1 a_5 + a_2 a_6)R_F X_F + (a_5^2 + a_6^2) \end{pmatrix}}{\begin{pmatrix} (a_7^2 + a_8^2)R_F^2 + 2(a_7 a_{11} + a_8 a_{12})R_F \\ +(a_9^2 + a_{10}^2)X_F^2 + 2(a_9 a_{11} + a_{10} a_{12})X_F \\ +2(a_7 a_9 + a_8 a_{10})R_F X_F + (a_{11}^2 + a_{12}^2) \end{pmatrix}} \tag{3.29}$$

Table 3.3: Coefficients of expression (3.29)

$a_1 = R_{Tx} + R_{gf}$	$a_2 = X_{Tx} + X_{gf}$	$a_3 = -a_2$
$a_4 = a_1$	$a_5 = R_{Tx}R_{gf} - X_{gf}X_{Tx}$	$a_6 = R_{gf}X_{Tx} - R_{Tx}X_{gf}$
$a_7 = a_1 + R_{SC}$	$a_8 = a_2 + X_{SC}$	$a_9 = a_3 - X_{SC}$
$a_{10} = a_7$	$a_{11} = a_1R_{gf} - a_2X_{gf}$	$a_{12} = a_1X_{gf} + a_2R_{gf}$

If the grid distortion profile $V_{SC}(h)$ is known, the optimal tuning of the filter can be defined by the null derivatives of (3.28) with respect to R and L, as follows:

$$\frac{d\mathrm{THD}_{\mathrm{V}}^2}{dR} = 0 = \sum_{h=5,7,11,13}\left[V_{SC}^2(h)2\frac{A_{2d}\left(c_1\frac{dR_F}{dR} + c_2\frac{dX_F}{dR}\right) - A_{2n}\left(c_3\frac{dR_F}{dR} + c_4\frac{dX_F}{dR}\right)}{A_{2d}^2}\right] = f_R \qquad \textbf{(3.30)}$$

$$\frac{d\mathrm{THD}_{\mathrm{V}}^2}{dL} = 0 = \sum_{h=5,7,11,13}\left[V_{SC}^2(h)2\frac{A_{2d}\left(c_1\frac{dR_F}{dL} + c_2\frac{dX_F}{dL}\right) - A_{2n}\left(c_3\frac{dR_F}{dL} + c_4\frac{dX_F}{dL}\right)}{A_{2d}^2}\right] = f_L \qquad \textbf{(3.31)}$$

where A_{2n} and A_{2d} are the numerator and the denominator of expression (3.29), c_1 to c_4 are given by expressions (3.32) to (3.35), with the b_1, …, b_{10} coefficients in Table 3.4 (calculated from the a_i coefficients of Table 3.3).

$$c_1 = b_1R_F + b_2 + b_3X_F \qquad \textbf{(3.32)} \qquad c_2 = b_4X_F + b_5 + b_3R_F \qquad \textbf{(3.33)}$$

$$c_3 = b_6R_F + b_7 + b_8X_F \qquad \textbf{(3.34)} \qquad c_4 = b_9X_F + b_{10} + b_8R_F \qquad \textbf{(3.35)}$$

Table 3.4: Coefficients of expressions (3.32) to (3.35)

$b_1 = a_1^2 + a_2^2$	$b_2 = a_1a_5 + a_2a_6$	$b_3 = a_1a_3 + a_2a_4$
$b_4 = a_3^2 + a_4^2$	$b_5 = a_3a_5 + a_4a_6$	$b_6 = a_7^2 + a_8^2$
$b_7 = a_7a_{11} + a_8a_{12}$	$b_8 = a_7a_9 + a_8a_{10}$	$b_9 = a_9^2 + a_{10}^2$
$b_{10} = a_9a_{11} + a_{10}a_{12}$		

3.3.3 Solving the equations for the optimal tuning

R and L to solve (3.30) and (3.31) are calculated with a Newton-Raphson iterative algorithm defined in (3.36), where the i sub-index denotes the current iteration, and the algorithm is initialized for a random R and L in a search space defined by the user.

$$\binom{R}{L}_{i+1} = \binom{R}{L}_i - \begin{pmatrix} \frac{df_R}{dR} & \frac{df_R}{dL} \\ \frac{df_L}{dR} & \frac{df_L}{dL} \end{pmatrix}_i^{-1} \binom{f_R}{f_L}_i \qquad \textbf{(3.36)}$$

The Jacobian is built with expressions (3.37) to (3.40).

$$\frac{df_R}{dR}=\sum_{h=5,7,11,13}\left[V_{SC}^2(h)\begin{pmatrix}A_{2d}^2\left(A_{2d}\dfrac{d^2A_{2n}}{dR^2}-A_{2n}\dfrac{d^2A_{2d}}{dR^2}\right)\\-2A_{2d}(A_{2d}D_{nR}-A_{2n}D_{dR})D_{dR}\end{pmatrix}A_{2d}^{-4}\right] \tag{3.37}$$

$$\frac{df_R}{dL}=\sum_{h=5,7,11,13}\left[V_{SC}^2(h)\begin{pmatrix}A_{2d}^2\begin{pmatrix}D_{nR}D_{dL}-D_{dR}D_{nL}\\+A_{2d}\dfrac{d^2A_{2n}}{dLdR}-A_{2n}\dfrac{d^2A_{2d}}{dLdR}\end{pmatrix}\\-2A_{2d}(A_{2d}D_{nR}-A_{2n}D_{dR})D_{dL}\end{pmatrix}A_{2d}^{-4}\right] \tag{3.38}$$

$$\frac{df_L}{dR}=\sum_{h=5,7,11,13}\left[V_{SC}^2(h)\begin{pmatrix}A_{2d}^2\begin{pmatrix}\dfrac{dA_{2n}}{dL}\dfrac{dA_{2d}}{dR}-\dfrac{dA_{2d}}{dL}\dfrac{dA_{2n}}{dR}\\+A_{2d}\dfrac{d^2A_{2n}}{dRdL}-A_{2n}\dfrac{d^2A_{2d}}{dRdL}\end{pmatrix}\\-2A_{2d}\left(A_{2d}\dfrac{dA_{2n}}{dL}-A_{2n}\dfrac{dA_{2d}}{dL}\right)\dfrac{dA_{2d}}{dR}\end{pmatrix}A_{2d}^{-4}\right] \tag{3.39}$$

$$\frac{df_L}{dL}=\sum_{h=5,7,11,13}\left[V_{SC}^2(h)\begin{pmatrix}A_{2d}^2\left(A_{2d}\dfrac{d^2A_{2n}}{dL^2}-A_{2n}\dfrac{d^2A_{2d}}{dL^2}\right)\\-2A_{2d}(A_{2d}D_{nL}-A_{2n}D_{dL})D_{dL}\end{pmatrix}A_{2d}^{-4}\right] \tag{3.40}$$

And the second derivates are given by expressions (3.41) to (3.48).

$$\frac{d^2A_{2n}(h)}{dR^2}=2\left(c_1\frac{d^2R_F}{dR^2}+c_2\frac{d^2X_F}{dR^2}+b_1\left(\frac{dR_F}{dR}\right)^2+b_4\left(\frac{dX_F}{dR}\right)^2+2b_3\frac{dR_F}{dR}\frac{dX_F}{dR}\right) \tag{3.41}$$

$$\frac{d^2A_{2d}(h)}{dR^2}=2\left(c_3\frac{d^2R_F}{dR^2}+c_4\frac{d^2X_F}{dR^2}+b_6\left(\frac{dR_F}{dR}\right)^2+b_9\left(\frac{dX_F}{dR}\right)^2+2b_8\frac{dR_F}{dR}\frac{dX_F}{dR}\right) \tag{3.42}$$

$$\frac{d^2A_{2n}(h)}{dLdR}=2\left(c_1\frac{d^2R_F}{dLdR}+c_2\frac{d^2X_F}{dLdR}+b_1\frac{dR_F}{dR}\frac{dR_F}{dL}+b_4\frac{dX_F}{dR}\frac{dX_F}{dL}+b_3\left(\frac{dR_F}{dR}\frac{dX_F}{dL}+\frac{dR_F}{dL}\frac{dX_F}{dR}\right)\right) \tag{3.43}$$

$$\frac{d^2A_{2d}(h)}{dLdR}=2\left(c_3\frac{d^2R_F}{dLdR}+c_4\frac{d^2X_F}{dLdR}+b_6\frac{dR_F}{dR}\frac{dR_F}{dL}+b_9\frac{dX_F}{dR}\frac{dX_F}{dL}+b_8\left(\frac{dR_F}{dR}\frac{dX_F}{dL}+\frac{dR_F}{dL}\frac{dX_F}{dR}\right)\right) \tag{3.44}$$

$$\frac{d^2A_{2n}(h)}{dRdL}=2\left(c_1\frac{d^2R_F}{dRdL}+c_2\frac{d^2X_F}{dRdL}+b_1\frac{dR_F}{dR}\frac{dR_F}{dL}+b_4\frac{dX_F}{dR}\frac{dX_F}{dL}+b_3\left(\frac{dR_F}{dL}\frac{dX_F}{dR}+\frac{dR_F}{dR}\frac{dX_F}{dL}\right)\right) \tag{3.45}$$

$$\frac{d^2A_{2d}(h)}{dRdL}=2\left(c_3\frac{d^2R_F}{dRdL}+c_4\frac{d^2X_F}{dRdL}+b_6\frac{dR_F}{dR}\frac{dR_F}{dL}+b_9\frac{dX_F}{dR}\frac{dX_F}{dL}+b_8\left(\frac{dR_F}{dL}\frac{dX_F}{dR}+\frac{dR_F}{dR}\frac{dX_F}{dL}\right)\right) \tag{3.46}$$

$$\frac{d^2A_{2n}(h)}{dL^2}=2\left(c_1\frac{d^2R_F}{dL^2}+c_2\frac{d^2X_F}{dL^2}+b_1\left(\frac{dR_F}{dL}\right)^2+b_4\left(\frac{dX_F}{dL}\right)^2+2b_3\frac{dR_F}{dL}\frac{dX_F}{dL}\right) \tag{3.47}$$

$$\frac{d^2A_{2d}(h)}{dL^2}=2\left(c_3\frac{d^2R_F}{dL^2}+c_4\frac{d^2X_F}{dL^2}+b_6\left(\frac{dR_F}{dL}\right)^2+b_9\left(\frac{dX_F}{dL}\right)^2+2b_8\frac{dR_F}{dL}\frac{dX_F}{dL}\right) \tag{3.48}$$

Finally, the filter components $R_F(h)$ and $X_F(h)$ are functions of R and L. For the C-type filter, expression (3.25) can be developed into expressions (3.49) to (3.52), and their corresponding derivatives of expressions (3.53) to (3.62) for the iterative tuning procedure. This set of expressions (3.49) to (3.62) is changed if another filter topology is used instead.

$$h_L = (h - h^{-1})^{-1}L^{-1} \quad \textbf{(3.49)} \qquad h_{RL} = R^{-2} + h_L^2 \quad \textbf{(3.50)}$$

$$R_F = \frac{1}{h_{RL}R} \quad \textbf{(3.51)} \qquad X_F = \frac{h_L^2 L}{h_{RL}} - \frac{1}{hC_1} \quad \textbf{(3.52)}$$

$$\frac{dR_F}{dR} = \frac{(R^{-2} - h_L^2)}{h_{RL}R^2} \quad \textbf{(3.53)} \qquad \frac{dR_F}{dL} = \frac{2h_L^2}{h_{RL}RL} \quad \textbf{(3.54)}$$

$$\frac{dX_F}{dR} = \frac{2h_L^2 L}{h_{RL}R^3} \quad \textbf{(3.55)} \qquad \frac{dX_F}{dL} = \frac{(h_L^2 - R^{-2})}{h_{RL}L^2} \quad \textbf{(3.56)}$$

$$\frac{d^2R_F}{dR^2} = 2\frac{(h_L^2 - 3R^{-2})}{h_L^{-2}h_{RL}^3R^3} \quad \textbf{(3.57)} \qquad \frac{d^2R_F}{dL^2} = 2\frac{(h_L^2 - 3R^{-2})}{h_L^{-2}h_{RL}^3RL^2} \quad \textbf{(3.58)}$$

$$\frac{d^2X_F}{dR^2} = 2\frac{(R^{-2} - 3h_L^2)}{h_L^{-1}h_{RL}^3R^4} \quad \textbf{(3.59)} \qquad \frac{d^2X_F}{dL^2} = 2\frac{(R^{-2} - 3h_L^2)}{h_L^{-1}h_{RL}^3R^2L^2} \quad \textbf{(3.60)}$$

$$\frac{d^2R_F}{dLdR} = \frac{d^2R_F}{dRdL} = 2\frac{(3R^{-2} - h_L^2)}{h_L^{-2}h_{RL}^3R^2L} \quad \textbf{(3.61)} \qquad \frac{d^2X_F}{dLdR} = \frac{d^2X_F}{dRdL} = 2\frac{(3h_L^2 - R^{-2})}{h_L^{-1}h_{RL}^3R^3L} \quad \textbf{(3.62)}$$

3.3.4 Summary of the filter tuning procedure

The previous filter tuning procedure can be implemented into a simple script as follows:

1) Calculate C_1 with (3.26).
2) Set an initial value for R and L using the approach described in the Appendix G.
3) Calculate C_2 with (3.27).
4) For every h, calculate R_F and X_F and the derivatives with (3.49) to (3.62). These expressions must be replaced if another filter topology is used instead.
5) For every h, calculate (3.29) and (3.32) to (3.35).
6) For every h, calculate (3.30) and (3.31) and check if the tolerance of error is met. If yes, end the algorithm, else, go to step 7).
7) Check if the maximum iteration was reached. If yes, set a new random guess for R and L and go to step 3), else, go to step 8).
8) For every h, calculate (3.41) to (3.48).

9) Calculate the Jacobian with (3.37) to (3.40).
10) Recalculate R and L with (3.36) and go to step 3).

3.3.5 Filter tuning results and validation

The tuning procedure to mitigate the total harmonic distortion of voltage was implemented for the 64 MVA wind park in Figure 3.21, which has a 34.5 kV capacitor bank with two discrete stages, each of Q_C/S_{WP}=15% for power factor correction, so the filter is tuned for Q_C/S_{WP}=15%. The wind park is connected to a 230 kV grid with short-circuit ratio S_{SC}/S_{WP}=5, reactance to resistance ratio of X/R=10, and a voltage distortion at the 5th, 7th, 11th and 13th harmonics of $V_{SC}(5) = \cdots = V_{SC}(13) = 1\%$ [8].

The proposed tuning "$\mathrm{THD}_\mathrm{V}^\mathrm{min}$" is compared to the resonance-free shunt capacitor tuning "RFSC" proposed in [58] (with a harmonic amplification at resonance HAR=1.2 and tuned to the 5th harmonic), and to the original capacitor bank "C. bank". The tunings and the performance for harmonic mitigation and fundamental frequency are shown in Table 3.5.

Table 3.5: Filter tuning results

	Type-III			Type-IV		
	$\mathrm{THD}_\mathrm{V}^\mathrm{min}$	RFSC	C. bank	$\mathrm{THD}_\mathrm{V}^\mathrm{min}$	RFSC	C. bank
C_1, μF	21.39	21.39	21.39	21.39	21.39	21.39
L, mH	8.57	345.93	-	5.07	345.93	-
C_2, μF	821.04	20.34	-	1386.77	20.34	-
R, Ω	50.20	127.13	-	27.19	127.13	-
$\mathrm{THD_V}$, %	0.96	1.19	1.43	0.74	1.68	1.24
Losses, kW	0	0	0	0	0	0
Q_C/S_{WP}, %	15	15	15	15	15	15

Notice the filters have no losses at fundamental frequency while they also provide the reactive power compensation of the original capacitor bank. The proposed $\mathrm{THD}_\mathrm{V}^\mathrm{min}$ tuning is more effective in reducing the $\mathrm{THD_V}$ at terminals as it considers the wind park and grid impedances, whereas filters tunned according to the characteristics at their connection point can worsen the $\mathrm{THD_V}$ at the PCC (see the RFSC for the Type-IV wind park).

Finally, the tunings were tested with EMT simulation of the wind park with detailed generator models by including a grid distortion profile of $V_{SC}(5) = V_{SC}(7) = V_{SC}(11) = V_{SC}(13) = 1\%$ of the fundamental frequency. The results of the $\mathrm{THD_V}$ calculation at PCC obtained in the EMT simulations are shown by the "x" markers in Figure 3.24, where a sequence of stages of Q_C/S_{WP}=5% were connected in parallel. The high accuracy of the results validates the use of impedance equivalent models to tune the harmonic filters for THD_V mitigation at PCC.

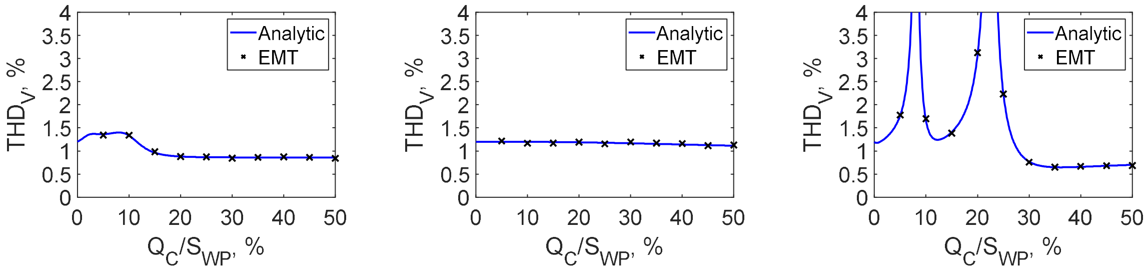

a) THD_V^{min}, Type-III b) RFSC, Type-III c) C. bank, Type-III

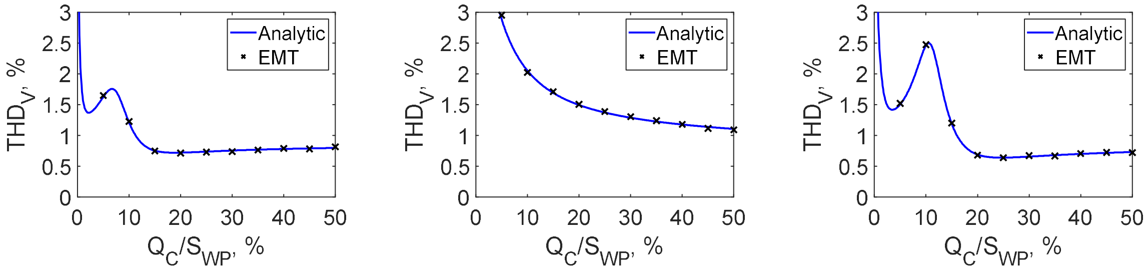

d) THD_V^{min}, Type-IV e) RFSC, Type-IV e) C. bank, Type-IV

Figure 3.24: THD_V profile validation with EMT simulation

3.3.6 Component loading

Another interesting result from the proposed tuning method is that it yields smaller R and L values than the RFSC alternative, while it requires larger C_2 values. The implications of these requirements can be evaluated with the loading of each component in Table 3.6 and Table 3.7.

The loading of the filter components is quantified with the indices recommended in [82], [87]: the rms voltage V_{rms}; the peak voltage across the component V_{peak}; the RMS current I_{rms}; and the apparent power S. Reference [87] recommends the limits (in proper basis of each component) in Table 3.1 for the capacitors, while reference [88] recommends for harmonic filter inductors to follow the same V_{rms} and I_{rms} limits as their capacitor in series. For compatibility, the capacitor limits in Table 3.1 were adopted for all components. This study is analog to a design phase, so the current and the power are shown in SI units for a better notion of magnitude and component feasibility. As a first result, notice the loading indices do not change significantly when more stages of the filter are connected, which is a desirable characteristic.

Table 3.6: Loading of the filter components, Type-III wind park

THD_V^{min}	V_{rms}, pu		V_{peak}, pu		I_{rms}, A		S, MVA	
Q_C/S_{WP}	15%	30%	15%	30%	15%	30%	15%	30%
C_1	1.00	1.00	1.02	1.02	161.3	161	9.64	9.62
L	0.03	0.03	-	-	161.2	160.9	0.28	0.27
C_2	0.03	0.03	0.03	0.03	161.2	160.9	0.25	0.25
R	0.01	0.01	-	-	4.75	3.78	0	0
RFSC	V_{rms}, pu		V_{peak}, pu		I_{rms}, A		S, MVA	
Q_C/S_{WP}	15%	30%	15%	30%	15%	30%	15%	30%
C_1	1.00	1.00	1.00	1.01	160.7	160.7	9.6	9.6
L	1.05	1.05	-	-	160.7	160.7	10.1	10.1
C_2	1.05	1.05	1.05	1.05	160.7	160.7	10.1	10.1
R	0.02	0.02	-	-	2.27	3.59	0	0.01

Table 3.7: Loading of the filter components, Type-IV wind park

THD_V^{min}	V_{rms}, pu		V_{peak}, pu		I_{rms}, A		S, MVA	
Q_C/S_{WP}	15%	30%	15%	30%	15%	30%	15%	30%
C_1	1.00	1.00	1.02	1.02	161.1	160.9	9.63	9.62
L	0.02	0.02	-	-	161.0	160.9	0.16	0.16
C_2	0.02	0.02	0.02	0.02	161.0	160.9	0.15	0.15
R	0.01	0.00	-	-	4.37	3.82	0.00	0.00
RFSC	V_{rms}, pu		V_{peak}, pu		I_{rms}, A		S, MVA	
Q_C/S_{WP}	15%	30%	15%	30%	15%	30%	15%	30%
C_1	1.00	1.00	1.01	1.01	160.7	160.7	9.60	9.60
L	1.05	1.05	-	-	160.7	160.7	10.1	10.1
C_2	1.05	1.05	1.05	1.05	160.7	160.7	10.1	10.1
R	0.02	0.03	-	-	3.87	4.80	0.01	0.01

The current through L and C_2 is equal to the current through C_1 for both filters, as L and C_2 were designed to resonate at fundamental frequency. However, the voltage across the components for the THD_V^{min} tuning is much lower than the RFSC tuning, given that the resulting impedance of the components is much smaller for the THD_V^{min} tuning. Consequently, the apparent power exchanged between the components of the THD_V^{min} tuning is much lower than the RFSC tuning.

The large C_2 required by the THD_V^{min} tuning is not a problem due to the low voltage through the component and the low apparent power exchange, so it is both feasible and cheap.

3.3.7 Cost of the filter

With the loading of the filter components reported in Table 3.6, it is possible to estimate the cost of the filters. An estimate cost of commercial capacitors and inductors is presented in Table 3.8 and Table 3.9, respectively. These values were adapted from reference [80] for a United States Dollar inflation of 14% since date of publication. The cost of switches, protection devices, and installation was not included. The cost of the resistors was fixed to 100 $/kW after consulting manufacturers. However, the resistor cost is not significant when compared to the inductors and capacitors required for the filter.

Table 3.8: Table to calculate the cost of capacitors

Rated voltage	<1kV	1kV~10kV	10kV~25kV	25kV~50kV
Cost / kvar	$ 17.1	$ 22.8	$ 45.6	$ 74.1

Table 3.9: Table to calculate the cost of inductors

Rated current / voltage	1kV~10kV	10 kV~25kV
<100A	$ 1596	$ 3192
100A~0.5kA	$ 1938	$ 3876
0.5 kA~1kA	$ 2166	$ 4332

The costs of the filter components are shown in Table 3.10.

Table 3.10: Cost of the filter components

	C_1	L	C_2	R	Total cost
Type-III wind park					
$\mathrm{THD}_{\mathrm{V}}^{\mathrm{min}}$	0.88 M$	11 628 $	8587 $	1056 $	0.9 M$
RFSC	0.88 M$	23 256 $	0.92 M$	618 $	1.82 M$
Type-IV wind park					
$\mathrm{THD}_{\mathrm{V}}^{\mathrm{min}}$	0.88 M$	11 630 $	5 077 $	440 $	0.895 M$
RFSC	0.88 M$	23 256 $	0.92 M$	618 $	1.82 M$

The filter cost for the Type-III and IV wind parks is very similar. Notice the most expensive component is the capacitance for the original capacitor bank C_1 (two stages of Q_C/S_{WP} = 15% each, for a total of 0.88 M$), while the cost of the filter resulting from the $\mathrm{THD}_{\mathrm{V}}^{\mathrm{min}}$ is 0.9 M$, so the additional components increase the cost by only about 2.3% when compared to the original capacitor bank. On the other hand, the filter resulting from the RFSC tuning costs 1.82 M$, which is double the value of the original capacitor bank. The $\mathrm{THD}_{\mathrm{V}}^{\mathrm{min}}$ tuning strategy is more cost effective because the power dissipated by the components L and C_2 (from the LC branch tuned to the fundamental frequency) is much lower, which reflects on the price. These results demonstrate the proposed procedure for filter tuning is cost-effective.

3.3.8 Filter performance and robustness

The $\mathrm{THD}_{\mathrm{V}}^{\mathrm{min}}$ methodology designs a filter to replace the smallest stage of the capacitor bank, and to build the bank, several of these small filters are connected in parallel. The changes of the harmonic response at PCC with these consecutive connections are shown in Figure 3.25, which compares the different tuning strategies and the two stages of the filter.

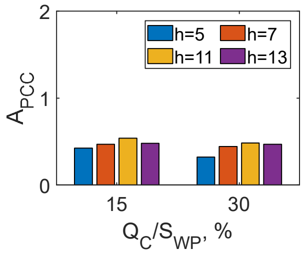

a) $\mathrm{THD}_{\mathrm{V}}^{\mathrm{min}}$, Type-III

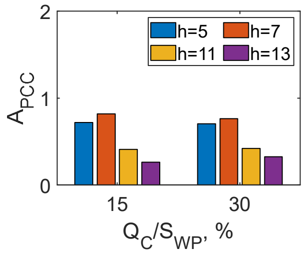

b) RFSC, Type-III

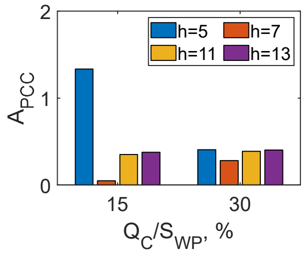

c) C. bank, Type-III

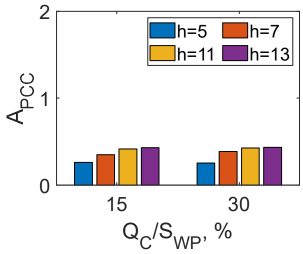

d) $\mathrm{THD}_{\mathrm{V}}^{\mathrm{min}}$, Type-IV

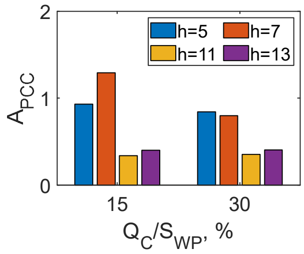

e) RFSC, Type-IV

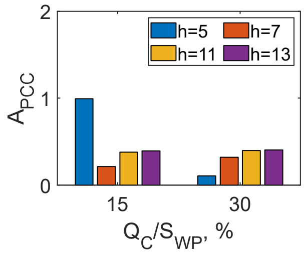

e) C. bank, Type-IV

Figure 3.25: Harmonic amplification at PCC for different filter tunings

Notice the proposed methodology has the lowest amplification levels, tends to equalize the contribution of all harmonics, and remains constant for the connection of additional stages. On the other hand, the RFSC method and the original capacitor bank have an uneven amplification profile and have greater value changes when more stages are connected to the circuit.

The $\mathrm{THD}_{\mathrm{V}}$ profile in terms of the reactive power compensation of the wind park is presented in Figure 3.26, where the markers correspond to the compensation ratios of the Q_C/S_{WP}=15% and Q_C/S_{WP}=30% stages. The horizontal dashed line of $\mathrm{THD}_{\mathrm{V}}$=1.5% denotes the limit recommended by IEEE Std 519-2014 [8] for systems rated at 138 kV or higher. Notice the scenario of the original capacitor bank (red line) has compensation ratios that lead to very high distortions due to resonance at specific harmonics. These peaks are damped by converting the capacitor bank to a passive filter. For the Type-III wind park, both filter tuning strategies are effective, however, the THD_V^{min} tuning presents lower distortion values for all stages of Q_C/S_{WP}>10%. And for the Type-IV wind park, only the THD_V^{min} strategy is effective, as the RFSC strategy increases the distortion when compared to the original case that uses only a capacitor bank, and it even goes above the limit for stages of Q_C/S_{WP}<20%.

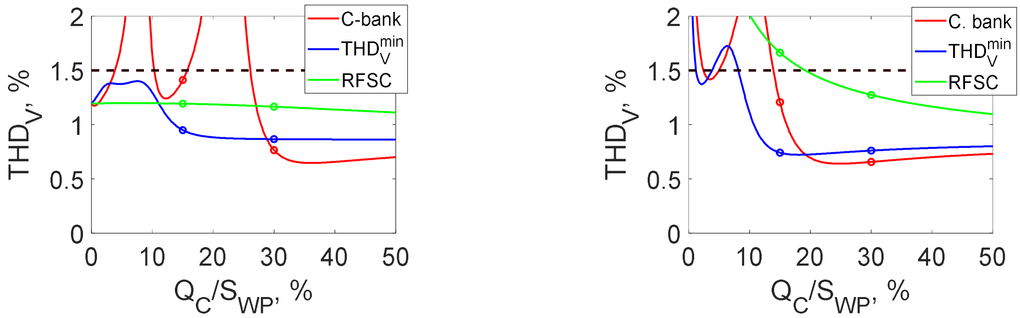

a) Type-III wind park **b) Type-IV wind park**

Figure 3.26: Total harmonic distortion at PCC vs. reactive power compensation level

Another important aspect to evaluate the effectiveness of the filter tuning is to take into account the imperfections of the manufacturing processes that lead to deviations from the specified characteristics. IEEE Std 1531-2020 [82] recommends a tolerance range for the inductance of reactors of ±3%, for the capacitance of capacitors of ±5%, and for the quality factor of reactors of ±20%. The tolerance of resistors was fixed to ±5%. The internal resistance of reactors was modeled with the expected reactance to resistance ratio of X/R = 80 for reactors as specified in IEEE Std C37.010-2016 [89]. The dielectric losses of the capacitors were also modeled with a ratio of 0.2 W/kvar after evaluating MV capacitors datasheets which follow the recommendation of IEC 60871-1:2014 [90].

The parameters of the filters in Table 3.5 were randomized within the specified tolerance bands by considering a uniform distribution with its average at the design value, and the internal resistance was included. A total of 1×10^5 random combinations were tested. The results of the performance at harmonic frequencies are presented in Figure 3.27. The losses of the tuning are compared in Figure 3.28 and the effective reactive power supplied to the circuit is shown in Figure 3.29.

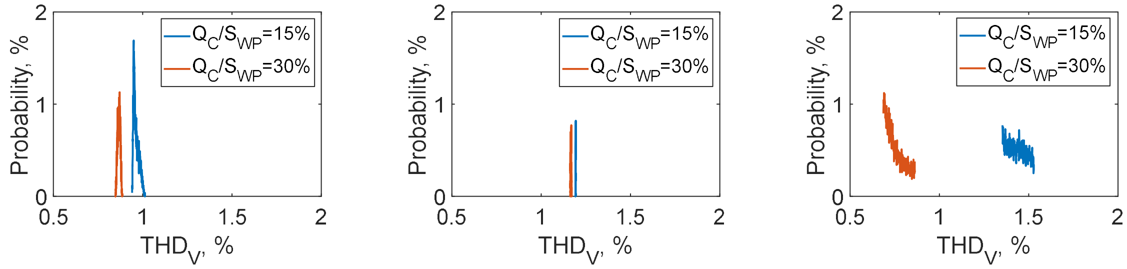

a) THD_V^{min}, Type-III   b) RFSC, Type-III   c) C. bank, Type-III

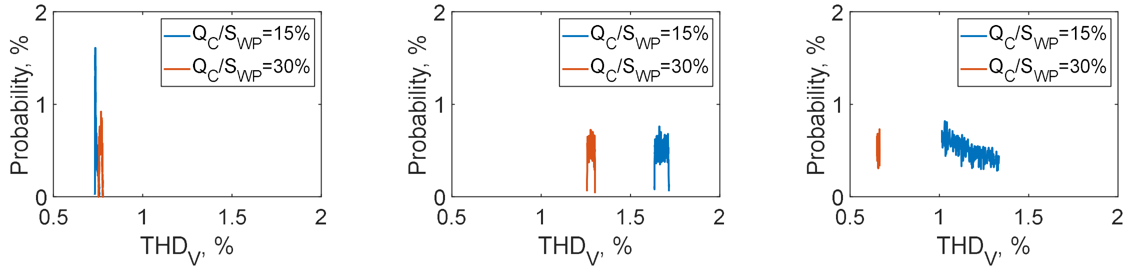

d) THD_V^{min}, Type-IV   e) RFSC, Type-IV   e) C. bank, Type-IV

Figure 3.27: Harmonic performance at PCC for different filter tunings

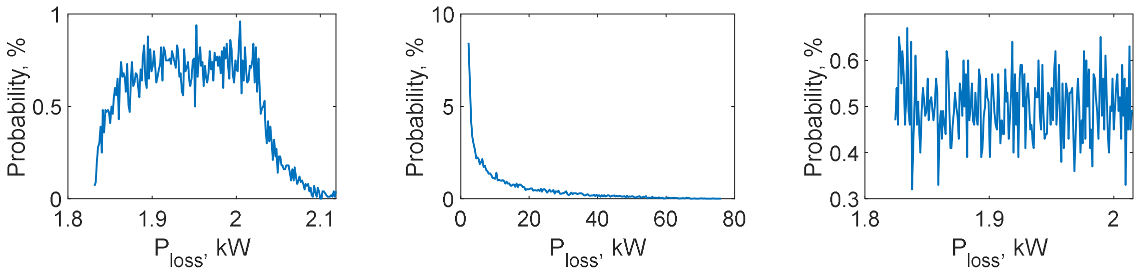

a) THD_V^{min}, Type-III   b) RFSC, Type-III   c) C. bank, Type-III

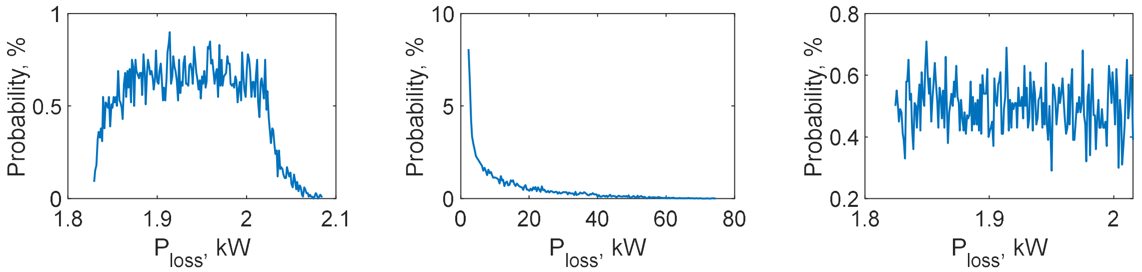

d) THD_V^{min}, Type-IV   e) RFSC, Type-IV   e) C. bank, Type-IV

Figure 3.28: Active power losses for different filter tunings

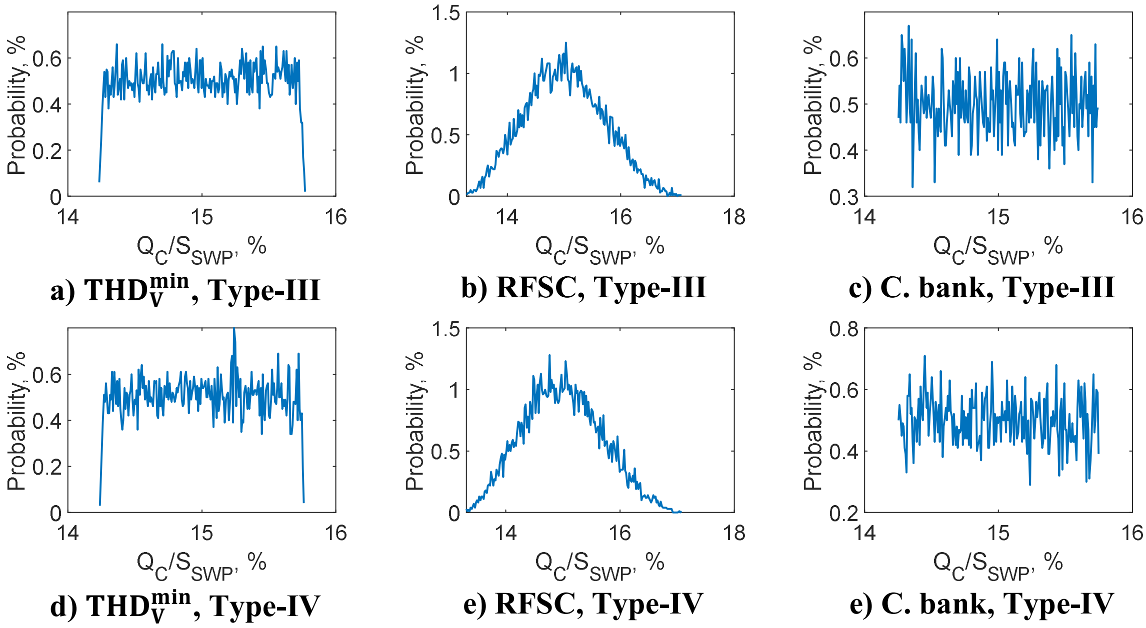

Figure 3.29: Reactive power compensation for different filter tunings

Notice both filter tuning methodologies are robust to parameter deviations in terms of their THD_V mitigation at PCC. However, the THD_V^{min} strategy has the lower average values for both wind parks. As for the active power losses at the fundamental frequency, the THD_V^{min} filter and the original capacitor bank are practically the same, which can be considered ideal. On the other hand, certain parameter deviations for the RFSC filter can lead to much higher losses which occur due to detuning of L and C_2 from the fundamental frequency. And finally, the effective reactive power compensation ratio provided by both filter tunings is very similar to that of the original capacitor bank. However, the dispersion of the effective reactive power compensation provided by THD_V^{min} strategy is lower as well. The deviations from the designed performance are related to component size, and as the THD_V^{min} strategy requires much smaller components, it is more robust to detuning.

3.3.9 Sensitivity studies

This section presents a series of additional studies to demonstrate the robustness and flexibility of the proposed strategy for filter tuning.

3.3.9.1 *Grid short circuit capacity at PCC of the wind park*

The first characteristic under evaluation is the grid strength. The grid short-circuit ratio that was used for the design is S_{SC}/S_{WP}=5. The blue areas in Figure 3.30 are circuit configurations leading to distortion levels at PCC of THD_V>1.5%.

In this figure, the horizontal red line denotes the Q_C/S_{WP}=15% value used to design the filter, and a problematic condition is obtained only when the blue region is above this horizontal line that represents the size of each stage of the capacitor bank (in this case, Q_C/S_{WP}=15%). Scenarios with 0% < Q_C/S_{WP} < 15% do not occur in practice (either the capacitor bank is disconnected, Q_C/S_{WP}=0%, or at least its smallest stage is connected, Q_C/S_{WP}=15%).

The risk of resonance in Figure 3.30 is calculated by the proportion of the area drawn by all circuit configurations with THD_V>1.5% above the red horizontal line, with respect to the area of all circuit configurations (see the shaded area in Figure 3.30 c)).

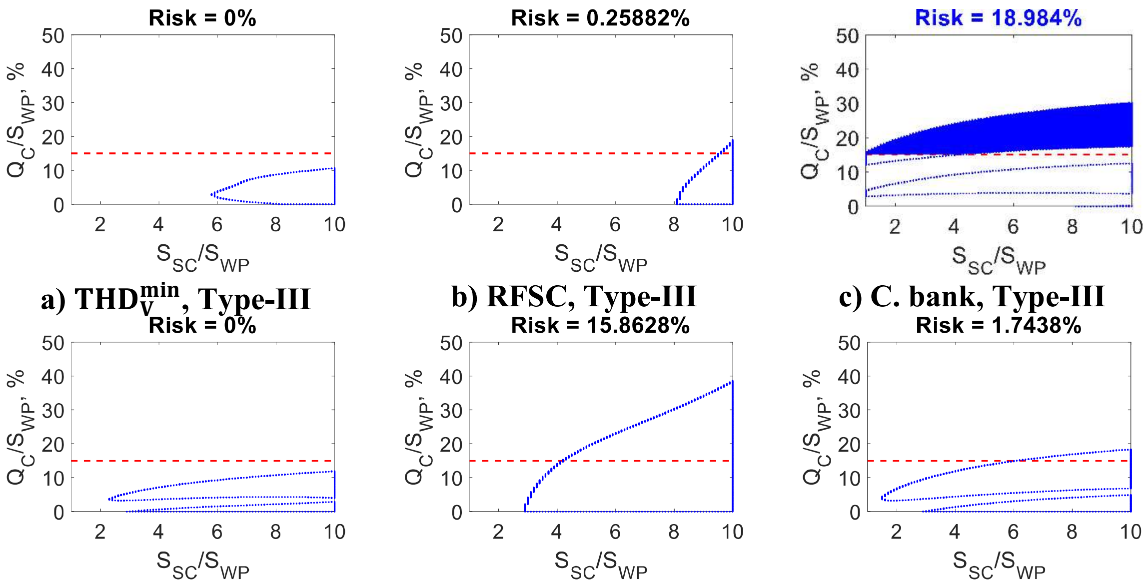

a) THD_V^{min}, Type-III **b) RFSC, Type-III** **c) C. bank, Type-III**

d) THD_V^{min}, Type-IV **e) RFSC, Type-IV** **e) C. bank, Type-IV**

Figure 3.30: Map of problematic THDv at PCC for different grid configurations

Notice that with the original capacitor bank, there are several Q_C/S_{WP} vs. S_{SC}/S_{WP} configurations which violate the THD_V limit, especially for the Type-III wind park. However, when the THD_V^{min} strategy is implemented, no configuration above the design Q_C/S_{WP} value violates the THD_V limit, so the risk is 0%. This is a highly desirable characteristic as it means the wind park will be robust to distortions when connecting the remaining capacitor bank stages, in both weaker and stronger grid conditions, which is not the case for the RFSC tuning. For the RFSC tuning, there are some circuit configurations in the stronger grids that are risky for the Type-III wind park, and the risk increased over 10 times the original value in the Type-IV wind park for not considering the wind park and grid impedances into the RFSC tuning strategy.

3.3.9.2 Harmonic impedance profile of the grid equivalent

The proposed methodology is also applicable for any harmonic impedance profile of the grid equivalent. Table 3.11 presents the impedance profile of bus 5 from the IEEE 14 buses test system [60]. For a Type-III wind park, the corresponding tuning, performance and cost results are shown in Table 3.12. Again, the $\mathrm{THD}_{\mathrm{V}}^{\mathrm{min}}$ methodology is the most cost-effective alternative.

Table 3.11: Grid equivalent impedance profile Z_{SC}, pu (64 MVA, 230 kV)

$h = 5$	$h = 7$	$h = 11$	$h = 13$
0.0225+j0.0745	0.0810+j0.1231	0.0604-j0.0187	0.0352+j0.0453

Table 3.12: Filter tuning for special harmonic impedance profile of the grid

	$\mathrm{THD}_{\mathrm{V}}^{\mathrm{min}}$	RFSC	C. bank		$\mathrm{THD}_{\mathrm{V}}^{\mathrm{min}}$	RFSC	C. bank
C_1, μF	21.39	21.39	21.39	$\mathrm{THD}_{\mathrm{V}}$, %	1.186	1.20	1.78
L, mH	13.33	345.93	-	Losses, kW	0	0	0
C_2, μF	527.73	20.34	-	Q_C/S_{WP}, %	15	15	15
R, Ω	43.14	127.13	-	Cost, M$	0.903	1.82	0.88

3.3.9.3 Harmonic distortion profile of the grid equivalent

The $\mathrm{THD}_{\mathrm{V}}^{\mathrm{min}}$ filter tuning procedure uses the voltage distortion profile of the grid equivalent as an input. This sensitivity study calculates the filter tunings from several distortion profiles, and then, verifies the performance of each filter tuning for all distortion profiles. To this end, consider the 14 distortion profiles in Table 3.13 with the individual harmonic distortion values corresponding to the limits in IEEE Std. 519-2014 [8] for transmission grids of 161 kV and above.

Table 3.13: Distortion profiles for sensitivity analysis

Profile	v_5, %	v_7, %	v_{11}, %	v_{13}, %	Profile	v_5, %	v_7, %	v_{11}, %	v_{13}, %
1	1	0	0	0	8	1	1	1	0
2	0	1	0	0	9	1	1	0	1
3	0	0	1	0	10	0	1	1	0
4	0	0	0	1	11	0	1	0	1
5	1	1	0	0	12	0	1	1	1
6	1	0	1	0	13	0	0	1	1
7	1	0	0	1	14	1	1	1	1

The resulting tunings for a Type-III wind park are shown in Table 3.14.

Table 3.14: C-type filter tunings for distortion profiles in Table 3.13

Tuning	C_1, μF	C_2, μF	R, Ω	L, mH	Tuning	C_1, μF	C_2, μF	R, Ω	L, mH
1	21.39	1172.70	100	6	8	21.39	1407.24	44	5
2	21.39	Inf	0	0	9	21.39	1407.24	100	5
3	21.39	70.36	100	100	10	21.39	Inf	0	0
4	21.39	Inf	0	0	11	21.39	Inf	0	0
5	21.39	1407.24	100	5	12	21.39	Inf	0	0
6	21.39	1005.17	95	7	13	21.39	70.36	100	100
7	21.39	1172.70	100	6	14	21.39	1407.24	36	5

The algorithm determined for the profiles 2, 4, 10, 11 and 12, a filter tuning which is equal to using the original capacitor bank, which is equal to the minimum value of the search space of R and L. For the profiles 3 and 13, it determined a filter tuning at the maximum value of the search space of R and L. These profiles have in common that either or both 5th and 7th order harmonics are zero, which are the harmonics that contribute the most to the THD_V at PCC.

Consider the filter is designed with profile 6 *i.e.*, v_h = [1, 0, 1, 0] % (this is the "design profile"). Such profile results in the tuning C_1 = 21.39 μF, C_2 = 1005.17μF, R = 95 Ω and L = 7 mH, and a THD_V = 0.9 %. If this tuning is tested for profile 2, *i.e.*, v_h = [0, 1, 0, 0] %, it results in a THD_V = 0.5 %, whereas if tested for profile 14, *i.e.*, v_h = [1, 1, 1, 1] %, the THD_V = 1.2 %. So, in order to compare the performance of the tunings more fairly (as some profiles have four harmonics contributing to the THD_V, while others have only one), the THD_V^{min} values from the tests of all profiles were normalized by the THD_V value from the corresponding "design profile". This means that for the design profile 6, the normalized THD_V = 1 pu, and for the tests in profile 2 the normalized THD_V = 0.55 pu, and with profile 6 the normalized THD_V = 1.33 pu, respectively.

The normalized THD_V values from all tests are summarized in Figure 3.31. The lower the normalized THD_V value, the better the tuning performance at multiple distortion profiles. Observe the best results are obtained with the "design profile" 14, where all tests yield a distortion value at PCC below the THD_V = 1.5 % limit of IEEE Std. 519-2014 [8]. Profile 14 can be seen as a worst-case scenario, so in cases of less distortion, the filter is ensured to have an even better performance for mitigation. From the results, it is recommended to tune the filter with all harmonics at their limit of individual harmonic distortion.

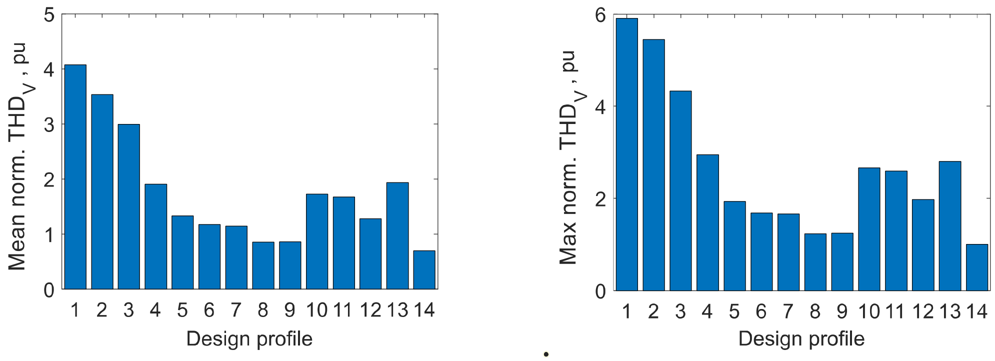

a) Mean THDv value **b) Maximum THDv value (worst case)**

Figure 3.31: Results from sensitivity study of distortion profiles

3.3.9.4 Other filter topologies

Finally, the $\mathrm{THD}_\mathrm{V}^\mathrm{min}$ tuning methodology was also applied to the third order high pass (3HP) filter topology in Figure 3.32 [58]. C_1 is tuned with the same criterion as for the C-type filter, but for C_2, the aim is to solve for the null derivative proportion of magnitudes of impedances in (3.63), which minimizes the interference of R, L and C_2 at fundamental frequency performance (losses and reactive power compensation). Expression (3.63) can be rearranged into a quadratic equation with one viable solution denoted by (3.64) (the other solution can yield very large values of C_2).

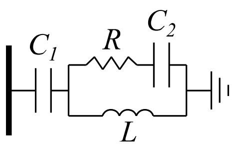

Figure 3.32: 3HP filter topology

$$\frac{d}{dC_2}\left(\frac{|((jL)^{-1}+(R+(jC_2)^{-1})^{-1})^{-1}|}{|(jC_1)^{-1}|}\right)=0 \quad \textbf{(3.63)}$$

$$C_2=\frac{2}{L+\sqrt{L^2+4R^2}} \quad \textbf{(3.64)}$$

With this result, again, the filter can be tuned in terms of R and L by calculating the respective $R_F(h)$ and $X_F(h)$ expressions, as well as their derivatives. The expressions for this 3HP filter are shown in the Appendix F.

The algorithm was compared once again to the tuning procedure for the 3HP filter in [58], and the results are summarized in Table 3.15.

Table 3.15: Tuning comparison for 3HP filter topology

	Type-III			Type-IV		
	THD_V^{min}	RFSC	C. bank	THD_V^{min}	RFSC	C. bank
C_1, μF	21.39	21.39	21.39	21.39	21.39	21.39
L, mH	7.7	13.16	-	4.54	13.16	-
C_2, μF	51.9	36.37	-	98.2	36.37	-
R, Ω	49.67	31.25	-	26.14	31.25	-
THD_V, %	0.95	1.04	1.43	0.74	0.94	1.15
Losses, kW	7.1	11.6	0	4.62	11.6	0
Q_C/S_{WP}, %	15.37	15.66	15	15.22	15.66	15
Cost, M$	0.94	0.97	0.88	0.92	0.97	0.88

The filters have a similar cost as their tunings are also closer than for the results of the tuning for the C-type topology, however the THD_V^{min} tuning is once again cheaper and provides higher THD_V damping, with less losses and less deviation from the original reactive power compensation value.

3.4 Chapter summary

This chapter studied the weakly damped resonance phenomenon (harmonic resonance) in wind parks after their connection to a point of the transmission grid with pre-existing voltage distortion to excite the resonance. Two simplified graphical tools were proposed based on impedance-equivalent models of the grid and the wind park to monitor the risk of such problematic resonances in the circuit:

1) The Harmonic Resonance Chart: To study the amplification of grid harmonic distortions at the point of common connection (PCC) between the wind park and the grid. The chart corelates the short-circuit ratio S_{SC}/S_{WP} of the grid to the reactive power compensation ratio Q_C/S_{WP} of the wind park capacitor bank, to delimit in regions in the chart where a problematic resonance is more likely to occur.
2) The Component Loading Chart: To determine the level of voltage distortion at PCC required to overload wind park components. As the shunt capacitor bank is the most vulnerable element of the wind park to overloads due to harmonic resonance, its apparent power index was used to draw the boundary of a region that corelates each value of Q_C/S_{WP} to the harmonic voltage necessary at the PCC of the wind park to overload the capacitor.

Note that no computer simulation is required in these first-screening assessments. They can quickly filter out risk-free conditions and narrow down to only a few cases that are problematic and, as such, need to be investigated in more detail.

To mitigate these harmonic resonance problems, a method was proposed to design a passive filter that can be installed in the park and is capable of both, providing the necessary reactive power compensation to the park and avoid a problematic resonance. The proposed methodology tunes the filter to minimize the THD_V at PCC in a cost/effective fashion, while it ensures the same performance at fundamental frequency of the original capacitor bank. This methodology was compared to existing methods in the literature and proved to lead to more cost-effective filters.

4 UNSTABLE RESONANCE

When the negative damping provided by Type-III and Type-IV wind generators exceeds the positive damping from the rest of the system at a given resonance frequency, the resonance becomes unstable. This leads to growing voltage and current oscillations at such frequency until the system is reconfigured by component disconnection via protection devices, or by control actions. Unlike the stable (harmonic) resonance studied in Chapter 3, this type of events can cause catastrophic damages in a short timeframe (few minutes or even seconds). These events are also known as "unstable control interactions", since the wind generator controllers normally have an important role in the characteristics of the event [3], [15].

As defined in Section 2.5, unstable resonances due to control interactions between the wind parks and the grid can be divided into three categories according to the typical frequency range where the event occurs: 1) Sub-synchronous (from 0 Hz to 40 Hz); 2) Near-synchronous (from 40 Hz to 80 Hz); and 3) Harmonic frequency range (from 80 Hz to 1.5 kHz).

Supported by the developments in Chapter 2, this chapter first defines the impedance-based criteria to study the stability of control interactions between the wind park and the grid, and then, studies the practical likelihood of the necessary conditions for each of the aforementioned unstable resonances to occur in the field. From the results of this study, a chart is proposed for sub-synchronous resonance risk assessment, as it is the most probable type of unstable resonance involving wind parks with Type-III generators.

4.1 Impedance-based stability criteria and the origin of resonance

The Nyquist impedance-based stability analysis is widely used in the literature of power-electronics based generators [15], [19], [20], [23], [26]. The "Generalized Nyquist" criterion [40] can be applied at any bus of the grid (*i.e.*, "point of analysis") by defining two equivalent impedances as in Figure 4.1 and then applying expression (4.1), where $\boldsymbol{Z}_{or}$ is the equivalent positive-negative sequence impedance matrix of the "origin of resonance" and $\boldsymbol{Z}_{eq}$ is the equivalent positive-negative sequence impedance matrix of the rest of the grid. The "origin of resonance" is defined in this thesis (to facilitate the stability analysis) as the element with the highest participation factor at the resonance frequency (participation factors are calculated from the eigenvalues of the system's admittance matrix at the resonance frequency [41]).

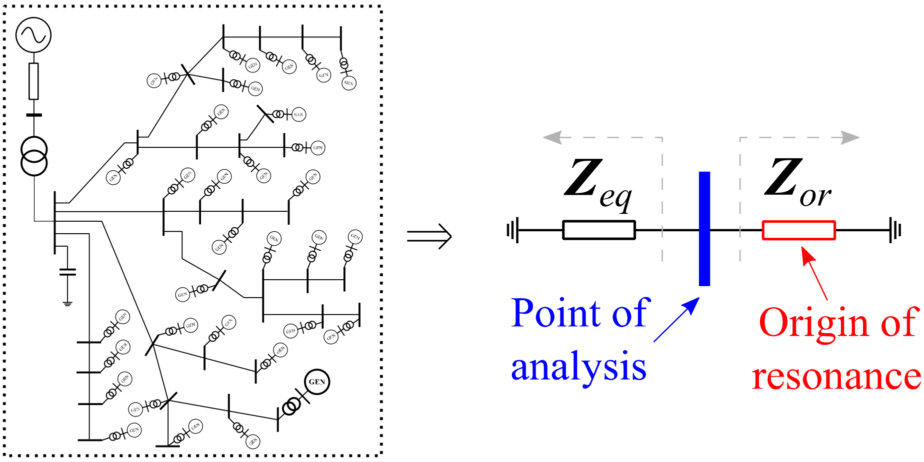

Figure 4.1: Point of analysis and origin of resonance

$$\mathbf{0} = \mathbf{1} - \boldsymbol{Z}_{eq}(f)\boldsymbol{Z}_{or}^{-1}(f)$$

$$\boldsymbol{Z}_{eq}(f) = \begin{bmatrix} z_{eq,pp}(f) & z_{eq.pn}(f) \\ z_{eq,np}(f) & z_{eq,nn}(f) \end{bmatrix} \qquad \boldsymbol{Z}_{or}(f) = \begin{bmatrix} z_{or,pp}(f) & z_{or,pn}(f) \\ z_{or,np}(f) & z_{or,nn}(f) \end{bmatrix} \quad \textbf{(4.1)}$$

The Nyquist criterion dictates that, if the trajectory of the resulting eigenvalues through the frequency spectrum encircles the (-1,0) point clockwise in the complex plane, the system is unstable. The frequency where the eigenvalues cross the unitary circle corresponds to the resonance frequency. To illustrate, consider the example in Figure 4.2. Notice scenario 2 encircles the (-1,0) point, indicating the system will have unstable oscillations at 11 Hz and 109 Hz. Whereas scenario 1 presents stable oscillations at 7 Hz and 113 Hz.

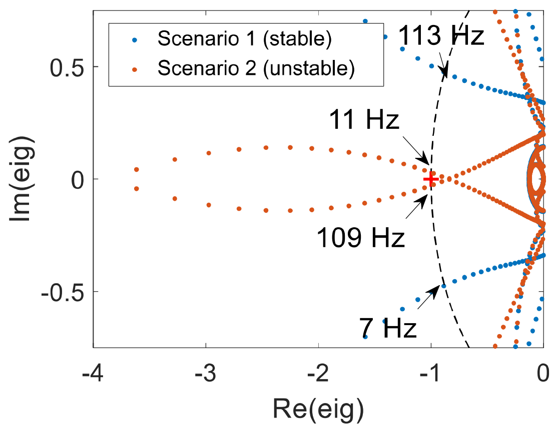

Figure 4.2: Generalized Nyquist stability criteria example

The “Generalized Nyquist” criterion is used when analyzing the stability of control interactions at the near the synchronous range (NSR), which involve non-negligible sequence couplings (see the impedance profiles of the generators in Figure 2.11 and Figure 2.12). In this case, the wind park, as a whole, acts as the "origin of resonance" (the rest of the grid is considered without sequence couplings). However, for the sub-synchronous range (SSR), the "origin of the resonance" is a series capacitor of a transmission line, and for the harmonic frequency range (HFR), the "origin of resonance" is the wind park's shunt capacitor.

Considering capacitor banks have no sequence couplings, a simplified stability criterion can be derived from expression (4.1) based on the positive sequence impedance described by expression (4.2). This criterion is known as the "sum of impedances" criterion,

$$
\begin{gathered}
z_{sum}(f) = z_{eq,p}(f) + z_{or,p}(f) = 0 \\
z_{eq,p}(f) = z_{eq,pp}(f) - \frac{z_{eq,np}(f) z_{eq,pn}(f)}{z_{eq,nn}(f)} \\
z_{or,p}(f) = z_{or,pp}(f) - \frac{z_{or,np}(f) z_{or,pn}(f)}{z_{or,nn}(f)} = z_{or,pp}(f)
\end{gathered}
\tag{4.2}
$$

Notice $z_{eq,p}(f)$ is the decoupled positive sequence impedance of all the elements of the grid, except the capacitor which is the "origin of resonance". The expression for $z_{or,p}(f)$ corresponds to the positive sequence component of the impedance matrix as the sequence couplings of balanced capacitors are null. These expressions were obtained in the same way as expression (2.25) for a dominant positive sequence phenomenon.

The "sum of impedances" criterion dictates the system is unstable when the damping at the resonance frequency f_{res} is negative, *i.e.*, when the conditions of expression (4.3) are met. Basically, the net reactance X_{sum} zero-crossings are checked to find the resonance frequencies, and, if the net damping R_{sum} at such resonance frequency is negative, then the system is unstable.

$$
\begin{gathered}
\mathrm{Im}\{z_{sum}(f)\} = X_{sum}(f) = 0 \Rightarrow f = f_{res} \\
\mathrm{Re}\{z_{sum}(f_{res})\} = R_{sum}(f_{res}) < 0
\end{gathered}
\tag{4.3}
$$

To illustrate the sum of impedances criterion, consider the scenarios in Figure 4.3. The resonance of scenario 2 occurs at 11 Hz and at a point of negative damping, so the scenario is unstable (red marker). On the other hand, scenario 1 is stable as the resonance frequency occurs at 7 Hz and it has a net positive damping (green marker).

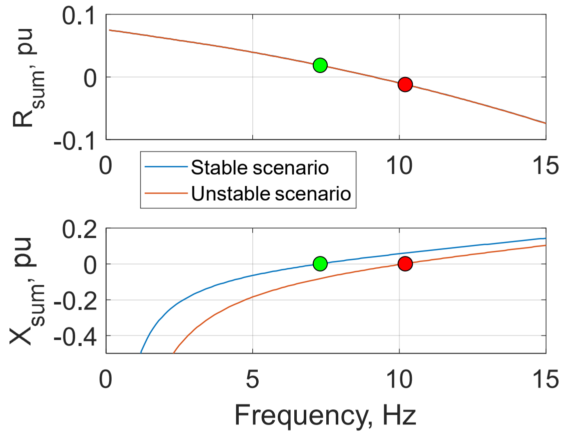

Figure 4.3: Sum of impedances stability criteria example

4.2 Stability criteria validation

The validity of the "Generalized Nyquist" criterion and the "Sum of impedances" criterion to study the stability at the different ranges of frequency can be determined by their accuracy to match the frequency and damping sign (positive sign for stable, negative sign for unstable) of the oscillation which arises after a small disturbance in the circuit. The output current of the wind park from the EMT simulation was measured, and Fast Fourier Transform (FFT) was applied to observe the frequency spectrum. Only phase A results are shown for visualization purposes.

4.2.1 Sub-synchronous range

For this subsection, the grid equivalent was modeled as a series RL branch with impedance $Z_{SC} = R_{SC} + jhL_{SC}$, calculated with expression (3.3) for a reactance to resistance ratio at fundamental frequency of X/R=10, and a short-circuit ratio of the grid at wind park PCC of S_{SC}/S_{WP} = 3. This model of the grid equivalent is used by the IEEE Task Force on Wind Sub-Synchronous Oscillations [3]. A capacitor with reactance $X_C = (hC_S)^{-1}$ was added in series, and its capacitance was calculated for a fixed X_C/X_L ratio at fundamental frequency, in pu, as follows:

$$C_S = 1/\big(L_{SC}(X_C/X_L)\big) \quad \textbf{(4.4)}$$

The EMT simulation was set to start at a stable configuration, with the wind park injecting P = 0.5 pu and Q = 0 pu, and no series capacitor, *i.e.*, X_C/X_L = 0%. At 9 seconds of simulation, a stage of the capacitor was switched-in, for a compensation ratio of X_C/X_L = 10%. The simulation results are shown in Figure 4.4. The Type-III wind park presents two unstable oscillations, a large one at 12 Hz with positive sequence, and a small one at 108 Hz with negative sequence (reflection of the 12 Hz oscillation due to the sequence coupling effect of the generators). On the other hand, the Type-IV wind park remained stable. These results match field events reported in the literature, where only Type-III wind parks become unstable when fed radially by series capacitors.

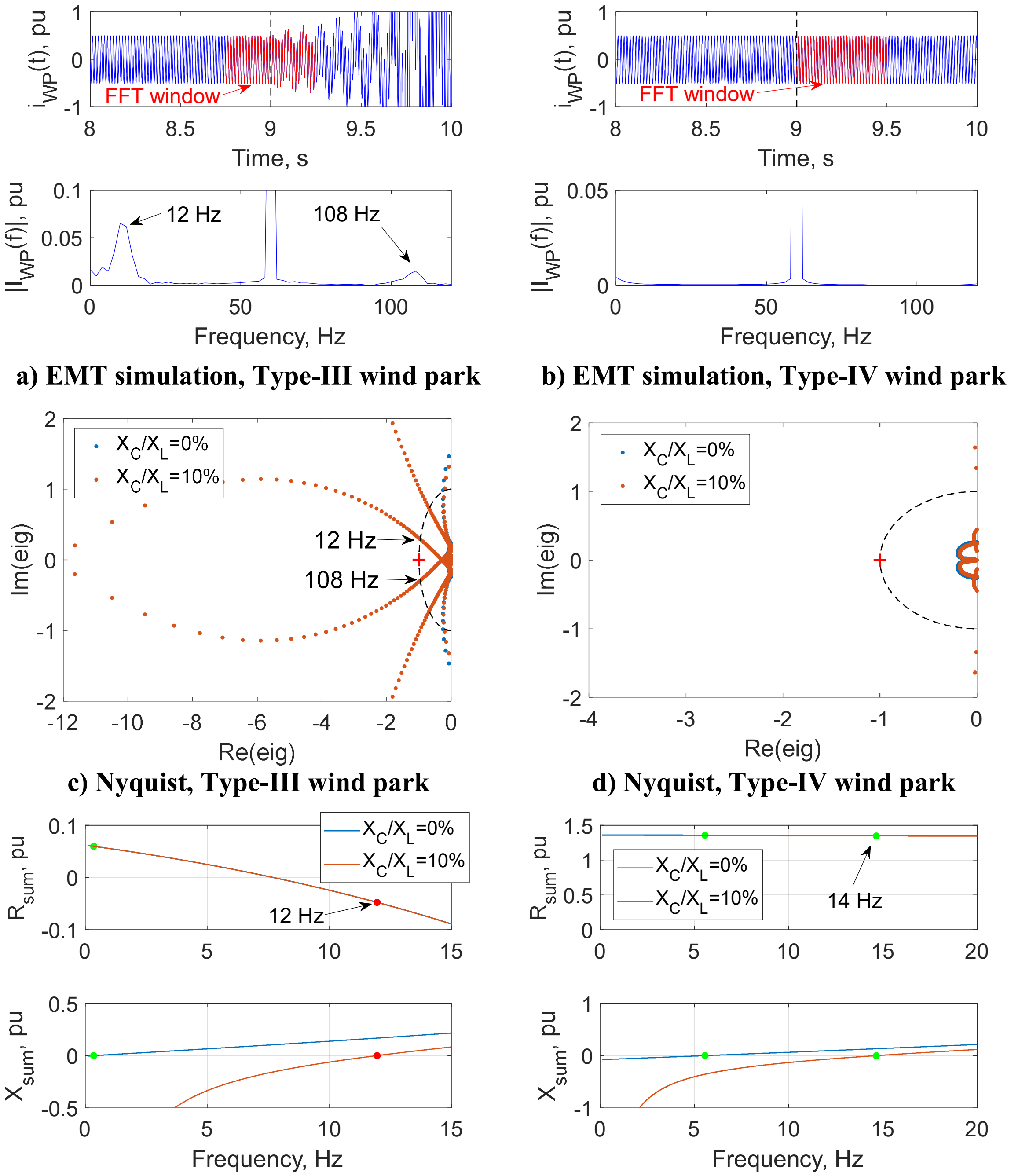

a) EMT simulation, Type-III wind park b) EMT simulation, Type-IV wind park

c) Nyquist, Type-III wind park d) Nyquist, Type-IV wind park

e) Sum of impedances, Type-III wind park f) Sum of impedances, Type-IV wind park

Figure 4.4: Validation of impedance-based stability criterion at SSR

The eigenvalues in the "Generalized Nyquist" criterion of the Type-III wind park encircle the (-1,0) point denoted by the red marker, therefore, the capacitor connection leads to instability at 12 Hz and 108 Hz (the crossings of the eigenvalues with the unitary circle denote the oscillation frequencies). On the other hand, the "Sum of impedances" criterion also shows the Type-III wind park is unstable at 12 Hz, but the 108 Hz component resulting from the coupling was neglected as the phenomena was considered to have a dominant positive sequence (this is validated by comparing the magnitudes of the components in the frequency spectrum from the FFT).

As for the Type-IV wind park, both the "Generalized Nyquist" and the "Sum of Impedances" determined the system remains stable after the capacitor switching. Notice that, although the resonance exists, both criteria demonstrate a very large stability margin of system at the SSR because the Type-IV generators provide high positive damping at the SSR.

The impedance-based stability criteria match the EMT simulation results in the SSR with great accuracy (frequency and damping sign of the oscillation), for both wind parks.

4.2.2 Near synchronous range

For this subsection, the wind parks were configured with a poor PLL tuning that leads to a large bandwidth (large integral gain K_{iPLL} = 4500, this is expanded on in Section 4.3). As in the SSR study, the grid equivalent was modeled in the NSR as a series RL branch with impedance $Z_{SC} = R_{SC} + jhL_{SC}$, calculated with expression (3.3) for a reactance to resistance ratio at fundamental frequency of X/R=10. The disturbance is modeled by a reconfiguration of the transmission system, which changed the short-circuit ratio at PCC of the wind park from S_{SC}/S_{WP} = 2 to S_{SC}/S_{WP} = 1.5, thus, entering a weak grid condition according to [15].

The simulation results for the NSR are shown in Figure 4.5. From the current waveforms, notice that the Type-III wind park remained stable with damped oscillations at 51 Hz and 69 Hz, whereas the Type-IV became unstable with oscillations at 52 Hz and 68 Hz. From the FFT of the current oscillations, it is possible to observe that both the positive sequence (<60 Hz) and the negative sequence (>60 Hz) have very similar magnitudes, which indicates they are equally important in the phenomenon and neither of them can be neglected.

For both the Type-III and the Type-IV wind parks, the frequency of the oscillation and the sign of its damping were estimated correctly by the "Generalized Nyquist" criterion. However, the "Sum of impedances" criterion does not yield accurate results in the NSR as explained previously, because the simplification of dominant sequence that was used to derive this "sum of impedances" criterion is not valid for NSR. There are important sequence couplings at this range.

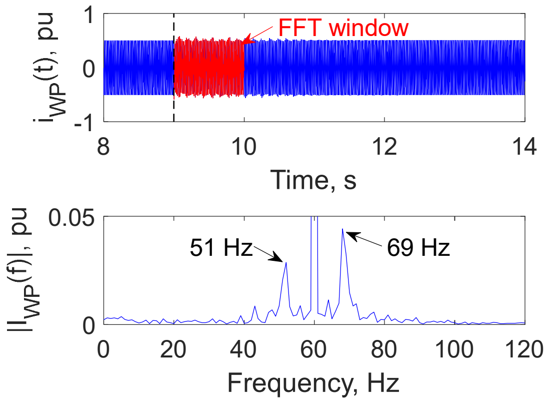

a) EMT simulation, Type-III wind park

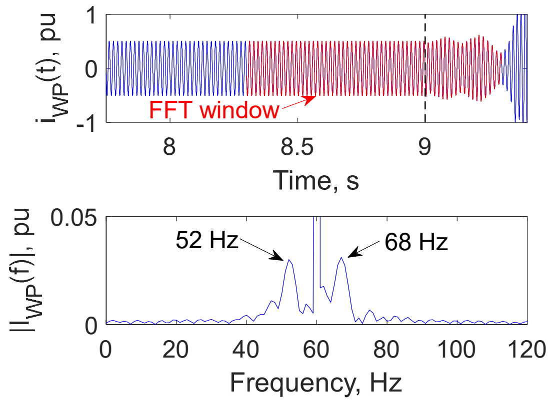

b) EMT simulation, Type-IV wind park

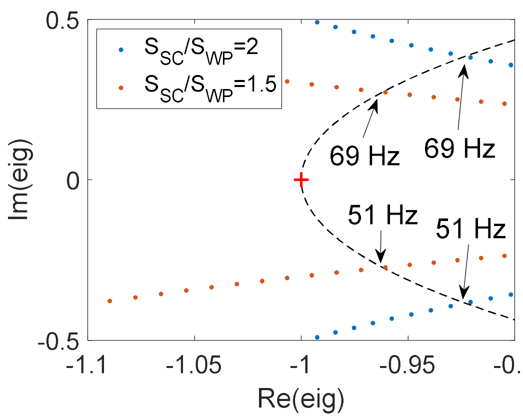

c) Nyquist, Type-III wind park

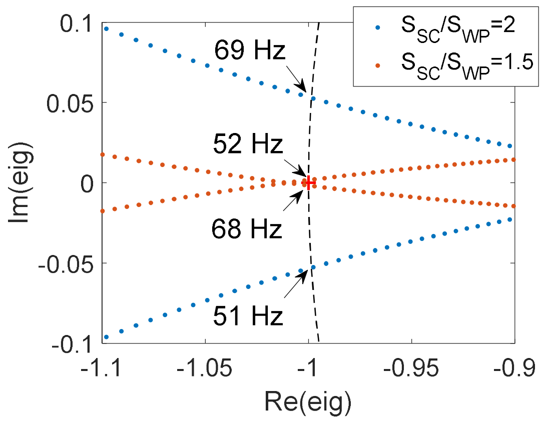

d) Nyquist, Type-IV wind park

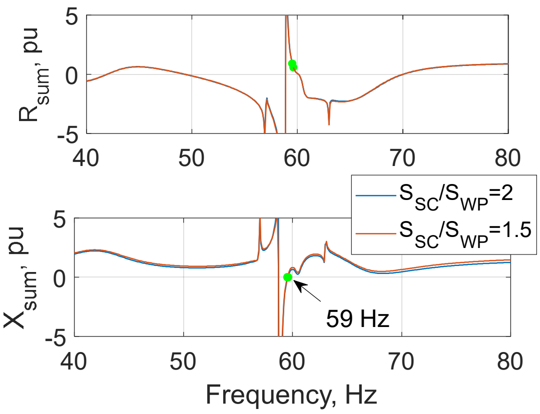

e) Sum of impedances, Type-III wind park

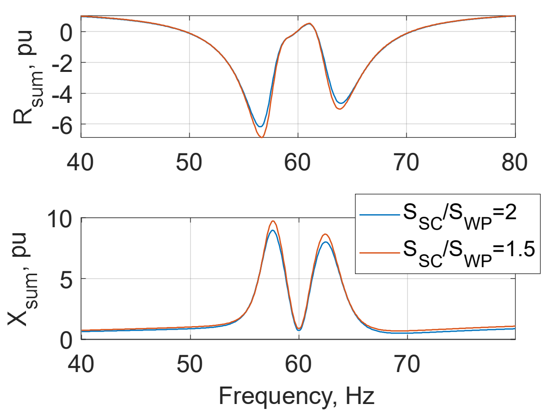

f) Sum of impedances, Type-IV wind park

Figure 4.5: Validation of impedance-based stability criterion at NSR

Therefore, the “Generalized Nyquist” impedance-based stability criteria matches the EMT simulation results in the NSR with great accuracy (frequency and damping sign of the oscillation), for both wind parks. However, as stated during its development, the “Sum of Impedances” criterion is not accurate in the NSR due to the importance of sequence couplings.

4.2.3 Harmonic frequency range

Exciting unstable oscillations in the HFR under practical conditions is rather difficult, and this will be expanded upon in Section 4.3. For validation purposes, the grid equivalent was modeled as a series RL branch with impedance $Z_{SC} = R_{SC} + jhL_{SC}$, calculated with expression (3.3) for a reactance to resistance ratio at fundamental frequency of X/R=10 and a short-circuit ratio of $S_{SC}/S_{WP} = 5$.

The 64 MVA wind park was configured with a shunt capacitor bank of rated capacity $Q_C = 6.4$ MVAr for power factor correction, so that it provides a reactive power compensation ratio of $Q_C/S_{WP} = 10\%$.

To excite unstable resonance in the HFR in this validation example, feeder impedances of the wind park were neglected, so that it is possible to simplify all wind generators into a single machine equivalent. And then, the capacitor of the LCL front-end filter of the GSC was disconnected, which leads to unstable oscillations in the HFR, where the “center of resonance” is the shunt capacitor bank for reactive power compensation.

The simulation results are shown in Figure 4.6. Notice the current waveforms show an unstable oscillation in the harmonic range of frequencies with positive sequence, at 485 Hz for the Type-III wind park, and at 430 Hz for the Type-IV wind park.

The “Generalized Nyquist” is able to determine correctly both the frequency of the oscillation and the sign of its damping. Unlike for the SSR and the NSR, only the positive sequence oscillation is highlighted as the resonance is located at a frequency beyond 120 Hz, so that its reflected component for the negative sequence has no physical meaning as it corresponds to a negative frequency.

The “Sum of Impedances” criterion is also able to characterize the stability of the resonance with high accuracy, in both the frequency and the sign of the damping of the oscillation. From this criterion, it is possible to visualize the capacitor of the LCL filter has a considerable effect on the shape of the generator impedance profile in the HFR (see the comparison between Figure 2.13 and Figure 2.14), so the negative damping region of the generator is eliminated, which makes the system stable.

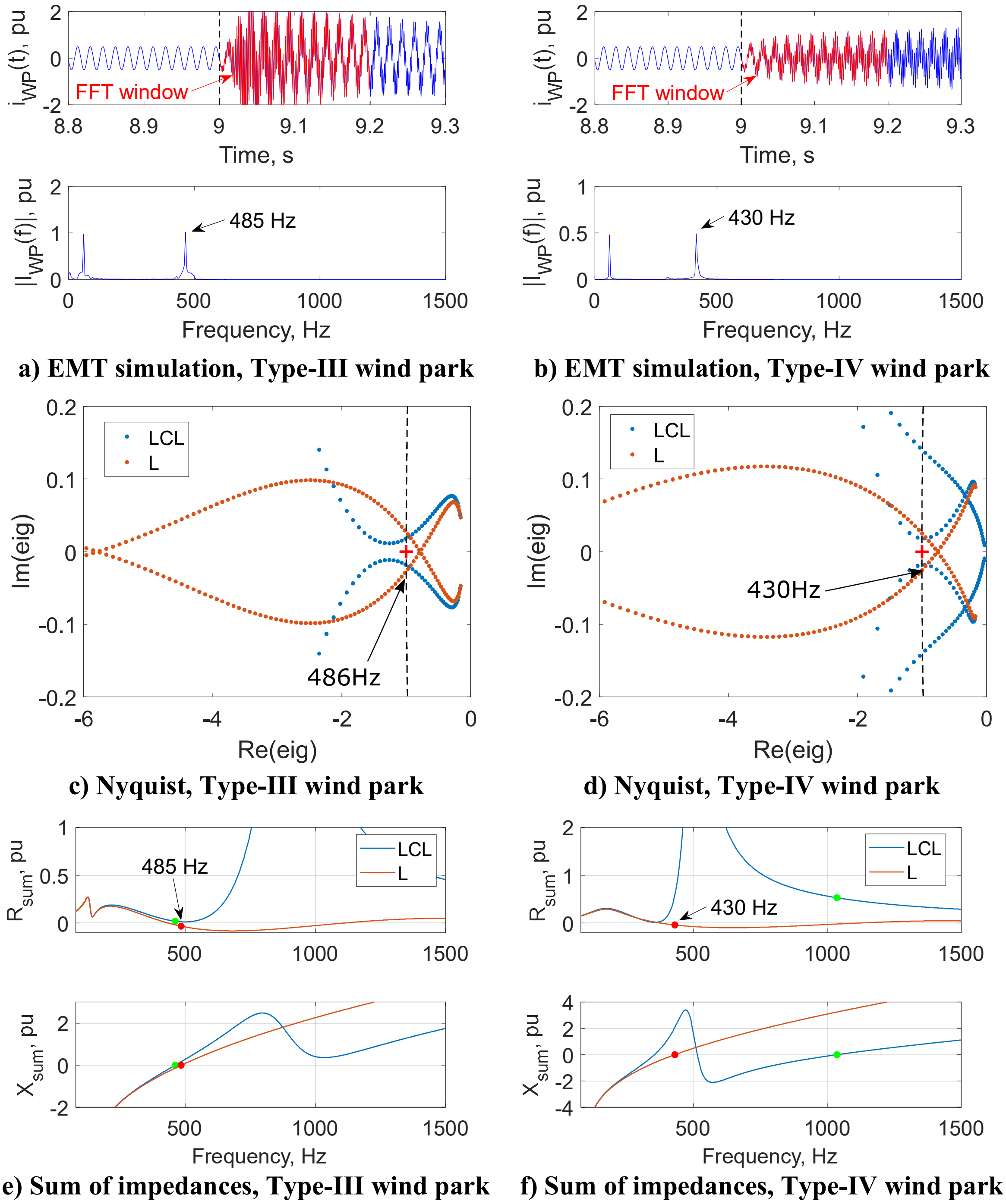

Figure 4.6: Validation of impedance-based stability criterion at HFR

4.3 Mapping conditions for unstable resonance in a practical wind park

Unstable resonance involving wind parks has been studied extensively in the literature as there are several reports of these events in practical power systems [3], [15]. However, several of these works such as [23], [24] and [46], study the phenomena without taking into account the wind park topology, use simplified generator models, or set generator controllers to uncommon tunings. Although these assumptions are useful to demonstrate the theoretical background of the unstable resonances, they do not allow a proper risk assessment of instabilities that are more likely to take place in practice.

In order to evaluate the likelihood of unstable resonance to occur in a practical wind park (*i.e.*, with realistic topology and properly tuned generators), this section presents the results of an extensive sensitivity study with thousands of tests that were conducted to map the circuit configurations more likely to face unstable control interactions between the wind park and the grid at the: 1) Sub-synchronous range (SSR) from 0 Hz to 40 Hz; 2) Near-synchronous range (NSR) from 40 Hz to 80 Hz; and the 3) Harmonic frequency range (HFR) from 80 Hz to 1.5 kHz. The feasibility of these necessary conditions for the unstable resonances is discussed to assign a qualitative risk to each type of event in practical power systems.

The following variables of the grid were tested:

- Grid strength: From weak $S_{SC}/S_{WP} = 1$, to strong grids $S_{SC}/S_{WP} = 10$.
- Grid series capacitive compensation: From no compensation $X_C/X_L = 0$ % to high compensation $X_C/X_L = 50$ %.
- Grid damping at fundamental frequency: from high $X/R = 2$, to low damping $X/R = 10$.
- Grid impedance profile: Using either an RL series branch, or a more complex impedance profile such as profiles extracted from the IEEE 14-bus test system [60].

The following variables of the wind park were tested:

- Wind park feeder type: Underground or overhead.
- Wind park feeders length: From half to twice the original value.
- Wind park shunt capacitor size: From no reactive power compensation $Q_C/S_{WP} = 0$ % to a high reactive power compensation $Q_C/S_{WP} = 50$ %.
- Wind park generator outages: From 0 units to 16 units (*i.e.*, 50 %).

- Wind park main transformer impedance: From half to twice its original value.

And the following variables of the wind generators were tested:

- Wind generator type: Type-III or Type-IV.
- Wind generator front-end filter of the GSC: LCL filter or L filter.
- Wind generator active power injection: From P = 0.1 pu to P = 1 pu.
- Wind generator terminal voltage: From V = 0.95 pu to V = 1.05 pu.
- Wind generator control gains.

The base configuration of the system for the sensitivity study was set as follows:

- Grid equivalent: RL series branch model with a strength of S_{SC}/S_{WP} = 5, damping of X/R = 5, and no series capacitive compensation X_C/X_L = 0 %.
- Wind park: 64 MVA wind park with zero outages, underground feeders and no shunt capacitive compensation Q_C/X_{WP} = 0 %.
- Wind generators: Active power injection of P = 0.5 pu and terminal voltage of V = 1 pu, LCL front-end filter of the GSC, and the control gains of Appendix A.

To restrict the pool of test scenarios (based on the relevance of the controllers for each range of frequency shown in Figure 2.16 and Figure 2.17), only the gains of the controllers in Table 4.1 were tested.

Table 4.1: Control loops tested in the sensitivity study

Range	SSR	NSR	HFR
Controller	• Converter current control loop • DC bus control • PLL	• Converter current control loop • DC bus control • PLL	• Converter current control loop • DC bus control • Measurement filter • Control delay

4.3.1 Sub-synchronous range

The "Sum of Impedances" criterion is used to present the results in this subsection. Unstable resonance in the SSR was only identified with Type-III wind parks especially due to the presence of the induction machine effect, however for the sake of completeness and comparison, some Type-IV wind park results are also shown.

First, the grid variables are analyzed. Figure 4.7 demonstrates that very small compensation levels can lead to instability in Type-III wind parks (X_C/X_L = 10 % and above). On the other hand, Type-IV wind parks are immune to instability in the SSR due to their high positive damping.

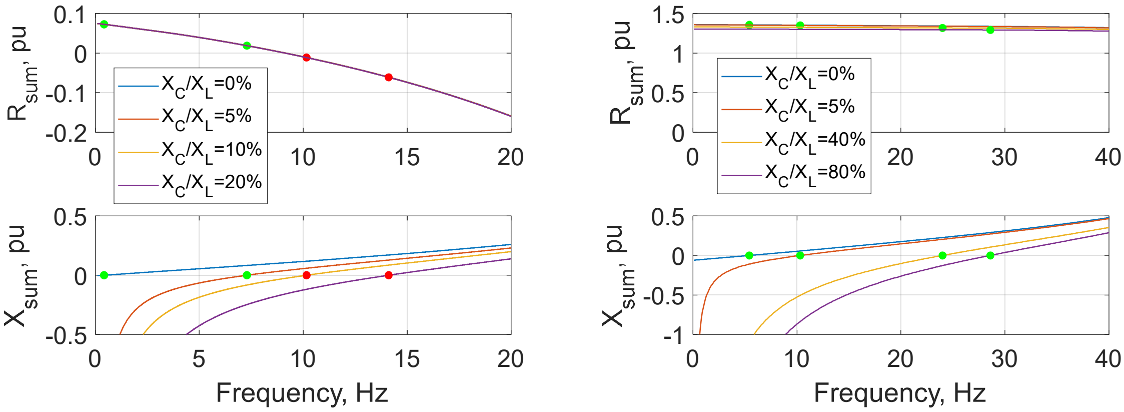

a) Type-III wind park **b) Type-IV wind park**

Figure 4.7: Stability at SSR, sensitivity to series capacitive compensation

Figure 4.8 demonstrates that instability can occur with both strong and weak short-circuit ratios. The main effect in this case is not the grid strength, but the amount of damping provided by the grid. The compensation ratio for this test was set to X_C/X_L = 10%. For this test, the scenarios of the Type-III wind park with low damping (*i.e.*, X/R=10) became unstable. And again, the Type-IV wind park is immune to this type of unstable resonance.

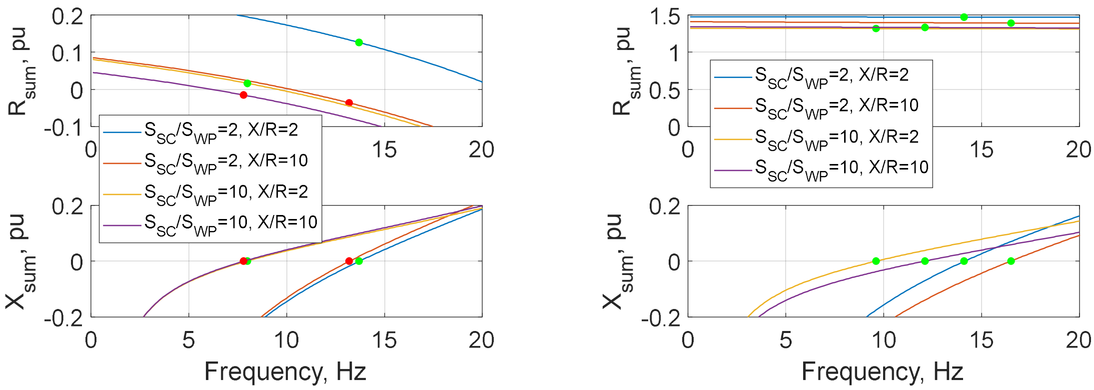

a) Type-III wind park **b) Type-IV wind park**

Figure 4.8: Stability at SSR, sensitivity to grid strength and damping ratio

To show that instability at the SSR can only occur when the wind park is fed radially by a series capacitor, the IEEE 14 buses test system from [60] was modified by adding a series capacitor to the transmission line between buses 2 and 3 with a compensation ratio of X_C/X_L =

40%, and the synchronous generator in bus 3 was replaced by a wind park complex of 192 MVA (*i.e.*, three units of the 64 MVA wind park used in this thesis) as shown in Figure 4.9. Notice the transmission line is very close to the wind park complex, and that is has a high compensation ratio. Two grid topologies were tested, and the results are shown in Figure 4.10.

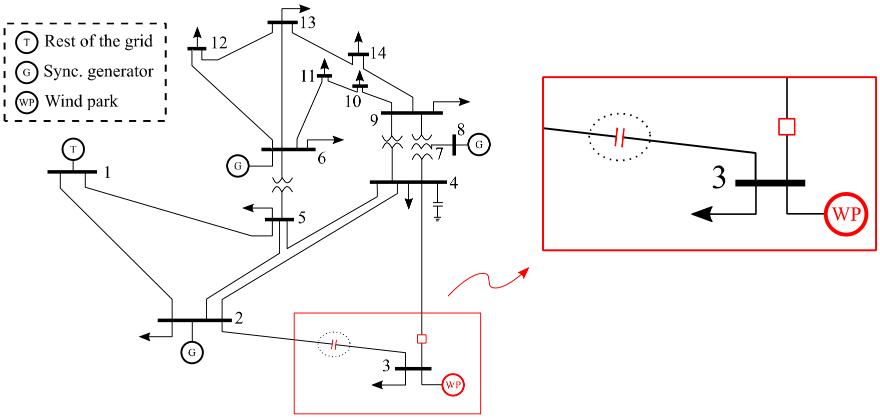

Figure 4.9: Modified IEEE 14 buses test system for grid topology analysis at SSR

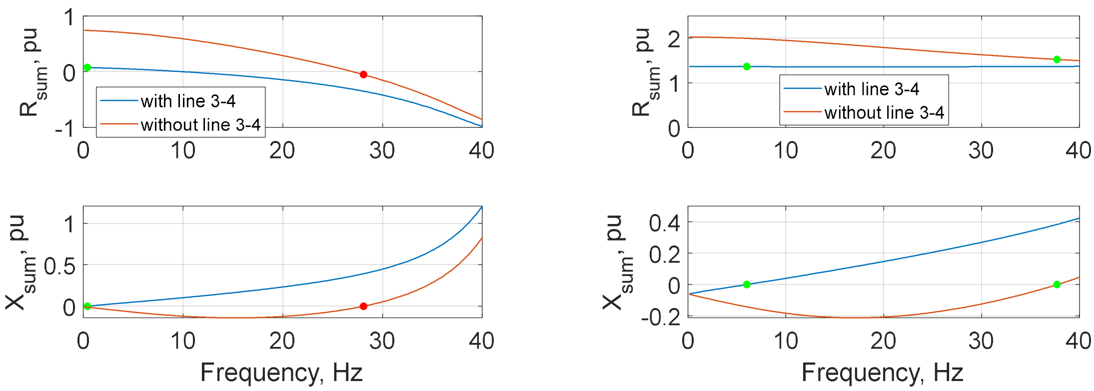

a) Type-III wind park **b) Type-IV wind park**

Figure 4.10: Stability at SSR, sensitivity to grid topology

When all transmission lines are operational, the system is stable. However, when the transmission line between buses 3 and 4 is disconnected, the wind park complex is fed radially by the series capacitor, which leads to unstable resonance in the SSR at 28 Hz for the Type-III wind park. Once again, the Type-IV wind park remained stable.

Many other grid topologies were tested, with different locations of the capacitors and the wind park, however, only those resulting in a wind park being fed radially by the capacitor led to instability under sufficiently large compensation levels.

Now, the grid wind park circuit variables are analyzed. Figure 4.11 presents a study of the characteristics of the MV feeder of the wind park. The type of feeder was tested (underground (ug), overhead (oh)), and the length of the original feeders was changed. The compensation ratio for this test was set to X_C/X_L = 10%. The feeders did not present any relevant in the SSR due to the following reasons: 1) their original length is short (see Table E.2), and 2) their series impedance is low due to the low frequency of the phenomenon.

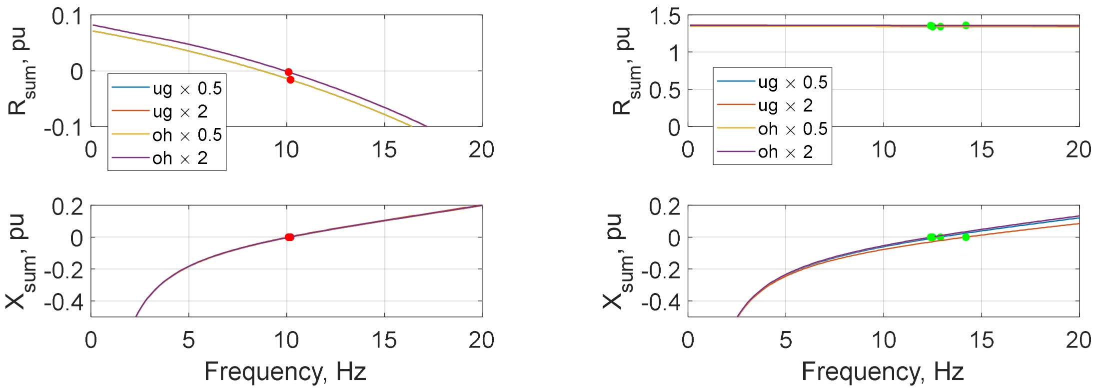

a) Type-III wind park **b) Type-IV wind park**

Figure 4.11: Stability at SSR, sensitivity to feeder type and length

Figure 4.12 shows how effect of the main transformer impedance on the stability at the SSR. The compensation ratio for this test was set to X_C/X_L = 10%. The predominantly inductive impedance of the transformer opposes the grid capacitor reactance, so larger capacitors are required to make the system unstable with larger transformer impedances.

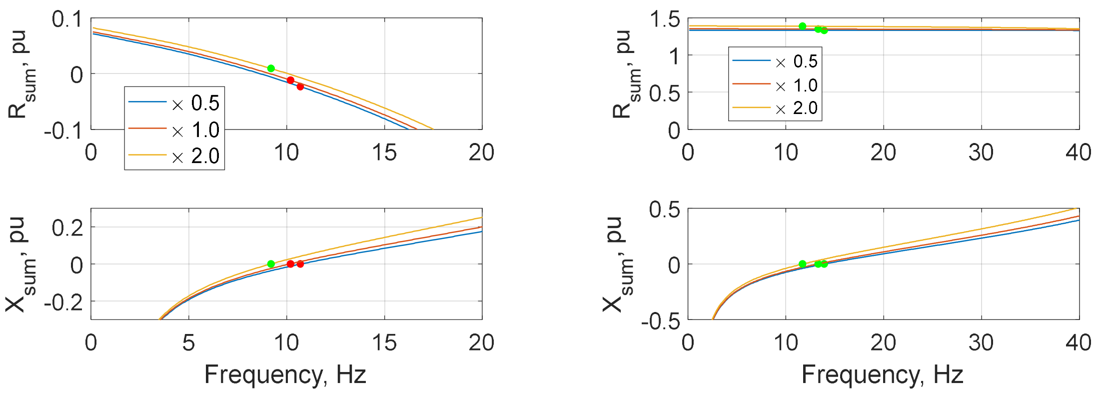

a) Type-III wind park **b) Type-IV wind park**

Figure 4.12: Stability at SSR, sensitivity to main transformer impedance

Figure 4.13 demonstrates the shunt capacitor bank has no significant effect on the stability at the SSR, which is expected as shunt capacitors at low frequencies have a very large impedance. The compensation ratio for this test was set to X_C/X_L = 10%.

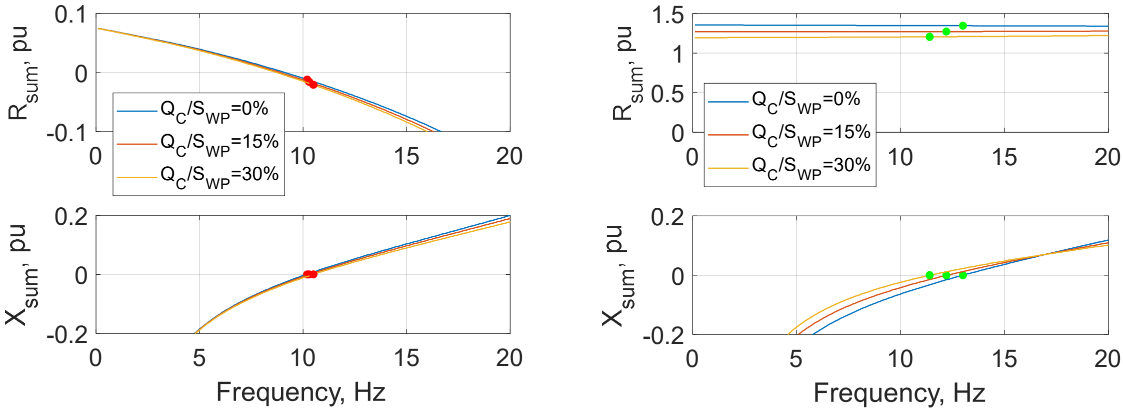

a) Type-III wind park **b) Type-IV wind park**

Figure 4.13: Stability at SSR, sensitivity to shunt capacitor bank

Figure 4.14 shows the generator outages have an important effect on the stability at SSR. The compensation ratio for this test was set to X_C/X_L = 10%. The more the number of generators disconnected, the larger the WP equivalent impedance, so a larger negative damping provided by the Type-III wind park worsens the instability. This is one reason why generator disconnections did not solve the unstable resonance problems in the SSR reported in China [21].

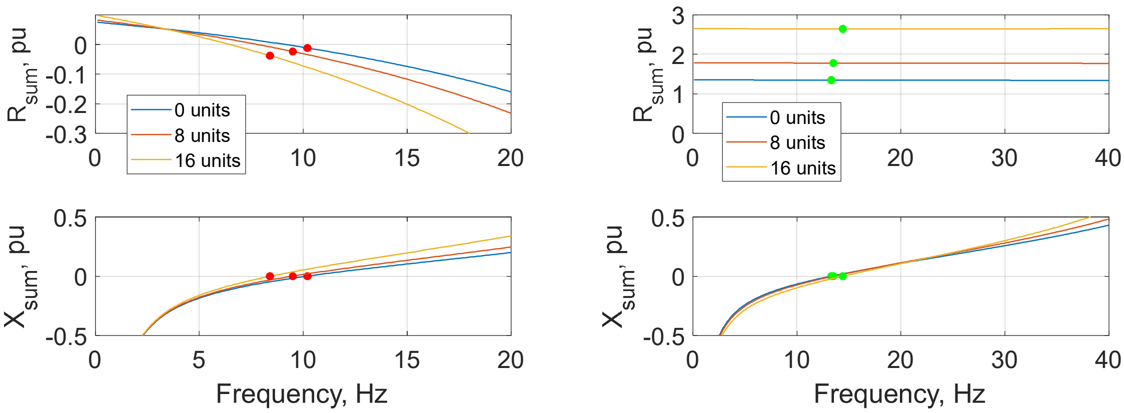

a) Type-III wind park **b) Type-IV wind park**

Figure 4.14: Stability at SSR, sensitivity to generator outages

Finally, the generator variables are analyzed. Figure 4.15 shows the front-end filter capacitance is not relevant in the SSR. The compensation ratio for this test was set to X_C/X_L =

10%. As for the shunt capacitor bank, the effect of the LCL filter capacitor can be neglected at the SSR due to its high impedance of the capacitor at low frequencies.

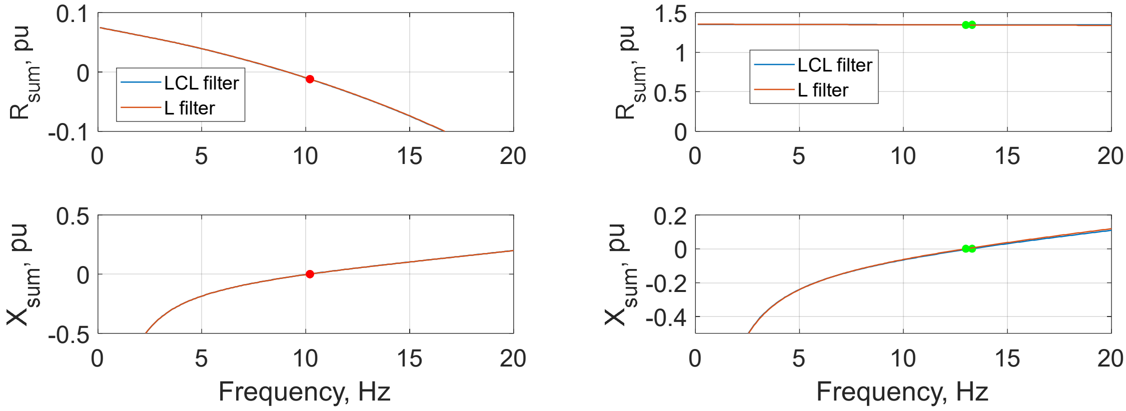

a) Type-III wind park **b) Type-IV wind park**

Figure 4.15: Stability at SSR, sensitivity to GSC front-end filter

Figure 4.16 shows the active power injection of the generators has important influence on the stability at the SSR. For the Type-III wind park, lower power injections are associated with more negative damping and lower resonance frequencies due to the change on the induction machine impedance. This result matches the reports in the literature of instabilities at low wind.

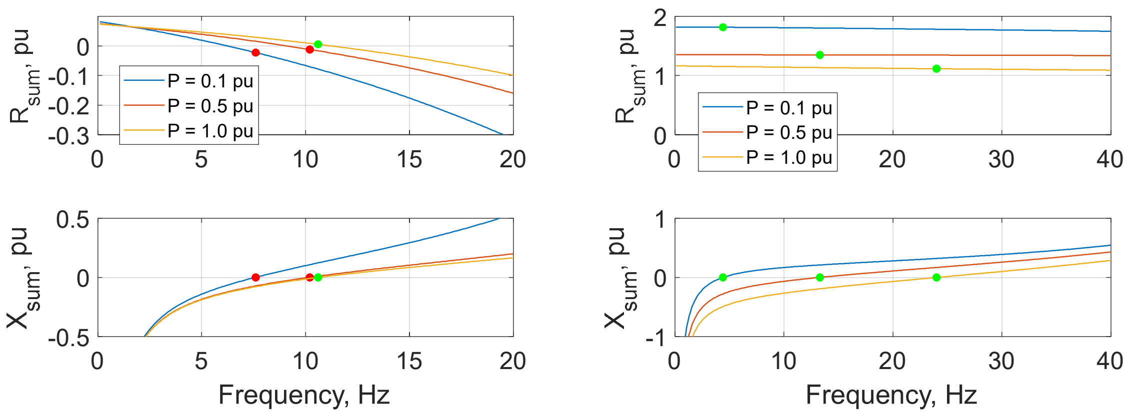

a) Type-III wind park **b) Type-IV wind park**

Figure 4.16: Stability at SSR, sensitivity to active power injection

Notice that although the system remains stable, the damping and resonance frequency results of the Type-IV wind park change considerably with the active power, indicating a strong influence of the operational setpoint on the equivalent impedance of the converter. Figure 4.17, which evaluates the effect of the terminal voltage on the stability at the SSR, confirms the Type-

IV generator indeed depends on the operational setpoint of the controllers. On the other hand, the Type-III generator does not as the impedance is dominated by the induction machine.

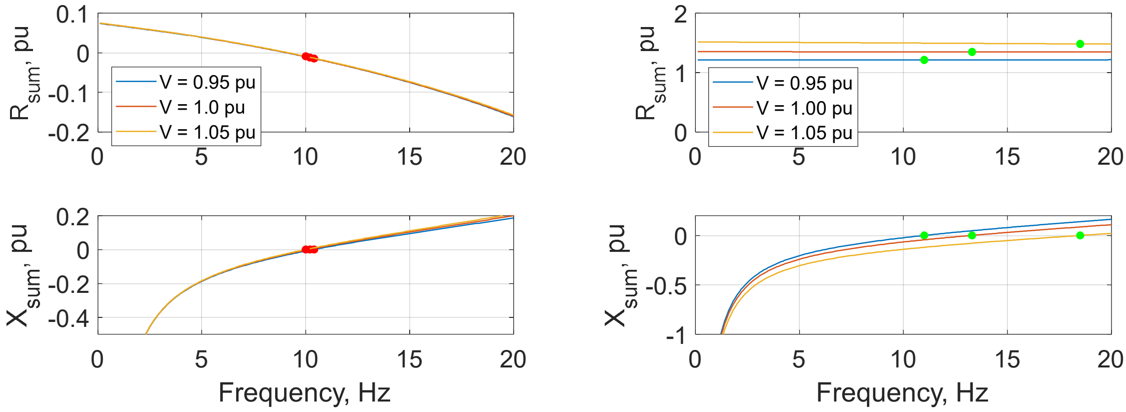

a) Type-III wind park **b) Type-IV wind park**

Figure 4.17: Stability at SSR, sensitivity to terminal voltage

Although several scenarios of instability were achieved prior to modifying the control tunings of the generators, Figure 4.18 to Figure 4.20 are presented to show the effect of the most relevant control gains on the stability at resonance at the SSR. The compensation ratio for this test was set to $X_C/X_L = 10\%$, where the Type-III wind park is unstable. Lower gains of the current control and the DC voltage control loops tend to stabilize the system, whereas larger gains increase the risk of instability. Notice the PLL gains require larger changes to evidence the influence in the SSR (see the bandwidth and damping effect in the Appendix D). The effect of the PLL is visible in Type-III wind parks for frequencies greater than 20 Hz, so it can be necessary to model it in detail in presence of transmission lines with high series compensation levels.

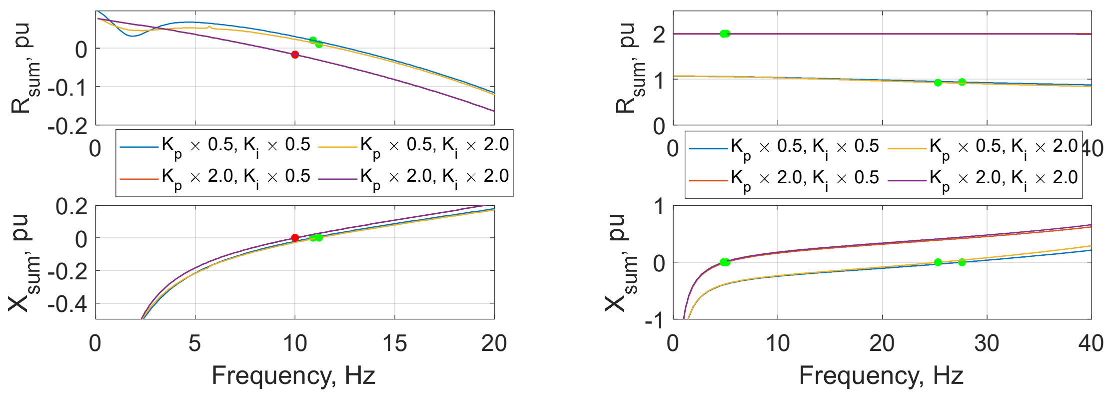

a) Type-III wind park **b) Type-IV wind park**

Figure 4.18: Stability at SSR, sensitivity to converter current control gains (K_{pGSC}, K_{iGSC})

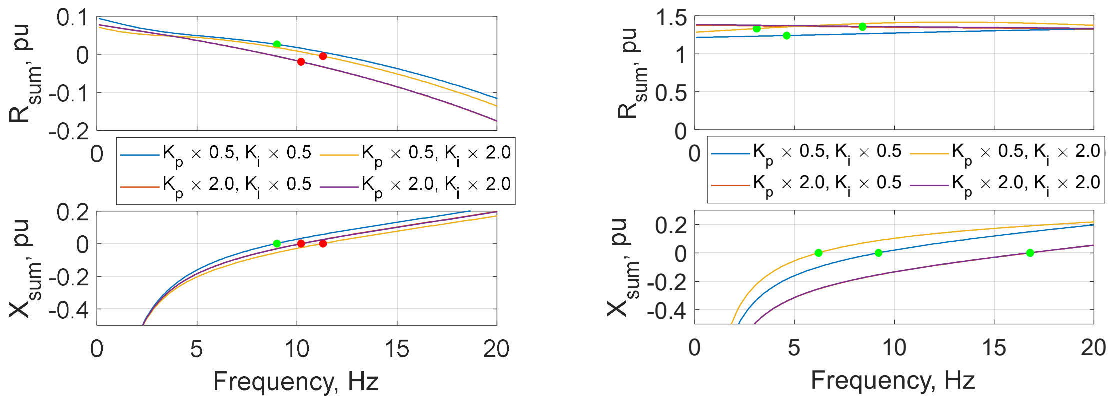

a) Type-III wind park

b) Type-IV wind park

Figure 4.19: Stability at SSR, sensitivity to DC bus voltage control gains (K_{pdc}, K_{idc})

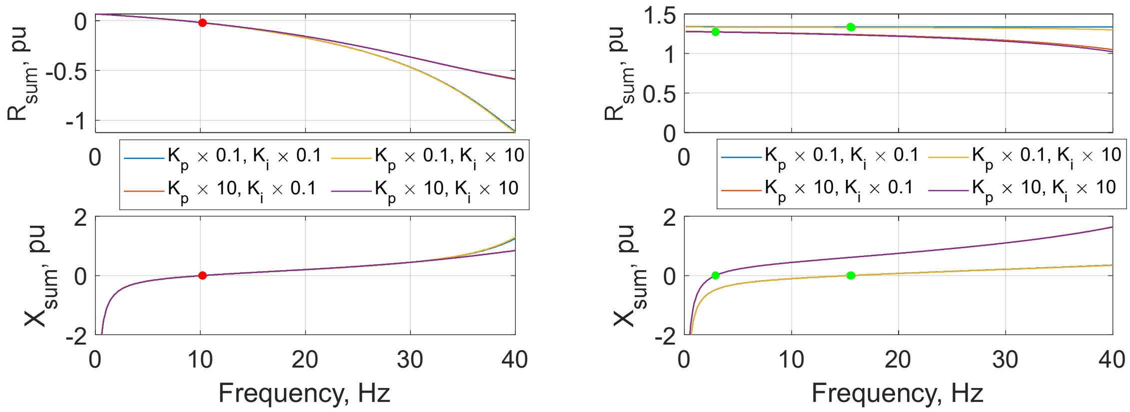

a) Type-III wind park

b) Type-IV wind park

Figure 4.20: Stability at SSR, sensitivity to PLL control gains (K_{pPLL}, K_{iPLL})

As control tunings and topologies can vary significantly from vendor to vendor, it is important to be able to model the controllers of the generators with flexibility for greater accuracy instead of using over simplified models to facilitate the algebra. This further justifies the usefulness of the modeling methodology proposed in Chapter 2 of this thesis.

4.3.2 Near synchronous range

The "Generalized Nyquist" criterion is used to present the results in this subsection. After extensive testing, it was determined that unstable control interactions in the NSR can occur for both Type-III and Type-IV wind parks, but the wind park has to be connected to a weak grid (*i.e.*, providing a low short-circuit ratio of $S_{SC}/S_{WP} \leq 2$ [15]) and the tuning of the PLL must deviate significantly from the original value [46]. Scenarios with tunings deviating more than 10 times the original value are considered to be improperly tuned in this thesis.

The sensitivity of the system to the grid strength is first analyzed in Figure 4.21 using the original PLL gains K_{pPLL}=15 and K_{iPLL}=45. Notice that the system is stable for both the Type-III and Type-IV wind park at all grid strengths as the trajectory of the eigenvalues do not encircle the (-1,0) point. This indicates that a properly tuned PLL is able to ensure a good stability margin at the NSR, even at grids with low short-circuit ratios.

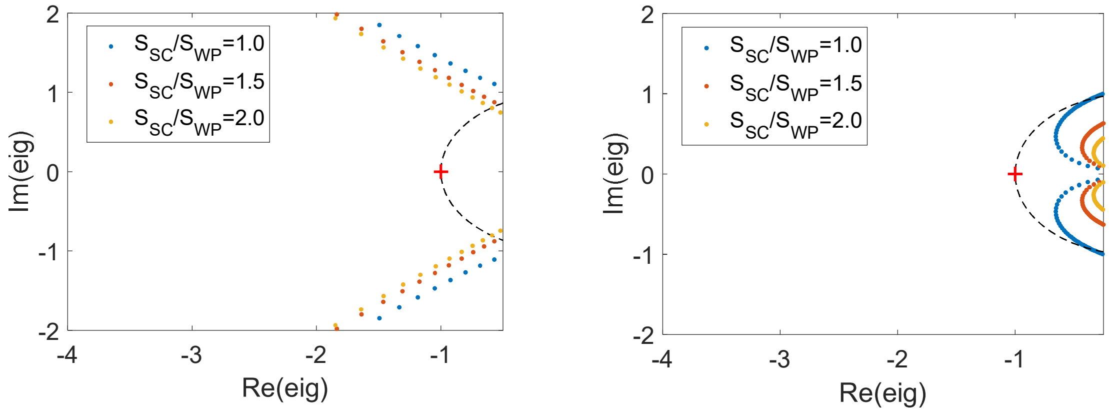

a) Type-III wind park **b) Type-IV wind park**

Figure 4.21: Stability at NSR, sensitivity to grid strength with adequate PLL tuning

Now, the grid strength is fixed at the largest of the short-circuit ratios from Figure 4.21, *i.e.*, S_{SC}/S_{WP} = 2, and the PLL tuning is changed. Notice that even though both wind parks remained stable for all tunings, the tuning with the lowest proportional gain was the closest to instability. According to the results in the Appendix D, the lower proportional gains provide less damping to the oscillations of the PLL output.

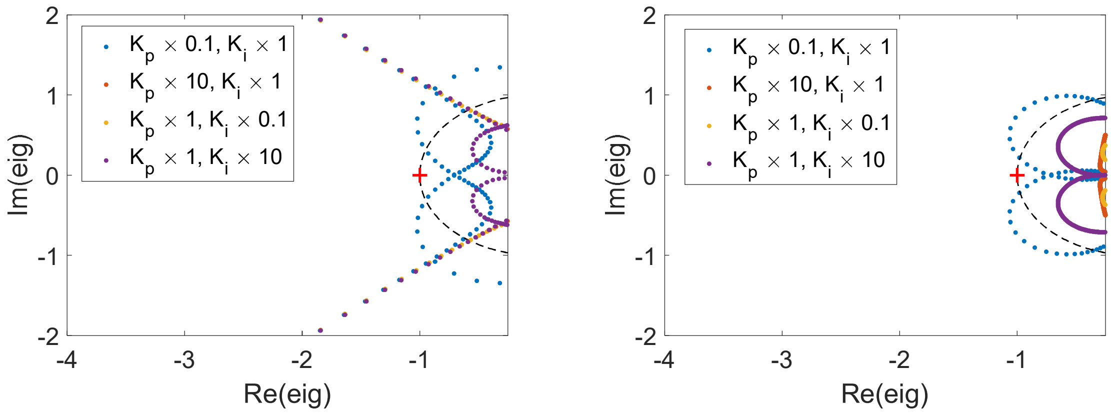

a) Type-III wind park **b) Type-IV wind park**

Figure 4.22: Stability at NSR, sensitivity at strong grid to PLL gains (K_{pPLL}, K_{iPLL})

Figure 4.23 presents the results of the same PLL tuning scenarios from Figure 4.22, but with a weaker grid, *i.e.*, S_{SC}/S_{WP} = 1. Notice that now both the Type-III and the Type-IV wind park became unstable for the tuning with the lowest proportional gain. Moreover, the tuning with the large integral gain also came close to making the Type-IV wind park unstable.

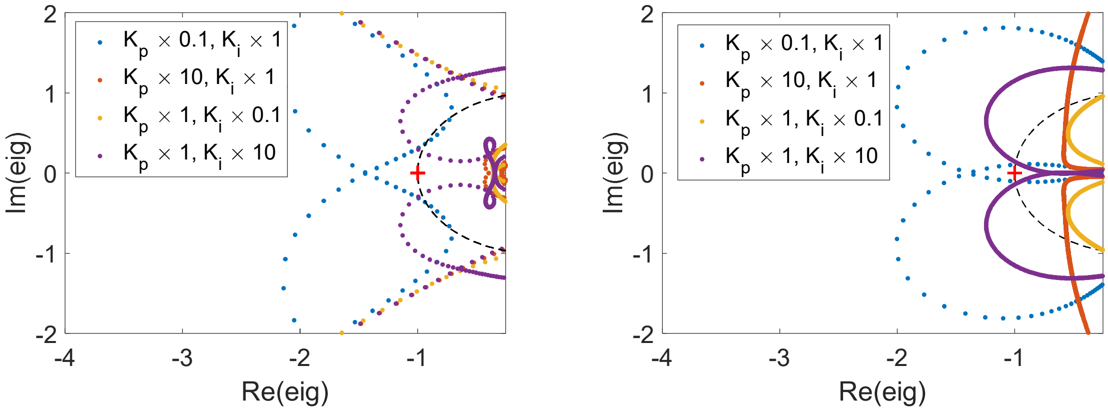

a) Type-III wind park **b) Type-IV wind park**

Figure 4.23: Stability at NSR, sensitivity at weak grid to PLL gains (K_{pPLL}, K_{iPLL})

For the remaining sensitivity studies in this subsection, the grid strength is fixed to S_{SC}/S_{WP} = 1.5, and the proportional gain of the PLL to K_{pPLL} = 3 (1/5 of the original value), for the system to be stable but close to its limit. Figure 4.24 studies the effect of series capacitors in the transmission system feeding the wind park. Only the Type-IV wind park results are shown since the Type-III wind park can easily become unstable at the SSR with very low capacitive compensation levels. Notice that connecting capacitors in series is analog to strengthening the grid, which in turn, increases the stability margin of the system.

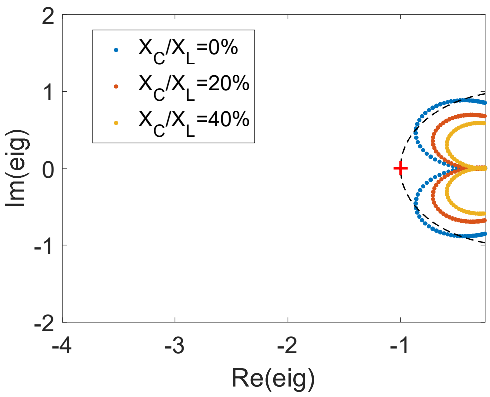

Figure 4.24: Stability at NSR, sensitivity to series capacitor, Type-IV wind park

Figure 4.25 presents the effect of the grid damping ratio on the stability at the NSR. A larger resistive component from the grid can also contribute to weakening the voltage at wind park PCC. Therefore, lower *X/R* ratios move the system closer to instability in the NSR.

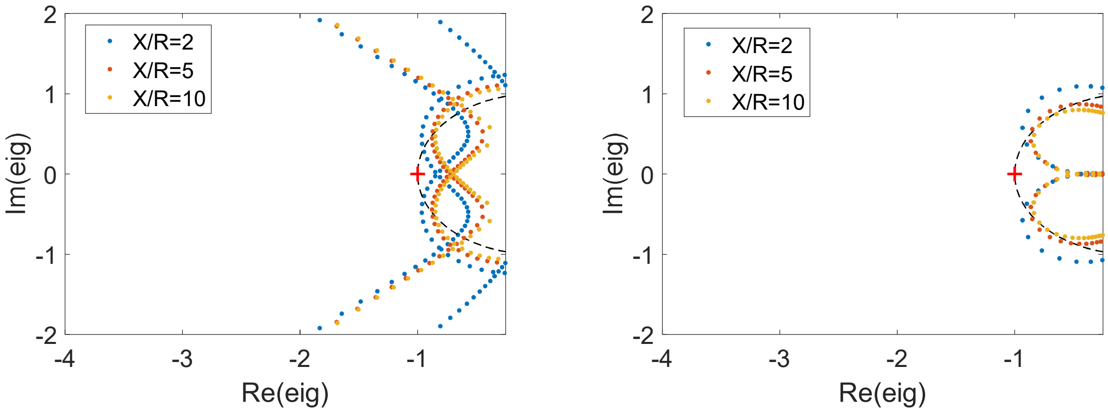

a) Type-III wind park **b) Type-IV wind park**

Figure 4.25: Stability at NSR, sensitivity to grid damping ratio

Consider the IEEE 14 buses transmission system in Figure 4.26 to study the influence of the grid topology on the stability at the NSR. The generator at bus 3 was replaced by 10 units of the wind park complex in Figure E.1 (the original complex has a rated capacity of 64 MVA, so the total installed capacity in this test is 640 MVA). With this change, the wind park sees an equivalent short-circuit ratio at PCC of $S_{SC}/S_{WP} = 2.71$. Both the Type-III and the Type-IV wind parks are stable at this condition.

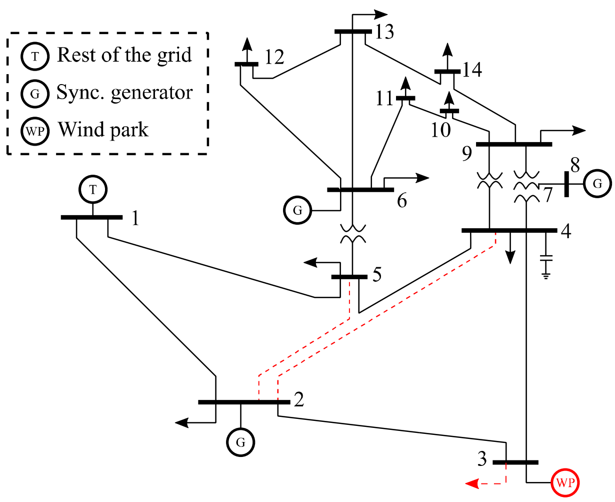

Figure 4.26: Modified IEEE 14 buses test system for grid topology analysis at NSR

Now consider the grid reconfiguration scenarios in Figure 4.27. If the lines between buses 2-4 and 2-5 are disconnected, the short-circuit ratio at wind park PCC drops to S_{SC}/S_{WP} = 2.22. Although the system is weakened, both the Type-III and Type-IV wind parks remain stable. However, without the load at bus 3, the short-circuit ratio drops even further to a value of S_{SC}/S_{WP} = 1.44, where the Type-III wind park becomes unstable at the NSR, but the Type-IV remains stable although closer to its limit.

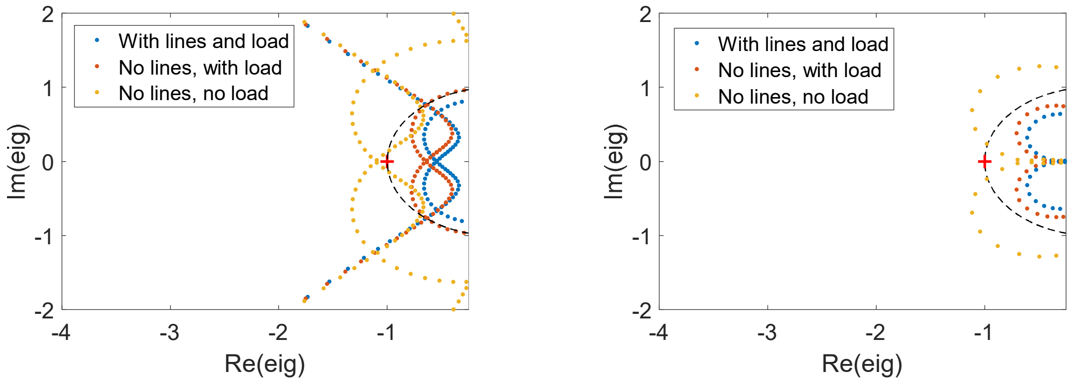

a) Type-III wind park **b) Type-IV wind park**

Figure 4.27: Stability at NSR, sensitivity to grid topology

Now, the variables of the wind park are studied. Figure 4.28 presents the effect on the stability at the NSR, of the wind park feeder type, underground (ug) and overhead (oh), and their length. For all tests, the system remained stable since the feeders are short, and the frequency of the studied range is not high, so their impedances can be neglected and the stability at the NSR is not affected significantly. Nevertheless, the tendency shows that longer feeders reduce the stability margin as the grid equivalent seen by each generator is weaker.

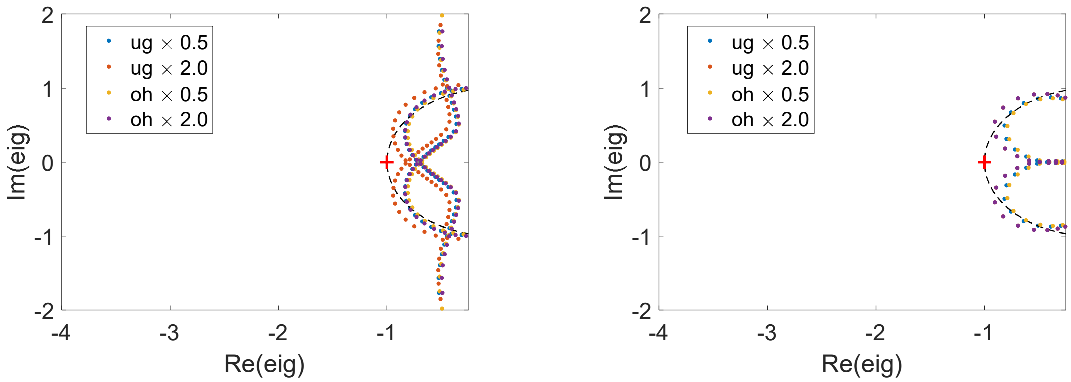

a) Type-III wind park **b) Type-IV wind park**

Figure 4.28: Stability at NSR, sensitivity to wind park feeder type and length

Figure 4.29 presents the sensitivity of the stability at the NSR to the size of the shunt capacitor bank of the wind park. The larger capacitors raise the voltage of the wind park feeders, so the generators have to absorb more reactive power to meet their terminal voltage setpoint. The impedance of Type-IV wind generators is more heavily influenced by the operational point, and the higher reactive power absorption changes their impedance so the system becomes more easily unstable. The opposite occurs for Type-III wind parks, where larger capacitor banks increase the stability margin as the generator impedance is dominated by the induction machine.

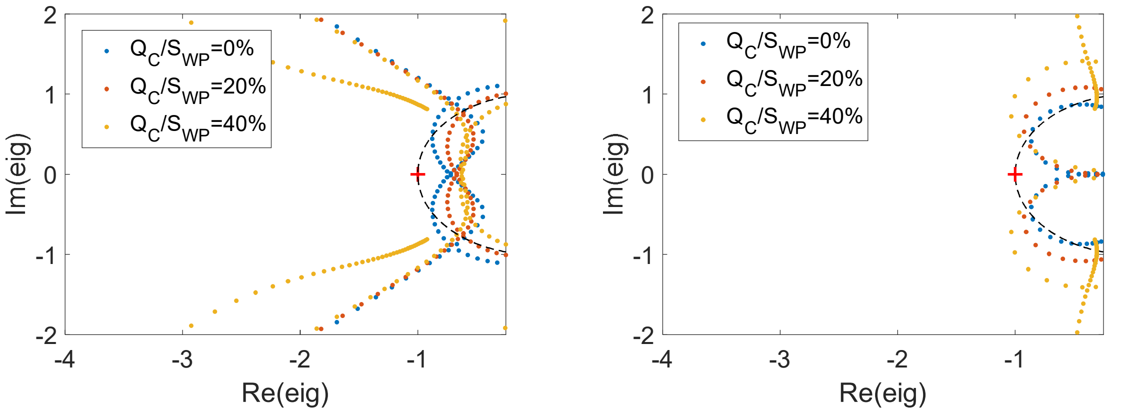

a) Type-III wind park **b) Type-IV wind park**

Figure 4.29: Stability at NSR, sensitivity to wind park shunt capacitor bank

Figure 4.30 presents the sensitivity to the main transformer impedance. Increasing this impedance's value is analog to weakening the grid equivalent seen by the generators, so higher impedances facilitate the system to instability in the NSR, for both types of wind parks.

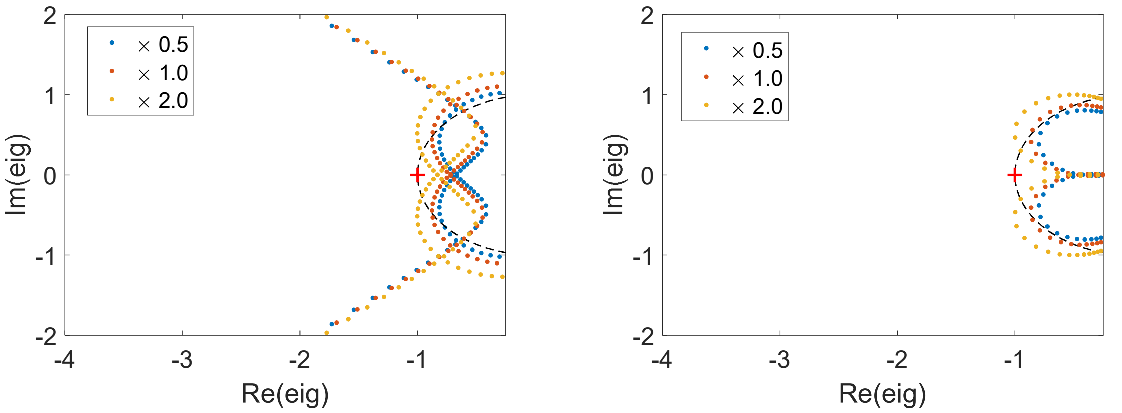

a) Type-III wind park **b) Type-IV wind park**

Figure 4.30: Stability at NSR, sensitivity to wind park main transformer impedance

The effect of the generator outages is shown in Figure 4.31. The disconnection of generators is analog to increasing the short-circuit ratio S_{SC}/S_{WP} of the wind park at PCC, so that the more disconnections, the less risk of unstable control oscillations in the NSR.

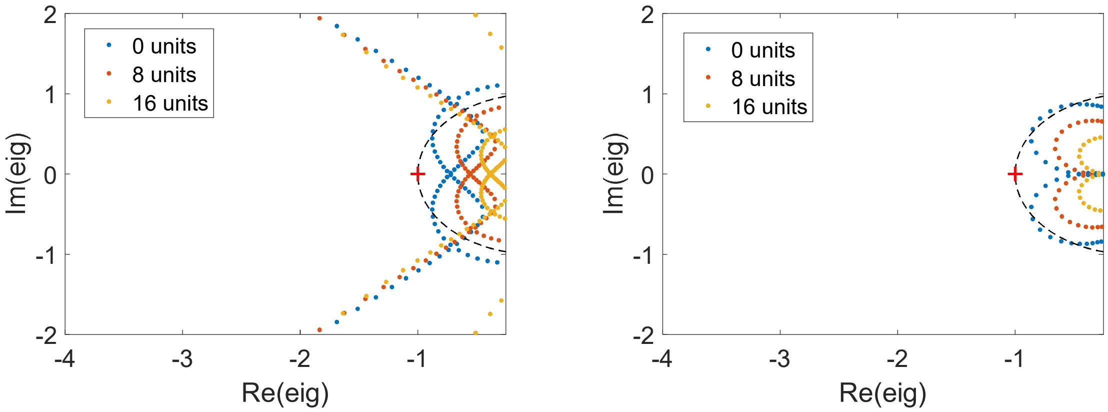

a) Type-III wind park **b) Type-IV wind park**

Figure 4.31: Stability at NSR, sensitivity to wind park generator outages

Now, the variables of the generator are studied as follows. Figure 4.32 demonstrates the front-end filter topology has no significant impact on the stability at NSR (recall the L filter is derived from the LCL filter, but without the shunt capacitor). This occurs because the impedance resulting from the LCL filter capacitor, near synchronous frequency can be considered an open circuit in this range of frequencies.

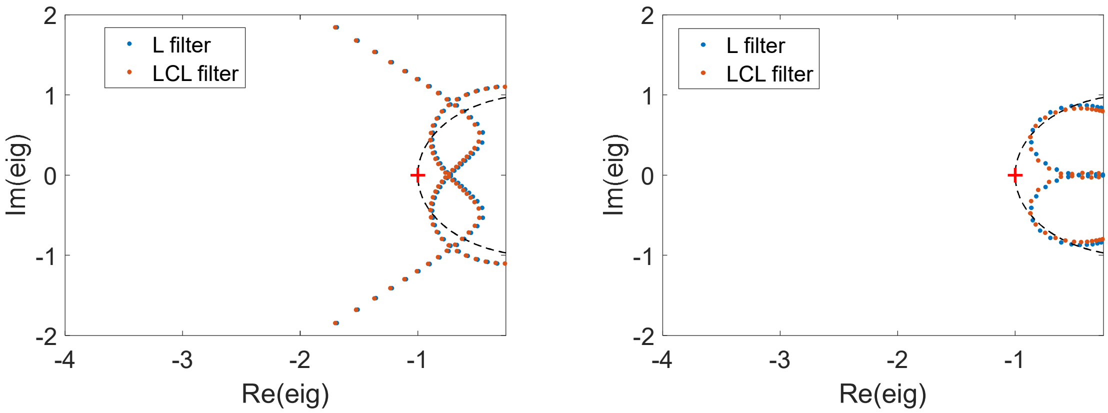

a) Type-III wind park **b) Type-IV wind park**

Figure 4.32: Stability at NSR, sensitivity to front-end filter of the GSC

The effect of the active power setpoint of the generators is shown in Figure 4.33. Notice that the system has a higher risk of unstable oscillations in the NSR with higher power injections.

This happens predominantly due to the changes on generator impedance resulting from the slip of the induction machine (Type-III) and the setpoint of the controllers (Type-IV).

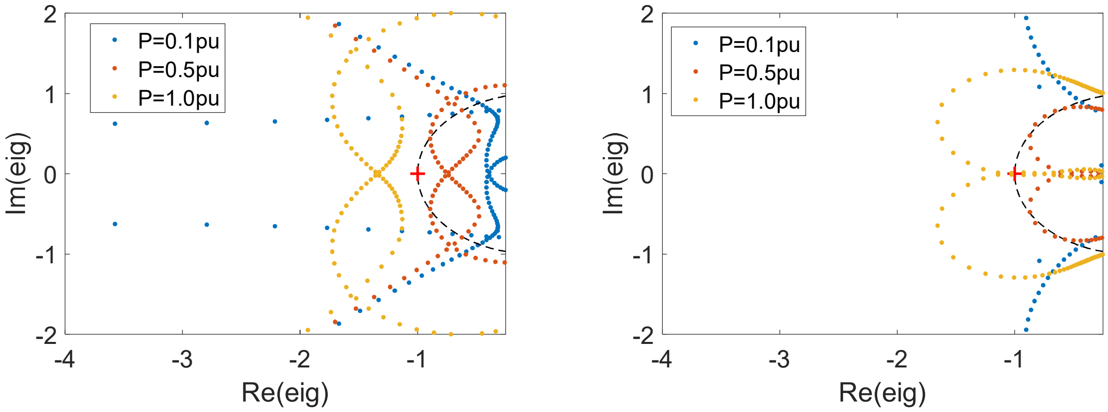

a) Type-III wind park **b) Type-IV wind park**

Figure 4.33: Stability at NSR, sensitivity to active power injection

The effect of the terminal voltage setpoint of the generators is shown in Figure 4.34. Notice that similar to the shunt capacitor bank results, the lower voltages require reactive power absorption and can increase the risk of instability, whereas the higher voltages can reduce it.

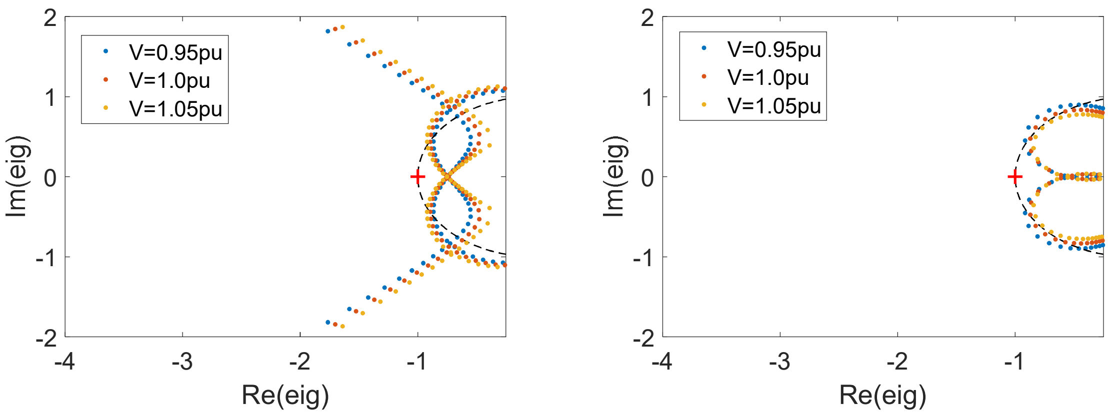

a) Type-III wind park **b) Type-IV wind park**

Figure 4.34: Stability at NSR, sensitivity to terminal voltage

Finally, the control gains of the GSC current control loop are analyzed in Figure 4.35, and the gains of the DC bus voltage control loop in Figure 4.36, respectively. Although the PLL control gains were analyzed in the beginning of this subsection, these other loops also demonstrated a relevant MAS index in the studies of Chapter 2. Notice that in presence of a poorly tuned PLL and a weak grid, the lower proportional gains of the current control can lead to instability, whereas higher values increase the stability margin, in both Type-III and Type-IV wind parks. As for the DC bus voltage control loop gains, the Type-III generator is more sensitive, where the higher proportional gains can lead to instability in the NSR. These results confirm the claims in the literature that all of these control subsystems participate in the oscillation stability at the NSR, *i.e.*, weak grid oscillations [3], [46]. However, as shown by the sensitivity studies in this subsection, these oscillations are only possible in a practical wind park topology with improperly tuned and non-robust PLLs.

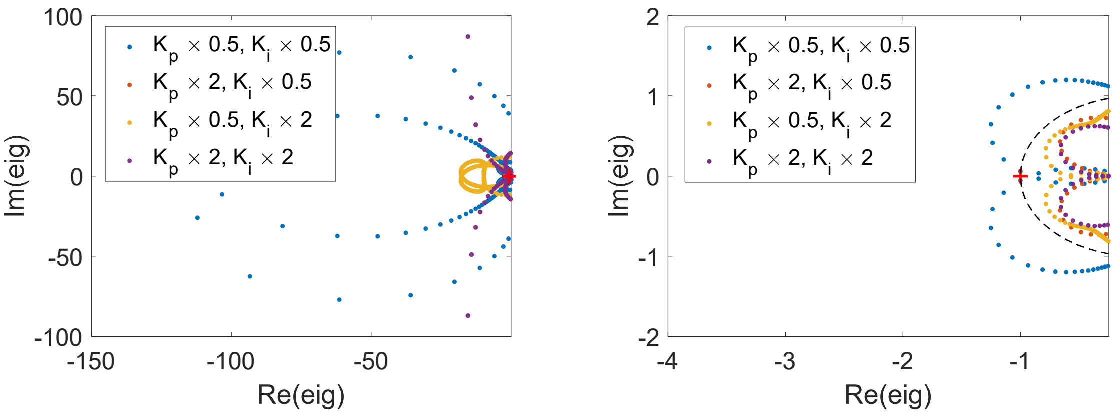

a) Type-III wind park **b) Type-IV wind park**

Figure 4.35: Stability at NSR, sensitivity to current control loop gains (K_{pGSC}, K_{iGSC})

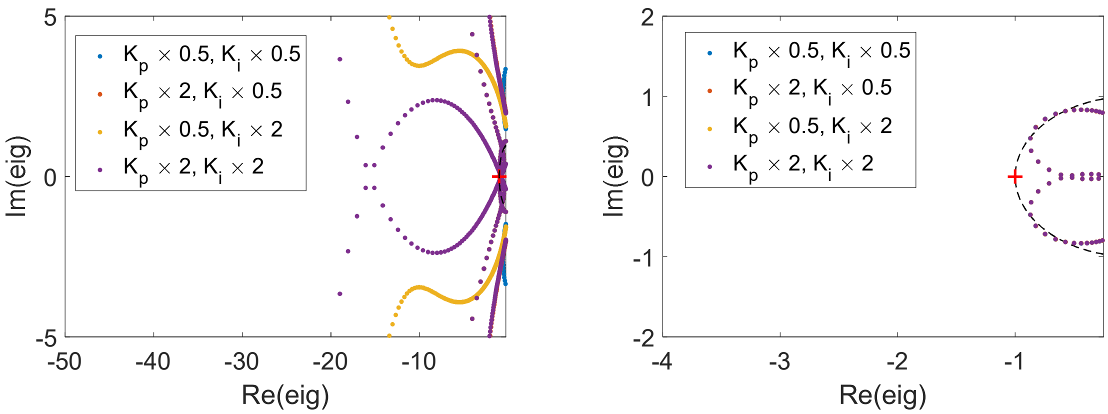

a) Type-III wind park **b) Type-IV wind park**

Figure 4.36: Stability at NSR, sensitivity to DC voltage control loop gains (K_{pdc}, K_{idc})

4.3.3 Harmonic frequency range

The “Sum of impedances” criterion is used to present the results in this subsection. Although instability in the HFR is difficult to achieve under practical conditions (*i.e.*, with a real wind park topology and properly tuned generators), it is possible at least in theory for both Type-III and Type-IV wind parks if the shunt capacitor bank produces a resonance frequency in the range of typical grid harmonics (f < 1500 Hz), where the wind generator controllers provide negative damping as shown in Figure 2.13. However, this instability also requires very low active power injections (Type-IV wind parks), or the absence of all other circuit capacitances (feeder capacitive effect, and the capacitor of the generator's filter).

To demonstrate the previous affirmations, first notice in Figure 4.37 that the resonance frequencies due to the shunt capacitor bank range from 120 Hz to 500 Hz in the practical circuit (for the largest capacitor bank Q_C/S_{WP} = 50% and the smallest Q_C/S_{WP} = 10%, respectively), which confirms that resonance of the shunt capacitor bank is indeed possible in the range of negative damping of the generators. The capacitor bank size does not affect the damping but defines the resonance frequency. Notice that the smaller capacitor banks are closer to the point of lowest damping, which is located before the point of resonance of the LCL filter of the generators. Therefore, although all capacitor banks in this test are stable as the damping is always positive, the smaller banks have a higher risk of instability than the larger banks. For the remaining of the tests in this subsection, the capacitor bank was fixed to Q_C/S_{WP} = 10%.

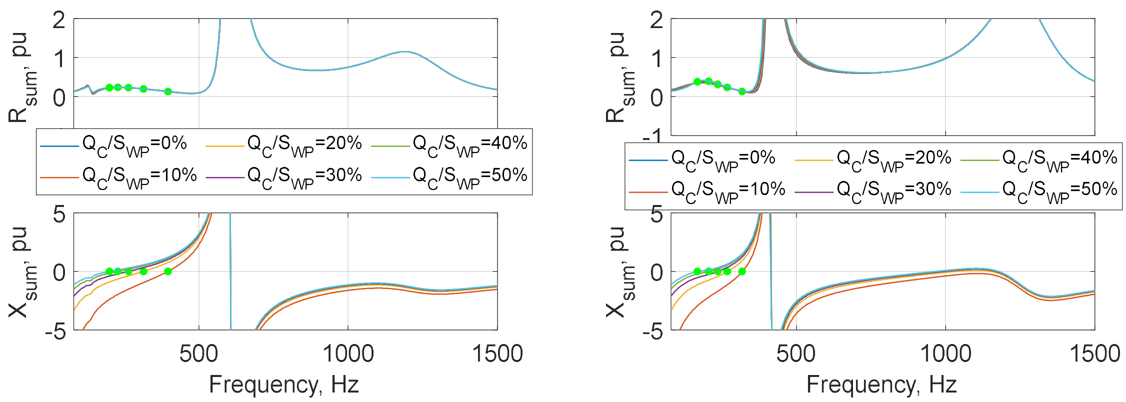

a) Type-III wind park **b) Type-IV wind park**

Figure 4.37: Stability at HFR, sensitivity to shunt capacitor size

Figure 4.38 was built to show the effect on the stability at the HFR of the grid strength and the damping ratio. Notice that the stronger grid provides less damping and higher resonance frequencies. Their equivalent resistance is lower as it is closer to the resonance of the front-end filters so it increases the risk of instability, whereas the weaker grid has a higher damping that reduces the risk of instability. Then again, all tested configurations remained stable. Changes in the grid damping ratio did not show significant impact on the results.

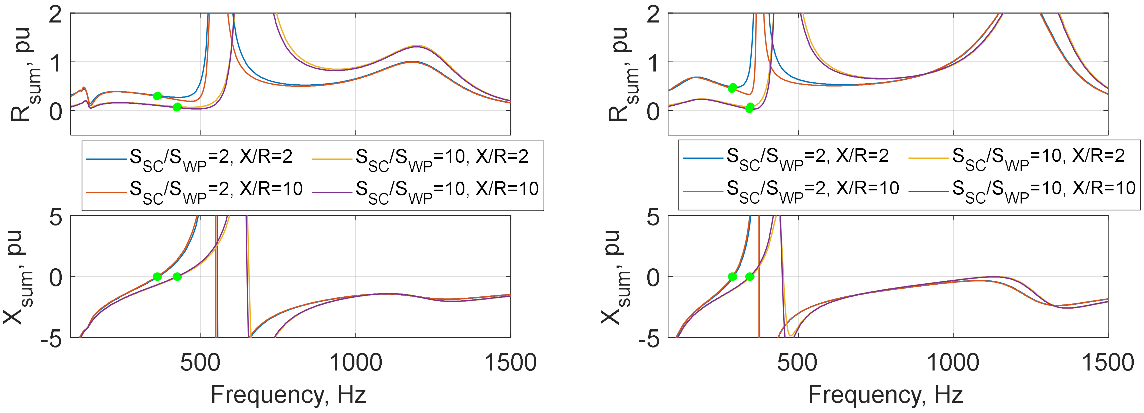

a) Type-III wind park **b) Type-IV wind park**

Figure 4.38: Stability at HFR, sensitivity to grid strength and damping ratio

The series capacitive compensation effect on the stability at the HFR is shown in Figure 4.39, however, only the results of the Type-IV wind park are shown since very low series compensation levels are able to produce unstable resonance in the SSR with Type-III wind parks. The grid was fixed to S_{SC}/S_{WP} = 5. Notice this characteristic of the grid equivalent has no impact on the stability at the HFR which is expected as capacitors at high frequencies have a very low impedance.

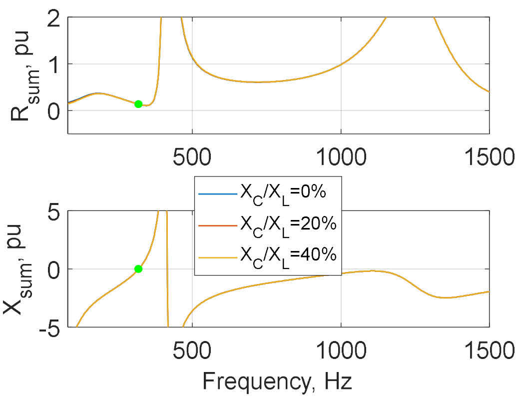

Figure 4.39: Stability at HFR, sensitivity to series capacitor, Type-IV wind park

Now, in order to evaluate the impedance profile of the grid equivalent, consider the circuit in Figure 4.40, which corresponds to a modified version of the IEEE 14 buses test system. The transmission lines highlighted in blue model their capacitive effect which is relevant at the HFR.

Two tests are conducted with the system to evaluate the possibility of unstable resonance at the HFR with shunt capacitors inside and outside the wind park:

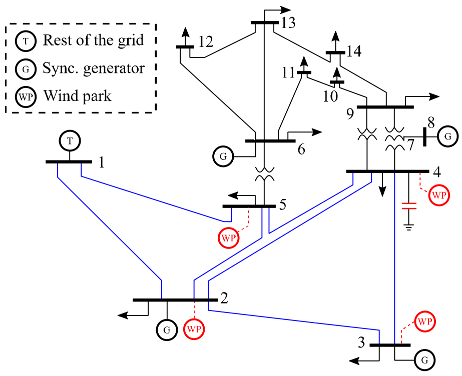

Figure 4.40: Modified IEEE 14 buses test system for grid topology analysis at HFR

1) Inside the wind park: Ten units of a 64 MVA wind park complex (640 MVA wind park) are connected at bus 2, then moved to bus 3, bus 4 and bus 5. The shunt capacitor bank at medium voltage of the wind parks is fixed to Q_C/S_{WP}=10%.
2) Outside the wind park: Ten units of a 64 MVA wind park complex (640 MVA wind park) without shunt capacitor bank at medium voltage are connected at bus 4, which already has a shunt capacitor at high voltage. Then, the size of the capacitor is changed to evaluate different compensation levels.

Figure 4.41 presents the results for test 1) with several locations of the wind park. The resulting short-circuit ratios are S_{SC}/S_{WP} =10 (Bus 2), S_{SC}/S_{WP} =2.7 (Bus 3), S_{SC}/S_{WP} =8.5 (Bus 4), and S_{SC}/S_{WP}=14.9 (Bus 5). Notice that even though most short-circuit ratios are high and provide lower damping than a lower short-circuit ratio, the wind parks remained stable. The effect of the capacitances of the transmission lines becomes more relevant at frequencies beyond 1 kHz.

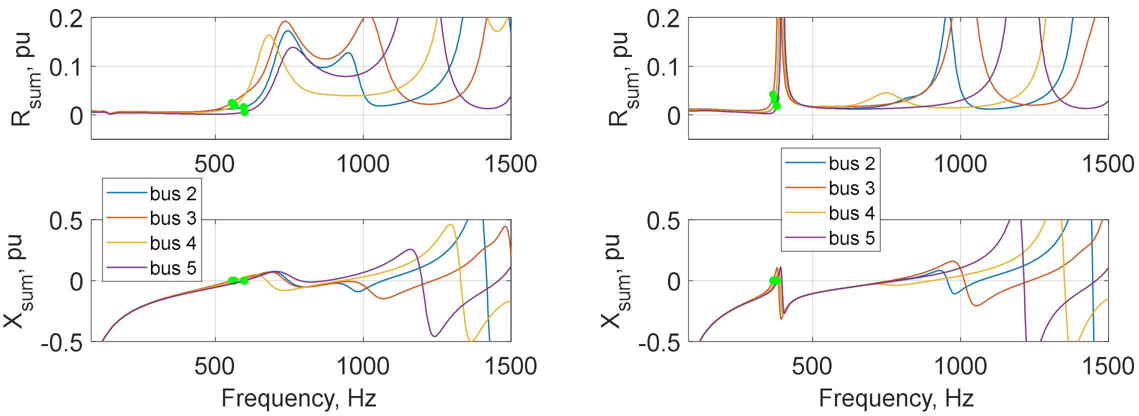

a) Type-III wind park b) Type-IV wind park

Figure 4.41: Stability at HFR, sensitivity to grid impedance profile, test 1

Figure 4.42 presents the results from test 2. Notice that the capacitor bank at bus 4 was modified to provide the reactive power compensation ratio required by the wind park complex. Here, the damping observed by the capacitor is even more positive than when the capacitor is placed at the MV bus, because of the decoupling effect of the wind park's main transformer impedance, which is rather large. All scenarios are stable at the HFR.

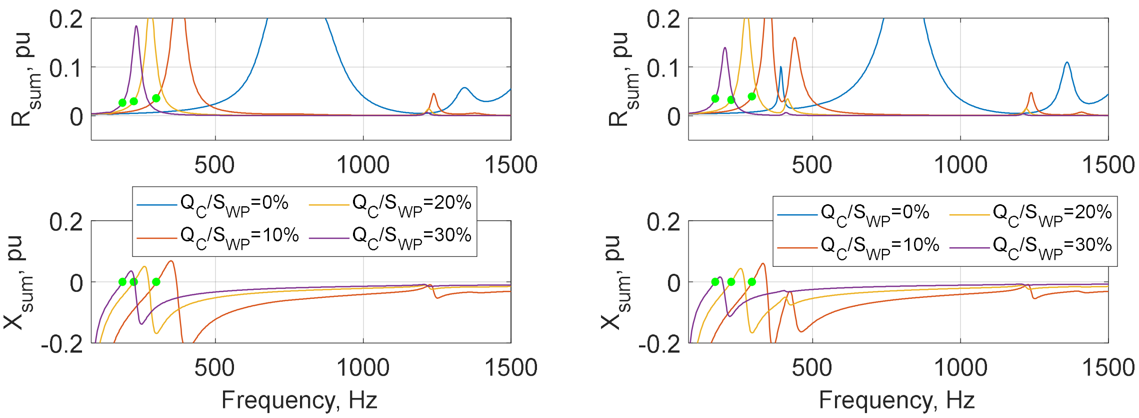

a) Type-III wind park b) Type-IV wind park

Figure 4.42: Stability at HFR, sensitivity to grid impedance profile, test 2

Moving on to the wind park variables, Figure 4.43 presents the effect of the main transformer impedance. Notice there is no significant impact, although larger impedance values reduce the risk of instability, analog to the higher impedance from weaker grids.

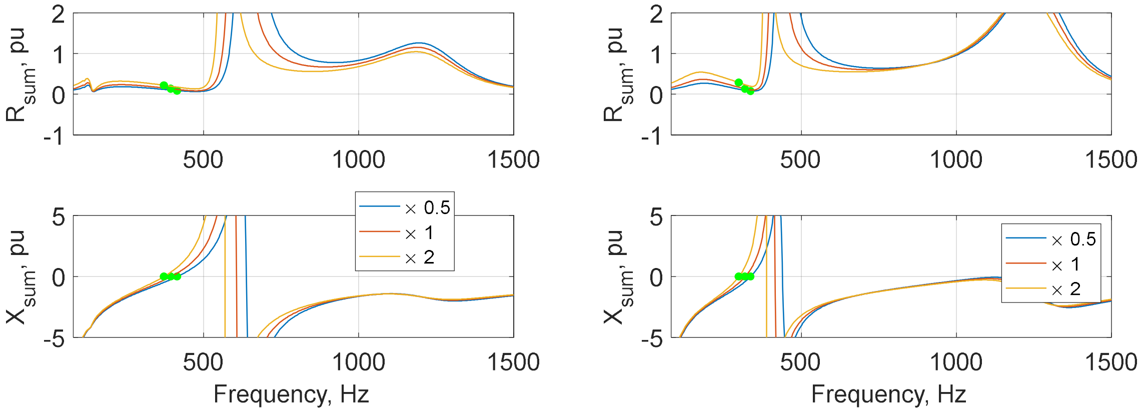

a) Type-III wind park **b) Type-IV wind park**

Figure 4.43: Stability at HFR, sensitivity to main transformer impedance

And Figure 4.44 shows that disconnecting generators has no significant impact on the stability at the HFR, but it provides a slight reduction of the negative damping.

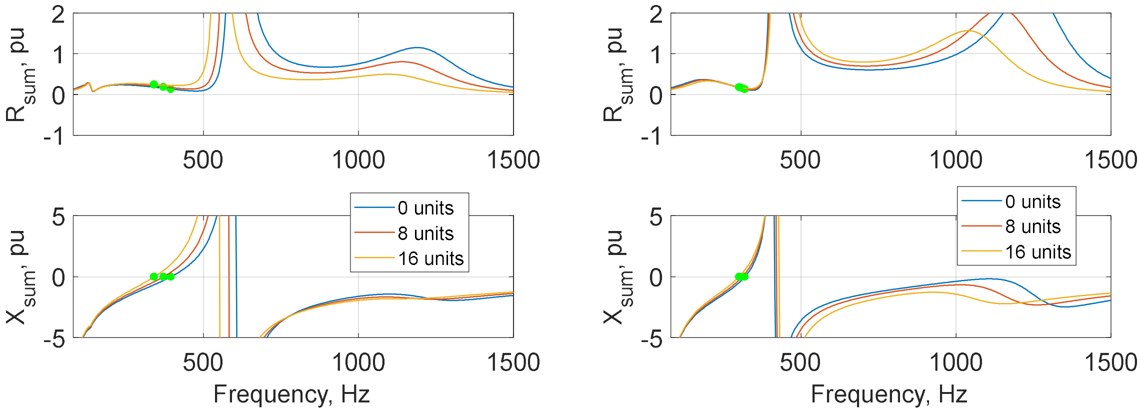

a) Type-III wind park **b) Type-IV wind park**

Figure 4.44: Stability at HFR, sensitivity to generator outages

The previous tests evidence the difficulty of inducing unstable oscillations at the HFR in a practical wind park as the overall damping is positive. To force the instability, as mentioned at the beginning of this subsection, the capacitances of the wind park have to be eliminated. Figure 4.45 was built to demonstrate this for a 64 MVA wind park with a shunt capacitor bank of Q_C/S_{WP} = 10% and a grid of S_{SC}/S_{WP} =5. Notice that the only scenario which resulted in instability is the one with overhead feeders and L front-end filter, *i.e.*, without capacitances.

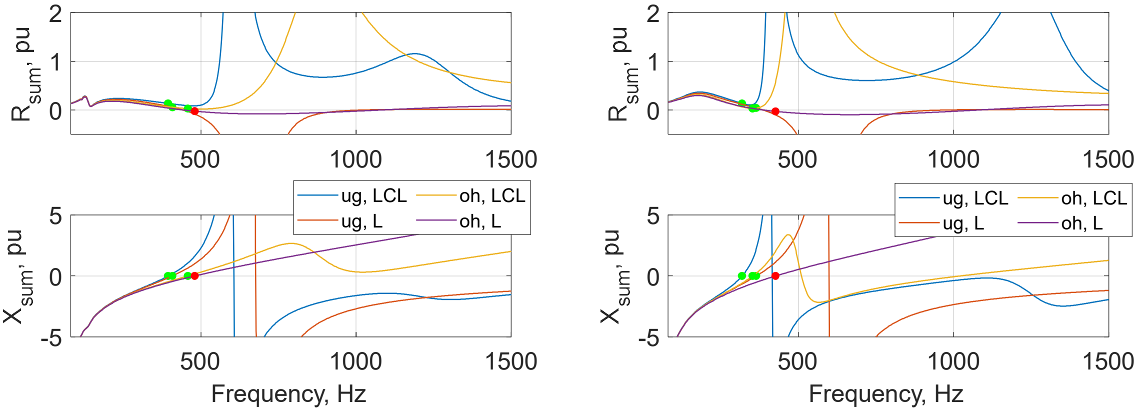

a) Type-III wind park b) Type-IV wind park

Figure 4.45: Stability at HFR, sensitivity to feeder type and front-end filter

On-shore practical wind parks are more commonly designed with underground feeders, and additionally, the most common wind generator topology for the front-end filter used to damp switching harmonics is the LCL topology. These circuit conditions required for instability at the HFR are unlikely to occur in the field and can be avoided by a robust control design.

Next, the variables of the generator are studied. The active power injection results are shown in Figure 4.46 and from the terminal voltage in Figure 4.47. Notice that lower power injections slightly increase the risk of instability as the setpoint has an effect on the generator impedance. The *P*=0.1 pu power injection value was able to create a negative damping region which led to instability for the Type-IV wind park. On the other hand, the terminal voltage had no significant effect on the stability at the HFR.

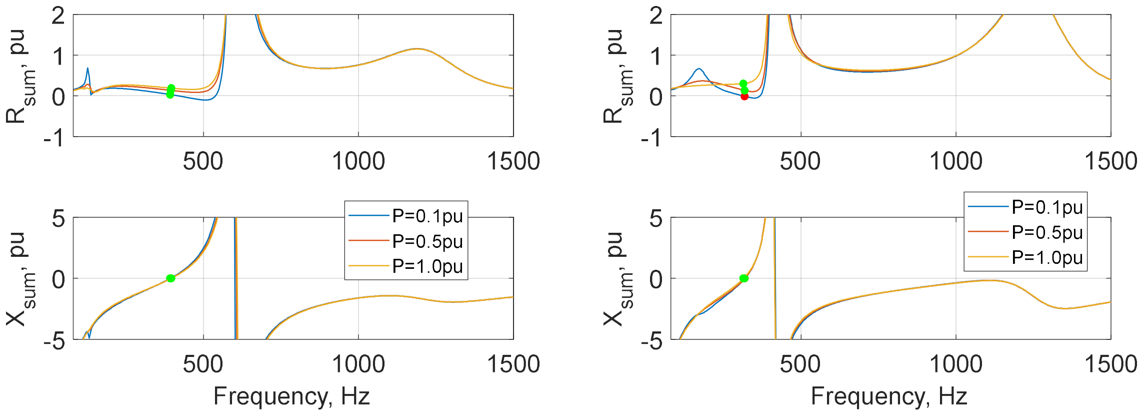

a) Type-III wind park b) Type-IV wind park

Figure 4.46: Stability at HFR, sensitivity to active power injection

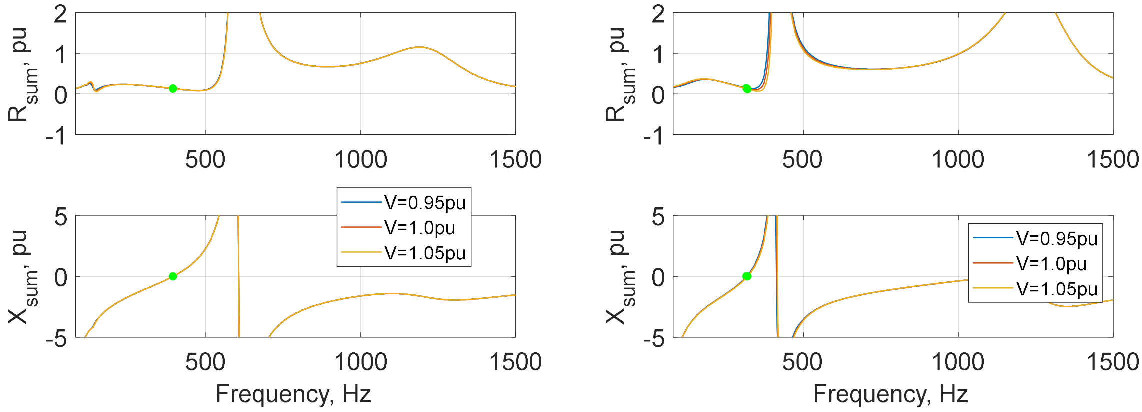

a) Type-III wind park b) Type-IV wind park

Figure 4.47: Stability at HFR, sensitivity to terminal voltage

As this instability is difficult to achieve, the controllers of the generators are also studied. Figure 4.48 evaluates the effect on the stability at the HFR of the delay produced by the controllers and by the measurement filter. As expected, eliminating these delays slightly improves the damping at the HFR, which reduces the risk of instability.

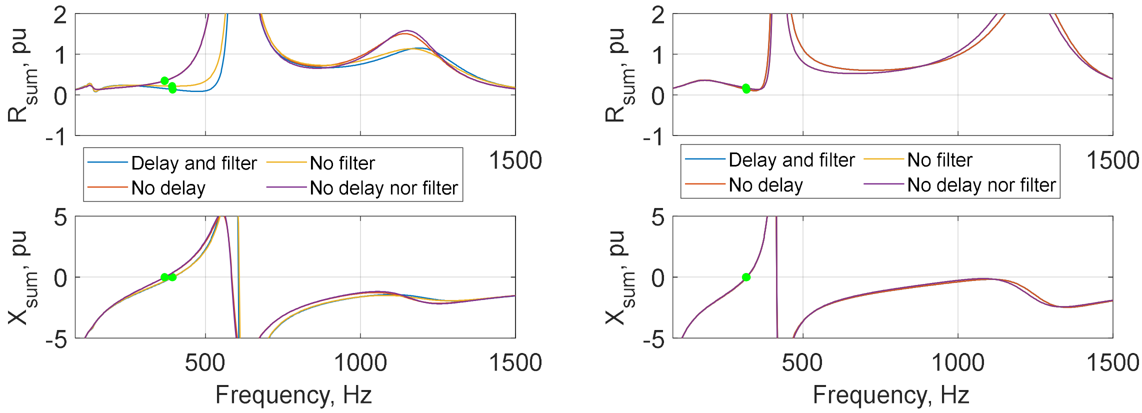

a) Type-III wind park b) Type-IV wind park

Figure 4.48: Stability at HFR, sensitivity to control delays

Figure 4.49 presents the effect of different tunings on the current control loop of the GSC. The proportional gain has a higher influence than the integral, and this is more visible for the Type IV generator whose equivalent impedance is directly provided by the GSC controller impedance, where higher proportional gains led to a negative damping region, but all tested scenarios remained stable.

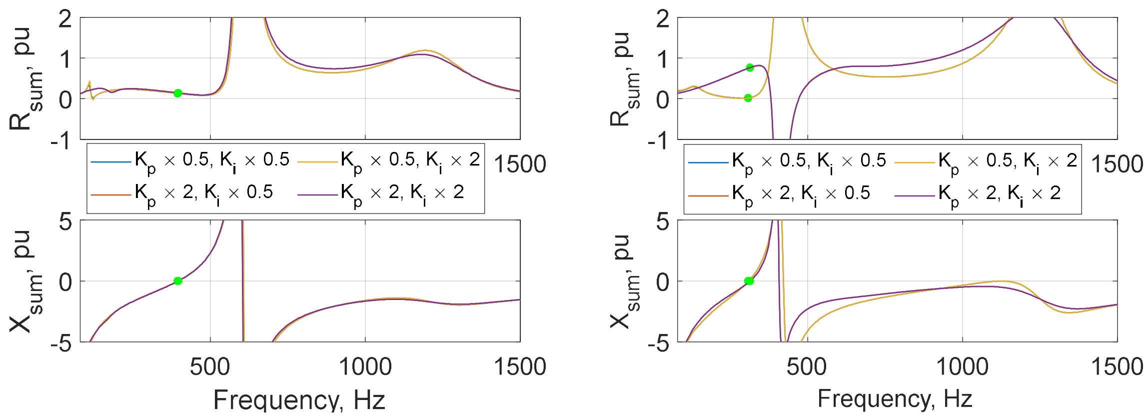

a) Type-III wind park **b) Type-IV wind park**

Figure 4.49: Stability at HFR, sensitivity to current control loop gains (K_{pGSC}, K_{iGSC})

And the effect of the gains of the DC bus voltage control are evaluated in Figure 4.50. Again, the Type-IV wind park is more affected than the Type-III. The higher proportional gains of the DC bus controller were also able to produce a negative damping region in the Type IV wind park, but as in the current control case, all scenarios remained stable.

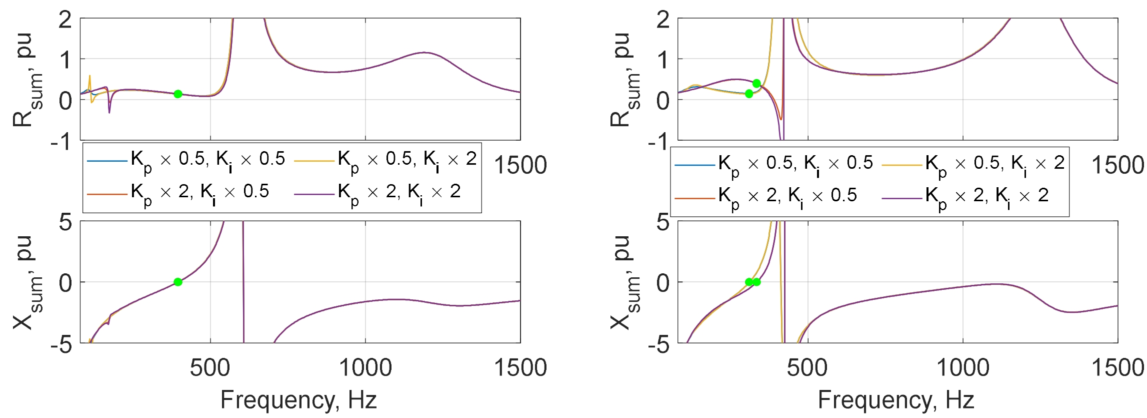

a) Type-III wind park **b) Type-IV wind park**

Figure 4.50: Stability at HFR, sensitivity to DC voltage control loop gains (K_{pdc}, K_{idc})

4.3.4 Summary of necessary conditions for unstable resonance

The conditions for unstable resonance to occur at each range of frequency are summarized in Table 4.2, based on the results the sensitivity studies in sections 4.3.1, 4.3.2 and 4.3.3. The most important characteristics to achieve the instabilities are highlighted in bold font.

The last row of Table 4.2 presents a qualitative designation of the risk for the instabilities to occur in a practical circuit based on the experiences collected from the studies, which matches the reports of instability in the literature. The risk designation is further detailed as follows:

1) Moderate-high risk in the SSR: Wind parks are frequently built at remote locations with dedicated and long transmission lines. These transmission lines may have series capacitors to increase the power transfer capability, and grid reconfigurations (line outages) can lead to radial connection between Type-III wind parks and a transmission line with a series capacitor, which in turn, results in unstable sub-synchronous oscillations. Other factors that increase the risk are the capacity factor of wind parks which is typically low (around 30%, *i.e.*, low power injection), the Type-III generators being the most common technology in the field, and the possibility to occur at any grid strength and control gains setting (without built-in mitigation).
2) Low-moderate risk in the NSR: Weak grid oscillations can arise in both Type-III and Type-IV wind parks if the proportional gain of the PLL is low and the integral gain is high. However, properly tuned PLLs are able to effectively shield the wind park at very weak grids. Other factors that increase the risk of instability are high power injections and low terminal voltages which reduce the stiffness of the terminal voltage that the generators use to synchronize to the grid. Certain tunings of the DC bus voltage controller and the current controller of the GSC are also able to participate in the weak grid oscillations if not properly tuned.
3) Very low risk in the HFR: Shunt capacitor banks for power factor correction of the wind park are able to resonate below 1.5 kHz. This resonance can become unstable in both Type-III and Type-IV wind parks if the capacitances of the wind park feeders are low and if the front-end filters of the generators have no capacitor. However, this condition is unlikely as LCL filters are the most common topology in wind generators, and wind park feeders are typically underground, which have a considerable capacitive effect. Unlike the stability at SSR and NSR, the stability at the HFR is not a system scale phenomenon as the origin of resonance is located inside the wind park. Other factors that can increase the risk of instability are low active power injections, and high gains of the GSC current control and the DC bus voltage control.

Table 4.2: Conditions that create risk of unstable resonance in practical wind parks

Range	Sub-synchronous	Near synchronous	Harmonic frequency
Origin of resonance	**Grid HV series capacitor**	Wind generators	**Wind park MV shunt capacitor**
Type of generator	Type-III	Type-III, Type-IV	Type-III, Type-IV
Grid topology	**Radial**	Any	Any
Grid strength	Any	**Weak**	More risk at stronger grids
Control gains	More risk with: - GSC current (high proportional) - DC bus (high proportional, high integral)	**More risk with: - PLL gains (low proportional, high integral) - GSC current (low proportional) - DC bus (high proportional)**	More risk with: - GSC current (high proportional) - DC bus (high proportional, high integral)
Active power injection / wind	**More risk at low power / wind**	**More risk at high power / wind**	**Slightly higher risk at low power / wind**
Terminal voltage	Any	More risk at low voltage	Any
Other	-	-	**Absence of MV feeder capacitance and front-end filter capacitor**
Unstable resonance risk	**Moderate - high**	**Low - moderate**	**Very low**

4.4 Graphical approach for sub-synchronous resonance assessment

Although series capacitor banks near wind park facilities are very rare in Brazil, this is not the case in other countries such as the United States and China. From the analysis in Section 4.3, and from the literature review on event reports presented in Subsection 1.1.2, it can be seen that the most concerning type of instability in practical wind parks is at the sub-synchronous range due to Type-III wind parks being fed radially by series capacitors. The risk of these unstable sub-synchronous oscillations (SSO) is commonly assessed by utilities with EMT simulation after a topology search, which can be a time-consuming process. However, not all operating scenarios present risk of SSO and require such a detailed investigation. This section proposes two charts based on impedance equivalents of wind generators obtained through frequency scans to map the combinations of parameters leading to unstable SSOs. With the information, engineers can immediately filter out scenarios with no risk of instability and conduct detailed studies on fewer scenarios that are truly critical. These charts are obtained with simple equations that use only information readily available in practice, without the need to run repetitive computer simulations. The charts also reveal the key operating conditions that can increase the risk of an unstable SSO and provide real-time quantitative insights into how close a wind park is to an instability. Application examples are provided to illustrate how this approach can help engineers speed up studies to identify the risk of SSO.

4.4.1 Method for screening of unstable SSO

Transmission grids are typically meshed and can have several series capacitors, but unstable SSOs arises only when the circuit can be represented by the configuration shown in Figure 4.51, *i.e.*, when a Type-III wind park is connected to the rest of the grid through a one specific series compensated transmission line, which may occur both on normal operation [21] and because of contingencies [91].

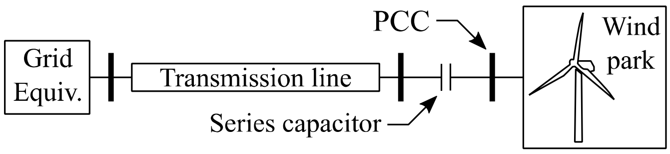

Figure 4.51: Wind park radially connected to series compensated line

As shown in Section 4.3.1, the sub-synchronous resonance created by the interaction between the series capacitor and the rest of the circuit is unstable if the negative damping from the Type-III generators overcomes the damping provided by the rest of the circuit. One can apply this criterion to a real transmission network by considering the contingencies that result in the topology of one series capacitor radially connected to the wind park under study.

4.4.1.1 Predictive, offline analysis

Two charts are presented in Figure 4.52 to help engineers further narrow down the critical scenarios that must be investigated in detail after detecting the problematic radial configuration. The first chart in Figure 4.52 a) consists of two curves that divide the S_{SC+lin}/S_{WP} vs. X_C/X_L plane in three regions (S_{SC+lin} is the combined short-circuit capacity of the grid equivalent and the transmission line without the series capacitor, at the PCC of the wind park; S_{WP} is the rated capacity of the wind park; and X_C/X_L is the capacitive reactance to inductive reactance ratio of the transmission line). All scenarios in the region below the lower boundary curve (red line) have no risk of unstable SSO regardless of the active power injected by the park P_{inj} and, therefore, can be neglected without any further analysis. On the other hand, combinations above the upper boundary curve (blue line) have an unstable SSO regardless of P_{inj} and a more detailed investigation must be conducted to analyze these instabilities. Finally, for scenarios between both boundary curves, the outcome on whether the system is unstable depends on the active power injection P_{inj}. The second chart shown in Figure 4.52 b) must be analyzed in this case, where if the operating condition is below the boundary curve, the system is stable and no further analysis is necessary. However, if the operating condition is above the boundary, the system will have an unstable SSO. A detailed investigation must be performed in this latter case.

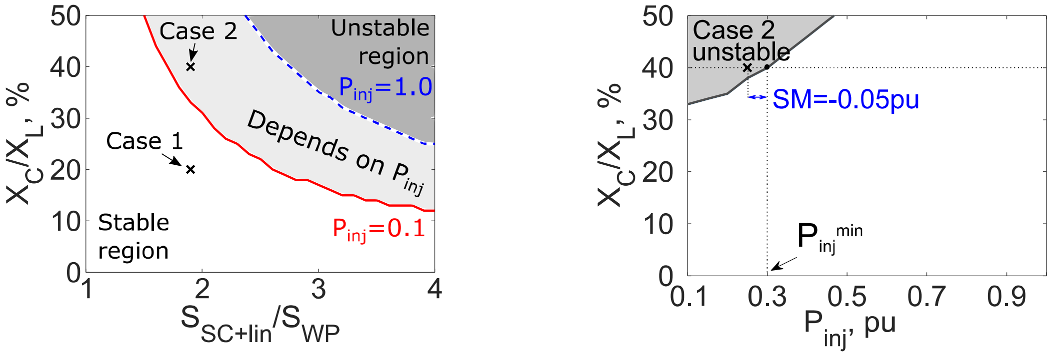

a) Capacity chart **b) Power injection chart**

Figure 4.52: Charts for predictive SSO screening

To illustrate the charts usage, one may consider the example shown in Figure 4.51, where the short-circuit level at the PCC without the series capacitor is 380 MVA, the transmission line has two stages of series compensation level ($X_C/X_L = 20\%$ and $X_C/X_L = 40\%$), and a 200 MVA wind park is to be connected at the PCC. This circuit is plotted in Figure 4.52 a) where Case 1 and Case 2 represent the cases with $X_C/X_L = 20\%$ and $X_C/X_L = 40\%$ compensation, respectively. Case 1 is in the safe region and no instability is expected in this case. Case 2 is in the region where instabilities can occur depending on the active power injection of the park. According to Figure 4.52 b), Case 2 will remain stable if power injection is above 0.3 pu. Otherwise, an instability will emerge, and a detailed analysis is recommended to investigate this scenario.

In summary, with these two charts, one can immediately (a) filter out scenarios with no risk of unstable SSO, (b) identify scenarios whose stability depends on the active power injection of the wind park, and finally (c) pinpoint the specific critical scenarios that must be investigated in detail. This screening saves significant analysis time as it greatly reduces the number of detailed simulations and analyses that must be conducted.

Figure 4.52 indicates that scenarios with X_C/X_L = 0% are risk free. This is true for SSO that involve interactions between a series capacitor in the grid and wind generators. However, as indicated in Section 4.3.2, unstable oscillations near the synchronous resonance due to weak grid may also occur as they do not require a series capacitor in the grid, but this phenomenon is out of the scope of the proposed charts as they were designed for SSO mapping.

4.4.1.2 Real time, online analysis

Consider the examples of Capacity chart and Power injection charts in Figure 4.52 for SSO assessment. The Power injection chart in Figure 4.52 b) can be used to outline the minimum active power injection P_{inj}^{min} of the wind park to ensure the system remains stable during a contingency. With this information and with the active power injected by the park P_{inj} (which is known in real time), it is possible to quantify how close the system is to instability by using the stability margin (*SM*) defined as follows:

$$SM\ (pu) = P_{inj} - P_{inj}^{min} \quad \textbf{(4.5)}$$

As long as *SM* remains positive, there is no risk of an unstable SSO in the park. If *SM* is negative, the system will become unstable if a contingency that results in the park radially connected to the series compensated line takes place. Preventive actions may be undertaken in the latter case.

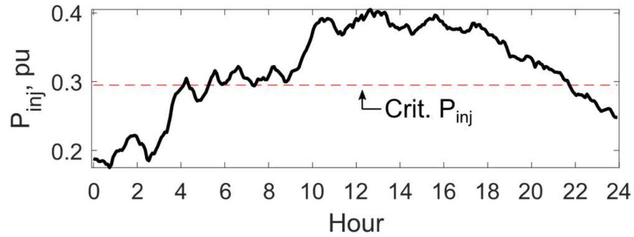

a) 24-hour power injection profile

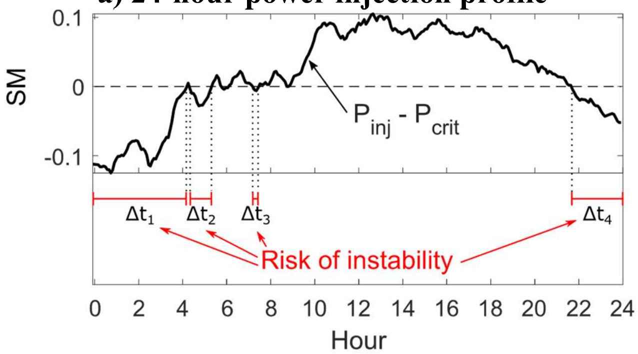

b) 24-hour stability margin of the wind park

Figure 4.53: 24-hour stability margin of the wind park

Figure 4.52 illustrates in blue the stability margin *SM* of the park operating at Case 2. If the 24-hour power injection profile of the wind park (extracted from [92]) is the one in Figure 4.53 a), the real time stability margin of this circuit will be as presented in Figure 4.53 b). The *SM* is negative, *i.e.*, there is instability risk, in 7.44 h (Δt_1 = 4.08 h, Δt_2 = 0.96 h, Δt_3 = 0.22 h, Δt_4 = 2.18 h) or 31% of the day. This stability margin is useful as utilities can determine a minimum *SM* threshold or a maximum percentage of time with a negative *SM* that will trigger an action from the operator.

4.4.2 Determination of the proposed charts

The boundaries of the proposed charts can be obtained with impedance equivalents and simple equations. To facilitate the use of the charts, all system parameters are written in terms of information known in practice by engineers such as wind park capacity S_{WP}, short-circuit level of the background grid S_{SC}, power transfer limit of the transmission line without the series compensation S_{lin}, and its series compensation level X_C/X_L.

4.4.2.1 System model

The studied circuit from Figure 4.51 can be modeled as in Figure 4.54. The utility grid, with multiple lines, generators, loads, and other transmission system components is generally modeled in practice by a RL series branch (named short-circuit impedance, $Z_{sc} = R_{sc} + jX_{sc}$) [3], [19], [91]. This impedance can be obtained from two fundamental frequency parameters used to represent a grid equivalent, the short-circuit level, S_{SC}, and the X/R ratio of the grid at fundamental frequency, $(X/R)_{SC}$. The short-circuit level is given by (4.6) where V_{rated} is the rated voltage of the system and f_0 is the fundamental frequency.

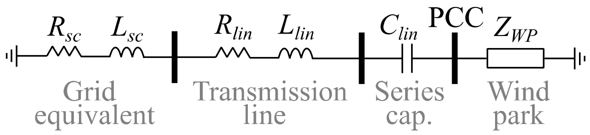

Figure 4.54: Equivalent circuit model of wind park with series compensated line at sub-synchronous frequencies

$$S_{SC} = \frac{V_{rated}^2}{\sqrt{R_{sc}^2 + X_{sc}^2(f_0)}} = \frac{V_{rated}^2}{R_{sc}\sqrt{1 + (X/R)_{SC}^2}} \tag{4.6}$$

By isolating the resistance R_{sc} in (4.6) and transforming it into per unit based on the rated voltage V and wind park capacity S_{WP} ($Z_{base} = V_{rated}^2 / S_{WP}$), one obtains (4.7). The approximation shown in (4.7) is valid when $(X/R)_{SC}^2 >> 1$.

$$R_{sc} = \left[1 + \left(\frac{X}{R}\right)_{SC}^2\right]^{-0.5} \left(\frac{S_{SC}}{S_{WP}}\right)^{-1} \approx \left(\frac{X}{R}\right)_{SC}^{-1} \left(\frac{S_{SC}}{S_{WP}}\right)^{-1} \tag{4.7}$$

The equivalent inductance L_{sc} in per unit of the wind park capacity can be obtained by multiplying (4.7) by $(X/R)_{sc}$ (this multiplication is valid because, at fundamental frequency and in per unit, $X_{sc} = L_{sc}$) and the result is:

$$L_{sc} = \left[1 + \left(\frac{X}{R}\right)_{SC}^{-2}\right]^{-0.5} \left(\frac{S_{SC}}{S_{WP}}\right)^{-1} \approx \left(\frac{S_{SC}}{S_{WP}}\right)^{-1} \tag{4.8}$$

Finally, the equivalent impedance Z_{sc} in per unit can be calculated for any frequency f as (4.9) where f_n is the frequency f normalized by the fundamental frequency f_0 ($f_n = f / f_0$).

$$Z_{sc}(f_n) = R_{sc} + jf_n L_{sc} \tag{4.9}$$

A lumped RL circuit is used to model the transmission line. The line resistance R_{lin} and inductance L_{lin} can be written in per unit of S_{WP} and V_{rated} similar to (4.7)-(4.9):

$$R_{lin} = \left[1 + \left(\frac{X}{R}\right)_{lin}^2\right]^{-0.5} \left(\frac{S_{lin}}{S_{WP}}\right)^{-1} \approx \left(\frac{X}{R}\right)_{lin}^{-1} \left(\frac{S_{lin}}{S_{WP}}\right)^{-1} \tag{4.10}$$

$$L_{lin} = \left[1 + \left(\frac{X}{R}\right)_{lin}^{-2}\right]^{-0.5} \left(\frac{S_{lin}}{S_{WP}}\right)^{-1} \approx \left(\frac{S_{lin}}{S_{WP}}\right)^{-1} \quad \textbf{(4.11)}$$

$$Z_{lin}(f_n) = R_{lin} + jf_n L_{lin} \quad \textbf{(4.12)}$$

where $(X/R)_{lin} = L_{lin}/R_{lin}$ is the X/R ratio of line impedance at the fundamental frequency, $S_{lin} = V_{rated}^2/|Z_{lin\Omega}|$ is the theoretical power transfer limit of the line and $Z_{lin\Omega}$ is the line impedance in ohms at fundamental frequency. The approximation in (4.10) and (4.11) is valid when $(X/R)_{lin}^2 >> 1$. This lumped RL model is adequate for the sub-synchronous frequency range studied in this paper because, at these low frequencies, the shunt capacitive effect can be neglected and the short line model can be used [93].

The series capacitor impedance Z_C is given by (4.13), where X_C/X_L is the series compensation level of the line at the fundamental frequency, between 0% and 100%.

$$Z_C(f_n) = -jX_C = -j\frac{(X_C/X_L)L_{lin}}{f_n} = -j\frac{(X_C/X_L)}{f_n(S_{lin}/S_{WP})} \quad \textbf{(4.13)}$$

As for the wind park impedance $Z_{WP}(f_n) = R_{WP}(f_n) + jX_{WP}(f_n)$, it is calculated with the topology from Figure E.1 and with the positive sequence decoupled impedance profiles of Figure 2.14 in Chapter 2. The effect of the active power injection on the equivalent impedance of the Type-III generator at sub-synchronous frequencies can be seen in Figure 4.55 a) and on the wind park impedance in Figure 4.55 b). Notice how these impedance profiles are heavily dependent on active power injection setpoint, and it does not have a linear dependency.

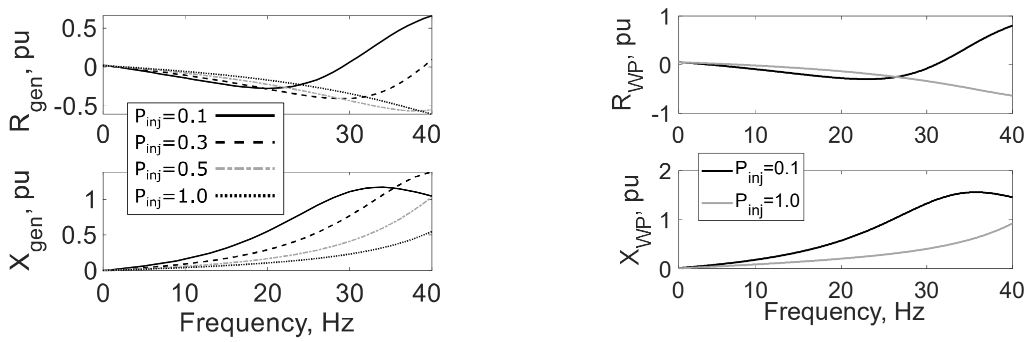

a) Type-III generator (690 V, 2 MVA) **b) Wind park (230 kV, 64 MVA)**

Figure 4.55: Equivalent impedance profiles for different active power injections

In practice, manufacturers do not disclose all the detailed parameters of their generators, but they provide a black-box models for EMT simulations. Utilities can then perform frequency scans on the black-box models [3], [17] and extract their detailed frequency-dependent impedance, considering the effect of all generator controls, for different wind speeds and active power injections.

Finally, notice there may be more than one wind park in the same region of the system, and they can still be aggregated into a single equivalent impedance Z_{WP}. For example, on the ERCOT circuit shown in Figure 4.56 [91], if there is an event that disconnects the line between Del Sol and Pomelo, the Wind farm 2 will be radially connected to a series compensated line and the Wind farm 1 will be part of the background grid. If there is an event that disconnects the line between Pomelo and N Edinburg, the Wind farm 1 will remain part of the background grid, while Wind farms 2 and 3 and the line between Del Sol and Pomelo will be aggregated to form a single wind park complex, represented by a single equivalent impedance. The proposed method can still be applied in both contingencies as the resulting circuit is still in the form of the circuit in Figure 4.54 if all elements involved can be modeled as equivalent impedance profiles.

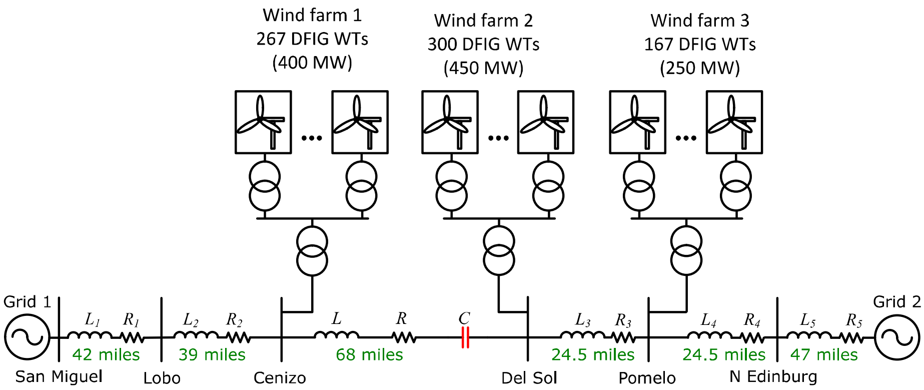

Figure 4.56: Meshed transmission circuit with series compensation and wind generation

4.4.2.2 Analytical derivation of the Capacity Chart

The components of the total equivalent impedance $Z_{eq}(f_n) = Z_{eq}(f_n) + jX_{eq}(f_n)$ of the circuit in Figure 4.54 at frequency f_n are:

$$R_{eq}(f_n) = R_{sc} + R_{lin} + R_{WP}(f_n) \tag{4.14}$$

$$X_{eq}(f_n) = f_n L_{sc} + f_n L_{lin} - \frac{(X_C/X_L)L_{lin}}{f_n} + X_{WP}(f_n) \tag{4.15}$$

According to the "Sum of Impedances" criterion developed in Section 4.1, the circuit will be stable if $R_{eq} > 0$ at the sub-synchronous resonance frequency. Thus, the boundary between an unstable and stable SSO is when the equivalent circuit resistance R_{eq} is zero at the resonance frequency f_n^{res}. Therefore, this critical resonance frequency can be obtained by finding the frequency f_n^{res} that makes $R_{eq}(f_n^{res}) = 0$. If one replaces R_{sc} by (4.7) and R_{lin} by (4.10) in (4.14), the equation $R_{eq}(f_n^{res}) = 0$ can be written as:

$$R_{eq}(f_n^{res}) = \frac{1}{(X/R)_{SC}(S_{SC}/S_{WP})} + \frac{1}{(X/R)_{lin}(S_{lin}/S_{WP})} + R_{WP}(f_n^{res}) = 0 \quad \textbf{(4.16)}$$

After solving (4.16) and identifying the frequency f_n^{res} where the resonance is undamped, the next step is to determine which series compensation level X_C/X_L will create a resonance on f_n^{res}. This can be identified by equaling (4.15) to zero at f_n^{res}. If one replaces L_{sc} by (4.8) and L_{lin} by (4.11) in (4.15), the equation $X_{eq}(f_n^{res}) = 0$ can be written as:

$$X_{eq}(f_n^{res}) = \frac{f_n^{res}}{(S_{SC}/S_{WP})} + \frac{f_n^{res}}{(S_{lin}/S_{WP})} - \frac{(X_C/X_L)}{f_n^{res}(S_{lin}/S_{WP})} + X_{WP}(f_n^{res}) = 0 \quad \textbf{(4.17)}$$

To simplify the notation, the first two terms of the right side of (4.17) can be put together:

$$\frac{f_n^{res}}{(S_{SC}/S_{WP})} + \frac{f_n^{res}}{(S_{lin}/S_{WP})} = \frac{f_n^{res}}{(S_{SC+lin}/S_{WP})} \quad \textbf{(4.18)}$$

So that:

$$X_{eq}(f_n^{res}) = \frac{f_n^{res}}{(S_{SC+lin}/S_{WP})} - \frac{(X_C/X_L)}{f_n^{res}(S_{lin}/S_{WP})} + X_{WP}(f_n^{res}) = 0 \quad \textbf{(4.19)}$$

From (4.19), the series compensation level X_C/X_L that will lead to an unstable SSO is:

$$\frac{X_C}{X_L} = f_n^{res}(S_{lin}/S_{WP})\left[\frac{f_n^{res}}{(S_{SC+lin}/S_{WP})} + X_{WP}(f_n^{res})\right] \quad \textbf{(4.20)}$$

Equation (4.20) provides the X_C/X_L vs. S_{SC+lin}/S_{WP} combinations that form the boundary between the stable and unstable SSO in the proposed Capacity chart in Figure 4.52 a). Summarizing, the boundary of the chart is obtained analytically as follows:

1. Set the short-circuit ratio of the background grid to $S_{SC}/S_{WP} = 1.0$;
2. Calculate the frequency with zero damping f_n^{res} by using (4.16);
3. Calculate short-circuit ratio S_{SC+lin}/S_{WP} by using (4.18);

4. Calculate the series compensation level X_C/X_L that will lead to the resonance frequency f_n^{res} by using (4.20). The resulting pair X_C/X_L vs. S_{SC+lin}/S_{WP} is one point of the boundary of the chart in Figure 4.52 a);
5. If S_{SC}/S_{WP} is below a pre-determined limit (*e.g.,* S_{SC}/S_{WP}<30), increase S_{SC}/S_{WP} by 0.1 and return to Step 2. Otherwise, finish the process.

There are two boundaries in Figure 4.52 a), the upper one considers the wind park injecting its maximum active power capacity (P_{inj} = 1.0 pu) and the lower one considers the wind park injecting minimum active power (P_{inj} = 0.1 pu). Both curves can be obtained with the same procedure described above. The difference is that, for the upper boundary, one must use the equivalent impedance of the wind park Z_{WP} calculated for P_{inj} = 1.0 pu, and for the lower boundary, one must use Z_{WP} calculated for P_{inj} = 0.1 pu.

4.4.2.3 Analytical derivation of the Power Injection Chart

The boundary of the Power Injection chart in Figure 4.52 b) can be obtained with the same rationale used to determine the boundary of the Capacity chart, with the difference that the instantaneous active power injection P_{inj} of the park is used in the x-axis instead of S_{SC+lin}/S_{WP}.

For each P_{inj} value, the first step is to update the frequency spectrum of the wind park equivalent impedance $Z_{WP} = R_{WP} + jX_{WP}$. The second step is to calculate the frequency with zero damping (f_n^{res}) by using (4.16). Finally, the series compensation level X_C/X_L that will lead to the resonance frequency f_n^{res} can be determined by using (4.20). The resulting pair X_C/X_L vs. P_{inj} is one point of the chart boundary.

4.4.3 Validation of the charts

Detailed EMT simulations were conducted to verify the accuracy of the analytical method for obtaining the chart boundaries. To lighten the computational requirements for the validation studies due to the high number of simulations, the wind park topology from Figure E.1 was simplified by neglecting the feeders (as they are short and the analysis occurs at low frequencies which reduces their series impedance), which allows to combine all generators and step-up transformers into a single machine equivalent. The resulting impedance profile from this simplification is shown in Figure 4.57.

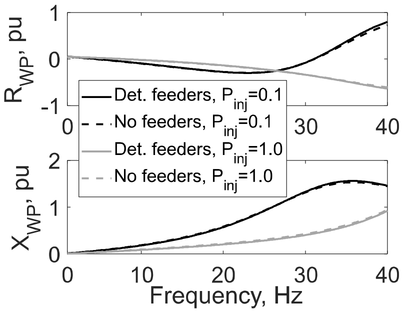

Figure 4.57: Simplification of detailed wind park into single-machine equivalent

The circuit shown in Figure 4.51 was modeled in the Matlab/Simscape Power Systems software. It consists of a 200 MVA wind park connected to the 345 kV grid through a 200 km series compensated transmission line. The transmission line is modeled with its distributed parameters. The wind park is modeled in detail with its main transformer, internal feeders, the generators and their step-up transformers. The EMT model of the Type-III generator from Appendix A was used.

To obtain the Capacity chart, the short-circuit level of the background grid S_{SC} is varied from 230 MVA to 1630 MVA, which corresponds to varying S_{SC+lin}/S_{WP} from 1.0 to 4.0. The series compensation of the transmission line X_C/X_L is varied between 0% and 50%. An EMT simulation is run for each X_C/X_L vs. S_{SC+lin}/S_{WP} combination and those cases with an unstable SSO are marked with an "x" in the charts shown in Figure 4.58. In total, 961 scenarios are simulated to map the entire chart for each power injection value.

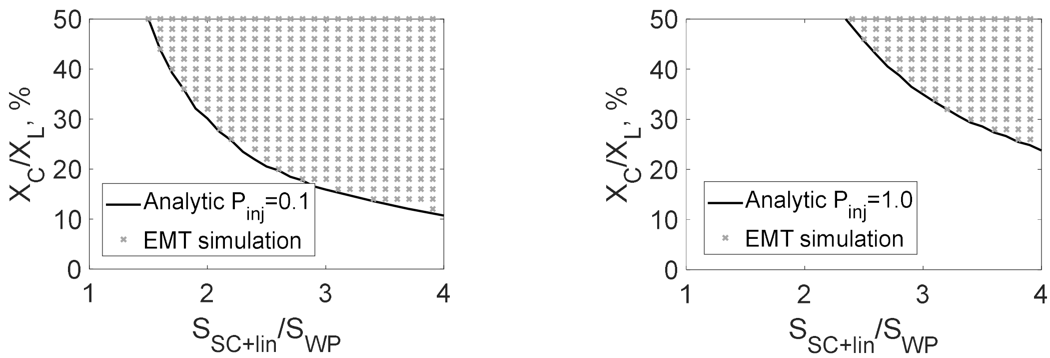

a) Boundary for P_{inj} = 0.1 pu **b) Boundary for P_{inj} = 1.0 pu**

Figure 4.58: Validation of the Capacity chart with EMT simulation

The boundaries of the problematic regions were also obtained analytically by using (4.16) and (4.20) and are plotted in the charts, which show the analytic method can delimit the risk regions with good accuracy. This confirms that the chart can be obtained analytically, without running any simulation, which greatly facilitates its use in practice.

The same circuit is used to validate the method for obtaining the boundaries of the Power Injection chart. In this case, the power injection P_{inj} is varied between 0.1 pu and 1.0 pu, and the series compensation level X_C/X_L is varied between 0% and 50%. An EMT simulation is run for each X_C/X_L vs. P_{inj} combination and those cases with an unstable SSO are marked with an "x" in the chart shown in Figure 4.59.This study is conducted for two short-circuit ratios (S_{SC+lin}/S_{WP} equal to 1.9 and 2.75). The boundaries of the problematic regions were also obtained analytically and are plotted in the charts. Again, the analytic method can delimit the risk regions with good accuracy, which confirms this chart can also be obtained analytically, without simulation.

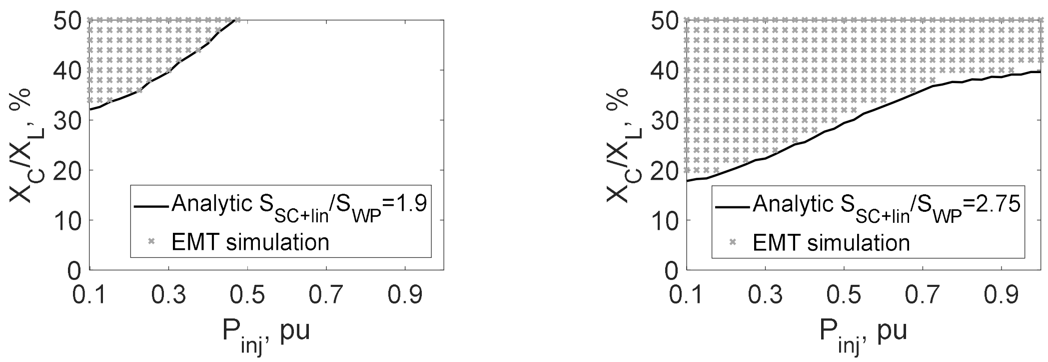

a) Boundary for P_{inj} = 0.1 pu **b) Boundary for P_{inj} = 1.0 pu**

Figure 4.59: Validation of the Power injection chart with EMT simulation

4.4.4 Sensitivity studies

The derivation process of the proposed charts showed the boundaries between safe and problematic regions are sensitive to three parameters that can change during wind park operation: 1) short-circuit level S_{SC}; 2) X/R ratio of the background grid $(X/R)_{SC}$; and 3) number of generators disconnected from the wind park.

The effect of increasing the short-circuit level of the background grid S_{SC} (based on (4.18), this is equivalent to increasing the S_{SC+lin}/S_{WP} ratio) is shown in Figure 4.60. The problematic regions increase, which means that instabilities become more probable. The same effect can be seen in Figure 4.61, which presents the effect of increasing the X/R ratio of the background grid $(X/R)_{SC}$, from 5 to 50. The higher the $(X/R)_{SC}$ ratio, the larger the problematic regions, which means higher risk of unstable SSO.

Both results can be explained by using (4.7), which outlines that a higher S_{SC} and a higher $(X/R)_{SC}$ are associated with a smaller equivalent resistance of the background grid and, as such, less damping to resonances. Therefore, the resistive portion of the background grid is of key importance for SSO studies and should not be neglected. If neglected, one will obtain overly conservative results.

It is important to mention that the variations of S_{SC} and $(X/R)_{SC}$ shown in Figure 4.60 and Figure 4.61 are not frequent during wind park operation. Most variations in the grid such as load changes typically do not affect the equivalent grid impedance significantly and, as such, do not affect the chart boundary. Even larger contingencies or line switching may not affect the grid equivalent if they take place far from the wind park. Only major contingencies or large line switching in the vicinity of the wind park are likely to affect this equivalent impedance.

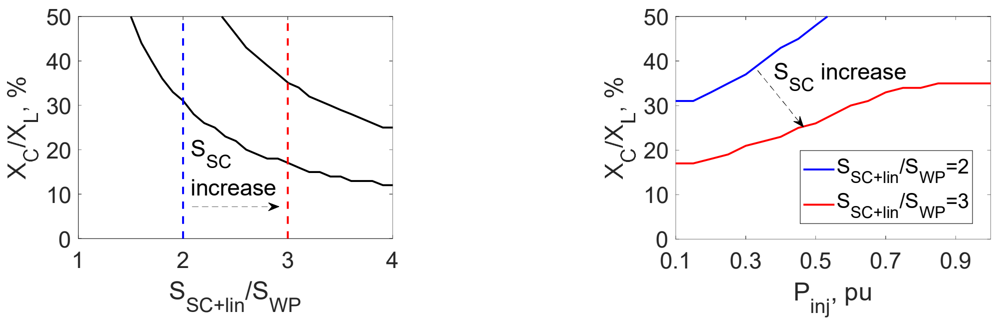

a) Capacity chart **b) Power injection chart**

Figure 4.60: Effect of the short-circuit level of the background grid

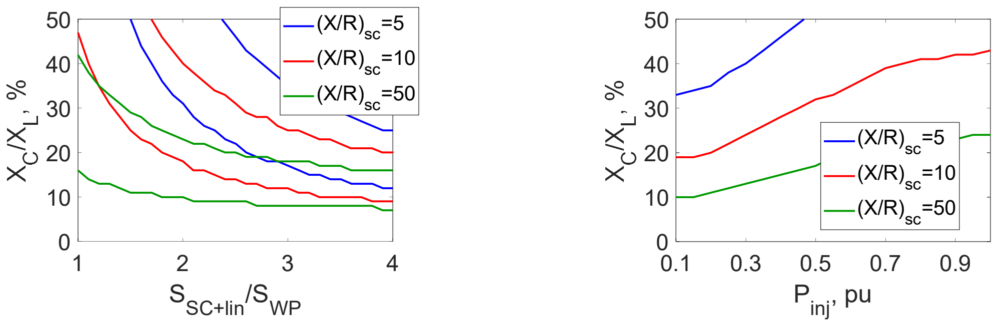

a) Capacity chart **b) Power injection chart**

Figure 4.61: Effect of the X/R ratio of the background grid

During wind park operation, generator units can be disconnected either due to an event or planned maintenance. The impact of this condition is shown in Figure 4.62, which reveals the effect of disconnecting 10, 20 and 40 wind generators out of the 100 units of the park.

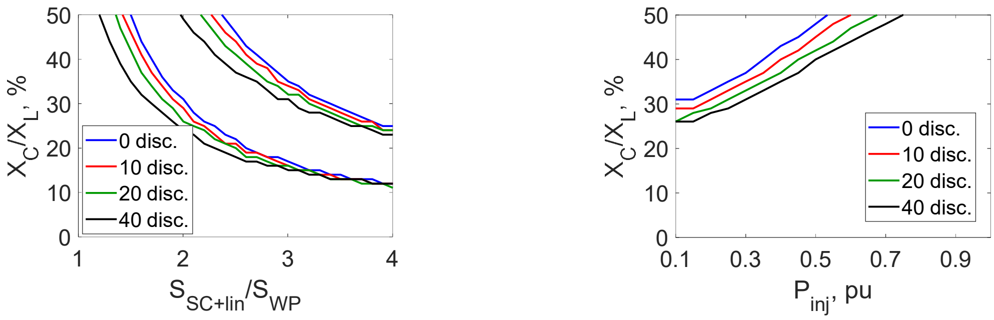

a) Capacity chart **b) Power injection chart**

Figure 4.62: Effect of number of wind generators disconnected from the circuit

First, the effect of disconnecting up to 20% of the generators is small for the studied wind park especially in the Capacity chart. After that, the higher the number of disconnections, the higher the risk of instability. To explain this, one must consider that the wind park impedance can be written as:

$$Z_{WP}(f_n) = Z_{MainTx}(f_n) + \frac{Z_{suTx}(f_n) + Z_{gen}(f_n)}{N_{total} - N_{disconnected}} \quad \textbf{(4.21)}$$

where Z_{MainTx} is the impedance of the main transformer of the park. This impedance is unchanged regardless the number of generators disconnected as the main transformer remains in the circuit. Z_{gen} and Z_{suTx} are, respectively, the impedance of one gemerator and its step-up transformer; N_{total} is the total number of generators in the park and $N_{disconnected}$ is the number of generators disconnected from the circuit. The impedance of the internal feeders is neglected in this analysis.

Based on (4.21), when generators are disconnected, the magnitude of the wind park impedance increases and the frequency where the total equivalent resistance of the circuit is zero decreases. This is exemplified in Figure 4.63 with the frequency-dependent profile of the total circuit resistance. If the park has no disconnections, the frequency with zero resistance (f_n^{res}) is 13.1 Hz. If 20 generators are disconnected, f_n^{res} decreases to 11.6 Hz.

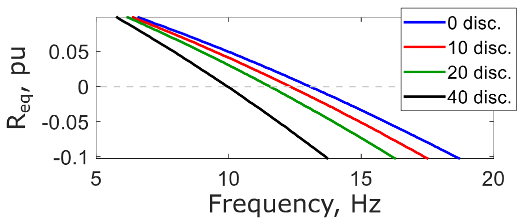

Figure 4.63: Total resistance for different numbers of generator disconnections (P_{inj} = 0.3 pu, S_{SC} = 370 MVA).

According to (4.20), if f_n^{res} decreases, the series compensation level of the chart boundary will also decrease. This effect is more pronounced on weaker grids (*i.e.*, on grids with lower S_{SC+lin}/S_{WP} values) because X_C/X_L is inversely proportional to S_{SC+lin}/S_{WP} (as shown in (4.20)) and, as such, lower S_{SC+lin}/S_{WP} ratios have a higher effect on X_C/X_L.

Overall, results in Figure 4.62 suggest that the effect on chart boundaries is small for up to 20% of generators disconnected. However, if a utility intends to draw the chart boundaries as accurate as possible, there are two possible approaches to deal with this characteristic:

1. Draw the boundaries of the charts conservatively, by considering a given number of units (e.g., 20% of the units) will always be disconnected (the number of units disconnected can be determined based on previous experience from the engineer). This approach can be adopted both during planning and operation;
2. Update the boundaries of the charts based on the number of units disconnected. This can be done through a recalculation of the equivalent impedance of the wind park as shown in (4.20).

4.4.5 Application example

The proposed approach was applied to a real event to diagnose the risk of unstable SSO in a circuit with a wind park radially connected to a series compensated line.

4.4.5.1 Capacity Chart and Power Injection Chart

The circuit shown in Figure 4.64 is considered. Its parameters are based on the event that occurred in Texas, USA in 2009 [3]. The term “wind park cluster” is used in the figure because there are multiple wind parks and transmission lines in this region, but they can be aggregated into a single equivalent impedance radially connected to the series compensated transmission line. As a result, the circuit becomes equal to the circuit shown in Figure 4.51 and the proposed method can be applied. The series capacitor of the transmission line has two stages that can compensate 26% and 51% of the line reactance. When both stages are connected, the series compensation level is 77%. The wind park cluster was modeled as a single machine equivalent with 340 units of 2 MVA Type-III generators.

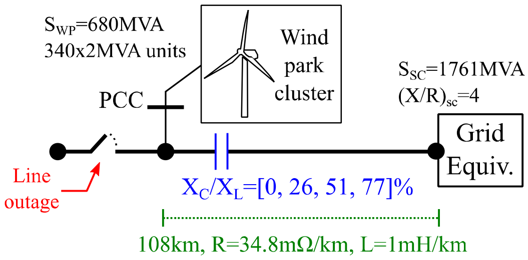

Figure 4.64: Circuit considered in the application studies

4.4.5.2 Capacity chart and Power injection chart

Figure 4.65 presents the resulting charts for this case, with the four possible scenarios of series compensation (0%, 26%, 51% and 77%) highlighted with red “x” markers. Based on the Capacity chart in Figure 4.65 a), the first scenario (0%) presents no risk of SSO regardless the active power injection of the park, which is expected as there is no capacitor in the circuit. The second scenario (26%) presents risk of instability depending on the active power injection. According to Figure 4.65 b), this second scenario is stable for power injections above 0.23 pu. Detailed studies should be conducted only for cases with an active power injection below 0.23 pu. Finally, the third and fourth cases (51% and 77% series compensation) are in the problematic region and, as such, are unstable regardless the active power injection of the park. Detailed studies must be conducted for these two cases.

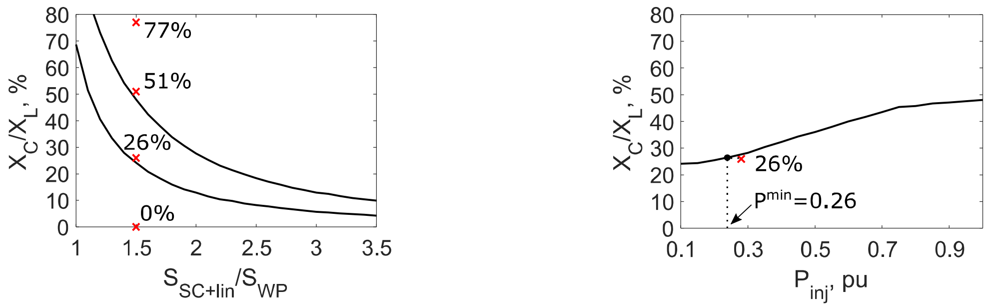

a) Capacity chart **b) Power injection chart**

Figure 4.65: SSR risk assessment for the circuit in Figure 4.64 before mitigation action

To verify these results, detailed EMT simulations were run for the three scenarios with series compensation above 0% and Figure 4.66 shows the resulting PCC current. At the time instant $t = 0.1$ s, a series capacitor is connected to the circuit. In all scenarios, the active power injection is 0.28 pu. According to Figure 4.65, only the case with 26% compensation should be stable. The EMT simulation results indeed confirm this outcome.

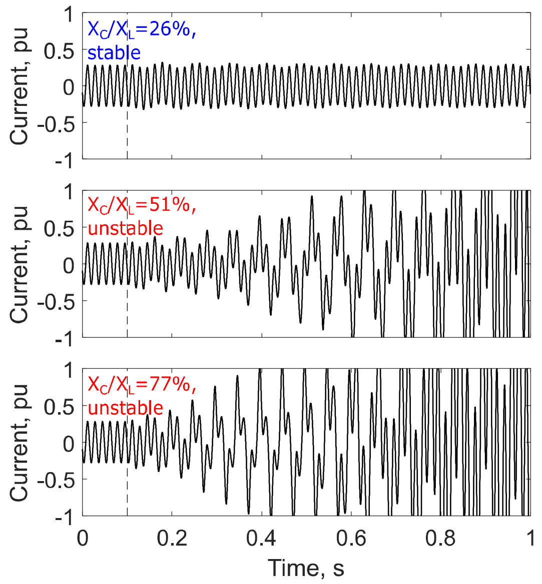

Figure 4.66: Phase A current at the wind park PCC for the circuit shown in Figure 4.64

After the unstable event took place in 2009, the series compensation level of the transmission line was reduced to 16% and 30% (total of 46% if both stages are connected). The updated circuit is plotted as blue circle markers in the charts in Figure 4.67. One can notice that there is no risk of instability for 16% compensation level, and the stability of 30% and 46% levels depends on the active power injection of the wind park. According to Figure 4.67 b), the cases with 30% and 46% are unstable only if the wind park power injection is below 0.34 and 0.82 pu, respectively.

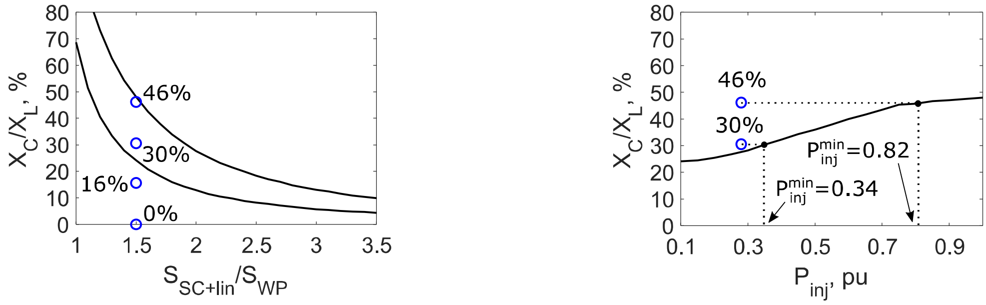

a) Capacity chart **b) Power injection chart**

Figure 4.67: SSR risk assessment for the circuit in Figure 4.64 after mitigation action

4.4.5.3 Real Time Monitoring of the Stability Margin

If the 1-year wind speed profile shown in Figure 4.68 (extracted from [92]) is applied to the circuit shown in Figure 4.64 with 26% series compensation, the resulting online stability margin of this park will be the one shown in Figure 4.69, considering all generators of the wind park are in service. This information is useful in practice as it can help engineers to continuously monitor which wind parks in their system are under higher risk of instability.

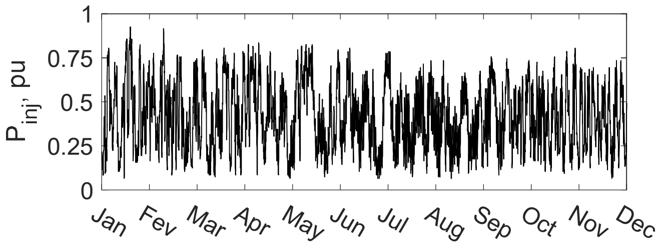

Figure 4.68: Wind generation profile measured in Texas, USA during 1 year with 1-hour time resolution

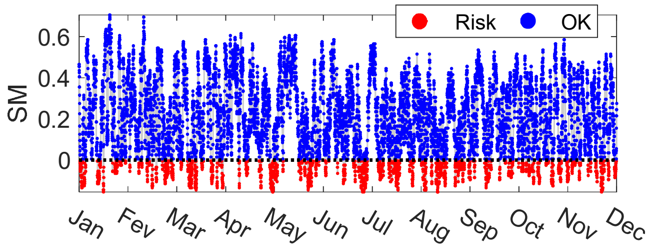

Figure 4.69: Stability margin of the wind park

Figure 4.69 also reveals that the wind park will be under risk of unstable SSO during 18% of the time. This type of aggregate index is also useful as utilities can establish thresholds of this index that will trigger specific actions on the wind park or on the circuit near the park to reduce the risk of instability.

Figure 4.69 was obtained considering that the boundary of the Power injection chart was constant over the year, to illustrate how the risk of SSO can be monitored during operation. In practice, however, the boundary of the Power injection chart may change if there are variations in the grid that affect S_{SC} or $(X/R)_{SC}$ or if some generators are disconnected in the wind park as shown in Section 4.4.4. This alters the minimum active power injection for stable operation (P_{inj}^{min} in (4.5)), but the method to obtain the stability margin remains the same. In addition, no new frequency scan calculation of the background grid impedance and of the wind park impedance are needed in the operation stage as the most critical circuit and wind park variations are identified and characterized previously, during the planning stage.

4.5 Chapter summary

This chapter was dedicated to the study of unstable resonance in power systems involving Type-III and Type-IV wind parks. The study was based on impedance equivalent models of the wind park and the grid, and two impedance-based stability criteria were defined to study the conditions which led to unstable control interactions between the wind park and the grid.

The first part of the chapter presented a comprehensive sensitivity analysis, based on a practical wind park topology, to determine the necessary conditions for unstable resonance to occur in the sub-synchronous range (SSR), near synchronous range (NSR) and the harmonic frequency range (HFR). The study evaluated grid variables, wind park variables, and generator variables (including the most relevant control gains per range of frequency). It demonstrated that instability in the SSR due to series capacitors is able to occur in Type-III wind parks only, especially for low wind conditions, and the necessary circuit conditions can be easily met in the field. Therefore, it was assigned a moderate to high risk.

As for the stability of control interactions at the NSR, it was determined that they can occur for both Type-III and Type-IV wind parks, due to lack of grid stiffness when the PLL tracking system is unable to lock into the terminal voltage. This occurs at weak grids and with improperly tuned PLL gains, and it is more likely for high wind conditions. Therefore, it was assigned a low to moderate risk.

The instability of control interactions at the HFR due to the shunt capacitor for reactive power compensation was achieved after eliminating the capacitances of the wind park feeders and the front-end filter of the generators, and it is more likely for very low wind conditions. As LCL front-end filters and underground feeders are the most common in practical wind parks, this instability was assigned a very low risk to occur in the field.

Finally, based on the results of the extensive characterization of the instabilities performed in the first three sections of this chapter, it was concluded that the instability that is most likely to occur in practice is the subsynchronous instability due to a series compensated line in the grid. A simplified graphical approach was then developed to aid the analysis of these unstable sub-synchronous oscillations once a radial topology is detected, which consists of two charts that delimit a boundary that separates the stable and unstable circuit configurations of Type-III wind parks connected to transmission systems with series capacitive compensation. These charts allow engineers to monitor the risk of instabilities in a wind park without running any computer simulation. The charts can be applied both offline during the wind park planning, and online during wind park operation, where the stability margin of the park can be monitored in real time.

5 CONCLUSIONS

This thesis has presented a series of new methods to improve a proper management (anticipation, detection, and mitigation) of the risk of weakly damped resonances and unstable resonances in wind parks with Type-III and Type-IV generators. The proposed methods are simplified, based on charts and simple equations that depend on parameters that are readily available in practice to engineers. With these tools, engineers can perform a quick first-screening assessment of the risk of resonances and component overloading in the park by simply consulting these charts, without the need to run any computer simulation. If this first-screening analysis indicates no risk of resonance, the engineer can directly conclude that this is a safe scenario, and no further investigation is required. On the other hand, if a risk of resonance is detected, further investigation based on detailed simulations studies performed by specialized personnel must be conducted.

The contributions and conclusions from each chapter of the thesis are presented below.

5.1 Chapter 2: Model of Type-III and Type-IV wind generators for resonance assessment in wind parks

This chapter derived frequency-dependent impedance models of the Type-III and Type-IV wind generators, which were used in the remaining of the thesis. A numerical procedure was developed based on descriptor-state space models (which is a state space model able to handle algebraic equations without the need to incorporate them into the differential equations) to obtain these frequency-dependent impedance models numerically, without the need for complex algebraic manipulations.

With such tool to facilitate the creation of the impedance models of the generators, an investigation was conducted to verify the impedance-profile sensitivity to the different control parameters of the generators. The results of this study revealed which are most relevant control and generator parameters for stability assessment at three different frequency ranges: 1) Sub-synchronous (0 Hz to 40 Hz); Near synchronous (40 Hz to 80 Hz); and Harmonic (80 Hz to 1.5 kHz). This is an important information that was used when deriving and validating the methods presented in the other chapters.

With the obtained models for Type III and Type IV generators, it was also possible to compare their characteristics at different frequencies. One of the key results to highlight in this comparison, is that the magnitude of the impedance of the Type-IV generator is greater than the Type-III as the front-end filter of the Type-IV is larger (filter were tuned according to each converter bridge capacity, with the same methodology). Moreover, if the DC bus link is considered to decouple the converter dynamics, the induction machine can be seen as an additional branch in parallel with the filter, which further explains the lower impedance magnitude of the Type-III generator.

The greatest difference in the shape of the equivalent impedance between the generators was found at the subsynchronous range of frequencies. The negative damping of the Type-III generator due to the induction machine asynchronous coupling with the grid at these frequencies was confirmed, as well as the high positive damping of the Type-IV in such range. There are also negative damping regions in the harmonic range of frequencies, for both generators, due to the control delays from measurement and filtering, as well as the switching algorithms in the converters.

5.2 Chapter 3: Weakly damped resonance

This chapter was dedicated to characterizing and developing methods for better management of weakly damped harmonic resonances. Two simple charts were proposed, one to monitor the risk of exceeding harmonic distortion limits at the PCC, and one to monitor the risk of overloading components of the wind park due to a resonance. Both charts can be obtained analytically, without running any computer simulation, and consulted by using only information that is readily available in practice to engineers. Finally, to mitigate the excessive harmonic distortions due to these weakly damped resonances, an impedance-based iterative procedure was designed to design passive harmonic filters for the park. The proposed methodology tunes the filter to minimize the THD_V at PCC in a cost/effective fashion, while it ensures the same performance at fundamental frequency of the original capacitor bank installed for reactive power compensation of the wind park.

All these procedures were tested in a real 64 MVA wind park circuit and validated with detailed EMT simulations. Sensitivity studies were also conducted to identify the main factors affecting the risk of resonance under different conditions and to demonstrate the robustness and flexibility of the proposed methodologies.

The equivalent impedance models of the generators developed in the previous chapter allowed for accurate analyses of harmonic resonance, to determine both the resonance frequency and the magnitude of the amplification of harmonic distortions. Moreover, the simplification of considering the harmonic current injections by the generators to be negligible when compared to the background voltage distortions from the grid, *i.e.*, considering the wind generators as pure impedances, also proved to be valid. It was determined that the converter impedance must be included in the impedance profile calculation. Neglecting it leads to adequate values of resonance frequency, but also to incorrect amplification values of the grid harmonic distortions.

Modeling the detailed topology of the MV feeders of the wind park (including their capacitances), as well as properly modeling the front-end filter of the generators, proved to be determinant for an accurate harmonic resonance analysis. In particular, the presence of capacitances in this range of frequencies can change the impedance profile significantly.

Overall, it was found that Type-III wind parks have a greater risk of leading to problematic harmonic resonances than Type-IV wind parks, both at the PCC between the wind park and the grid, and inside the wind park as well. This was confirmed though multiple sensitivity studies of grid, wind park and generator parameters.

Finally, it is important to highlight that the shunt capacitor bank for reactive power compensation of the wind park is the key element to evaluate the risk of problematic harmonic resonances between the wind park and the grid, and it is the most sensitive component of the wind park to overloads due to harmonic distortions. Eliminating the shunt capacitor can mitigate most of the problematic harmonic resonances. It could be substituted by alternatives such as using the wind generators spare capacity, or static var compensators. However, if eliminating the capacitor bank is not viable, passive harmonic filters, such as the one proposed in this chapter, can be a cost/effective mitigation strategy.

5.3 Chapter 4: Unstable resonance

This chapter was dedicated to characterizing and developing methods for better management of unstable resonances. Initially, an extensive investigation mapped the most critical parameters for three different types of instabilities: unstable subsynchronous resonances (SSR) due to interactions with series compensated transmission lines; unstable interactions between the generator control and weak grids near the synchronous frequency (NSR); and unstable resonances at frequencies in the low order harmonic range up to 1.5 kHz (HFR). This study evaluated parameters from the grid, from the wind park, and from the generators and identified their effect on the risk of unstable resonances. It was found that SSR have a moderate to high risk of occurring in the field under practical conditions, NSR was found to have a low to moderate risk of occurring in practice, and HFR was found to have a very low risk of occurring in practice.

Based on the finding that unstable subsynchronous resonances in parks with Type-III generators have the most risk of occurring in practice, a graphical approach was designed to detect the risk of these oscillations both during planning and operation studies. Two charts were proposed, and they can be built analytically based on information from the circuit that is readily available in practice to engineers, without the need to run any simulation. They can be used offline during planning, and online during operation to determine, in real-time, the stability margin of the park.

During the development of this thesis, it was noted that there are no works available in the literature addressing how likely are the necessary conditions for unstable resonance to occur. Simplified wind park circuits and grid equivalents are used to demonstrate the possibility of instabilities, both in simulation and experimental environments. After extensive testing it was noted that indeed, the instability at the SSR is the most possible phenomenon, which matches the reports in the literature. This occurs due to an intrinsic characteristic of the Type-III generators, which is the slip of the asynchronous machine at such frequencies, which leads to negative damping.

On the other hand, instabilities at the NSR require a combination of weak grid conditions and poorly tuned PLLs. These can occur for both Type-III and Type-IV wind parks. However, a robust design and tuning of the PLL subsystem is sufficient to avoid the instabilities. This result also matches the reports in the literature, which exist, but are very few.

Finally, instabilities in the HFR were found to occur only at an improbable condition, which is the absence of capacitances in the wind park, both at the feeders and the front-end filters of the generators, and when the PLL is improperly tuned on the generator controllers. There are no reports of this type of instability occurring in the field, which matches the results in this thesis. Moreover, eliminating the shunt capacitor for reactive power compensation will also mitigate this type of instability.

5.4 Future Work

The following topics are recommended to continue the research presented in this thesis:

5.4.1 Determine responsibility factors for harmonic resonance

Assigning a percentage of responsibility of the different power system components to a harmonic resonance is an open discussion that needs further investigation. Methodologies have been proposed for distribution networks and consumers. It would be interesting to study if these methodologies can also be applied to high voltage grids at the PCC between a wind park and the transmission system, and even considering the contributions of internal components of the wind parks and control parameters of the wind generators.

5.4.2 Investigate harmonic current injections by wind generators and wind parks

Even though modern technologies of wind generators such as the Type-III and Type-IV generators are expected to produce negligible distortions in the low order harmonic range of frequencies, it is important to verify if this condition is, in fact, observed in practice. An extensive measurement campaign and analysis of different wind generators connected to different wind parks and with different operating conditions can shed lights on this important characteristic.

Synchronized gapless waveform measurements at the generator terminals, at key points of the feeders and at the secondary of the main transformer would allow the calculation of not only about the magnitude of the distortions, but also their angle, in order to determine the participation of different components, as well as the path and origin of the oscillations.

5.4.3 Investigate other wind park topologies

In order to generalize the findings of this thesis, it is desirable to apply the methods developed herein to other real wind park topologies such as offshore wind parks, wind parks with longer feeders and wind parks with other generation technologies (Type-I and Type-II generators) or with a mix of technologies. This study would require first to collect other real wind park topologies from developers or grid operators and then building the models. The starting point is to apply the same tools developed in this thesis, evaluate their performance and, if necessary, adjust them to address the limitations identified.

5.4.4 Test the methodologies for photovoltaic generators

The same methodologies proposed in this thesis for impedance calculation, as well as for risk assessment and mitigation of harmonic resonance and instability can be applied to parks of photovoltaic generators. This can be done for both transmission level facilities and for residential and commercial low voltage circuits with high penetration of generators.

5.4.5 Different control topologies and their impact on the equivalent impedance profile of the converters

The methodology proposed in Chapter 2 of this thesis can also be used to model different generator control loops, for example, those which are implemented in the converters for compensation of harmonic frequencies. Another example which needs further investigation is the inclusion of feed-forward terms into the current control loops.

These modifications may lead to an important impact on harmonic resonance studies, as well as for the studies of stability in the harmonic range of frequencies.

5.4.6 Impact of the reactive power compensation strategy on the characteristics at harmonic resonance

As mentioned in Chapter 3, the shunt capacitor bank is the key element for problematic resonance analysis in the harmonic range of frequencies. It is interesting to evaluate how removing such component from the wind park, and using the generators reactive power compensation capacity, can impact on the characteristics of the harmonic resonances.

This change is expected to significantly reduce the risk of problematic harmonic resonances, while the equivalent impedance profile of the wind generators is expected to remain relatively unchanged. However, other characteristics such as spare capacity, terminal voltages of the generators, and grid code requirements for low voltage ride through remain to be assessed.

5.4.7 Studies of harmonic resonance and stability in isolated grids

It is interesting to expand the application of the techniques developed in this thesis to study isolated networks. This would mean to update the converter control topology from grid-following to grid-forming (which changes the equivalent impedance profile), as well as working with low short-circuit level capacities at converter terminals (weak networks).

5.4.8 Develop measurement-based techniques to detect and mitigate resonances

Detection and mitigation of resonances in wind parks is an open research topic. Many works in the literature focus on adding complementary control components to the generators to avoid the resonances. However, it is also possible to implement system level solutions without modifying the generators already in operation, and uninterrupted waveform measurements from different system locations can be used to detect and monitor the risk of such events taking place, and with this information, avoid catastrophic failures.

6 REFERENCES

[1] Wind World Wind Energy Association, Worldwide Wind Capacity Reaches 744 Gigawatts – An Unprecedented 93 Gigawatts added in 2020, 2021. [Online]. Available: https://wwindea.org/worldwide-wind-capacity-reaches-744-gigawatts/.

[2] ABEEólica, "Boletim Anual de Geração Eólica 2018," 2019. [Online]. Available: http://abeeolica.org.br/wp-content/uploads/2019/05/Boletim-Anual_2018.pdf.

[3] IEEE Wind SSO Task Force, "PES-TR80, Wind Energy Systems Sub-Synchronous Oscillations: Events and Modeling," IEEE Power & Energy Society, 2020.

[4] M. Ghorbaniparvar, "Survey on forced oscillations in power system," *Journal of Modern Power Systems and Clean Energy,* vol. 5, pp. 671-682, 2017.

[5] CIGRE Joint Working Group , "C4.24/CIRED Power Quality and EMT Issues with Future Electricity Networks," 2018.

[6] Z. Liu, J. Rong, G. Zhao and Y. Luo, "Harmonic Assessment for Wind Parks Based on Sensitivity Analysis," *IEEE Transactions on Sustainable Energy,* vol. 8, no. 4, pp. 1373-1382, 2017.

[7] K. Yang, M. Bollen and E. Larsson, "Aggregation and Amplification of Wind-Turbine Harmonic Emissions in a Wind Park," *IEEE Transactions on Power Delivery,* vol. 30, no. 2, pp. 791-799, 2015.

[8] IEEE, "IEEE Std. 519-2014 Recommended Practice and Requirements for Harmonic Control in Electric Power Systems," IEEE, 2014.

[9] Operador Nacional do Sistema (ONS), "Gerenciamento dos indicadores de desempenho da rede básica e de seus componentes, PROREDE - Submódulo 2.8," 2008.

[10] C. Buchhagen, C. Rauscher, A. Menze and J. Jung, "BorWin1 – First Experiences with harmonic interactions," in *International ETG Congress 2015; Die Energiewende - Blueprints for the new energy age*, Bonn, Germany, 2015.

[11] P. Sørensen, P. Hauge, A. Vikkelsø, K. Kølbæk, K. Fathima, A. Unnikrishnan and Z. Lakaparampil, "Power Quality and Integration of Wind Farms in Weak Grids in India," Risø-R, Denmark, 2000.

[12] J. Balcells and D. Gonzáles, "Harmonics due to Resonance in a Wind Power Plant," in *8th International Conference on Harmonics and Quality of Power (ICHQP)*, Athens, Greece, 1998.

[13] R. Gregory, G. Troncha, B. Gianesini, C. Chaves and I. Santos, "Impact Studies of Connecting Tuned Harmonic Filters onto a Brazilian Wind Farm," in *18th International Conference on Renewable Energies and Power Quality (ICREPQ'20)*, Granada, Spain, 2020.

[14] L. Kocewiak, B. Kramer, O. Holmstrøm, K. Jensen e L. Shuai, “Resonance damping in array cable systems by wind turbine active filtering in large offshore wind power plants,” *IET Renewable Power Generation,* vol. 11, nº 7, pp. 1069-1077, 2017.

[15] IEEE PES Power System Dynamic Performance Committee Task Force on Stability definitions and characterization of dynamic behavior in systems with high penetration of power electronic interfaced technologies, "Technical report PES-TR77 Stability definitions and characterization of dynamic behavior in systems with high penetration of power electronic interfaced technologies," IEEE, 2020.

[16] J. Ramamurthy and L. Bohmann, "Wind plant interaction in a 345-kv series-compensated power system electromagnetic transient program modeling and event analysis," *Electric Power Components and Systems,* vol. 44, no. 15, pp. 1745-1756, 2016.

[17] ABB-ERCOT, "CREZ Reactive Power Compensation Study," North Carolina, USA, 2010.

[18] P. Belkin, "Event of 10-22-09," January 2010. [Online]. Available: http://www.ercot.com/content/meetings/rpg-crez/keydocs/2010/0126/8Belkin_Event%20of%2010.ppt.

[19] X. Xie, X. Zhang, H. Liu, H. Liu, Y. Li and C. Zhang, "Characteristic Analysis of Subsynchronous Resonance in Practical Wind Farms Connected to Series-Compensated

Transmissions," *IEEE Transactions on Energy Conversion,* vol. 32, no. 3, pp. 1117-1126, 2017.

[20] H. Liu, X. Xie, J. He, T. Xu, Z. Yu, C. Wang and C. Zhang, "Subsynchronous Interaction Between Direct-Drive PMSG Based Wind Farms and Weak AC Networks," *IEEE Transactions on Power Systems,* vol. 32, no. 6, pp. 4708-4720, 2017.

[21] X. Xie, Y. Zhan, J. Shair, Z. Ka and X. Chang, "Identifying the Source of Subsynchronous Control Interaction via Wide-Area Monitoring of Sub/Super-Synchronous Power Flows," *IEEE Transactions on Power Delivery,* vol. XX, no. XX, pp. 1-9, 2019.

[22] U. Karaagac, J. Mahseredjian, S. Jensen, R. Gagnon, M. Fecteau and I. Kocar, "Safe Operation of DFIG based Wind Parks in Series Compensated Systems," *IEEE Transactions on Power Delivery,* vol. 33, no. 2, pp. 709-718, 2018.

[23] E. Ebrahimzadeh, F. Blaabjerg, X. Wang and C. Leth-Bak, "Harmonic Stability and Resonance Analysis in Large PMSG-Based Wind Power Plants," *IEEE Transactions on Sustainable Energy,* vol. 9, no. 1, pp. 12-22, 2018.

[24] Y. Song and F. Blaabjerg, "Overview of DFIG-Based Wind Power System Resonances Under Weak Networks," *IEEE Transactions on Power Electronics,* vol. 32, no. 6, pp. 9105-9116, 2017.

[25] I. Vieto and J. Sun, "Sequence Impedance Modeling and Analysis of Type-III Wind Turbines," *IEEE Transactions on Energy Conversion,* vol. 33, no. 2, pp. 537-545, 2018.

[26] X. Wang and F. Blaabjerg, "Harmonic Stability in Power Electronic Based Power Systems: Concept, Modeling, and Analysis," *IEEE Transactions on Smart Grid,* vol. 10, no. 3, pp. 2858-2870, 2019.

[27] IEEE, "IEEE Std 3002.8-2018 Recommended Practice for Conducting Harmonic Studies and Analysis of Industrial and Commercial Power Systems," IEEE, 2018.

[28] Operador Nacional do Sistema (ONS), “ONS NT 009/2016 - Rev. 02,2018: Instruções para Realização de Estudos e Medições de QEE Relacionados aos Acessos à Rede Básica ou

nos Barramentos de Fronteira com a Rede Básica para Parques Eólicos, Solares, Consumidores Livres e Distribuidoras," 2016.

[29] W. Ren and E. Larsen, "A Refined Frequency Scan Approach to Sub-Synchronous Control Interaction (SSCI) Study of Wind Farms," *IEEE Transactions on Power Systems,* vol. 31, no. 5, pp. 3904-3912, 2016.

[30] R. Gagnon, "Wind Farm - DFIG Average Model," [Online]. Available: https://www.mathworks.com/help/physmod/sps/examples/wind-farm-dfig-average-model.html.

[31] R. Gagnon and J. Brochu, "Wind Farm - Synchronous Generator and Full Scale Converter (Type 4) Average Model," [Online]. Available: https://www.mathworks.com/help/physmod/sps/examples/wind-farm-synchronous-generator-and-full-scale-converter-type-4-average-model.html.

[32] Y. Sun, "The Impact of PLL Dynamics on the Low Inertia Power Grid: A Case Study of Bonaire Island Power System," *MDPI Energies,* vol. 12, 2019.

[33] D. Holmes and T. Lipo, Pulse Width Modulation for Power Converters: Principles and Practice, John Wiley & Sons, Inc., 2003.

[34] C. Larose, R. Gagnon, G. Turmel, P. Giroux, J. Brochu, D. McNabb e D. Lefebvre, "Large Wind Power Plants Modeling Techniques for Power System Simulation Studies," [Online]. Available: https://blob.opal-rt.com/medias/L00161_0673.pdf.

[35] M. Cespedes and J. Sun, "Impedance Modeling and Analysis of Grid-Connected Voltage-Source Converters," *IEEE Transactions on Power Electronics,* vol. 29, no. 3, pp. 1254-1261, 2014.

[36] G. Mendoça, H. Pereira and S. Silva, "Wind Farm and System Modelling Evaluation in Harmonic Propagation Studies," in *International Conference on Renewable Energies and Power Quality (ICREPQ'12)*, Santiago de Compostela, Spain, 2012.

[37] R. Kawakami, K. Heinz and S. Hadjiloucas, "Conversion of descriptor representations to state-space form: an extension of the shuffle algorithm," *International Journal of Control,* vol. 91, no. 10, pp. 2199-2213, 2018.

[38] G.-R. Duan, Analysis and design of descriptor linear systems, New York: Springer, 2010.

[39] S. Shah and L. Parsa, "Impedance Modeling of Three-Phase Voltage Source Converters in DQ, Sequence, and Phasor Domains," *IEEE Transactions on Energy Conversion,* vol. 32, no. 3, pp. 1139-1150, 2017.

[40] J. Sun, "Impedance-Based Stability Criterion for Grid-Connected Inverters," *IEEE Trans. on Power Electronics,* vol. 26, no. 11, pp. 3075-3078, 2011.

[41] W. Xu, Z. Huang, Y. Cui and H. Wang, "Harmonic resonance mode analysis," *IEEE Transactions on Power Delivery,* vol. 20, no. 2, pp. 1182-1190, 2005.

[42] C. Zhang, X. Cai, A. Rygg and M. Molinas, "Sequence Domain SISO Equivalent Models of a Grid-Tied Voltage Source Converter System for Small-Signal Stability Analysis," *IEEE Transactions on Energy Conversion,* vol. 33, no. 2, pp. 741-749, 2018.

[43] W. Xu, X. Liu and Y. Liu, "Assessment of harmonic resonance potential for shunt capacitor applications," *Electric Power Systems Research,* vol. 57, pp. 97-104, 2001.

[44] A. Nassif, "Modeling, Measurement and Mitigation of Power System Harmonics," Doctoral Thesis, University of Alberta, Edmonton, Alberta, 2009.

[45] I. Vieto and J. Sun, "Refined Small-Signal Sequence Impedance Models of Type-III Wind Turbines," in *IEEE Energy Conversion Congress and Exposition (ECCE)*, Portland, Oregon, 2018.

[46] L. Fan and Z. Miao, "Wind in Weak Grids: 4 Hz or 30 Hz Oscillations?," *IEEE Transactions on Power Systems,* vol. 33, no. 5, pp. 5803-5804, 2018.

[47] A. Argüello, "Simplified Analytic Procedure to Calculate the Electric Variables at Steady State of Type-III and Type-IV Wind Generators," in *IEEE T&D LA 2020*, Montevideo, Uruguay, 2020.

[48] J. Liu, W. Yao, J. Wen, J. Fang, L. Jiang, H. He and S. Cheng, "Impact of Power Grid Strength and PLL Parameters on Stability of Grid-Connected DFIG Wind Farm," *IEEE Transactions on Sustainable Energy,* vol. 11, no. 1, pp. 545-557, 2020.

[49] R. Dugan, M. McGranaghan, S. Santoso and H. Beaty, Electrical Power Systems Quality, 3rd edition, McGraw-Hill Education, 2012.

[50] M. Bollen and K. Yang, "Harmonic aspects of wind power integration," *Journal of Modern Power Systems and Clean Energy,* vol. 1, pp. 14-21, 2013.

[51] M. Bollen and S. Rönnberg, "Primary and secondary harmonics emission; harmonic interaction - a set of definitions," in *7th International Conference on Harmonics and Quality of Power (ICHQP)*, Minas Gerais, Brazil, 2016.

[52] IEEE PES Wind plant Collector System Design Working Group, "Reactive Power Compensation for Wind Power Plants," in *IEEE Power and Energy Society General Meeting*, Alberta, Canada, 2009.

[53] IEEE PES Wind plant Collector System Design Working Group, "Harmonics and Resonance Issues in Wind Power Plants," in *IEEE PES General Meeting*, Detroit, USA, 2011.

[54] A. Argüello, "M.Sc. Thesis: Resonance assessment in power systems with DFIG-based wind parks," 2019. [Online]. Available: http://repositorio.unicamp.br/jspui/handle/REPOSIP/334064.

[55] R. Vazquez, M. Muñoz, M. Alonso, H. Amaris and C. Alvarez, "Background harmonic distortion measurement at power networks with wind farms," in *International Conference on Renewable Energies and Power Quality (ICREPQ)*, Madrid, Spain, 2016.

[56] C. Larose, R. Gagnon, M. F. P. Prud'Homme and M. Asmine, "Type-III Wind Power Plant Harmonic Emissions: Field Measurements and Aggregation Guidelines for Adequate Representation of Harmonics," *IEEE Transactions on Sustainable Energy,* vol. 4, no. 3, pp. 797-804, 2013.

[57] K. Yang, M. Bollen, H. Amaris and C. Alvarez, "Decompositions of harmonic propagation in wind power plant," *Electric Power Systems Research,* vol. 141, pp. 84-90, 2016.

[58] W. Xu, T. Ding, X. Li and H. Liang, "Resonance-Free Shunt Capacitors - Configurations, Design Methods and Comparative Analysis," *IEEE Transactions on Power Delivery,* vol. 31, no. 5, pp. 2287-2295, 2016.

[59] International Electrotechnical Commission (IEC), "Electromagnetic compatibility (EMC) - Part 4-30: Testing and measurement techniques - Power quality measurement methods," 2015.

[60] Illinois Center for a Smarter Electric Grid, Grainger College of Engineering, "IEEE 14 buses test system," [Online]. Available: https://icseg.iti.illinois.edu/ieee-14-bus-system/.

[61] C. Jensen, L. Kocewiak and Z. Emin, "C4-112 Amplification of Harmonic Background Distortion in Wind Power Plants with Long High Voltage Connections," CIGRE, Paris, France, 2016.

[62] Y. Fillion and S. Deschanvres, "Background harmonic amplifications within offshore wind farm connection projects," in *Int. Conf. on Power Systems Transients (IPST2015)*, Cavtat, Croatia, 2015.

[63] IEEE PES Wind Plant Collector System Design Working Group, "Harmonics and Resonance Issues in Wind Power Plants," in *IEEE PES General Meeting*, Detroit, USA, 2011.

[64] S. Papathanassiou and M. Papadopoulos, "Harmonic Analysis in a Power System with Wind Generators," *IEEE Transactions on Power Delivery,* vol. 21, no. 4, pp. 2006-2016, 2006.

[65] F. Ghassemi and K. Koo, "Equivalent Network for Wind Farm Harmonic Assessments," *IEEE Transactions on Power Delivery,* vol. 25, no. 3, pp. 1808-1815, 2010.

[66] P. Bagheri, W. Xu and K. Shaloudegi, "New Indices to Evaluate the Impact of Harmonic Currents on Power Transformers," in *18th Int. Conf. on Harmonics and Quality of Power (ICHQP)*, Ljubljana, Slovenia, 2018.

[67] IEC, "IEC 61000-4-7: Testing and measurement techniques General guide on harmonics and interharmonics measurements and instrumentation," Geneva, Switzerland, 2008.

[68] IEEE, "IEEE Std C57.110 Recommended Practice for Establishing Liquid Immersed and Dry-Type Power and Distribution Transformer Capability when Supplying Nonsinusoidal Load Currents," 2018.

[69] *IEEE Std C57.12.00 Standard for General Requirements for Liquid-Immersed Distribution, Power and Regulating Transformers,* 2015.

[70] *IEEE Std 1036 Guide for Application of Shunt Power Capacitors,* 2010.

[71] *ENEL Global Standard GSC001 Medium Voltage Cables with Rated Voltage U0/Uc(Um),* 2016.

[72] J. Das, Power System Harmonics and Passive Filter Designs, vol. 40, Wiley-IEEE Press, 2015, pp. 232-241.

[73] B. Badrzadeh and M. Gupta, "Practical Experiences and Mitigation Methods of Harmonics in Wind Power Plants," *IEEE Transactions on Industry Applications,* vol. 49, no. 5, pp. 2279-2289, 2013.

[74] E. Guest, K. Jensen and T. Rasmussen, "Mitigation of Harmonic Voltage Amplification in Offshore Wind Power Plants by Wind Turbines with Embedded Active Filters," *IEEE Transactions on Sustainable Energy,* vol. 11, no. 2, pp. 785-794, 2020.

[75] J. Das, "Passive filters - potentialities and limitations," *IEEE Transactions on Industry Applications,* vol. 40, no. 1, pp. 232-241, 2004.

[76] G. Jang, "Harmonic Mitigation Using Passive Harmonic Filters: Case Study in a Mill Power System," *MDPI Energies,* vol. 14, 2021.

[77] D. Junesco, S. Al-Youif, M. Jabbar-Mnati and M. Ali-Tofigh, "Various Passive Filter Designs Proposed for Harmonic Extenuation in Indsutrial Distribution Systems," *International Journal of Engineering & Technology,* vol. 7, pp. 75-84, 2018.

[78] X. Li, W. Xu and T. Ding, "Damped High Passive Filter - A New Filtering Scheme for Multipulse Rectifier Systems," *IEEE Transactions on Power Delivery,* vol. 32, no. 1, pp. 117-124, 2017.

[79] A. Nassif, W. Xu and W. Freitas, "An Investigation on the Selection of Filter Topologies for Passive Filter Applications," *IEEE Transactions on Power Delivery,* vol. 24, no. 3, pp. 1710-1718, 2009.

[80] T. Ding and W. Xu, "A Filtering Scheme to Reduce the Penetration of Harmonics into Transmission Systems," *IEEE Transactions on Power Delivery,* vol. 31, no. 1, pp. 59-66, 2016.

[81] K. Hasan, K. Rauma, A. Luna, J. Candela and P. Rodríguez, "Harmonic Compensation Analysis in Offshore Wind Power Plants Using Hybrid Filters," *IEEE Transactions on Industry Applications,* vol. 50, no. 3, pp. 2050-2060, 2014.

[82] IEEE, "IEEE Std 1531-2020 Guide for the Application and Specification of Harmonic Filters," 2020 .

[83] D. Gonzalez and J. McCall, "Design of filters to reduce harmonic distortion in industrial power systems," *IEEE Transactions on Industry Applications,* vol. 23, pp. 504-512, 1987.

[84] Y. Wang, P. Chen, J. Yong, W. Xu, S. Xu and K. Liu, "A Comprehensive Investigation on the Selection of High-Pass Harmonic Filters," *IEEE Transactions on Power Delivery (Early Access),* 2022.

[85] A. Zobaa, "Mixed-Integer Distributed Ant Colony Multi-Objective Optimization of Single-Tuned Passive Harmonic Filter Parameters," *IEEE Access,* vol. 7, pp. 44862-44870, 2019.

[86] H. Ginn and L. Czarnecki, "An optimization-based method for selection of resonant harmonic filter branch parameters," *IEEE Transactions on Power Delivery,* vol. 21, no. 3, pp. 1445-1451, 2006.

[87] "IEEE Std 18-2012, "IEEE Standard for Shunt Power Capacitors," (Revision of IEEE Std 18-2002)," 2013.

[88] "IEEE Std C57.16-2011, "IEEE Standard for Requirements, Terminology, and Test Code for Dry-Type Air-Core Series-Connected Reactors," (Revision of IEEE Std C57.16-1996)," 2012.

[89] "IEEE Std C37.010-2016, IEEE Application Guide for AC High-Voltage Circuit Breakers > 1000 Vac Rated on a Symmetrical Current Basis," 2016.

[90] "IEC 60871-1:2014, Shunt capacitors for A.C. power systems having a rated voltage above 1 000 V - Part 1: General," 2014.

[91] Y. Li, L. Fan and Z. Miao, "Replicating Real-World Wind Farm SSR Events," *IEEE Transaction on Power Delivery,* vol. 35, no. 1, pp. 339-348, 2020.

[92] ERCOT, "Generation - Wind Power Production historic data," [Online]. Available: http://www.ercot.com/gridinfo/generation..

[93] J. Grainger and W. Stevenson, Power System Analysis, McGraw-Hill, Inc., 1994.

[94] A. Reznik, M. Simões, A. Al-Durra and S. Muyeen, "LCL Filter Design and Performance Analysis for Grid-Interconnected Systems," *IEEE Transactions on Industry Applications,* vol. 50, no. 2, pp. 1225-1232, 2014.

[95] I. Villanueva, N. Vázquez, J. Vaquero, C. Hernández, H. López and R. Osorio, "L vs. LCL Filter for Photovoltaic Grid-Connected Inverter: A Reliability Study," *International Journal of Photoenergy,* pp. 1-10, 2020.

APPENDIX A: WIND GENERATOR MODELS

This appendix presents the expands on the models of the wind generators used in this thesis. The variables of all expressions are first defined, and the numerical values of the parameters are given. The schematics of the generators are shown in Figure A.1 and Figure A.2. The generator expressions are presented in dq frame as their control is already performed in dq frame. The Type-III generator uses a doubly-fed induction machine, whereas the Type-IV uses a permanent magnet synchronous generator.

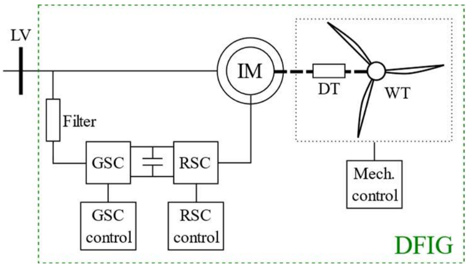

Figure A.1: Schematic of Type-III wind generator

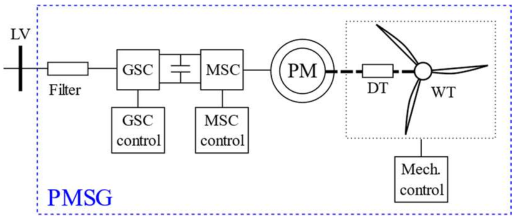

Figure A.2: Schematic of Type-IV wind generator

The generators have separate controls which change the pitch angle of the turbines for speed, torque and power regulation. In this case, they follow a maximum power point tracking algorithm depending on the available wind.

Both generators have power-electronics converter bridges of voltage source converters in back-to-back configuration, coupled by a DC bus with a capacitance. Each converter has internal current control loops which offer 2 degrees of freedom to control active power, reactive power, terminal AC bus voltage and DC bus voltage. The Type-III converter bridge is sized to 30% of the machine's rated capability (0.66 MVA), whereas the Type-IV is sized to 100% (2 MVA).

The LCL filter topology of the GSC to damp the high frequency distortion from the PWM switching is shown in Figure A.3.

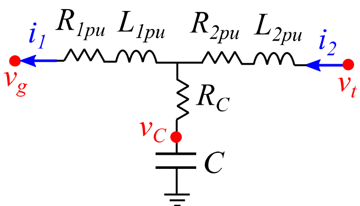

Figure A.3: LCL filter topology

Current i_2 is controlled by the converter. The filter parameters were calculated to damp the harmonics of the PWM carrier at 2700 Hz with [94].

The LCL filter topology is used in this thesis because the converter is a voltage source so it requires an inductor first at its terminals (for current source converters, a CLC filter topology is used instead). The LCL topology is more used for high power applications because it allows smaller inductor sizes and a greater flexibility for THD_V mitigation [95].

A.1 Type-III generator model

Table A.1: Type-III generator model parameters

Parameter	Value	Description
$[K_{pPLL}, K_{iPLL}]$	[15, 45]	PI control gains of the PLL
$[\omega_0, f_0]$	[120π, 60]	Grid frequency
$\omega_{fv} = \omega_{fi}$	5000π rad/s	Measurement filter cutoff frequency
$\xi_{fv} = \xi_{fi}$	0.7	Measurement filter damping coefficient
P_{nom}	2 MW	Turbine rated power
$[\lambda_{nom}, C_{pnom}]$	[9.95, 0.5]	Rated wind/rotor tip speed ratio, and power coefficient
v_{wnom}	11 m/s	Rated wind speed
ω_{wtnom}	1.2 pu	Rated rotor speed
$[c_1, c_2, c_3, c_4, c_5, c_6, c_7]$	[0.645, 116, 0.4, 5, 21, 0.0091, 0.08]	Turbine model constants
H_{wt}	4.32 s	Turbine inertia constant
$[K_{sh}, D_m]$	[1.1, 1.5]	Shaft stiffness and damping constants
$[L_{1pu}, R_{1pu}]$	[1.43, 0] pu	Inductance and resistance of RL branch closer to the converter of LCL filter
$[L_{2pu}, R_{2pu}]$	[0.18, 0] pu	Inductance and resistance of RL branch closer to the grid of LCL filter
$[C_{pu}, R_{Cpu}]$	[0.02, 1.03] pu	Capacitance and damping resistance of RC branch of LCL filter
C_{dcpu}	3.3238 pu	DC bus capacitance
$[K_{pdc}, K_{idc}]$	[8, 400]	DC bus voltage PI control gains
$[K_{pGSC}, K_{iGSC}]$	[0.83, 5]	GSC PI control gains
T_{swGSC}	1/2700 s	GSC delay time constant
$[K_{pRSC}, K_{iRSC}]$	[0.6, 8]	RSC PI control gains
T_{swRSC}	1/1620 s	RSC delay time constant
$[K_{pP}, K_{iP}]$	[0.1, 3]	Active power PI control gains
$[K_{pQ}, K_{iQ}]$	[0.1, 1]	Reactive power PI control gains
T_{ω}	5 s	Rotor speed filter time constant
$[K_{p\omega}, K_{i\omega}]$	[50, 100]	Rotor speed PI control gains
T_{β}	0.01 s	Pitch angle actuator time constant
$[L_m, L_{ls}, L_{lr}]$	[2.9, 0.18, 0.16] pu	Magnetization, stator leakage, and rotor leakage inductances
$[R_s, R_r]$	[0.023, 0.016] pu	Stator and rotor resistance
H_m	0.685 s	Induction machine inertia constant

Table A.2: Type-III generator algebraic variables

Variable	Description	Variable	Description
i_{td}, i_{tq}	Terminal currents	T_{wt}	Wind turbine torque
ω_{PLL}	PLL frequency output	T_s	Shaft torque
$\underset{m}{v_{td}}', \underset{m}{v_{tq}}'$	Meas. terminal voltage after PLL	T_e	Electric torque
$\underset{m}{i_{sd}}', \underset{m}{i_{sq}}'$	Meas. stator current after PLL	v_{gd}, v_{gq}	GSC voltage
$\underset{m}{i_{2d}}', \underset{m}{i_{2q}}'$	Meas. GSC current after PLL	v_{rd}, v_{rq}	RSC voltage
$\underset{m}{i_{rd}}', \underset{m}{i_{rq}}'$	Meas. rotor current after PLL	P_{GSC}	GSC active power
$\underset{m}{i_{td}}', \underset{m}{i_{tq}}'$	Meas. terminal current after PLL	P_{RSC}	RSC active power
$\underset{m}{P_{out}}, \underset{m}{Q_{out}}$	Terminal active and reactive power	β^{ref}	Reference blade pitch angle
i_{sd}, i_{sq}	Stator current	i_{gd}^{ref}	d axis reference current of GSC
i_{rd}, i_{rq}	Rotor current	$v_{gd}^{ref}, v_{gq}^{ref}$	Refence voltage of GSC
λ	Wind to rotor tip speeds ratio	$i_{rd}^{ref}, i_{rq}^{ref}$	Reference current of RSC
x_1, x_2	Aux. variables for turbine calculations	$v_{rd}^{ref}, v_{rq}^{ref}$	Reference voltage of RSC
C_p	Wind turbine power coefficient	ω_{r1}^{ref}	Reference rotor speed

Table A.3: Type-III generator model differential variables

Variable	Description	Variable	Description
x_{PLL}	Auxiliary variable for PLL integrator	β	Blade pitch angle
θ_{PLL}	PLL angle output	δ	Torsional shaft angle
$\underset{m}{v_{td}}, \underset{m}{v_{tq}}$	Measured terminal voltage	ω_r	Rotor speed
$\underset{m}{i_{sd}}, \underset{m}{i_{sq}}$	Measured stator current	θ_r	Rotor angle
$\underset{m}{i_{2d}}, \underset{m}{i_{2q}}$	Measured GSC current	ω_{r2}^{ref}	Reference rotor speed after filter
$\underset{m}{i_{rd}}, \underset{m}{i_{rq}}$	Measured rotor current	x_ω	Aux. variable for rotor speed control
$x_{f1}, \dots, x_{f6}$	Auxiliary variables for measurement filter	v_{dc}	DC bus voltage
i_{1d}, i_{1q}	Current of RL branch of the LCL filter closer to the grid	x_{dc}	Aux. variable for DC voltage integrator
i_{2d}, i_{2q}	Current of RL branch of the LCL filter closer to the converter	$v_{gd}^{ref\prime}, v_{gq}^{ref\prime}$	GSC reference voltage after delay
v_{Cd}, v_{Cq}	Voltage of the capacitor of the LCL filter	$v_{rd}^{ref\prime}, v_{rq}^{ref\prime}$	RSC reference voltage after delay
ψ_{sd}, ψ_{sq}	Stator flux	x_{dGSC}, x_{qGSC}	Aux. variable for GSC control integrator
ψ_{rd}, ψ_{rq}	Rotor flux	x_P, x_Q	Aux. variable for power control integrator
ω_{wt}	Wind turbine rotational speed	x_{dRSC}, x_{qRSC}	Aux. variable for RSC control integrator

Table A.4: Type-III gen. model inputs

Variable	Description
v_{td}, v_{tq}	Terminal voltage
v_w	Wind speed
v_{dc}^{ref}	DC bus voltage reference
P^{ref}, Q^{ref}	Active and reactive reference power
ω_{pu}	Grid frequency
i_{qg}^{ref}	q axis reference current of GSC

Table A.5: Type-III gen. model outputs

Variable	Description
i_{td}, i_{tq}	Terminal currents

Expressions

Terminal currents:

$$i_{td} = i_{sd} + i_{2d} \qquad\qquad i_{tq} = i_{sq} + i_{2q}$$

Phase-locked loop and measurement filters:

$$\omega_{PLL} = K_{pPLL}\underset{m}{v_{tq}'} + K_{iPLL}x_{PLL} \qquad \frac{dx_{PLL}}{dt} = \underset{m}{v_{tq}'} \qquad \frac{d\theta_{PLL}}{dt} = \omega_0 + \omega_{PLL} \qquad \begin{aligned}\theta &= \theta_{PLL} - \omega_0 t\\ \vartheta_r &= \theta_r - \omega_0\omega_r t\end{aligned}$$

$$\begin{pmatrix}\underset{m}{v_{td}'}\\ \underset{m}{v_{tq}'}\end{pmatrix} \approx \begin{pmatrix}1 & \theta\\ -\theta & 1\end{pmatrix}\begin{pmatrix}\underset{m}{v_{td}}\\ \underset{m}{v_{tq}}\end{pmatrix} \qquad \begin{pmatrix}\underset{m}{i_{rd}'}\\ \underset{m}{i_{rq}'}\end{pmatrix} \approx \begin{pmatrix}1 & \theta - \vartheta_r\\ -(\theta - \vartheta_r) & 1\end{pmatrix}\begin{pmatrix}\underset{m}{i_{rd}}\\ \underset{m}{i_{rq}}\end{pmatrix}$$

$$\begin{pmatrix}\underset{m}{i_{sd}'}\\ \underset{m}{i_{sq}'}\end{pmatrix} \approx \begin{pmatrix}1 & \theta\\ -\theta & 1\end{pmatrix}\begin{pmatrix}\underset{m}{i_{sd}}\\ \underset{m}{i_{sq}}\end{pmatrix} \qquad \begin{pmatrix}\underset{m}{i_{2d}'}\\ \underset{m}{i_{2q}'}\end{pmatrix} \approx \begin{pmatrix}1 & \theta\\ -\theta & 1\end{pmatrix}\begin{pmatrix}\underset{m}{i_{2d}}\\ \underset{m}{i_{2q}}\end{pmatrix} \qquad \begin{aligned}\underset{m}{i_{td}'} &= \underset{m}{i_{sd}'} + \underset{m}{i_{2d}'}\\ \underset{m}{i_{tq}'} &= \underset{m}{i_{sq}'} + \underset{m}{i_{2q}'}\end{aligned}$$

$$\frac{dx_{f1}}{dt} = \omega_{fv}^2\left(v_{td} - \underset{m}{v_{td}}\right) \qquad \frac{dx_{f2}}{dt} = \omega_{fv}^2\left(v_{tq} - \underset{m}{v_{tq}}\right) \qquad \frac{dx_{f3}}{dt} = \omega_{fi}^2\left(i_{2d} - \underset{m}{i_{2d}}\right)$$

$$\frac{d\underset{m}{v_{td}}}{dt} = x_{f1} - 2\omega_{fv}\xi_{fv}\underset{m}{v_{td}} \qquad \frac{d\underset{m}{v_{tq}}}{dt} = x_{f2} - 2\omega_{fv}\xi_{fv}\underset{m}{v_{tq}} \qquad \frac{d\underset{m}{i_{2d}}}{dt} = x_{f3} - 2\omega_{fi}\xi_{fi}\underset{m}{i_{2d}}$$

$$\frac{dx_{f4}}{dt} = \omega_{fi}^2\left(i_{2q} - \underset{m}{i_{2q}}\right) \qquad \frac{dx_{f5}}{dt} = \omega_{fi}^2\left(i_{rd} - \underset{m}{i_{rd}}\right) \qquad \frac{dx_{f6}}{dt} = \omega_{fi}^2\left(i_{rq} - \underset{m}{i_{rq}}\right)$$

$$\frac{d\underset{m}{i_{2q}}}{dt} = x_{f4} - 2\omega_{fi}\xi_{fi}\underset{m}{i_{2q}} \qquad \frac{d\underset{m}{i_{rd}}}{dt} = x_{f5} - 2\omega_{fi}\xi_{fi}\underset{m}{i_{rd}} \qquad \frac{d\underset{m}{i_{rq}}}{dt} = x_{f6} - 2\omega_{fi}\xi_{fi}\underset{m}{i_{rq}}$$

$$\underset{m}{P_{out}} = \underset{m}{v_{td}'}\underset{m}{i_{td}'} + \underset{m}{v_{tq}'}\underset{m}{i_{tq}'} \qquad\qquad \underset{m}{Q_{out}} = \underset{m}{v_{tq}'}\underset{m}{i_{td}'} - \underset{m}{v_{td}'}\underset{m}{i_{tq}'}$$

Turbine and drive train:

$$\lambda = K_1\frac{\omega_{wt}}{v_w} \qquad T_{wt} = \frac{K_2}{P_{nom}}\frac{C_p v_w^3}{\omega_{wt}} \qquad K_1 = \lambda_{nom}\frac{v_{wnom}}{\omega_{wtno}} \qquad K_2 = 0.75\frac{P_{nom}}{C_{pnom}v_{wnom}^3}$$

$$x_1 = (2.5 + \beta) \qquad x_2 = (\lambda + c_7 x_1)^{-1} - c_8(1 + x_1^3)^{-1} \qquad C_p = c_1(c_6\lambda + (-c_4 - c_3 x_1 + c_2 x_2)e^{-c_5 x_2})$$

$$\frac{d\omega_{wt}}{dt} = \frac{1}{2H_{wt}}(T_{wt} - T_s) \qquad \frac{d\delta}{dt} = \omega_0(\omega_{wt} - \omega_r) \qquad T_s = K_{sh}\delta + D_m(\omega_{wt} - \omega_r)$$

LCL front-end filter:

$$\frac{di_{2d}}{dt} = \frac{\omega_0}{L_{2pu}}\left(v_{td} - v_{Cd} - R_{Cpu}(i_{2d} - i_{1d}) - R_{2pu}i_{d2} + \omega_{pu}L_{2pu}i_{q2}\right)$$

$$\frac{di_{2q}}{dt} = \frac{\omega_0}{L_{2pu}}\left(v_{tq} - v_{Cq} - R_{Cpu}(i_{2q} - i_{1q}) - R_{2pu}i_{2q} - \omega_{pu}L_{2p}\ \ i_{2d}\right)$$

$$\frac{di_{1d}}{dt} = \frac{\omega_0}{L_{1pu}}\left(v_{Cd} - v_{gd} + R_{Cpu}(i_{2d} - i_{1d}) - R_{1p}\ \ i_{1d} + \omega_{pu}L_{1pu}i_{1q}\right)$$

$$\frac{di_{1q}}{dt} = \frac{\omega_0}{L_{1pu}}\left(v_{Cq} - v_{gq} + R_{Cpu}(i_{2q} - i_{1q}) - R_{1p}\ \ i_{1q} - \omega_{pu}L_{1p}\ \ i_{1d}\right)$$

$$\frac{dv_{Cd}}{dt} = \frac{\omega_0}{C_{pu}}\left(i_{2d} - i_{1d} + \omega_{pu}C_{pu}v_{Cq}\right) \qquad \frac{dv_{Cq}}{dt} = \frac{\omega_0}{C_{pu}}\left(i_{2q} - i_{1q} - \omega_{pu}C_{pu}v_{Cd}\right)$$

DC bus:

$$\frac{dv_{dc}}{dt} = \frac{\omega_0}{C_{dcpu}}\frac{(P_{GSC} - P_{RSC})}{v_{dc}} \qquad \begin{array}{l} P_{GSC} = v_{gd}i_{1d} + v_{gq}i_{1q} \\ P_{RSC} = v_{rd}i_{rd} + v_{rq}i_{rq} \end{array}$$

Speed control:

$$\omega_{r1}^{ref} = -0.67{P_{out}}_m^{\ 2} + 1.42\left(-{P_{out}}_m\right) + 0.51 \qquad \frac{d\omega_{r2}^{ref}}{dt} = \frac{1}{T_\omega}\left(\omega_{r1}^{ref} - \omega_{r2}^{ref}\right)$$

$$\beta^{ref} = K_{p\omega}\left(\omega_r - \omega_{r2}^{ref}\right) + K_{i\omega}x_\omega \qquad \frac{dx_\omega}{dt} = \omega_r - \omega_{r2}^{ref} \qquad \frac{d\beta}{dt} = \frac{1}{T_\beta}\left(\beta^{ref} - \beta\right)$$

Induction machine:

$$L_s = (L_m + L_{ls}) \qquad L_r = (L_m + L_{lr})$$

$$\frac{d\psi_{sd}}{dt} = \omega_0\left(v_{td} - R_s i_{sd} + \omega_{pu}\psi_{sq}\right) \qquad \frac{d\psi_{sq}}{dt} = \omega_0\left(v_{tq} - R_s i_{sq} - \omega_{pu}\psi_{sd}\right)$$

$$\frac{d\psi_{rd}}{dt} = \omega_0\left(v_{rd} - R_r i_{rd} + (\omega_{pu} - \omega_r)\psi_{rq}\right) \qquad \frac{d\psi_{rq}}{dt} = \omega_0\left(v_{rq} - R_r i_{rq} - (\omega_{pu} - \omega_r)\psi_{rd}\right)$$

$$i_{sd} = -\frac{L_r}{({L_m}^2 - L_sL_r)}\psi_{sd} + \frac{L_o}{({L_m}^2 - L_sL_r)}\psi_{rd} \qquad i_{sq} = -\frac{L_r}{({L_m}^2 - L_sL_r)}\psi_{sq} + \frac{L_o}{({L_m}^2 - L_sL_r)}\psi_{rq}$$

$$i_{rd} = \frac{L_o}{({L_m}^2 - L_sL_r)}\psi_{sd} - \frac{L_s}{({L_m}^2 - L_sL_r)}\psi_{rd} \qquad i_{rq} = \frac{L_o}{({L_m}^2 - L_sL_r)}\psi_{sq} - \frac{L_s}{({L_m}^2 - L_sL_r)}\psi_{rq}$$

$$T_e = \left(\psi_{sd}i_{sq} - \psi_{sq}i_{sd}\right) \qquad \frac{d\omega_r}{dt} = \frac{1}{2H_m}\left(T_s + T_e - F\omega_r\right) \qquad \frac{d\theta_r}{dt} = \omega_0\omega_r$$

Grid-side converter control and average model:

$$i_{gd}^{ref} = K_{pdc}\left(v_{dc}^{ref} - v_{dc}\right) + K_{idc}x_{dc} \qquad \frac{dx_{dc}}{dt} = v_{dc}^{ref} - v_{dc} \qquad i_{gq}^{ref} = 0$$

$$v_{gd}^{ref} = -K_{pGSC}\left(i_{gd}^{ref} - {i_{2d}'}_m\right) - K_{iGSC}x_{dGSC} + \frac{\omega_{PLL}}{\omega_0}\left(L_{1pu} + L_{2pu}\right){i_{2q}'}_m \qquad \frac{dx_{dGSC}}{dt} = i_{gd}^{ref} - {i_{2d}'}_m$$

$$v_{gq}^{ref} = -K_{pGSC}\left(i_{gq}^{ref} - {i_{2q}'}_m\right) - K_{iGSC}\ \ {}_{qGSC} - \frac{\omega_{PLL}}{\omega_0}\left(L_{1pu} + L_{2p}\ \ \right){i_{2d}'}_m \qquad \frac{dx_{qGSC}}{dt} = i_{gq}^{ref} - {i_{2q}'}_m$$

$$\begin{array}{l} v_{gd}^{ref\prime} = v_{gd}^{ref}e^{-T_{swGSC}s} \\ v_{gq}^{ref\prime} = v_{gq}^{ref}e^{-T_{swGSC}s} \end{array} \quad \text{(see Appendix A.3)} \qquad \begin{pmatrix} v_{gd} \\ v_{gq} \end{pmatrix} \approx \begin{pmatrix} 1 & -\theta \\ \theta & 1 \end{pmatrix}\begin{pmatrix} v_{gd}^{ref\prime} \\ v_{gq}^{ref\prime} \end{pmatrix}$$

Rotor-side converter control and average model:

$$i_{rd}^{ref} = K_{pP}\left(-P^{ref} + \underset{m}{P_{out}}\right) + K_{iP}x_P \qquad i_{rq}^{ref} = K_{pQ}\left(Q^{ref} - \underset{m}{Q_{out}}\right) + K_{iQ}x_Q$$

$$\frac{dx_P}{dt} = -P^{ref} + \underset{m}{P_{out}} \qquad \frac{dx_Q}{dt} = Q^{ref} - \underset{m}{Q_{out}}$$

$$v_{rd}^{ref} = K_{pRSC}\left(i_{rd}^{ref} - \underset{m}{i_{rd}'}\right) + K_{iRSC}x_{dRSC} - \left(\frac{\omega_{PLL}}{\omega_0} - \omega_r\right)(L_{ls} + L_{lr})\underset{m}{i_{rq}'} \qquad \frac{dx_{dRSC}}{dt} = i_{rd}^{ref} - \underset{m}{i_{rd}'}$$

$$v_{rq}^{ref} = K_{pRSC}\left(i_{rq}^{ref} - \underset{m}{i_{rq}'}\right) + K_{iRSC}x_{qRSC} + \left(\frac{\omega_{PLL}}{\omega_0} - \omega_r\right)(L_{ls} + L_{lr})\underset{m}{i_{rd}'} \qquad \frac{dx_{qRSC}}{dt} = i_{rq}^{ref} - \underset{m}{i_{rq}'}$$

$$\begin{array}{l} v_{rd}^{ref\prime} = v_{rd}^{ref} e^{-T_{swRSC}s} \\ v_{rq}^{ref\prime} = v_{rq}^{ref} e^{-T_{swRSC}s} \end{array}$$

(see Appendix A.3)

$$\begin{pmatrix} v_{rd} \\ v_{rq} \end{pmatrix} \approx \begin{pmatrix} 1 & -(\theta - \vartheta_r) \\ \theta - \vartheta_r & 1 \end{pmatrix} \begin{pmatrix} v_{rd}^{ref\prime} \\ v_{rq}^{ref\prime} \end{pmatrix}$$

A.2 Type-IV generator model

Table A.6: Type-IV generator model parameters

Parameter	Value	Description
$[K_{pPLL}, K_{iPLL}]$	[15, 45]	PLL PI control gains
$[\omega_0, f_0]$	[120π, 60]	Grid frequency
$\omega_{fv} = \omega_{fi}$	5000π	Measurement filter cutoff frequency
$\xi_{fv} = \xi_{fi}$	0.7	Measurement filter damping
$[L_{1pu}, R_{1pu}]$	[0.48, 0] pu	Inductance and resistance of RL branch closer to the converter of LCL filter
$[L_{2pu}, R_{2pu}]$	[0.06, 0] pu	Inductance and resistance of RL branch closer to the grid of LCL filter
$[C_{pu}, R_{Cpu}]$	[0.06, 0.34] pu	Capacitance and damping resistance of the LCL filter
H_m	0.5 s	PMSG machine inertia constant
D_m	0.01	PMSG damping constant
ϕ_{pmpu}	1.1884 pu	Magnetic flux constant of PMSG
$[L_d, L_q]$	[0.7, 1.11] pu	dq stator inductances of PMSG
R_s	0.017 pu	Stator resistance of PMSG
C_{dcpu}	3.3238 pu	DC bus capacitance
$[K_{pdc}, K_{idc}]$	[8, 400]	DC bus voltage PI control gains
$[K_{pQ}, K_{iQ}]$	[0.1 ,1]	Reactive power PI control gains
$[K_{pGSC}, K_{iGSC}]$	[0.83, 5]	GSC PI control gains
$[K_{pP}, K_{iP}]$	[1, 3]	Active power PI control gains
$[K_{pMSC}, K_{iMSC}]$	[0.1361, 2.7221]	MSC PI control gains
T_{swGSC}	1/2700 s	GSC delay time constant
T_{swMSC}	1/1620 s	MSC delay time constant
T_ω	3 s	Rotor speed filter time constant
$[K_{p\omega}, K_{i\omega}]$	[50, 10]	Rotor speed PI control gains
$[K_{sh}, D_{mwt}]$	[1.1, 1.5]	Shaft stiffness and damping constants
T_β	0.01 s	Pitch angle actuator time constant
H_{wt}	2.5 s	Wind turbine inertia constant
$[\omega_m^{nom}, \omega_r^{nom}]$	[3.8124, 1.1] pu	Rated mechanical and electric speeds
R	33.05 m	Turbine rotor radius
S_{nom}	$1.5\text{x}10^6$ VA	Generator rated power
ρ	1.12 kg/m^3	Air density

Table A.7: Type-IV generator model algebraic variables

Variable	Description	Variable	Description
i_{td}, i_{td}	Terminal currents	P_{GSC}	GSC active power
ω_{PLL}	PLL frequency output	P_{MSC}	MSC active power
v_{td_m}', v_{tq_m}'	Measured terminal voltage after PLL	$i_{gd}^{ref}, i_{gq}^{ref}$	Reference current of GSC
v_{md_m}', v_{mq_m}'	Measured stator voltage after PLL	$v_{gd}^{ref}, v_{gq}^{ref}$	Reference voltage of GSC
i_{2d_m}', i_{2q_m}'	Measured GSC current after PLL	i_{mq}^{ref}	q axis reference current of MSC
i_{md_m}', i_{mq_m}'	Measured MSC current after PLL	$v_{md}^{ref}, v_{mq}^{ref}$	Refence voltage of MSC
P_{out_m}, Q_{out_m}	Terminal active and reactive power	ω_r^{ref}	Reference rotor speed
v_{gd}, v_{gq}	GSC voltage	β^{ref}	Reference blade pitch angle
T_m	Mechanical torque	T_t	Turbine torque
T_e	Electric torque	C_p	Wind turbine power coefficient
v_{md}, v_{mq}	MSC voltage	λ	Wind to rotor tip speeds ratio

Table A.8: Type-IV generator model differential variables

Variable	Description	Variable	Description
x_{PLL}	Auxiliary variable for PLL integrator	v_{dc}	DC bus voltage
θ_{PLL}	PLL angle output	x_{dc}	Auxiliary variable for DC voltage integrator
θ_r	Rotor angle	x_P, x_Q	Auxiliary variable for power control integrator
v_{td_m}, v_{tq_m}	Measured terminal voltage	$v_{gd}^{ref\prime}, v_{gq}^{ref\prime}$	GSC reference voltage after delay
i_{2d_m}, i_{2q_m}	Measured GSC current	$v_{md}^{ref\prime}, v_{mq}^{ref\prime}$	MSC reference voltage after delay
i_{md_m}, i_{mq_m}	Measured PMSG stator current	$\omega_r^{ref\prime}$	Reference rotor speed after filter
$x_{f1}, \dots, x_{f6}$	Auxiliary variables for measurement filters	x_ω	Auxiliary variable for rotor speed control
i_{1d}, i_{1q}	Current of RL branch of the LCL filter closer to the grid	β	Blade pitch angle
i_{2d}, i_{2q}	Current of RL branch of the LCL filter closer to the converter	δ	Torsional shaft angle
v_{Cd}, v_{Cq}	Voltage of the capacitor of the LCL filter	ω_{wt}	Wind turbine rotational speed
i_{md}, i_{mq}	PMSG stator current	x_{dGSC}, x_{qGSC}	Auxiliary variable for GSC control integrator
ω_r	Rotor speed	x_{dMSC}, x_{qMSC}	Auxiliary variable for MSC control integrator

Table A.9: Type-IV gen. model inputs

Variable	Description
v_{td}, v_{tq}	Terminal voltage
v_w	Wind speed
v_{dc}^{ref}	DC bus voltage reference
P^{ref}, Q^{ref}	Active and reactive reference power
ω_{pu}	Grid frequency
i_{md}^{ref}	d axis reference current of MSC

Table A.10: Type-IV gen. model outputs

Variable	Description
i_{td}, i_{tq}	Terminal currents

Expressions:

Terminal currents:

$$i_{td} = i_{2d} \qquad\qquad i_{tq} = i_{2q}$$

PLL and measurements:

$$\omega_{PLL} = K_{pPLL}\underset{m}{v_{tq}}' + K_{iPLL}x_{PLL} \qquad \frac{dx_{PLL}}{dt} = \underset{m}{v'_{tq}} \qquad \frac{d\theta_{PLL}}{dt} = \omega_0 + \omega_{PLL} \qquad \begin{matrix} \theta = \theta_{PLL} - \omega_0 t \\ \theta_{r2} = \theta_r + \pi \end{matrix}$$

$$\begin{pmatrix} \underset{m}{v_{md}}' \\ \underset{m}{v_{mq}}' \end{pmatrix} \approx \begin{pmatrix} 1 & \theta_{r2} \\ -\theta_{r2} & 1 \end{pmatrix} \begin{pmatrix} \underset{m}{v_{md}} \\ \underset{m}{v_{mq}} \end{pmatrix} \qquad \begin{pmatrix} \underset{m}{v_{td}}' \\ \underset{m}{v_{tq}}' \end{pmatrix} \approx \begin{pmatrix} 1 & \theta \\ -\theta & 1 \end{pmatrix} \begin{pmatrix} \underset{m}{v_{td}} \\ \underset{m}{v_{tq}} \end{pmatrix}$$

$$\begin{pmatrix} \underset{m}{i_{2d}}' \\ \underset{m}{i_{2q}}' \end{pmatrix} \approx \begin{pmatrix} 1 & \theta \\ -\theta & 1 \end{pmatrix} \begin{pmatrix} \underset{m}{i_{2d}} \\ \underset{m}{i_{2q}} \end{pmatrix} \qquad \begin{pmatrix} \underset{m}{i_{md}}' \\ \underset{m}{i_{mq}}' \end{pmatrix} \approx \begin{pmatrix} 1 & \theta_{r2} \\ -\theta_{r2} & 1 \end{pmatrix} \begin{pmatrix} \underset{m}{i_{md}} \\ \underset{m}{i_{mq}} \end{pmatrix}$$

$$\frac{dx_{f1}}{dt} = \omega_{fv}{}^2\left(v_{td} - \underset{m}{v_{td}}\right) \qquad \frac{dx_{f2}}{dt} = \omega_{fv}{}^2\left(v_{tq} - \underset{m}{v_{tq}}\right) \qquad \frac{dx_{f3}}{dt} = \omega_{fi}{}^2\left(i_{2d} - \underset{m}{i_{2d}}\right)$$

$$\frac{d\underset{m}{v_{td}}}{dt} = x_{f1} - 2\omega_{fv}\xi_{fv}\underset{m}{v_{td}} \qquad \frac{d\underset{m}{v_{tq}}}{dt} = x_{f2} - 2\omega_{fv}\xi_{fv}\underset{m}{v_{tq}} \qquad \frac{d\underset{m}{i_{2d}}}{dt} = x_{f3} - 2\omega_{fi}\xi_{fi}\underset{m}{i_{2d}}$$

$$\frac{dx_{f4}}{dt} = \omega_{fi}{}^2\left(i_{2q} - \underset{m}{i_{2q}}\right) \qquad \frac{dx_{f7}}{dt} = \omega_{fi}{}^2\left(i_{md} - \underset{m}{i_{md}}\right) \qquad \frac{dx_{f8}}{dt} = \omega_{fi}{}^2\left(i_{mq} - \underset{m}{i_{mq}}\right)$$

$$\frac{d\underset{m}{i_{2q}}}{dt} = x_{f4} - 2\omega_{fi}\xi_{fi}i_{2q} \qquad \frac{d\underset{m}{i_{md}}}{dt} = x_{f7} - 2\omega_{fi}\xi_{fi}\underset{m}{i_{md}} \qquad \frac{d\underset{m}{i_{mq}}}{dt} = x_{f8} - 2\omega_{fi}\xi_{fi}i_{mq}$$

$$\underset{m}{P_{out}} = -\left(\underset{m}{v_{td}}'\underset{m}{i_{2d}}' + \underset{m}{v_{tq}}'\underset{m}{i_{2q}}'\right) \qquad \underset{m}{Q_{out}} = -\left(\underset{m}{v_{tq}}'\underset{m}{i_{2d}}' - \underset{m}{v_{td}}'\underset{m}{i_{2q}}'\right)$$

LCL front-end filter:

$$\frac{di_{2d}}{dt} = \frac{\omega_0}{L_{2pu}}\left(v_{td} - v_{Cd} - R_{Cpu}(i_{2d} - i_{1d}) - R_{2pu}i_{d2} + \omega_{pu}L_{2pu}i_{q2}\right)$$

$$\frac{di_{2q}}{dt} = \frac{\omega_0}{L_{2pu}}\left(v_{tq} - v_{Cq} - R_{Cpu}(i_{2q} - i_{1q}) - R_{2pu}i_{2q} - \omega_{pu}L_{2p}\ \ i_{2d}\right)$$

$$\frac{di_{1d}}{dt} = \frac{\omega_0}{L_{1pu}}\left(v_{Cd} - v_{gd} + R_{Cpu}(i_{2d} - i_{1d}) - R_{1pu}i_{1d} + \omega_{pu}L_{1p}\ \ i_{1q}\right)$$

$$\frac{di_{1q}}{dt} = \frac{\omega_0}{L_{1pu}}\left(v_{Cq} - v_{gq} + R_{Cpu}(i_{2q} - i_{1q}) - R_{1p}\ \ i_{1q} - \omega_{pu}L_{1pu}i_{1d}\right)$$

$$\frac{dv_{Cd}}{dt} = \frac{\omega_0}{C_{pu}}\left(i_{2d} - i_{1d} + \omega_{pu}C_{pu}v_{Cq}\right) \qquad \frac{dv_{Cq}}{dt} = \frac{\omega_0}{C_{pu}}\left(i_{2q} - i_{1q} - \omega_{pu}C_{pu}v_{Cd}\right)$$

Permanent magnet synchronous generator:

$$\frac{d\omega_r}{t} = \frac{\omega_0}{2H_m}(T_m + T_e - D_m\omega_r) \qquad \frac{d\theta_r}{dt} = \omega_0\omega_r \qquad T_e = \phi_{pmpu}i_{mq} + i_{md}i_{mq}\left(L_d - L_q\right)$$

$$\frac{di_{md}}{dt} = \frac{\omega_0}{L_d}\left(v_{md} - R_s i_{md} + \omega_r L_q i_{mq}\right) \qquad \frac{di_{mq}}{dt} = \frac{\omega_0}{L_q}\left(v_{mq} - R_s i_{mq} - \omega_r L_d i_{md} - \omega_r\phi_{pmpu}\right)$$

DC bus:

$$\frac{dv_{dc}}{dt} = \frac{\omega_0}{C_{dcpu}} \frac{(P_{GSC} - P_{MSC})}{v_{dc}} \qquad P_{GSC} = v_{gd} i_{1d} + v_{gq} i_{1q}$$
$$P_{MSC} = v_{md} i_{md} + v_{mq} i_{mq}$$

Grid-side converter control and average model:

$$i_{gd}^{ref} = K_{pdc}\left(v_{dc}^{ref} - v_{dc}\right) + K_{idc} x_{dc} \qquad \frac{dx_{dc}}{dt} = v_{dc}^{ref} - v_{dc}$$

$$i_{gq}^{ref} = K_{pQ}\left(Q^{ref} - \underset{m}{Q_{out}}\right) + K_{iQ} x_Q \qquad \frac{dx_Q}{dt} = Q^{ref} - \underset{m}{Q_{out}}$$

$$v_{gd}^{ref} = -K_{pGSC}\left(i_{gd}^{ref} - \underset{m}{i_{2d}{}'}\right) - K_{iGSC} x_{dGSC} + \frac{\omega_{PLL}}{\omega_0}\left(L_{1pu} + L_{2pu}\right)\underset{m}{i_{2q}{}'} \qquad \frac{dx_{dGSC}}{dt} = i_{gd}^{ref} - \underset{m}{i_{2d}{}'}$$

$$v_{gq}^{ref} = -K_{pGSC}\left(i_{gq}^{ref} - \underset{m}{i_{2q}{}'}\right) - K_{iGSC} x_{qGSC} - \frac{\omega_{PLL}}{\omega_0}\left(L_{1pu} + L_{2pu}\right)\underset{m}{i_{2d}{}'} \qquad \frac{dx_{qGSC}}{dt} = i_{gq}^{ref} - \underset{m}{i_{2q}{}'}$$

$$v_{gd}^{ref'} = v_{gd}^{ref} e^{-T_{swGSC}s}$$
$$v_{gq}^{ref'} = v_{gq}^{ref} e^{-T_{swGSC}s} \quad \text{(see Appendix A.3)} \qquad \begin{pmatrix} v_{gd} \\ v_{gq} \end{pmatrix} \approx \begin{pmatrix} 1 & -\theta \\ \theta & 1 \end{pmatrix} \begin{pmatrix} v_{gd}^{ref'} \\ v_{gq}^{ref'} \end{pmatrix}$$

Machine-side converter control and average model:

$$i_{md}^{ref} = 0 \qquad i_{mq}^{ref} = \frac{K_{pP}}{\phi_{pmpu}}\left(P^{ref} - \underset{m}{P_{out}}\right) + \frac{K_{iP}}{\phi_{pmpu}} x_P \qquad \frac{dx_P}{dt} = P^{ref} - \underset{m}{P_{out}}$$

$$v_{md}^{ref} = K_{pMSC}\left(i_{md}^{ref} - \underset{m}{i_{md}{}'}\right) + K_{iMSC} x_{dMSC} - \omega_r L_q \underset{m}{i_{mq}{}'} \qquad \frac{dx_{dMSC}}{dt} = i_{md}^{ref} - \underset{m}{i_{md}{}'}$$

$$v_{mq}^{ref} = K_{pMSC}\left(i_{mq}^{ref} - \underset{m}{i_{mq}{}'}\right) + K_{iMSC} x_{qMSC} + \omega_r L_d \underset{m}{i_{md}{}'} + \omega_r \phi_{pmpu} \qquad \frac{dx_{qMSC}}{dt} = i_{qm}^{ref} - \underset{m}{i_{mq}{}'}$$

$$v_{md}^{ref'} = v_{md}^{ref} e^{-T_{swMSC}s}$$
$$v_{mq}^{ref'} = v_{mq}^{ref} e^{-T_{swMSC}s} \quad \text{(see Appendix A.3)} \qquad \begin{pmatrix} v_{md} \\ v_{mq} \end{pmatrix} \approx \begin{pmatrix} 1 & -\theta_{r2} \\ \theta_{r2} & 1 \end{pmatrix} \begin{pmatrix} v_{md}^{ref'} \\ v_{mq}^{ref'} \end{pmatrix}$$

Speed and pitch angle control:

$$\omega_r^{ref} = \sqrt[3]{\underset{m}{P_{out}}} \qquad \frac{dx_\omega}{dt} = \omega_r - \omega_r^{ref'} \qquad \frac{d\omega_r^{ref'}}{dt} = \frac{1}{T_\omega}\left(\omega_r^{ref} - \omega_r^{ref'}\right) \qquad \beta^{ref} = K_{p\omega}\left(\omega_r - \omega_r^{ref'}\right) + K_{i\omega} x_\omega$$

Turbine, drive train and pitch mechanism:

$$\frac{d\beta}{dt} = \frac{1}{T_\beta}\left(\beta^{ref} - \beta\right) \qquad T_m = K_{sh}\delta + D_{mwt}(\omega_{wt} - \omega_r) \qquad \frac{d\delta}{dt} = \omega_0(\omega_{wt} - \omega_r) \qquad \frac{d\omega_{wt}}{dt} = \frac{1}{2H_{wt}}(T_t - T_m)$$

$$\lambda = \frac{R \frac{\omega_m^{nom}}{\omega_r^{nom}} \omega_{wt}}{v_w} \qquad T_t = \frac{1}{\omega_{wt}} \frac{1}{S_{nom}} \frac{\rho \pi \;^{2}}{2} C_p {v_w}^3 \qquad C_p = (0.44 - 0.0167\beta) \sin\left(\frac{\pi}{15}(\lambda - 3) - 0.3\beta\right) - 0.00184(\lambda - 3)\beta$$

A.3 Padé expansion of negative exponential function

The delay in the converters due to the control algorithm is modeled by a dead-time, which in frequency domain has an exponential transfer function $F_d(s)$. Such function can be represented by a polynomial expansion as follows:

$$F_d(s) = e^{-T_d s} = \frac{b_0 + b_1 T_d s + \ldots + b_l (T_d s)^l}{a_0 + a_1 T_d s + \ldots + a_k (T_d s)^k}$$

$$a_i = \frac{(l+k-i)!k!}{i!(k-i)!} \qquad\qquad b_j = (-1)^j \frac{(l+k-j)!l!}{j!(l-j)!}$$

where l is the maximum order of the numerator, k the maximum order from the denominator, j corresponds to the j-th term of the numerator and i corresponds to the i-th term of the denominator.

This thesis truncates the transfer function to $l = 5$ and $k = 5$ because the phase is accurate up to 2500 Hz, which is sufficient to model the generators up to 1500 Hz for the resonance studies in the harmonic range of frequencies.

Finally, it is possible to represent the polynomial expansion up to the 5th order by a state-space model (time-domain) with auxiliary variables $X_1, \ldots, X_5$ input x^{ref} and output x, as follows:

$$\frac{d}{dt}\begin{pmatrix} X_1 \\ X_2 \\ X_3 \\ X_4 \\ X_5 \end{pmatrix} = \begin{pmatrix} 0 & 1 & 0 & 0 & 0 \\ 0 & 0 & 1 & 0 & 0 \\ 0 & 0 & 0 & 1 & 0 \\ 0 & 0 & 0 & 0 & 1 \\ -\frac{1}{a_5 {T_d}^5} a_0 & -\frac{1}{a_5 {T_d}^4} a_1 & -\frac{1}{a_5 {T_d}^3} a_2 & -\frac{1}{a_5 {T_d}^2} a_3 & -\frac{1}{a_5 T_d} a_4 \end{pmatrix} \begin{pmatrix} X_1 \\ X_2 \\ X_3 \\ X_4 \\ X_5 \end{pmatrix} + \begin{pmatrix} 0 \\ 0 \\ 0 \\ 0 \\ \frac{1}{a_5 {T_d}^5} \end{pmatrix} x^{ref}$$

$$x = \left(\left(b_0 - \frac{b_5}{a_5} a_0\right) \quad \left(b_1 - \frac{b_5}{a_5} a_1\right) T_d \quad \left({}_2 - \frac{b_5}{a_5} a_2\right) {T_d}^2 \quad \left(b_3 - \frac{b_5}{a_5} a_3\right) {T_d}^3 \quad \left(b_4 - \frac{b_5}{a_5} a_4\right) {T_d}^4 \right) \begin{pmatrix} X_1 \\ X_2 \\ X_3 \\ X_4 \\ X_5 \end{pmatrix} + \left(\frac{b_5}{a_5}\right) x^{ref}$$

The a and b coefficients are:

$[a_0, a_1, a_2, a_3, a_4, a_5] = [1, 0.5000, 0.1111, 0.0139, 9.9206\times10^{-4}, 3.3069\times10^{-5}]$

$[b_0, b_1, b_2, b_3, b_4, b_5] = [1, -0.5000, 0.1111, -0.0139, 9.9206\times10^{-4}, -3.3069\times10^{-5}]$

APPENDIX B: DESCRIPTOR STATE SPACE HANDLING

This appendix shows how to expand or simplify the descriptor-state space model.

Adding a component

The DC voltage control is chosen for this example. Initially, one must consider the DC bus voltage control loop expressions:

$$i_{gd}^{ref} = K_{pdc}\left(v_{dc}^{ref} - v_{dc}\right) + K_{idc}x_{dc} \qquad \frac{dx_{dc}}{dt} = v_{dc}^{ref} - v_{dc}$$

where v_{dc}^{ref} is an input, i_{dg}^{ref} is an algebraic variable, and x_{dc} is a differential variable. The DC bus voltage v_{dc} is initially considered an input to the model. Thus, the linearized descriptor-state space version can be written as follows:

$$\begin{pmatrix} 0 & 0 \\ 0 & 1 \end{pmatrix}\dot{\begin{pmatrix} \Delta i_{dg}^{ref} \\ \Delta x_{dc} \end{pmatrix}} = \begin{pmatrix} -1 & K_{idc} \\ 0 & 0 \end{pmatrix}\begin{pmatrix} \Delta i_{dg}^{ref} \\ \Delta x_{dc} \end{pmatrix} + \begin{pmatrix} K_{pdc} & -K_{pdc} \\ 1 & -1 \end{pmatrix}\begin{pmatrix} \Delta v_{dc}^{ref} \\ \Delta v_{dc} \end{pmatrix}$$

Now, the model is enhanced by describing the DC bus voltage dynamics (linearized with the Δ operator around v_{dc0} = 1 pu, and $P_{GSC0} = P_{RSC0}$ where P_{GSC} and P_{RSC} are the active power flow from the GSC and RSC):

$$\dot{v}_{dc} = \frac{\omega_0}{C_{dc}v_{dc}}(P_{GSC} - P_{RSC}) \rightarrow \Delta\dot{v}_{dc} = \frac{\omega_0}{C_{dc}}[(\Delta P_{GSC} - \Delta P_{RSC}) - 0\Delta v_{dc}]$$

So v_{dc} is now a differential variable, P_{GSC} and P_{RSC} are inputs, and the state-space becomes:

$$\begin{pmatrix} 000 \\ 010 \\ 001 \end{pmatrix}\dot{\begin{pmatrix} \Delta i_{dg}^{ref} \\ \Delta x_{dc} \\ \Delta v_{dc} \end{pmatrix}} = \begin{pmatrix} -1 & K_{idc} & -K_{pdc} \\ 0 & 0 & -1 \\ 0 & 0 & 0 \end{pmatrix}\begin{pmatrix} \Delta i_{dg}^{ref} \\ \Delta x_{dc} \\ \Delta v_{dc} \end{pmatrix} + \begin{pmatrix} K_{pdc} & 0 & 0 \\ 1 & 0 & 0 \\ 0 & \omega_0 C_{dc}^{-1} & -\omega_0 C_{dc}^{-1} \end{pmatrix}\begin{pmatrix} \Delta v_{dc}^{ref} \\ \Delta P_{GSC} \\ \Delta P_{RSC} \end{pmatrix}$$

where the ***A*** and ***B*** matrices of the descriptor state space are split into the following subsets:

$$\boldsymbol{A} = \begin{pmatrix} [-1] & [K_{idc} \quad -K_{pdc}] \\ \begin{bmatrix} 0 \\ 0 \end{bmatrix} & \begin{bmatrix} 0 & -1 \\ 0 & 0 \end{bmatrix} \end{pmatrix} \qquad \boldsymbol{B} = \begin{pmatrix} [K_{pdc} \quad 0 \quad 0] \\ \begin{bmatrix} 1 & 0 & 0 \\ 0 & \omega_0 C_{dc}^{-1} & -\omega_0 C_{dc}^{-1} \end{bmatrix} \end{pmatrix}$$

Removing a component

The PLL is used in this example. The voltages measured at generator terminals are described by:

$$\omega_{PLL} = K_{pPLL}v_{tqm}' + K_{iPLL}x_{PLL} \qquad \frac{dx_{PLL}}{dt} = v_{tqm}' \qquad \frac{d\theta_{PLL}}{dt} = \omega_0 + \omega_{PLL} \qquad \begin{pmatrix} v_{tdm}' \\ v_{tdm}' \end{pmatrix} \approx \begin{pmatrix} 1 & \theta_{PLL} \\ -\theta_{PLL} & 1 \end{pmatrix}\begin{pmatrix} v_{tdm} \\ v_{tdm} \end{pmatrix}$$

The system is expressed by the following descriptor state space after linearization:

$$\begin{pmatrix}00000\\00000\\00000\\00010\\00001\end{pmatrix}\overset{\bullet}{\begin{pmatrix}\Delta v_{dtm}{}'\\\Delta v_{qtm}{}'\\\Delta\omega_{PLL}\\\Delta\theta_{PLL}\\\Delta x_{PLL}\end{pmatrix}}=\begin{pmatrix}-1&0&0&v_{qtm0}&0\\0&-1&0&-v_{dtm0}&0\\0&K_{pPLL}&-1&0&K_{iPLL}\\0&0&\omega_0&0&0\\0&1&0&0&0\end{pmatrix}\begin{pmatrix}\Delta v_{dtm}{}'\\\Delta v_{qtm}{}'\\\Delta\omega_{PLL}\\\Delta\theta_{PLL}\\\Delta x_{PLL}\end{pmatrix}+\begin{pmatrix}1&\theta_{PLL0}\\-\theta_{PLL0}&1\\0&0\\0&0\\0&0\end{pmatrix}\begin{pmatrix}\Delta v_{dtm}\\\Delta v_{qtm}\end{pmatrix}$$

The effect of the PLL on the terminal voltages which enter the controllers can be removed by simply eliminating the rows and columns of $\boldsymbol{E}$, $\boldsymbol{A}$ and $\boldsymbol{B}$ corresponding to ω_{PLL}, θ_{PLL} and x_{PLL}, and forcing any remaining variables in the expressions to 0 as follows:

$$\begin{pmatrix}00\\00\end{pmatrix}\overset{\bullet}{\begin{pmatrix}\Delta v_{dtm}{}'\\\Delta v_{qtm}{}'\end{pmatrix}}=\begin{pmatrix}-1&0\\0&-1\end{pmatrix}\begin{pmatrix}\Delta v_{dtm}{}'\\\Delta v_{qtm}{}'\end{pmatrix}+\begin{pmatrix}1&0\\0&1\end{pmatrix}\begin{pmatrix}\Delta v_{dtm}\\\Delta v_{qtm}\end{pmatrix}$$

APPENDIX C: SIMPLIFIED WIND GENERATOR IMPEDANCE MODELS

Table C.1 lists all subsystems per frequency range for both wind generators. According to the sensitivity of the impedance profiles, quantified with the MAS index from Section 2.5, each subsystem is tagged with the following code: ✓ must be modeled; and X can be neglected. In short, all subsystems tagged with a ✓ conform a recommendation of the minimal set of subsystems to be included in the impedance model in order to have a good accuracy for resonance studies in the following ranges of frequency: 1) Sub-synchronous range (SSR) from 0 Hz o 40 Hz; 2) Near synchronous range (NSR) from 40 Hz to 80 Hz; and 3) Harmonic frequency range (HFR) from 80 Hz to 1500 Hz.

The column "Lit." presents a simple model for the generators used in the literature for harmonic resonance analysis, and even some sub-synchronous resonance studies [24].

The decoupled positive sequence profiles of the models in Table C.1 are shown in Figure C.1 to Figure C.3. Notice the recommended "simplified" models match the "full" original model. The "literature" model has a poor match in the SSR, the NSR, and the resistance of the HFR, so it is only reliable to determine resonance frequency values for harmonic resonance studies, but not their damping, which is required for stability studies.

Table C.1: Recommended subsystems for impedance modeling of wind generators

Component	Type-III generator				Type-IV generator			
	SSR	NSR	HFR	Lit.	SSR	NSR	HFR	Lit.
Control delay	X	X	✓	✓	X	X	✓	✓
Voltage and current filter	X	X	✓	X	X	X	✓	X
Active power control	X	✓	X	X	X	X	X	X
Reactive power control	X	✓	X	X	✓	✓	✓	X
DC bus voltage control	✓	✓	✓	X	✓	✓	✓	X
PLL	✓	✓	X	X	✓	✓	X	X
GSC current control	✓	✓	✓	✓	✓	✓	✓	✓
RSC / MSC current control	✓	✓	✓	✓	X	X	X	X
Speed control and turbine	X	X	X	X	X	X	X	X
DC bus capacitor	✓	✓	✓	X	✓	✓	✓	X

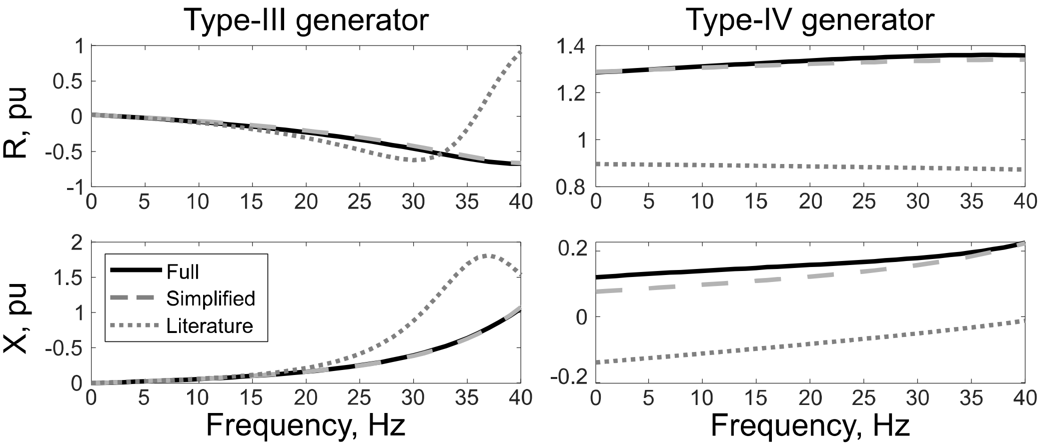

Figure C.1: Impedances in the SSR

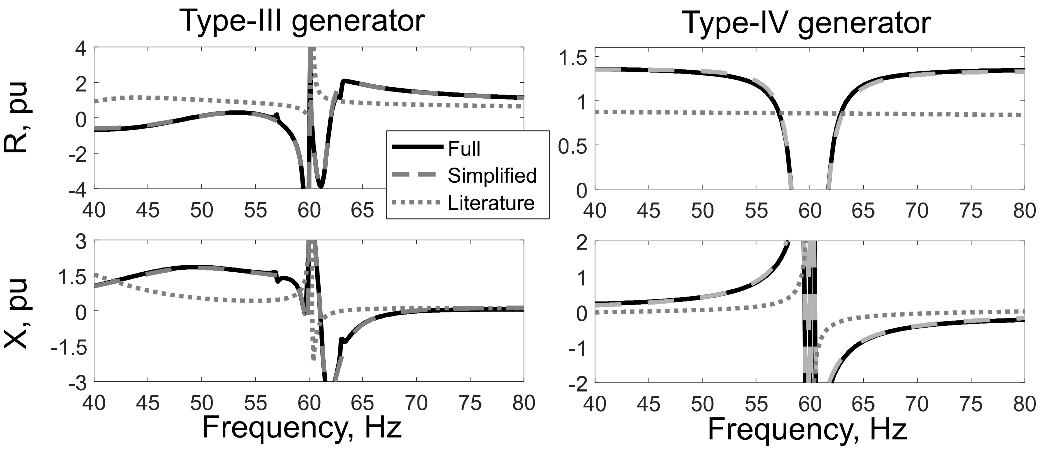

Figure C.2: Impedances in the NSR

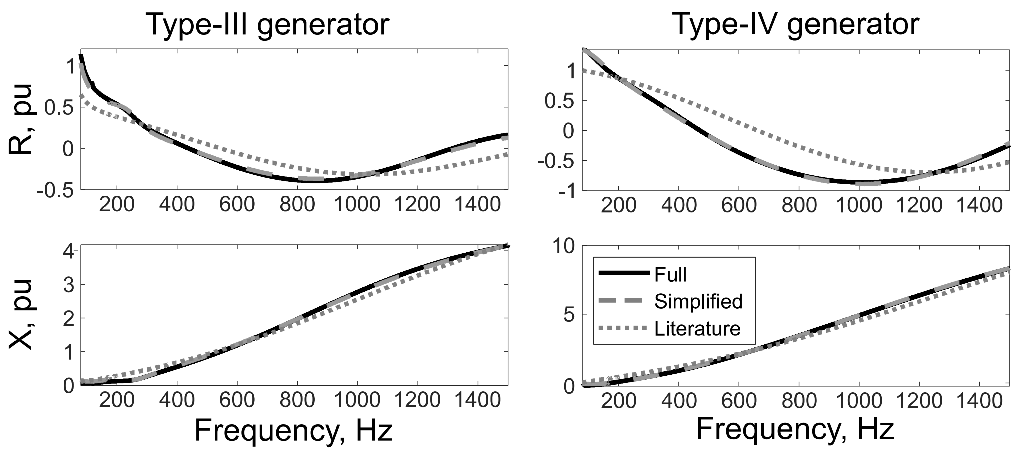

Figure C.3: Impedances in the HFR

APPENDIX D: PLL PERFORMANCE AND TUNING

The PLL plays an important role in the stability of control interactions in the NSR. However, it can also interfere in the SSR if its tunings lead to a large bandwidth. Consider the PLL tunings in Figure D.1, where the original tuning is K_{pPLL}=15 and K_{iPLL}=45, leading to a bandwidth of 2.8 Hz. Notice that larger gains lead to larger bandwidths, and that large proportional gains tend to dominate over the integral gains.

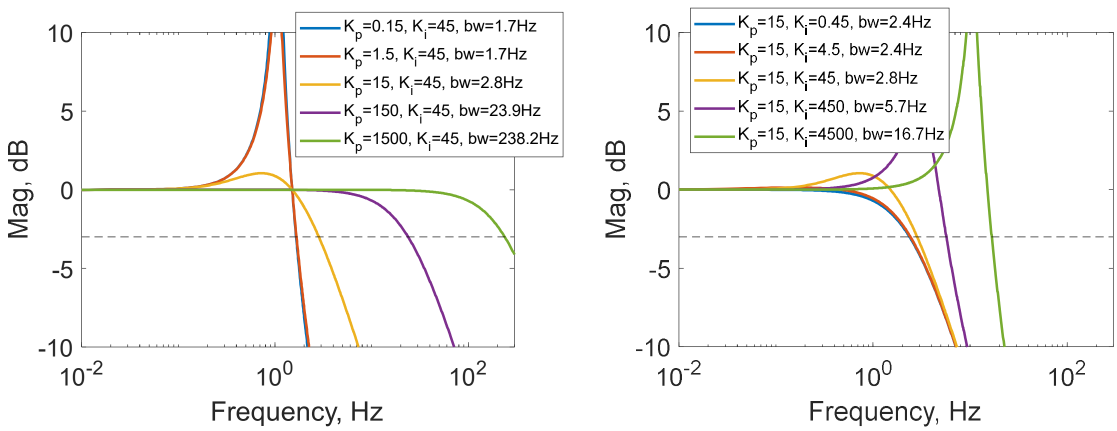

a) K_{pPLL} variation **b) K_{iPLL} variation**

Figure D.1: Bandwidth of the PLL according to its tuning

The step response of the PLL tunings in in Figure D.1, is shown in Figure D.2. Notice that increasing the K_{pPLL} leads outputs with higher damping, whereas increasing the integral gain K_{iPLL} leads to lesser damping. This indicates that tunings with large integral gains and low proportional gains have a greater risk of leading to instability.

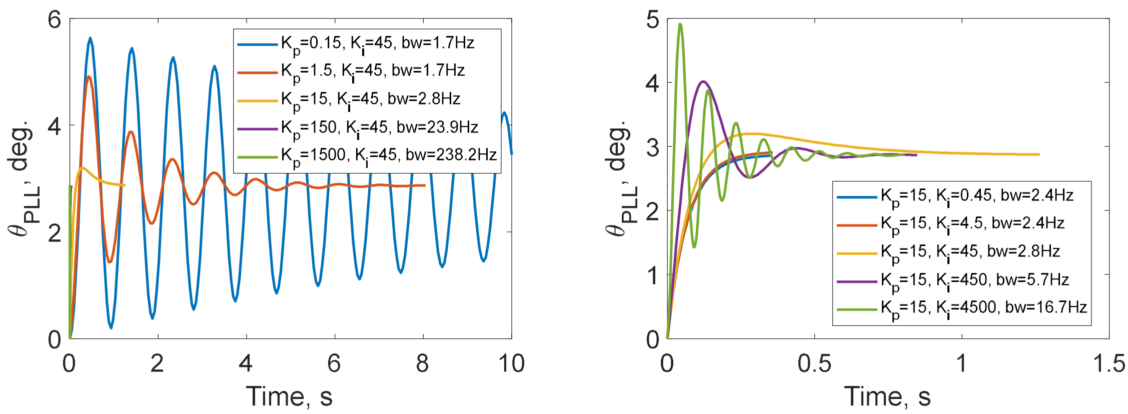

a) K_{pPLL} variation **b) K_{iPLL} variation**

Figure D.2: Response of the PLL to step of Δv_q = 0.05 pu

Appendix E: Real Wind Park Topology

The circuit in Figure E.1 is a real 64 MVA wind park complex in the northeastern region of Brazil with 32 generators, each of 2 MVA. The generators are originally Type-III, but they were changed to Type-IV in the comparative studies. The main transformer couples the grid at 230 kV with the medium voltage feeders at 34.5 kV, and the step-up transformers of each generator couple the medium voltage feeders with the generators at low voltage 0.69 kV. The wind park has a capacitor bank for reactive power compensation, *i.e.*, power factor correction.

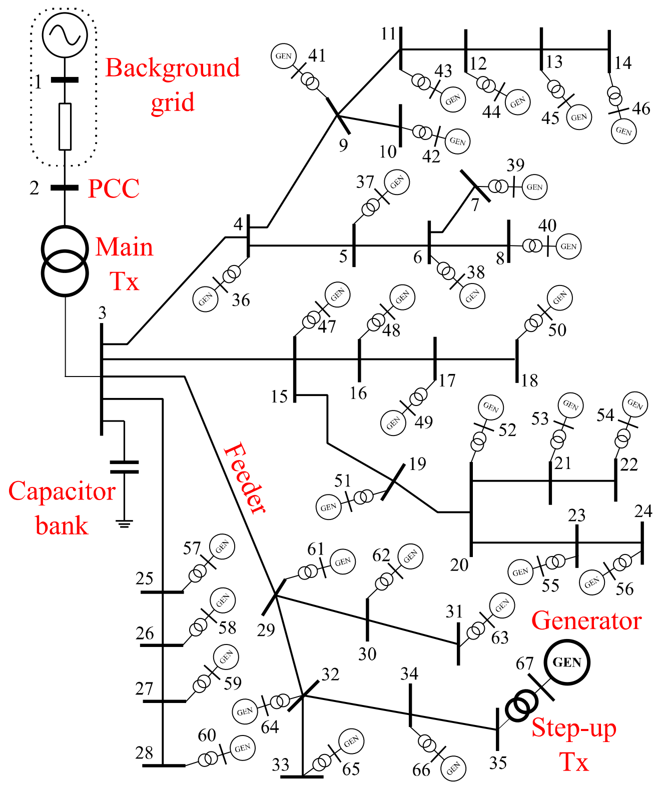

Figure E.1: Single line diagram of real Brazilian wind park

The feeders are underground cable segments modeled as π sections, and the transformers as RL series branches. Overhead (*oh*) line parameters were approximated from the parameters of underground (*ug*) cables with equivalent ampacity with the following relationships (reached after analyzing of a compilation of datasheets):

$$R_{oh} \approx R_{ug} \qquad\qquad L_{oh} \approx L_{ug}/3 \qquad\qquad C_{oh} \approx C_{ug}/25$$

Circuit parameters are shown in Table E.1 and Table E.2.

Table E.1: Wind park feeder and transformer parameters

	Code	R, Ω/km	L, mH/km	C, μF/km	Ampacity, A
Underground cables, 34.5 kV	1	0.3420	0.4270	0.1550	230
	2	0.2470	0.4580	0.1700	300
	3	0.1960	0.4390	0.1830	340
	4	0.0974	0.4000	0.2280	450
Transformer			S, MVA	X_{sc}, pu	X/R
	Main 230/34.5 kV		64	0.15	50
	Step-up 34.5/0.69 kV		2	0.05	50

Table E.2: Feeder segment characteristics

Bus1-Bus2	Code	km	Bus1-Bus2	Code	km
3-4	4	3.68	19-20	3	1.19
4-5	1	1.58	20-21	1	1.43
5-6	1	1.67	21-22	1	1.12
6-7	1	0.83	20-23	1	1.16
6-8	1	1.23	23-24	1	1.64
4-9	2	1.14	3-25	1	1.22
9-10	1	0.92	25-26	1	0.91
9-11	1	1.40	26-27	1	0.78
11-12	1	0.77	27-28	1	0.76
12-13	1	0.89	3-29	2	0.38
13-14	1	0.90	29-30	1	1.31
3-15	4	2.24	30-31	1	0.75
15-16	1	1.67	29-32	1	1.49
16-17	1	1.02	32-33	1	1.51
17-18	1	1.35	32-34	1	1.48
15-19	2	1.00	34-35	1	0.93

APPENDIX F: EXPRESSIONS FOR THIRD ORDER HIGH PASS FILTER

This appendix presents the expressions of the third-order high pass (3HP) filter with the iterative procedure which minimizes the total harmonic distortion of voltage at PCC of the wind park. The impedance $Z_F(h) = R_F(h) + jX_F(h)$ and its derivatives are given are given in terms of R and L, and a variable K was added to simplify the algebra.

$$K = C_2^{-1} = \frac{L+\sqrt{L^2+4R^2}}{2} \qquad h_K = hL - h^{-1}K$$

$$R_F = \frac{h^2RL^2}{R^2+h_K^2} \qquad X_F = \frac{hL(R^2-KL)+h^{-1}LK^2}{R^2+h_K^2} - \frac{1}{hC_1}$$

The first derivatives are:

$$\frac{dR_F}{dR} = \frac{-h^2L^2(R^2-h_K{}^2)+2hRL^2h_K\frac{dK}{dR}}{\left(R^2+h_K{}^2\right)^2} \qquad \frac{dR_F}{dL} = \frac{2h^2RL(R^2-h^{-1}h_KK)+2hRL^2h_K\frac{dK}{dL}}{\left(R^2+h_K{}^2\right)^2}$$

$$\frac{dX_F}{dR} = \frac{2RL^2h^2h_K+hL^2(R^2-h_K{}^2)\frac{dK}{dR}}{\left(R^2+h_K{}^2\right)^2} \qquad \frac{dX_F}{dL} = \frac{\left(hR^2\left(R^2-(2h^{-1}h_KK+h^2L^2)\right)+h^{-1}h_K{}^2K^2\right)+hL^2(R^2-h_K{}^2)\frac{dK}{dL}}{\left(R^2+h_K{}^2\right)^2}$$

$$\frac{dK}{dR} = \frac{2R}{\sqrt{L^2+4R^2}} \qquad \frac{dK}{dL} = \frac{1}{2}\left(1+\frac{L}{\sqrt{L^2+4R^2}}\right)$$

The second derivatives are:

$$\frac{d^2R_F}{dR^2} = \frac{(R^2+h_K{}^2)A_1 + \left(h(R^2-h_K{}^2) - 2Rh_K\frac{dK}{dR}\right)hL^2B_1}{\left(R^2+h_K{}^2\right)^3}$$

$$\frac{d^2X_F}{dR^2} = \frac{(R^2+h_K{}^2)A_2 - \left(2hRh_K + (R^2-h_K{}^2)\frac{dK}{dR}\right)hL^2B_1}{\left(R^2+h_K{}^2\right)^3}$$

$$\frac{d^2R_F}{dLdR} = \frac{d^2R_F}{dRdL} = \frac{(R^2+h_K{}^2)A_3 + \left(h^2(\quad{}^2-h_K{}^2)L^2 - 2hRL^2h_K\frac{dK}{dR}\right)B_2}{\left(R^2+h_K{}^2\right)^3}$$

$$\frac{d^2X_F}{dLdR} = \frac{d^2X_F}{dRdL} = \frac{(R^2+h_K{}^2)A_4 - hL^2\left(2hRh_K + (R^2-h_K{}^2)\frac{dK}{dR}\right)B_2}{\left(R^2+h_K{}^2\right)^3}$$

$$\frac{d^2R_F}{dL^2} = \frac{(R^2+h_K{}^2)A_5 - \left(2h^2RL(R^2-h_Kh^{-1}K) + 2hRL^2h_K\frac{dK}{dL}\right)B_2}{\left(R^2+h_K{}^2\right)^3}$$

$$\frac{d^2X_F}{dL^2} = \frac{\left(R^2 + {h_K}^2\right)A_6 - \left(\left((R^2 - h^2L^2 - 2h^{-1}h_K K)hR^2 + K^2h^{-1}{h_K}^2\right) + hL^2\left(R^2 - {h_K}^2\right)\frac{dK}{dL}\right)B_2}{\left(R^2 + {h_K}^2\right)^3}$$

$$\frac{d^2K}{dR^2} = \frac{2L^2}{\left(\sqrt{L^2+4R^2}\right)^3} \qquad \frac{d^2K}{dLdR} = \frac{d^2K}{dRdL} = \frac{-2RL}{\left(\sqrt{L^2+4R^2}\right)^3} \qquad \frac{d^2K}{dL^2} = \frac{2R^2}{\left(\sqrt{L^2+4R^2}\right)^3}$$

$$A_1 = 2\left(-h^2 - \left(\frac{dK}{dR}\right)^2 + hh_K\frac{d^2K}{dR^2}\right)RL^2$$

$$A_2 = \left(2h_K\left(h^2 + \left(\frac{dK}{dR}\right)^2\right) + h\left(R^2 - {h_K}^2\right)\frac{d^2K}{dR^2}\right)L^2$$

$$A_3 = 2L\begin{pmatrix} h^2\left(hLh_K - R^2 + {h_K}^2\right) - hLh_K\frac{dK}{dL} \\ +hR(hL + 2h_K)\frac{dK}{dR} - RL\frac{dK}{dR}\frac{dK}{dL} + RLhh_K\frac{d^2K}{dLdR} \end{pmatrix}$$

$$A_4 = \begin{pmatrix} 2h^2RL(hL + 2h_K) - 2hRL^2\frac{dK}{dL} + 2hL\left(R^2 - hLh_K - {h_K}^2\right)\frac{dK}{dR} \\ +2L^2h_K\frac{dK}{dR}\frac{dK}{dL} + hL^2\left(R^2 - {h_K}^2\right)\frac{d^2K}{dLdR} \end{pmatrix}$$

$$A_5 = 2\left(h^2R\left(R^2 - (L + h_Kh^{-1})\right) + 2h^2RL^2\frac{dK}{dL} - RL^2\left(\frac{dK}{dL}\right)^2 + hRL^2h_K\frac{d^2K}{dL^2}\right)$$

$$A_6 = \begin{pmatrix} 4h(h^{-2}K(R^2 - h^{-1}(h_K + hL)K) + (h^{-1}K - h_K)hL^2)\frac{dK}{dL} \\ +2(-R^2h^2h_K + K^2h_K) + 2L^2h_K\left(\frac{dK}{dL}\right)^2 + hL^2\left(R^2 - {h_K}^2\right)\frac{d^2K}{dL^2} \end{pmatrix}$$

$$B_1 = 4\left(R - h^{-1}h_K\frac{dK}{dR}\right) \qquad B_2 = 4h_K\left(h - h^{-1}\frac{dK}{dL}\right)$$

APPENDIX G: INITIAL VALUE FOR ITERATIVE FILTER TUNING

Consider the C-type filter in Figure G.1 and the 3HP filter in Figure G.2.

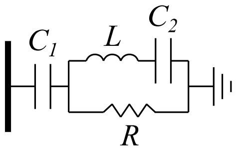

Figure G.1: C-type filter topology

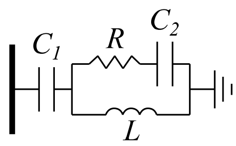

Figure G.2: 3HP filter topology

The normalized resonance frequency h_{res} (in pu of fundamental frequency 60 Hz) of these filters, and their quality factor QF, can be approximated with the following expressions:

$$h_{res} = \frac{1}{\sqrt{L\frac{C_1 C_2}{C_1 + C_2}}} \qquad QF = \frac{h_{res} L}{R}$$

The filter tuning procedures in this thesis set a constraint for C_1 in terms of the reactive power compensation of the original capacitor bank Q_C/S_{WP}, and for C_2 in terms of the filter elements. And the iterative algorithm determines which are the values for R and L that are used to minimize the $\mathrm{THD_V}$ at the PCC of the wind park. The iterative tuning of the filters proposed in this thesis requires to set an initial guess for the values of R and L.

This can be done either randomly, or with the set of expressions shown in Table G.1, in terms of a fixed resonance frequency h_{res} and a fixed quality factor of QF. And by rearranging, the initial guess for the filter parameters can be calculated with the expressions in Table G.2.

Table G.1: Constraints for initial value of filter tuning

C-type	$C_1 = Q_C/S_{WP}$	$C_2 = L^{-1}$	$h_{res} = \sqrt{\frac{C_1 + C_2}{L C_1 C_2}}$	$QF = \frac{h_{res} L}{R}$
3HP		$C_2 = \frac{2}{L + \sqrt{L^2 + 4R^2}}$		

Table G.2: Expressions for initial value of filter tuning

C-type	$C_1 = Q_C/S_{WP}$	$C_2 = C_1\left({h_{res}}^2 - 1\right)$	$L = {C_2}^{-1}$	$R = \frac{h_{res} L}{QF}$
3HP		$C_2 = \left(\frac{2{h_{res}}^2}{1 + \sqrt{1 + 4{h_{res}}^2 QF^{-2}}} - 1\right) C_1$	$L = \frac{C_1 + C_2}{{h_{res}}^2 C_1 C_2}$	

APPENDIX H: PUBLICATIONS

This appendix presents the scientific publications that were elaborated during the period of this Ph.D. research. The following journal papers were published:

1. **A. Argüello**, R. Torquato, W. Freitas, “Method for Assessing the Risk of Subsynchronous Oscillations in DFIG-Based Wind Parks,” accepted for publication on *IEEE Trans. on Power Delivery*;
2. **A. Argüello**, “Setpoint Feasibility and Stability of Wind Park Control Interactions at Weak Grids,” accepted for publication on *Modern Power Systems and Clean Energy Journal (MPCE)*;
3. **A. Argüello**, R. Torquato, W. Freitas, A. Padilha-Feltrin, “Graphical Method to Assess Component Overload due to Harmonic Resonances in Wind Parks,” *IEEE Trans. on Power Delivery*, vol. 36, no. 3, pp. 1819-1828, 2021;
4. **A. Argüello**, M. Rider, “A Discrete Time Domain-Based MILP Framework for Control Parameter Tuning,” *IEEE Systems Journal*, vol. 15, no. 3, pp. 3462-3469, 2021;
5. R. Torquato, **A. Argüello**, W. Freitas, “Practical Chart for Harmonic Resonance Assessment of DFIG-Based Wind Parks,” *IEEE Trans. on Power Delivery*, vol. 35, no. 5, pp. 2233-2242, Oct. 2020;
6. A. Guzmán, **A. Argüello**, J. Quirós-Tortós, G. Valverde, “Processing and Correction of Secondary System Models in Geographic Information Systems,” *IEEE Trans. on Industrial Informatics*, vol. 15, no. 6, pp. 3482-3491, Oct. 2018;

The following journal papers were submitted or are ready for submission:

7. R. Torquato, **A. Argüello**, W. Freitas, “Comparative Analysis Between the Effect of Type III and Type IV Generators on Risk of Harmonic Resonances in Wind Parks,” in first round of revision on *IEEE Trans. on Power Delivery* (TPWRD-00515-2022.R1);
8. **A. Argüello**, R. Torquato, B. Rosado, W. Freitas, “Modeling of Single-Phase Photovoltaic Generators for System-Wide Harmonic Power Flow Studies,” in first round of revision on *IEEE Trans. on Energy Conversion* (TEC-00362-2022.R1);
9. B. Rosado, R. Torquato, **A. Argüello**, W. Freitas, “Harmonic Resonance Assessment on Low Voltage Residential Distribution Systems,” to be submitted to *IEEE Trans. on Power Delivery*.

10. **A. Argüello**, R. Torquato, W. Freitas, **"**Passive Filter Design for Mitigation of Harmonic Resonances in Wind Parks," to be submitted to *IEEE Trans. on Power Delivery*.
11. **A. Argüello**, R. Torquato, W. Freitas, "Simplified Impedance Modeling of Type-III Generators to Study Stability of Control Interactions," to be submitted to *Elsevier Electric Power Systems Journal*;

The following conference papers were published:

12. R. Torquato, **A. Argüello**, W. Freitas, "Practical Methods for Online Monitoring of Harmonic Resonances in DFIG-Based Wind Parks," in Proc. *International Conference on Harmonics and Quality of Power (ICHQP)*, 2022, pp. 1-6;
13. **A. Argüello**, T. Fernandes, "Power quality study of fixed capacitor selection for rotary 1ph-3ph converters in rural facilities," in Proc. *2020 IEEE PES Transmission & Distribution Conference and Exhibition - Latin America (T&D-LA)*, 2020, pp. 1-6;
14. **A. Argüello**, "Simplified Analytic Procedure to Calculate the Electric Variables at Steady State of Type-III and Type-IV Wind Generators," in Proc. *2020 IEEE PES Transmission & Distribution Conference and Exhibition - Latin America (T&D-LA)*, 2020, pp. 1-6;
15. **A. Argüello**, G. Valverde, "Distribution Network Voltage Controller in Presence of Lost Measurements," in Proc. *2020 IEEE PES Transmission & Distribution Conference and Exhibition - Latin America (T&D-LA)*, 2020, pp. 1-6;
16. **A. Argüello**, L. Lugnani, D. Dotta, "DFIG Model Considering Turbine Mechanical Limitations for Frequency Response Control Studies" in Proc. *2019 IEEE PES Innovative Smart Grid Technologies Conference - Latin America (ISGT LA)*, 2019, pp. 1-5;
17. **A. Argüello**, G. Gómez, J. Quirós-Tortós, G. Valverde, "Distribution Network Element Model Parameters: Creation of Database," in *Proc. 2018 IEEE 38th Central America and Panama Convention (CONCAPAN XXXVIII)*, 2018, pp. 1-5;
18. **A. Argüello**, T. Ricciardi, M. Rider, "Control Tuning of Energy Storage Syste3ms based on Operating Point Consistency," in Proc. *2018 IEEE PES Transmission & Distribution Conference and Exhibition - Latin America (T&D-LA)*, 2018, pp. 1-5;
19. **A. Argüello**, W. Cunha, T. Ricciardi, R. Torquato, W. Freitas, "Dynamic Modeling in OpenDSS: An Implementation Sequence for Object Pascal," in Proc. *2018 IEEE Power & Energy Society General Meeting (PESGM)*, 2018, pp. 1-5.